

2021-08

Quantum chemical investigation of nitrogen containing substituted derivatives of thiophene of astrophysical interest

SIMBIZI, René

UB, Doctoral School of the University of Burundi

<https://repository.ub.edu.bi/handle/123456789/742>

Téléchargé depuis le dépôt institutionnel officiel de l'Université du Burundi



University of Burundi
Department of Physics
Doctoral School of the University
of Burundi

QUANTUM CHEMICAL INVESTIGATION OF
NITROGEN CONTAINING SUBSTITUTED DERIVATIVES OF
THIOPHENE OF ASTROPHYSICAL INTEREST

By
René SIMBIZI

*A thesis submitted for the degree of Doctor of
Philosophy
in
Astrophysics*

Orientation: Astrochemistry

Supervisors: Prof. Godefroid GAHUNGU (UB)
Prof. Minh Tho NGUYEN (KU Leuven)

Bujumbura, August 16, 2021

Composition of the thesis jury

Prof. Théophile NDIKUMANA	University of Burundi	President
Prof. Hippolyte NYENGERI	University of Burundi	Secretary
Prof. Daniel Escudero	KU Leuven	Member
Prof. Sébastien NIYONZIMA	University of Burundi	Member
Prof. Godefroid GAHUNGU	University of Burundi	Member
Prof. Minh Tho NGUYEN	KU Leuven	Member

Dedication

To my Wife,
To my Children,
To my late Father,
To my Mother,
To my Sisters and Brothers and their families,

for their love, encouragement, ...

Acknowledgements

First and foremost I would like to express my sincere gratitude to my supervisors Prof. Gahungu Godefroid and Prof. Minh Tho Nguyen, who have provided indebtedness and unwavering support and guidance throughout the course of the PhD program. This thesis is a result of their consistent encouragement and the fruitful discussions I had with them.

I would like to thank the Flemish Interuniversity Council, University Development Cooperation (VLIR-UOS) who has funded my stay at KU Leuven via the IUC project with University of Burundi. I thank too the Chinese Ministry of Sciences and Technology through the China-Africa Science and Technology Partnership (CASTEP) which has provided the Gaussian program to the University of Burundi.

My sincere thanks are also addressed to the members of the CRSNE (Centre de Recherche en Sciences Naturelles et de l'Environnement) who accepted me in their research center. Many thanks also to members of the CRMP (Centre de Recherche en Mathématiques et Physique) for their invaluable support. I'd like to thank too the computational research group of Minh Tho Nguyen at KU Leuven for their warm welcome and their unwavering support. I'm grateful also to Prof Jules Tshishimbi Muya of university of Kinshasa. His advice and encouragement during my stay at KU Leuven have been of great importance to my work.

Special thanks are due to my dear wife Nibogora Médiatrice and my two sons Ingabire Francis de Bonheur and Iradukunda Tony Charmant for their indefectible support. Their patience, their prayers, their encouragement always strengthened my morale by standing by me in all situations.

Most importantly, I wish to thank my parents: my late father Kazungu François and my mother Nzirorera Denise. They spared no effort in order to make me who I am today. I sincerely thank them.

Last but not the least, I address many thanks to my brother and sisters and their families and to you all who, in this way or another, have contributed to the completion of this hard work. Words cannot express my gratitude and appreciation for the support you provided to my work.

List of papers

This thesis is based on the collection of papers given below.

1. **Simbizi, R.**, Gahungu, G. and Nguyen, M.T., 2020. Molecular structure, IR, Raman and UV–VIS spectra of 2-cyanothiophene and 3-cyanothiophene: A comparative quantum chemical investigation. *Spectrochimica Acta Part A: Molecular and Biomolecular Spectroscopy*, 239, p.118393.
2. **Simbizi, R.**, Gahungu, G. and Nguyen, M.T., 2020. Hyperfine structures of 2-cyanothiophene and 3-cyanothiophene: A quantum chemical study. *Molecular Astrophysics*, 21, p.100099.
3. **Simbizi, R.**, Gahungu, G. and Nguyen, M.T., 2020. Theoretical investigation of protonated thiophene and two of its nitrile substituted derivatives (2-cyanothiophene and 3-cyanothiophene). *Physical Chemistry Chemical Physics*, 22(42), pp.24735-24743.

Abstract

Spectroscopic, experimental or theoretical data needed for the detection of new species in the interstellar medium (ISM) are missing or incomplete for five- and six-membered ring substituted derivatives. Besides spectroscopic information, geometrical structures and thermodynamical data, experimental and/or theoretical, are also missing for such species to fully characterize them in the ISM. To supplement the existing literature information and supply new data valuable for the characterization and detection of new species in the ISM, quantum chemical calculations, including geometrical optimizations, simulated IR, Raman and UV-VIS spectra, as well as rotational parameters need in rotational spectra computing, are carried out for 2-cyanothiophene (2CNT) and 3-cyanothiophene (3CNT) and some of their isotopologues and protonated forms. Following empirical corrections for systematic deficiencies of methods and basis sets to adjust geometrical parameters, the molecular geometry for the parent thiophene was determined and an excellent agreement with experiment achieved. An agreement between the available experimental and calculated values for the fundamental vibrational frequencies of the parent compound (thiophene) was also fulfilled. The same strategy was subsequently used for both cyano derivatives 2-cyanothiophene (2CNT and 3CNT). Geometrical parameters and thereby rotational, centrifugal, quadrupole constants, dipole moments, etc, of cyanothiophene derivatives and some of their isotopologues have thus been obtained. The structures that were obtained as mentioned above, are expected to be close to the corresponding experimental ones. A complete description of the IR and Raman spectra including IR frequency assignment and potential energy distribution (PED) analysis is provided. The IR and Raman spectra for deuterated and protonated forms and UV-VIS spectra for thiophene, 2CNT and 3CNT are also analyzed. Rotational spectra for 2CNT, 3CNT and some isotopologues are analyzed. ^{14}N , ^{33}S and ^2H quadrupole hyperfine constants, dipole moments for 2CNT, 3CNT, $^{33}\text{S}\text{-}^{2}\text{C}^{15}\text{NT}$, $^{33}\text{S}\text{-}^{3}\text{C}^{15}\text{NT}$, $^{2}\text{C}^{15}\text{NT}\text{-}^{3}\text{D}$ and $^{2}\text{C}^{15}\text{NT}\text{-}^{2}\text{D}$, $^{2}\text{CNTH}^+$ and $^{3}\text{CNTH}^+$ are also calculated and the corresponding hyperfine structures analyzed. Rotational lines intensities and line profiles are also discussed. Strongest transition lines and optimum regions of detectability are discussed too. Regarding thermodynamical properties, the proton affinity (PA) of R–CN, enthalpy, entropy as well as the Gibbs free energy changes ($\Delta_r\text{H}$, $\Delta_r\text{S}$ and $\Delta_r\text{G}$) for reactions producing R–CNH⁺ and R–CND⁺ are computed at G2(MP2) and G3B3 levels of theory at different temperatures and at two pressures (i.e., 1 and 10^{-5} atm) (here R≡C₄H₃S or H). The spontaneity for different reactions of formation of cyanothiophenes, their deuterated and protonated forms are also explored at different ISM environmental conditions. The analysis of calculated values of $\Delta_r\text{H}$, $\Delta_r\text{S}$ and $\Delta_r\text{G}$ for reactions yielding C₄H₃S–CN, C₄H₃S–CNH⁺ and C₄H₃S–CND⁺ reveals that, in the same way as in cases of reactions relating to HCN, all the reactions are spontaneous at different conditions. Similarly, the investigation on PA calculations shows that the protonation favors the nitrogen atom for cyanothiophenes and the α -sites for the thiophene rings. The present computed molecular data are intended to assist astro-scientists in the search of these species in the ISM.

Résumé

Les données spectroscopiques, expérimentales ou théoriques nécessaires dans l'identification de nouvelles espèces moléculaires telles que les dérivés substitués de cycles à cinq et six chaînons dans le milieu interstellaire (ISM) sont manquantes ou incomplètes. Outre les informations spectroscopiques, les structures géométriques et les données thermodynamiques, expérimentales et/ou théoriques, sont également manquantes pour que ces espèces soient complètement caractérisées dans le ISM. Pour compléter les informations existantes et fournir de nouvelles et fiables données nécessaires pour la caractérisation et l'identification de nouvelles espèces dans le ISM, des calculs utilisant les méthodes de la chimie quantique, y compris l'optimisation géométrique, simulation des spectres IR, Raman et UV-VIS, ainsi que le calcul des paramètres rotationnels nécessaires à la simulation des spectres rotationnels, sont effectués pour le 2-cyanothiophène (2CNT) et 3-cyanothiophène (3CNT) et certains de leurs isotopologues et formes protonées. Par des corrections empiriques des erreurs systématiques dues aux méthodes, en plus de petits ajustements basés sur certains paramètres géométriques, la géométrie moléculaire du thiophène (molécule mère) a été obtenue avec un excellent accord avec la géométrie expérimentale. Un accord entre les valeurs expérimentales disponibles et calculées pour les fréquences fondamentales de vibration du thiophène a également été observée. La même stratégie est donc ensuite appliquée aux dérivés substitués du thiophène, notamment, 2-cyanothiophène (2CNT) et 3-cyanothiophène (3CNT) et leurs isotopologues. Des paramètres géométriques, en particuliers, les constantes rotationnelles, centrifuges et quadrupolaires, les moments dipolaires, etc, des cyanothiophènes et quelques uns de leurs isotopologues sont obtenus. On s'attend à ce que les structures obtenues suivant la procédure ci-haut décrite soient proches des structures expérimentales correspondantes. Une description complète des spectres IR et Raman, y compris l'attribution de fréquences IR sur base de la distribution d'énergie potentielle (PED) a été aussi effectuée. Les spectres IR et Raman pour les formes deutérées et protonées et les spectres UV-VIS pour le thiophène, 2CNT et 3CNT sont analysés. Les spectres rotationnels pour 2CNT, 3CNT, leurs formes protonées et certains isotopologues sont également étudiés. Ainsi, les constantes de couplage hyperfine relatives aux noyaux quadrupolaires ^{14}N , ^{33}S et ^2H , les moments dipolaires pour 2CNT, 3CNT, ^{33}S -2C ^{15}NT , ^{33}S -3C ^{15}NT , 2C ^{15}NT -3D et 2C ^{15}NT -2D, 2CNT H^+ et 3CNT H^+ sont calculés et les structures hyperfines correspondantes analysées. Les intensités des raies des transitions rotationnelles et leurs profils sont aussi discutées. Les raies des transition les plus fortes et les régions optimales de détectabilité de ces différents composés sont aussi explorées. Des propriétés thermodynamiques telles que l'affinité du proton (PA) de R-CN (R=C $_4\text{H}_3\text{S}$ ou H), les variations d'enthalpie, d'entropie, mais aussi d'énergie libre de Gibbs ($\Delta_r\text{H}$, $\Delta_r\text{S}$ et $\Delta_r\text{G}$) pour les réactions produisant R-CN H^+ et R-CN D^+ sont calculées par les méthodes G2(MP2) et G3B3 pour différentes températures régnant dans le ISM et à deux pressions (1 et 10^{-5} atm). La spontanéité des différentes réactions conduisant à la formation des cyanothiophènes, leurs formes deutérées et protonées sont également explorées dans différentes conditions environnementales du ISM. L'analyse des valeurs calculées des variations $\Delta_r\text{H}$, $\Delta_r\text{S}$ et $\Delta_r\text{G}$ pour les réactions conduisant à C $_4\text{H}_3\text{S}$ -CN, C $_4\text{H}_3\text{S}$ -CN H^+ et C $_4\text{H}_3\text{S}$ -CN D^+ révèle que, comme celles relatives à HCN, toutes les réactions sont spontanées dans les différentes conditions considérées. De même, l'étude des calculs de PA montre que la protonation favorise l'atome d'azote pour les cyanothiophènes et le site α pour les cycles thiophéniques. Les résultats de cette thèse sont destinés à aider les astro-scientistes dans la recherche de ces espèces dans le ISM.

Contents

Composition of the thesis jury	i
Dedication	ii
Acknowledgements	iii
List of papers	iv
Abstract	v
Résumé	vi
Contents	vii
List of Figures	x
List of Tables	xi
Forward	xiv
1 General introduction	1
1.1 Context	1
1.2 Literature survey	1
1.3 Objectives	3
1.4 Importance of our results	4
1.5 References	5
2 Interstellar medium (ISM)	8
2.1 Interstellar matter	8
2.2 Physical properties and chemical composition of molecular clouds	9
2.2.1 Physical properties	9
2.2.2 Interstellar molecular abundance	12
2.3 Interstellar chemistry	15
2.4 Radiative transitions	17
2.4.1 Spontaneous emission, absorption and stimulated emission	17
2.4.2 Absorption cross section	19
2.4.3 Oscillator strength	19
2.4.4 Widths and line profiles	19
2.4.4.1 Natural broadening	20
2.4.4.2 Collisional and pressure broadening	21
2.4.4.3 Doppler or thermal broadening	21
2.5 References	22
3 Electronic structure calculation	26

3.1	Born-Oppenheimer approximation	26
3.2	Theory of molecular orbitals	29
3.3	Variational principle	32
3.4	ab initio methods	33
3.4.1	Hartree-Fock approximation	33
3.4.2	Post-Hartree-Fock methods	35
3.4.2.1	Configuration interaction (CI)	36
3.4.2.2	Multi-configurational methods: MCSCF and MRCI	37
3.4.2.3	Perturbative methods	37
3.4.3	Density functional theory (DFT)	39
3.4.3.1	The Hohenberg-Kohn theorem	40
3.4.3.2	Kohn-Sham (KS) equations	41
3.4.3.3	Hybrid density functional theory	42
3.4.4	Gaussian-n (G_n) theory	43
3.4.5	Basis sets	44
3.4.5.1	Slater type functions	44
3.4.5.2	Gaussian type functions	45
3.5	Gaussian software	46
3.5.1	Introduction	46
3.5.2	Electronic transitions	47
3.5.3	Molecular vibrations	48
3.5.3.1	Theory of molecular IR spectra	48
3.5.3.2	Molecular Raman transitions	51
3.5.4	Molecular rotations	53
3.5.5	Molecular thermodynamic properties	56
3.6	References	58
4	Molecular structure, IR, Raman and UV-VIS spectra of 2-cyano- thiophene and 3-cyanothiophene	62
4.1	Introduction	62
4.2	Computational details	64
4.3	Results and discussion	65
4.3.1	Molecular geometry	65
4.3.2	Effects of CN substitution in α - and β -position in compound 1	69
4.3.3	Vibrational Frequencies and Assignment	69
4.3.3.1	C-H and C-D vibrational modes.	77
4.3.3.2	C=C and C-C modes of vibration.	81
4.3.3.3	S-C modes of vibrations	81
4.3.3.4	C \equiv N vibrations.	81
4.3.4	UV-VIS spectra	82
4.4	Summary	85
4.5	References	85
5	Rotational spectra and hyperfine structures of 2-cyanothiophene and 3-cyanothiophene	89
5.1	Introduction	89
5.2	Computational details	91
5.3	Results and discussion	91
5.3.1	Molecular geometry	91
5.3.2	Microwave spectra	92
5.3.2.1	Rotational parameters and dipole moments.	92
5.3.2.2	Rotational spectra.	93
5.3.2.3	Isotopic analysis	96

5.3.2.4	Hyperfine structure analysis and optimum region of detectability. .	97
5.4	Summary	108
5.5	References	108
6	Thermodynamics of protonation of thiophene, 2-cyanothiophene and 3-cyanothiophene	111
6.1	Introduction	111
6.2	Computational details	113
6.3	Results and discussion	114
6.3.1	Geometrical parameters	114
6.3.2	Sites of protonation of thiophene and of its nitrile substituted derivatives.	115
6.3.3	Enthapy, Gibbs free energy changes and entropy changes (Δ_rH , Δ_rG and Δ_rS) of the reactions producing HCN, 2CNT, 3CNT and their protonated forms	119
6.3.4	Vibrational spectrum of H-CNH ⁺ <i>vs</i> vibrational spectrum of 2CNTH ⁺ and 3CNTH ⁺	123
6.3.5	Rotational spectrum of H-CNH ⁺ <i>vs</i> rotational spectrum of 2CNTH ⁺ and 3CNTH ⁺	130
6.4	Conclusions	134
6.5	References	134
7	General conclusions	138
A	Appendix	140
A.1	Geometric structure corrections	140

List of Figures

2.1	Absorption, Spontaneous Emission and Stimulated emission.	17
3.1	Bonding and antibonding orbitals in the molecule formed by atom A and B	30
3.2	Bonding and antibonding energy levels for $H_{BB} \gg H_{AA}$	31
3.3	Schematic view of the adiabatic potential curve (Electrical potential energy versus the internuclear separation).	47
3.4	Elastic and inelastic scatterings	52
4.1	M06-2X/6-31G(d,p) optimized geometries for (a) thiophene, (b) 2CNT and (c) 3CNT; yellow: S, gray=C, blue=N and light gray=H	65
4.2	M06-2X/6-31G(d,p) computed gas phase IR spectra (Figures 4.2a for 8 and 4.2b for 9) and Raman spectra (Figures 4.2c for 8 and 4.2d for 9).	79
4.3	M06-2X/6-31G(d,p) computed gas phase IR spectra (Figures 4.3a for deuterated 8 and 4.3b for deuterated 9) and Raman spectra (Figures 4.3c for deuterated 8 and 4.3d for deuterated 9).	80
4.4	Gas phase computed UV-Visible spectrum of compounds 1 , 8 & 9 using TD-M06-2X/6-31G(d,p).	83
4.5	Plots of main Molecular Orbitals involved in the electronic transitions.	84
5.1	Simulated rotational spectra for 8 (in red color), 9 (green color) and thiophene (blue color) at temperature $T = 10$ K.	96
5.2	Rotational spectra of 8 (5.2a) and 9 (5.2b) for temperatures $T = 8.6$ (red), 10.0 (green), 30.0 (blue) and 150.0 K (magenta color).	101
5.3	Hyperfine spectra of (a) $2C^{14}NT$ (1), $2C^{15}NT-3D$ (2) and $^{33}S-2C^{15}NT$ (3); (b) $3C^{14}NT$ (1), $^{33}S-3C^{15}NT$ (2) and $3C^{15}NT-2D$ (3) (red, green and blue colors for ^{14}N , ^{33}S and 2H quadrupolar nuclei, respectively) for $T = 10$ K.	103
6.1	M06-2X/6-31G(d,p) optimized geometries for (a) $HCNH^+$, (b) $2CNTH^+$ and (c) $3CNTH^+$; yellow: S, gray=C, blue=N and light gray=H.	114
6.2	Partial atomic charges calculated at HF/def2-def2-QZVPP using MKS model for (a) 2CNT and (b) 3CNT.	118
6.3	M06-2X/6-31G(d,p) gas phase simulated IR spectra of (a) $HCNH^+$, (b) $2CNTH^+$ and (c) $3CNTH^+$	127
6.4	M06-2X/6-31G(d,p) gas phase simulated Raman spectra of (a) $HCNH^+$, (b) $2CNTH^+$ and (c) $3CNTH^+$	129
6.5	Plots of rotational line transition intensities (including ^{14}N hyperfine quadrupole couplings) for (a) $HCNH^+$ and (b) $3CNTH^+$	131
6.6	Comparison of ^{14}N quadrupole hyperfine spectra of (a) $2CNTH^+$ and (b) $3CNTH^+$ for different temperatures ($T = 7, 10, 30, 100$ and 300 K).	131

List of Tables

2.1	The Interstellar gas phases.	9
2.2	Some interstellar sources of molecules	12
2.3	Molecules in the Interstellar Medium or Circumstellar Shells (as of 02/2020)	14
3.1	Possibilities of representation for an asymmetric molecule	55
4.1	Experimental and achieved geometries for 1 , 8 and 9 after empirical adjustments to some geometrical parameters (distances in Å°, angles in °).	67
4.2	Experimental <i>vs</i> calculated rotational constants (with empirical corrections), and dipole moments (M06-2X/6-31G(d,p)).	68
4.3	Experimental <i>vs</i> M06-2X/6-31G(d,p) calculated (from geometry with empirical corrections) frequencies (cm ⁻¹) for 8 and corresponding scaling factors.	70
4.4	Experimental <i>vs</i> M06-2X/6-31G(d,p) calculated (from geometry with empirical corrections) frequencies (cm ⁻¹) for 9 and corresponding scaling factors.	71
4.5	Potential energy distribution for 8	71
4.6	Potential energy distribution for 9	72
4.7	M06-2X/6-31G(d,p) calculated frequencies (cm ⁻¹), infrared intensities (km. mol ⁻¹) and Raman activities (Å ⁴ /amu) and Raman intensities (×10 ⁻²⁴ F ² .m ⁻¹ .kg ⁻¹) for compounds 8 and 9	74
4.8	Calculated frequencies (cm ⁻¹), infrared intensities (km. mol ⁻¹) and Raman activities (Å ⁴ /amu) and Raman intensities (×10 ⁻²⁴ F ² .m ⁻¹ .kg ⁻¹) for deuterated forms of 8 and 9	75
4.9	Potential energy distribution for the deuterated form of 8	75
4.10	Potential energy distribution for the deuterated form of 9	78
4.11	Lowest valence excited singlet states of 1 , 8 and 9 obtained using the TD-DFT (M06-2X/6-31G(d,p) method).	82
5.1	M06-2X/6-31G(d,p) best predicted after empirical corrections structures of 9 and 8 isotopologues (distances in Å°, angles in °)	92
5.2	Experimental and M06-2X/6-31G(d,p) calculated rotational parameters for 8 , ³³ S-2C ¹⁵ NT and 2C ¹⁵ NT-3D (a deuterated form of 8).	93
5.3	Experimental and M06-2X/6-31G(d,p) calculated rotational parameters for 9 , ³³ S-3C ¹⁵ NT and 3C ¹⁵ NT-2D (deuterated form of 9).	94
5.4	Comparison of experimental and calculated (using calculated rotational parameters in Table 5.2) rotational transitions and their corresponding frequencies ν (in MHz) for 9 , 8 and thiophene	95
5.5	Strongest microwave lines with corresponding hyperfine splitting components for 8 at 8.6, 9.375, 10.0 and 30.0 K.	98
5.6	Selected strongest line transitions and the corresponding hyperfine splitting components of 9 at different temperatures.	99
5.7	Hyperfine structures for deuterated 2C ¹⁵ NT – d ₃ and 3C ¹⁵ NT – d ₂ ; for ³³ S – 2C ¹⁵ NT and ³³ S – 2C ¹⁵ NT at 10.0 K.	100
5.8	Experimental and computed hyperfine splittings for 8	102
5.9	Experimental and computed hyperfine splittings for 9	103

5.10	Line profile parameters for stronger lines computed from the calculated χ_{aa} , χ_{bb} , χ_{cc} and χ_{ab} hyperfine constants at 10.0 K for 8	105
5.11	Line profile parameters for stronger lines computed from the calculated χ_{aa} , χ_{bb} , χ_{cc} and χ_{ab} hyperfine constants at 10.0 K for 9 (frequency in MHz, FWHM in kHz).	106
5.12	Line profiles for the first strongest lines for deuterated $2C^{15}NT - d_3$ and $3C^{15}NT - d_2$; for $^{33}S - 2C^{15}NT$ and $^{33}S - 2C^{15}NT$ at 10.0 K.	107
6.1	M06-2X/6-31G(d,p) structures (with empirical corrections) for $2CNTH^+$, $3CNTH^+$ and $HCNH^+$ (bond lengths and angles in Å and °).	114
6.2	Proton Affinity (PA in kJ/mol) of thiophene at different sites, for different levels of theory and at $T = 298$ K and $T = 10$ K.	115
6.3	G2(MP2) and G3B3 Proton Affinity (PA in kJ/mol) of 2CNT, 3CNT and HCN at different sites for $T = 298$ K.	115
6.4	Comparison of G2(MP2) and G3B3 Proton Affinity (PA in kJ/mol) computed at different sites of 2CNT and 3CNT for $T = 298$ K and $T = 150$ K.	116
6.5	Comparison of G2(MP2) and G3B3 Proton Affinity (PA in kJ/mol) computed at different sites of 2CNT and 3CNT for $T = 10$ K and $T = 5$ K.	116
6.6	MKS B3LYP/cc-pVQT calculated partial atomic charges (in electrons e) for 2CNT, 3CNT and HCN at $T = 298$ K	117
6.7	G2(MP2) Proton Affinity (PA in kJ/mol) at different sites of some dicyanothiophenes at $T = 10$ and 298 K.	119
6.8	Relationship between the reaction spontaneity and temperature.	119
6.9	Gase phase G2(MP2) and G3B3 calculated enthalpy, entropy and Gibbs free energy changes ($\Delta_r H$, $\Delta_r S$ and $\Delta_r G$ in kJ mol^{-1}) of reaction producing hydrogen cyanide, cyanothiophenes and their protonated forms ($T = 298$ K and $T = 10$ K for $P = 10^{-5}$ atm).	120
6.10	Gase phase G2(MP2) and G3B3 calculated enthalpy, entropy and Gibbs free energy changes ($\Delta_r H$, $\Delta_r S$ and $\Delta_r G$ in kJ mol^{-1}) of the reactions yielding hydrogen cyanide, cyanothiophenes and their protonated forms ($T = 298$ K and $T = 10$ K for $P = 1$ atm).	120
6.11	Gase phase G3B3 calculated enthalpy, entropy and Gibbs free energy changes for the reactions ($\Delta_r H$ and $\Delta_r G$ in kJ mol^{-1}) producing hydrogen cyanide, cyanothiophenes and their protonated forms ($T = 1000$ K and $T = 5$ K for $P = 10^{-5}$ atm).	121
6.12	Gase phase G2(MP2) calculated enthalpy, entropy and Gibbs free energy changes ($\Delta_r H$, $\Delta_r S$ and $\Delta_r G$ in kJ mol^{-1}) of the reactions producing $2CNTD^+$ and $2CNTD^+$ ($T = 298$ K and $T = 10$ K for $P = 10^{-5}$ atm).	122
6.13	Potential energy distribution for $2CNTH^+$	123
6.14	Potential energy distribution for $3CNTH^+$	124
6.15	M06-2X/6-31G(d,p) calculated frequencies (cm^{-1}), infrared intensities (km. mol^{-1}) and Raman activities ($\text{Å}^4/\text{amu}$) and Raman intensities ($\times 10^{-24} \text{F}^2 \cdot \text{m}^{-1} \cdot \text{kg}^{-1}$) for $2CNTH^+$ and $3CNTH^+$	128
6.16	Potential energy distribution for stretching and bending modes of $HCNH^+$ and IR intensities.	129
6.17	M06-2X/6-31G(d,p) calculated (including empirical corrections) rotational constants, and dipole moments.	130
6.18	M06-2X/6-31G(d,p) calculated frequencies and intensities for hyperfine structures of $HCNH^+$ and for strongest rotational lines of $2CNTH^+$ at 10 K.	132
6.19	M06-2X/6-31G(d,p) calculated frequencies and intensities for hyperfine strongest lines of $2CNTH^+$ and $3CNTH^+$ at 10 K.	133
A.1	Geometrical parameters of 1 (bond lengths in Å, bond angles in °) and rotational constants (in GHz) calculated at different levels of theory	141
A.2	Differences between experimental and calculated geometrical (bond lengths in Å, bond angles in °) and rotational parameters (A, B and C in GHz) at different levels of theory for 1	142

A.3	Geometrical parameters of 8 (bond lengths in Å, bond angles in °) and rotational constants (in GHz) calculated at different levels of theory	143
A.4	Geometrical parameters of 9 (bond lengths in Å, bond angles in °) and rotational constants (in GHz) calculated at different levels of theory	144
A.5	Variation of rotational constants of 1 , 8 and 9 with respect to the bond lengths variation.	145
A.6	Corrections for 1 geometrical parameters (bond lengths in Å, bond angles in degree) and their predicted values from analysis of compounds 2 , 3 , 4 , 5 , 6 and 7	146
A.7	Experimental and Calculated frequencies (cm^{-1}), infrared intensities (km mol^{-1}) and Raman activities ($\text{Å}^4/\text{amu}$) and Raman intensities ($\times 10^{-24} \text{F}^2 \cdot \text{m}^{-1} \cdot \text{kg}^{-1}$) of deuterated form of 1	149
A.8	Corrections for 8 geometrical parameters (bond lengths in Å, bond angles in degree) and their predicted values from analysis of similar compounds	150
A.9	Corrections for 9 geometrical parameters (bond lengths in Å, bond angles in degree) and their predicted values from analysis of similar compounds.	153
A.10	(continued)	154
A.10	(continued)	155
A.11	Difference between the original quantum chemical and the final results for geometrical and rotational parameters of 1 , 8 and 9 (distances in Å, angles in ° and rotational constants in MHz).	156
A.12	Experimental <i>vs</i> calculated frequencies (cm^{-1}), infrared intensities ($\text{km} \cdot \text{mol}^{-1}$) and Raman activities ($\text{Å}^4/\text{amu}$) and Raman intensities ($\times 10^{-24} \text{F}^2 \cdot \text{m}^{-1} \cdot \text{kg}^{-1}$) for 1	157
A.13	Potential energy distribution of fundamental vibrational modes of the compound 1	157
A.14	Experimental and M06-2X/6-31G(d,p) (with empirical corrections) calculated rotational parameters.	159
A.15	Comparison of experimental and calculated (from M06-2X/6-31G(d,p) results) rotational transitions and their corresponding frequencies (in MHz) for ^{34}S -3CNT and ^{15}N -3CNT	160
A.16	MKS and NPA HF/def2-QZVPP calculated partial atomic charges for thiophene and NPA B3LYP/def2-QZVPP calculated partial atomic charges for 9	161

FORWARD

Thiophene and its substituted derivatives are among not-yet detected five-membered ring molecules in the interstellar medium (ISM). For this reason, in this thesis, the author provides a thoughtful quantum chemical based study of cyanothiophenes, some of their isotopologues and their protonated forms which could help astrochemists and astrophysicists in the search of new molecular species in the ISM. This study is therefore undertaken in the aim of providing reliable geometrical structures and spectroscopic data, such as UV-VIS, IR, Raman and microwaves results lacking in the literature and which are also needed for their ISM identification.

The chapter 2 provides a brief overview on the physics and chemistry of the ISM. Chapter 3 presents the electronic structure calculations. Chapter 4 deals with molecular structure, IR, Raman and UV-VIS spectra of 2-Cyanothiophene and 3-Cyanothiophene through quantum chemical study. Chapter 5 discusses the rotational spectra as well as hyperfine structures of 2-cyanothiophene and 3-cyanothiophene. Chapter 6 explores theoretically the protonation of thiophene and two of its nitrile substituted derivatives such as the 2-Cyanothiophene and 3-Cyanothiophene, the production of protonated and non-protonated forms in the ISM and the characterization protonated forms based on their IR and microwave spectra. Lastly, the chapter 7 gives a general conclusion, whereas the following part A corresponds to the appendix.

GENERAL INTRODUCTION

1.1 Context

The *Earth*, the planet on which we live, is not an isolated island in space. It is, however, located in the middle of many other universe objects which may, in one way or another, influence its behaviour or the behaviour of its content. Indeed, the Earth is the third of the eight largest planets orbiting the *Sun*, which with the sun and other numerous moons, asteroids, comet materials, rocks, and dust are gravitationally bound in the so-called *Solar system*. Likewise, the Sun is one of the hundreds of billions of stars in the *Milky Way Galaxy*, which in turn is one among the billions of galaxies in the *Universe*^[1]. Galaxies in the *Universe* are, in turn, gravitationally organized into groups, clusters and superclusters, a galaxy being a bound system of stars, gas, dust and dark matter^[2,3].

Since the launch of Sputnik **1**, the first artificial Earth satellite, by the Soviet Union on October 4th, 1957^{[4][5]} up to now, a great number of space missions have been undertaken essentially by governments. The reasons for this passion of the space exploration are numerous. Governments have by then invested significantly in this area not only for scientific effects, but also for exhibiting national prestige and power, enhancing national security and military strength, and many other benefits to the general public. Of the benefits to the general public, numerous meteorologic and telecommunication satellites are orbiting the Earth and provide instantaneous corresponding information.

To fully understanding the complexity of the universe, a multidisciplinary interplay is required. On one hand, understanding its physical properties and dynamical behavior is of central interests for many areas of astronomy and astrophysics^[6]. These areas include the formation and evolution of galaxies and stars, cosmic nucleosynthesis, the origin of large complex, prebiotic molecules and the abundance, structure and growth of dust grains which constitute the fundamental building blocks of planets, etc. All these processes are intimately coupled to the physics of the interstellar medium (ISM). Likewise, on a large scale, understanding the structure and physical properties of the intergalactic medium (IGM) and its relation to galaxies has also intrigued researchers in astronomy and astrophysics^[7]. On the other hand, understanding the complex organic molecules formation, the ISM and IGM chemical evolution and the modelling and explanation of diverse chemical processes in the ISM and IGM has been the subject of numerous research works in astrochemistry, whereas the question about the evolution of life on Earth and the existence of life elsewhere through out the universe has been the origin of the new branch, i.e., the astrobiology^[8]. Knowledge of how atoms, molecules, ions, and free radicals interact outside of Earth's atmosphere contributes to the comprehension of geological processes on other planets and the conditions under which life might form on other planets and in outer space. Indeed, understanding the organic chemistry in molecular clouds, comets, and meteorites and their common link brings out constraints for the processes that lead to the origin, evolution, and distribution of life in the galaxy^[9].

1.2 Literature survey

Since the detection of the first molecular ions and radicals (CN, CH and CH⁺) in space in the 1930s and 1940s from visible absorption of diffuse clouds^[10,11], the number of detected molecules has increased remarkably. Up to now, more than 230 molecular species have been

detected in the interstellar and circumstellar media, extragalactic, protoplanetary disk, and exoplanetary environments by astronomical observations^[12]. A significant number of the detected species were identified via their rotational transitions, while a small number is by means of IR emissions and the remaining very small number by their UV emission^[13]. Of the detected molecular species, there are inorganic species (e.g. AlCl, NaCl, KCl^[14], HeH⁺^[15,16], PO^[17], AlOH^[18], etc) and organic compounds. Regarding organic compounds, molecular species belonging to different functional groups were detected in the ISM. These are, for instance, alcohols (e.g. vinyl alcohol (CH₂=CHOH)^[19], ethanol (CH₃CH₂OH)^[20], etc), ethers (e.g. dimethyl ether (CH₃OCH₃)^[21], trans-ethyl methyl ether (t-CH₃CH₂OCH₃)^[22,23]), aldehydes (e.g. propenal (CH₂CH₂CHO) and propanal (CH₃CH₂CHO)^[24], cyanoformaldehyde (CNCHO)^[25]), amines (e.g. Methylamine CH₃-NH₂^[26,27]), etc. The search of molecules of prebiotic interest, especially those which are believed to be intermediate in the prebiotic building blocks such as the glycolaldehyde (CH₂OHCHO)^[28], the glycolonitrile (HOCH₂CN), the urea (NH₂CONH₂)^[29,30], etc. Protonated species (e.g. HCNH⁺^[31,32], NCCNH⁺^[33], H₂COH⁺^[34], etc) as well as deuterated ones (e.g. D₂H⁺^[35], NH₂CDO, cis- and trans-NHDCHO, DNCO^[36], NHD and ND₂^[37], deuterated of interstellar polycyclic aromatic hydrocarbons (PAHs)^[38], etc) were also reported in the ISM and circumstellar environments. A non-negligible number of the detected molecular species contain the cyano (-C≡N) group^[39]. Very recent detections of molecules of this kind include C₁₀H₇CN^[40], c-C₅H₅CN,^[41] HC₁₁N^[42], HC₄NC^[43], HCCCH=CCHCN and H₂C=CHC₃N^[44].

Nonetheless, of the overall already detected molecular species, only four aromatic compounds have been identified in space. These are the benzene (C₆H₆) detected via its Q-branch of the ν_4 band at 673.9732 cm⁻¹ (= 14.8374 μ m) in the direction of the proto-planetary nebula CRL618^[45], the recently detected benzonitrile (c-C₆H₅CN) on the basis of its rotational transitions in the cold core Taurus Molecular Cloud 1 (TMC-1)^[46], and the very recently detected cyanocyclopentadiene (c-C₅H₅CN)^[41], a first five-membered ring, which is also found toward the starless cloud core TMC-1. The fourth aromatic molecule detected in the ISM is the 2-cyanocyclopentadiene (C₅H₅CN)^[47], a second five-membered ring found in the dense cloud TMC-1. Beside these four aromatic molecular compounds, no aromatic whether six-membered or five-membered molecular species is identified in space or formally confirmed by the astrophysicist and astrochemist communities yet. However, it has been reported that aromatic molecules and their substituted derivatives (heterocyclic or not) constitute an important component of the ISM^[48,49].

Nevertheless, the literature survey shows a small number of heterocyclic five-membered rings detected in carbonaceous meteorites. This is, for instance, the cases of benzofurans, i.e., O-heterocycles, detected in the Yamato-791198 meteorite, and N-heterocycles detected in carbonaceous chondrites, including Orgueil, Murchison, Murray, and LON 94102 (Nuevo et al.^[50] and references therein). Regarding S-heterocycles, the thiophene has been observed in high proportion in Murchison and Orgueil meteorites^[51], thiophene and its methyl substituted derivatives (2- and 3-methylthiophene) and many other sulfur-bearing compounds were observed in samples of Mudstones gathered from the Gale crater on Mars by gas chromatography-mass spectrometry (GC-MS) analysis^[52]. The benzothiophene has been also detected in the Murchison carbonaceous chondrite^[53]. Several works agree on the ISM origin of the meteorites investigated^[54-57]. It has been also identified that the extraterrestrial organic molecules may be delivered to Earth or other planets by meteorites^[58-60]. In addition, Lattalais et al.^[61] reported that pyrrole, furan and thiophene are unambiguously the most stable isomers of the C₄H₅N, C₄H₄O and C₄H₄S families, respectively, at the 10 – 50 K temperatures of the ISM. Five-membered heterocyclic molecules and their hydrogen substituted derivatives, specially thiophenes, may then exist in different ISM environments.

In the work by Martín-Doménech et al.^[62], sulfur is depleted in regions where it is expected to be abundant, especially around young stellar objects where already detected S-bearing species account for only 0.1% of its estimated cosmic abundance. Later, McGuire et al.^[63] suggested that new gas-phase sulfur-bearing molecules should play a key role in the observed sulfur depletion. As no S-bearing heterocyclic molecule is identified in the ISM yet, in addition to high abundance

of $-\text{C}\equiv\text{N}$ group containing compound, cyanothiophenes are likely the interstellar search targets. Indeed, nitriles, i.e., organic compounds with a $-\text{C}\equiv\text{N}$ functional group, play a pivotal role in understanding the kinematic and temperature probes in different ISM environments. Moreover, it has been reported that nitriles are of fundamental importance in prebiotic chemistry since they are key intermediates in the formation of amino acids, peptides, nucleic acids and nucleobases^[8,64].

Focusing then our attention, specially, on cyanothiophenes, the literature shows that only few works were performed for 2-cyanothiophene, 3-cyanothiophene (CNT, hereafter or **8** and **9** for 2CNT and 3CNT, respectively cf. Scheme 4.1) and their isotopologues species, particularly on their structures and in the area of spectroscopy. In fact, FT-IR and FT-Raman investigations were conducted on the solid and liquid states of **8**^[65], where line assignment was achieved but no potential energy distribution (PED) was attempted. A few modes among the 24 fundamental modes were missing both for IR or Raman results. Aleksanyan et al.^[66] experimentally explored the effect of the position and nature of the substituent on the vibration spectra of five-membered heteroaromatic systems, including **8** and **9**. Except that the number of fundamental frequencies observed was limited, no frequency assignment was also carried out. In addition, whether for IR and Raman data, no experimental intensities were reported. Microwave spectra for **8**^[67,68], **9**^[69]; $^{34}\text{S}^-$ and $^{15}\text{N}-3\text{CNT}$ ^[70] were reported. The survey of these works reveals that the number of rotational lines observed and assigned experimentally, but also that of hyperfine quadrupole splittings found are limited. Another shortcoming for all these rotational results is that they all correspond only to low values of the rotational quantum number J . The microwave transitions observed experimentally are likely weak for being useful in molecular species detection in ISM. UV-VIS spectral studies were conducted only for **8**^[71]. Lastly, a theoretical work on the structure, electronic properties and the photophysics of some substituted thiophenes was conducted by Solc et al.^[72], where they investigated the influence of the substitution of H by CN groups at different sites of a thiophene and terthiophene rings. Regarding geometrical structures, experimental geometric parameters are lacking in the literature. Previous estimations of geometrical parameters for **8**^[67] and **9**^[69] obtained by fitting the rotational constants proposed more than two sets of parameters for each compound.

1.3 Objectives

The main goal for this work is to furnish to the scientific community, especially, astro-physicists and astrochemists, the material required for the interstellar detection of new molecular species. Especially, S-bearing heterocyclic compounds containing the $-\text{C}\equiv\text{N}$ group has a great astrophysical relevance and therefore need to be explored. For this purpose, this work deals with the computation of microwave (including hyperfine structures), IR, Raman and UV-VIS spectra for cyanothiophenes in attempt of supplementing the incomplete spectroscopic data from the literature. Correction schemes are used to produce reliable predicted results such as accurate geometrical parameters and the above quoted spectra for both **8**, **9**, and their deuterated species and their protonated forms as well as frequency assignments on basis of the PED. A quantum chemical investigation of the rotational spectra, including the ^{14}N quadrupole hyperfine structures of **8** and **9**, their ^{33}S isotopologues (i.e., $^{33}\text{S}-3\text{C}^{15}\text{NT}$ and $^{33}\text{S}-2\text{C}^{15}\text{NT}$), and some of their deuterated forms (such as $3\text{C}^{15}\text{NT}-2\text{D}$ and $2\text{C}^{15}\text{NT}-3\text{D}$) is conducted. Here, 2D indicates that the H bonded to carbon atom in α -position of thiophene is substituted by ^2H and 2D refers to as the H bonded to C in β -position substituted by ^2H . The protonation of thiophene and two of its nitrile-substituted derivatives, such as **8** and **9**, is also analyzed in this work. Thus, the proton affinity (PA) of **8** and **9** as well as the enthalpies, entropies and Gibbs free energy changes ($\Delta_r\text{H}$, $\Delta_r\text{S}$ and $\Delta_r\text{G}$) of the reactions yielding these species and their protonated forms is computed using modern quantum chemical methods. In the present work, the protonated forms are also characterized by analysing their thermochemistry, and their vibrational and rotational spectra. The comparison of both thermochemical and spectroscopic properties for HCNH^+ , which has been already detected in the ISM,

and R-CN^+ , is made and is expected to provide insight to their detection and production in ISM environments. The cyanothiophenes investigated in this work are expected to be identified in the ISM environments based on this consistent set of spectroscopic results expected to be valuable in the search of new species in the ISM.

1.4 Importance of our results

There is a strong interplay between observation missions, laboratory and theoretical works. It has been reported that research data, i.e., different forms of scientific information (including raw numbers and field notes, machine tapes and notebooks, edited and categorized observations, interpretations and analyses, derived reagents and vectors, and tables, charts, slides, and photographs, etc) are the basis for reporting discoveries and experimental results^[73]. In fact, laboratory and theoretical researchers have as main goal providing to the community of researchers good and reliable results needed for the accomplishment of their missions. In astrophysics and astrochemistry or astrobiology, observation results are fitted or compared with experimental and theoretical ones acquired in the same spatial conditions in the validation and explanation of facts. Due to the availability of new facilities with high angular resolution and high sensitivity, new molecular species are then expected to be discovered in a variety of environments in the universe. The new facilities include, especially, the Atacama Large Millimeter/Submillimeter Array (ALMA)^[74], the Stratospheric Observatory for Infrared Astronomy (SOFIA)^[75], the two observatories [GOTHAM (GBT Observations of TMC-1: Hunting Aromatic Molecules) and ARKHAM (A Rigorous K-band Hunt for Aromatic Molecules)^[76]] whose particular and main goal is to search for aromatic compounds, ect. Both reliable theoretical and experimental data are of paramount importance for these observatories in order to fulfill their missions. Indeed, by June 2003, preliminary detections of both ethyl methyl ether ($\text{C}_2\text{H}_5\text{OCH}_3$) and diethyl ether ($\text{C}_2\text{H}_5\text{OC}_2\text{H}_5$) in ISM were already reported. However, due to the lack of laboratory spectra, their definitive detections were not yet confirmed^[77] and thus, theoretical and/or experimental data are of the same utility as observation results in the search of new molecular species. In the same way, the first results from GOTHAM and ARKHAM, especially those from GOTHAM, have recently resulted in the detection of the largest cyanopolyne (HC_{11}N) in the interstellar medium^[42], molecule with earlier disputed detections. In fact, HC_{11}N was detected early in the circumstellar envelope of the cool carbon star IRC + 10 °216 based on three rotational transitions ($J = 70 \rightarrow 69$, $71 \rightarrow 70$ and $72 \rightarrow 71$)^[78]. This molecule was also detected in the Cold Dust Cloud TMC-1 through two rotational transitions ($J = 39 \rightarrow 38$ and $38 \rightarrow 37$)^[79]. However, the two detections have thereafter been both disputed. For instance, concerning its detection in IRC + 10 °216, Travers et al.^[80] found that its nearest microwave rotational transitions lie 0.13% lower in frequency than the lines identified in cloud TMC-1, meaning that the astronomical lines were something else entirely, and results then in no detection conclusion. Moreover, Loomis et al.^[81], on the basis of the derivation of HC_{11}N column density in TMC-1, found also an upper limit column density significantly below than that reported by Bell et al.^[79]. Thus, this results also on an no detection. In order then to identify a molecular species in the ISM environment, the results of the observation are fitted or compared with its laboratory (theoretical or experimental) and verify their agreement. In other words, laboratory data are needed to confirm or infirm the detection of a given molecule in space. In such way, our results are expected to assist strophysicists and astrochemists in the search of these aromatic species in the interstellar space, as well as to influence or induce other research works, particularly, experimental ones whether in UV-VIS, IR and Microwave domains of the electromagnetic spectrum.

1.5 References

- [1] J. R. Percy. *JAAVSO*, 35:248–254, 2006.
- [2] E. Herbst. *Annu. Rev. Phys. Chem.*, 46(1):27–54, 1995.
- [3] E. Mateo-Marti, O. Prieto-Ballesteros, G. Munoz Caro, C. González-Díaz, V. Muñoz-Iglesias, and S. Gálvez-Martínez. *Life*, 9(3):72, 2019.
- [4] A. P. Cracknell and C. A. Varotsos. Editorial and cover: Fifty years after the first artificial satellite: from sputnik 1 to envisat, 2007.
- [5] R. D. Hall, S. David, and B. Vis. *Russia’s Cosmonauts: Inside the Yuri Gagarin Training Center*. Springer Science & Business Media, 2007.
- [6] R. S. Klessen and S. C. Glover. Physical processes in the interstellar medium. In *Star Formation in Galaxy Evolution: Connecting Numerical Models to Reality*, pages 85–249. Springer, 2016.
- [7] A. A. Meiksin. *J Rev. Mod. Phys.*, 81(4):1405, 2009.
- [8] V. Rivilla, J. Martín-Pintado, I. Jiménez-Serra, S. Zeng, S. Martin, J. Armijos-Abendano, M. Requena-Torres, R. Aladro, and D. Riquelme. *MNRAS*, 483(1):L114–L119, 2019.
- [9] P. Ehrenfreund and S. B. Charnley. *ARA&A*, 38(1):427–483, 2000.
- [10] P. Swings and L. Rosenfeld. *Astrophys. J.*, 86:483–486, 1937.
- [11] A. Douglas and G. Herzberg. *ApJ*, 94:381, 1941.
- [12] B. A. McGuire. The 2020 census of interstellar, circumstellar, extragalactic, protoplanetary disk, and exoplanetary molecules: What are the pressing spectroscopic needs from the laboratory? International Symposium on Molecular Spectroscopy, 2020.
- [13] B. A. McGuire. *Astrophys. J. Suppl. Ser.*, 239(2):17, 2018.
- [14] J. Cernicharo and M. Guélin. *A&A*, 183:L10–L12, 1987.
- [15] R. Güsten, H. Wiesemeyer, D. Neufeld, K. M. Menten, U. U. Graf, K. Jacobs, B. Klein, O. Ricken, C. Risacher, and J. Stutzki. *Nature*, 568(7752):357–359, 2019.
- [16] S. Lepp. *Nat. Astron*, 3(5):382–383, 2019.
- [17] J. Bernal, L. Koelemay, and L. Ziurys. *ApJ*, 906(1):55, 2021.
- [18] E. Tenenbaum and L. Ziurys. *Astrophys. J. Lett.*, 712(1):L93, 2010.
- [19] B. E. Turner and A. J. Apponi. *Astrophys. J. Lett.*, 561(2):L207, 2001.
- [20] B. Zuckerman, B. Turner, D. Johnson, F. Clark, F. Lovas, N. Fourikis, P. Palmer, M. Morris, A. Lilley, J. Ball, et al. *ApJ*, 196:L99–L102, 1975.
- [21] L. Snyder, D. Buhl, P. Schwartz, F. Clark, D. Johnson, F. Lovas, and P. Giguere. *ApJ*, 191: L79, 1974.
- [22] B. Tercero, J. Cernicharo, A. López, N. Brouillet, L. Kolesniková, R. Motiyenko, L. Margulès, J. Alonso, and J.-C. Guillemin. *A&A*, 582:L1, 2015.
- [23] A. Bergantini, R. Frigge, and R. I. Kaiser. *ApJ*, 859(1):59, 2018.
- [24] J. M. Hollis, P. R. Jewell, F. J. Lovas, A. Remijan, and H. Møllendal. *Astrophys. J. Lett.*, 610 (1):L21, 2004.
- [25] A. J. Remijan, J. Hollis, F. Lovas, W. D. Stork, P. Jewell, and D. Meier. *Astrophys. J. Lett.*, 675(2):L85, 2008.
- [26] N. Fourikis, K. Takagi, and M. Morimoto. *ApJ*, 191:L139, 1974.
- [27] N. Kaifu, M. Morimoto, K. Nagane, K. Akabane, T. Iguchi, and K. Takagi. *ApJ*, 191:L135–L137, 1974.
- [28] J. M. Hollis, F. J. Lovas, and P. R. Jewell. *Astrophys. J. Lett.*, 540(2):L107, 2000.
- [29] A. Belloche, R. Garrod, H. Müller, K. Menten, I. Medvedev, J. Thomas, and Z. Kisiel. *A&A*, 628:A10, 2019.
- [30] A. Belloche, R. Garrod, H. Müller, K. Menten, I. Medvedev, J. Thomas, and Z. Kisiel. *A&A*, 637:C4, 2020.
- [31] L. M. Ziurys and B. Turner. *ApJ*, 302:L31–L36, 1986.
- [32] L. M. Ziurys, A. Apponi, and J. Yoder. *ApJ*, 397:L123–L126, 1992.
- [33] M. Agúndez, J. Cernicharo, P. De Vicente, N. Marcelino, E. Roueff, A. Fuente, M. Gerin, M. Guélin, C. Albo, A. Barcia, et al. *A&A*, 579:L10, 2015.

- [34] A. Bacmann, E. García-García, and A. Faure. *A&A*, 588:L8, 2016.
- [35] C. Vastel, T. Phillips, and H. Yoshida. *Astrophys. J. Lett.*, 606(2):L127, 2004.
- [36] A. Coutens, J. Jørgensen, M. Van der Wiel, H. Müller, J. Lykke, P. Bjerkeli, T. Bourke, H. Calcutt, M. Drozdovskaya, C. Favre, et al. *A&A*, 590:L6, 2016.
- [37] M. Melosso, L. Bizzocchi, O. Sipilä, B. Giuliano, L. Dore, F. Tamassia, M.-A. Martin-Drumel, O. Pirali, E. Redaelli, and P. Caselli. *A&A*, 641:A153, 2020.
- [38] E. Peeters, L. Allamandola, C. Bauschlicher Jr, D. Hudgins, S. Sandford, and A. Tielens. *ApJ*, 604(1):252, 2004.
- [39] D. McNaughton, M. K. Jahn, M. J. Travers, D. Wachsmuth, P. D. Godfrey, and J.-U. Grabow. *Mon. Not. R. Astron. Soc.*, 476(4):5268–5273, 2018.
- [40] B. A. McGuire, A. M. Burkhardt, R. A. Loomis, C. N. Shingledecker, K. L. K. Lee, S. B. Charnley, M. A. Cordiner, E. Herbst, S. Kalenskii, E. Momjian, et al. *Astrophys. J. Lett.*, 900(1):L10, 2020.
- [41] M. C. McCarthy, K. L. K. Lee, R. A. Loomis, A. M. Burkhardt, C. N. Shingledecker, S. B. Charnley, M. A. Cordiner, E. Herbst, S. Kalenskii, E. R. Willis, et al. *Nat. Astron*, pages 1–5, 2020.
- [42] R. A. Loomis, A. M. Burkhardt, C. N. Shingledecker, S. B. Charnley, M. A. Cordiner, E. Herbst, S. Kalenskii, K. L. K. Lee, E. R. Willis, C. Xue, et al. *Nat. Astron*, pages 1–9, 2021.
- [43] C. Xue, E. R. Willis, R. A. Loomis, K. L. K. Lee, A. M. Burkhardt, C. N. Shingledecker, S. B. Charnley, M. A. Cordiner, S. Kalenskii, M. C. McCarthy, et al. *Astrophys. J. Lett.*, 900(1):L9, 2020.
- [44] K. L. K. Lee, R. A. Loomis, A. M. Burkhardt, I. R. Cooke, C. Xue, M. A. Siebert, C. N. Shingledecker, A. Remijan, S. B. Charnley, M. C. McCarthy, et al. *arXiv preprint arXiv:2101.05858*, 2021.
- [45] J. Cernicharo, A. M. Heras, A. Tielens, J. R. Pardo, F. Herpin, M. Guélin, and L. Waters. *Astrophys. J. Lett.*, 546(2):L123, 2001.
- [46] B. A. McGuire, A. M. Burkhardt, S. Kalenskii, C. N. Shingledecker, A. J. Remijan, E. Herbst, and M. C. McCarthy. *Science*, 359(6372):202–205, 2018.
- [47] K. L. K. Lee, P. B. Changala, R. A. Loomis, A. M. Burkhardt, C. Xue, M. A. Cordiner, S. B. Charnley, M. C. McCarthy, and B. A. McGuire. *Astrophys. J. Lett.*, 910(1):L2, 2021.
- [48] A. G. Tielens. *Annu. Rev. Astron. Astrophys.*, 46:289–337, 2008.
- [49] Z.-C. Wang and V. M. Bierbaum. *J. Phys. Chem. A.*, 121(19):3655–3661, 2017.
- [50] M. Nuevo and S. A. Sandford. *ApJ*, 800(2):116, 2015.
- [51] M. Sephton, C. Pillinger, and I. Gilmour. *Planet. Space Sci.*, 49(1):101–106, 2001.
- [52] J. L. Eigenbrode, R. E. Summons, A. Steele, C. Freissinet, M. Millan, R. Navarro-González, B. Sutter, A. C. McAdam, H. B. Franz, D. P. Glavin, et al. *Science*, 360(6393):1096–1101, 2018.
- [53] M. A. Sephton. *Philos. Trans. Royal Soc. A*, 363(1837):2729–2742, 2005.
- [54] F. Robert and S. Epstein. *Geochim. Cosmochim. Acta*, 46(1):81–95, 1982.
- [55] J. Kerridge and S. Chang. *Meteoritics*, 18:323, 1983.
- [56] J. Yang and S. Epstein. *Nature*, 311(5986):544, 1984.
- [57] M. Bose, R. Root, and S. Pizzarello. *Meteorit. Planet. Sci.*, 52(3):546–559, 2017.
- [58] J. Oró. *Nature*, 190(4774):389–390, 1961.
- [59] M. P. Bernstein, J. P. Dworkin, S. A. Sandford, G. W. Cooper, and L. J. Allamandola. *Nature*, 416(6879):401–403, 2002.
- [60] E. Bianchi, C. Codella, C. Ceccarelli, F. Vazart, R. Bachiller, N. Balucani, M. Bouvier, M. De Simone, J. Enrique-Romero, C. Kahane, et al. *Mon. Not. R. Astron. Soc.*, 483(2):1850–1861, 2019.
- [61] M. Lattalais, Y. Ellinger, A. Matrane, and J.-C. Guillemin. *Phys. Chem. Chem. Phys.*, 12(16):4165–4171, 2010.
- [62] R. Martín-Doménech, I. Jiménez-Serra, G. M. Caro, H. Müller, A. Occhiogrosso, L. Testi,

- P. Woods, and S. Viti. *A&A*, 585:A112, 2016.
- [63] B. A. McGuire, C. N. Shingledecker, E. R. Willis, K. L. K. Lee, M.-A. Martin-Drumel, G. A. Blake, C. L. Brogan, A. M. Burkhardt, P. Caselli, K.-J. Chuang, et al. *ApJ*, 883(2):201, 2019.
- [64] N. Balucani. *Int. J. Mol. Sci.*, 10(5):2304–2335, 2009.
- [65] R. S. Cataliotti, F. Antolini, A. Morresi, F. Santinelli, and S. Santini. *J. Raman Spectrosc.*, 19(6):423–428, 1988.
- [66] V. Aleksanyan, N. Magdesieva, Y. K. Yur’ev, et al. *J. Struct. Chem.*, 7(1):36–41, 1967.
- [67] T. Avirah, T. Malloy Jr, and R. L. Cook. *J. Mol. Struct.*, 29(1):47–52, 1975.
- [68] J. Wiese, L. Engelbrecht, and H. Dreizler. *Z. Naturforsch.*, 32(2):152–155, 1977.
- [69] J. Wiese and D. H. Sutter. 32, 08 1977.
- [70] J. Wiese, R. Schwarz, and D. Sutter. *Z. Naturforsch.*, 35(7):770–772, 1980.
- [71] F. S. Boig, G. W. Costa, and I. Osvar. *J. Org. Chem.*, 18(7):775–778, 1953.
- [72] R. Solc, V. Lukeš, E. Klein, M. Griesser, and A.-M. Kelterer. *J. Phys. Chem. A*, 112(43): 10931–10938, 2008.
- [73] R. A. Rosenbaum. Responsible science: Ensuring the integrity of the research process (volume i), 1993.
- [74] L. Pagani, E. Bergin, P. Goldsmith, G. Melnick, R. Snell, and C. Favre. 2019.
- [75] A. Krabbe. Sofia telescope. In *Airborne Telescope Systems*, volume 4014, pages 276–282. International Society for Optics and Photonics, 2000.
- [76] B. A. McGuire, A. M. Burkhardt, K. Lee, R. Loomis, S. B. Charnley, M. Cordiner, E. Herbst, S. Kalenskii, C. N. Shingledecker, E. R. Willis, et al. Gotham and arkham: First results from programs to explore aromatic chemistry at the earliest stages of star formation. In *74th International Symposium on Molecular Spectroscopy*, 2019.
- [77] I. Medvedev, M. Winnewisser, F. C. De Lucia, E. Herbst, E. Yi, L. P. Leong, R. P. Bettens, E. Białkowska-Jaworska, O. Desyatnyk, L. Pszczółkowski, et al. *Astrophys. J. Suppl. Ser.*, 148 (2):593, 2003.
- [78] M. Bell, P. Feldman, S. Kwok, and H. Matthews. *Nature*, 295(5848):389, 1982.
- [79] M. Bell, P. Feldman, M. Travers, M. McCarthy, C. Gottlieb, and P. Thaddeus. *Astrophys. J. Lett.*, 483(1):L61, 1997.
- [80] M. Travers, M. McCarthy, P. Kalmus, C. Gottlieb, and P. Thaddeus. *Astrophys. J. Lett.*, 469 (1):L65, 1996.
- [81] R. A. Loomis, C. N. Shingledecker, G. Langston, B. A. McGuire, N. M. Dollhopf, A. M. Burkhardt, J. Corby, S. T. Booth, P. B. Carroll, B. Turner, et al. *Mon. Not. R. Astron. Soc.*, 463(4):4175–4183, 2016.

INTERSTELLAR MEDIUM (ISM)

2.1 Interstellar matter

Cosmological observations have shown that over 95 % of the total mass of the universe is composed of dark energy and dark matter whereas the contribution of baryons, i.e., atoms and molecules from which galaxies, stars, and planets form, is only $\approx 5\%$ ^[1,2]. The universe is organized in a hierarchical structure in which matter is concentrated in large organizations known as galaxies, which occupy only a small fraction of space. Galaxies are found in a variety of shapes and forms. The three main types are spiral, elliptical and irregular galaxies. Our solar system is located in one arm of a spiral galaxy - the *Milky Way* - where it is situated approximately at 8.5 kpc (pc stands for parsec; 1 pc = 3.26 light years) from the center^[3].

The space between the stars in galaxies and around galaxies in the universe is not empty, but rather is filled with material composed of gas and dust. This material spread between stars is referred to as the *interstellar medium* (ISM)^[3,4], whereas, on large scale, the material between galaxies is referred to as *intergalactic medium* (IGM). In the galaxy, stars form from the ISM, interact with it, but also *pollute* it with new materials. For this reason, understanding its properties and nature is of paramount importance. Likewise, on a cosmological scale, understanding the properties of the IGM and its link with galaxies is also crucial when one is addressing the problem of the formation and evolution of galaxies.

The existence of interstellar matter was first unveiled by the presence of many dark clouds silhouetted against the background starlight in the 1927 photographic atlas of the Milky Way by E. E. Barnard which gave impression of the absence of stars. The analysis of this photography revealed that such dark patches are not due to a lack of stars in these regions but to the starlight blocked from view by intervening interstellar dust absorption^[5]. Interstellar reddening, i.e., the modification of the colors of stars as a result of selective extinction of starlight by dust in the ISM, provides further evidence of the presence of interstellar matter.

Most of the ISM is occupied by low density gas ($\sim 1 \text{ H cm}^{-3}$), which makes up about 99% by mass of the material in this environment, the dust accounts for the remaining portion (1% with $\sim 10^{-11} \text{ grains cm}^{-3}$)^[6]. Regions with intermediate and high density also exist. The ISM is mainly composed of hydrogen (H) and helium (He) gas as well as dust. However, the latter accounts only for 1% by mass of the ISM material^[7]. In more detail, the chemical composition of the interstellar gas is distributed into H (93.38%), He (6.49%) and biogenic elements such as oxygen, carbon, and nitrogen which account for 0.11% (O:C:N \approx 7:3:1). The third-row elements neon, silicon, magnesium, and sulfur are less copious (0.002%) and have relative abundances of 8:3:3:2; all remaining elements furnish only 0.02%^[6]. These elements can be neutral, ionized, or in molecular form and in the gas phase or in the solid state. For instance, a significant fraction of the interstellar H is in the molecular form; even though molecular hydrogen is extremely difficult to observe, especially at millimeter and sub-millimeter regions of the electromagnetic spectrum due to the absence of permanent dipole moment^[8]. Interstellar molecules are of particular importance. Indeed, prebiotic interstellar molecules may serve, for example, as the first steps toward life in the universe. Molecules can be also used as "*dye*" to tracer important processes in the ISM. Molecules provide also a unique information on the physical conditions of a wide variety of regions, etc^[9]. The dust is composed of solid silicate and carbon-based particles, mainly less than $\sim 1 \mu\text{m}$ in size present throughout interstellar clouds that provide surfaces for accretion of gas phase species and

subsequent grain surface chemistry^[10–12]. In addition, particular spectral features were observed in the extinction curve, such as the 217.5 nm bump or the infrared bands at 9.7 μm and 18 μm and were attributed to particular types of dust grain: *graphite* in the case of the 217.5 nm bump^[13] and *amorphous silicates* in the case of the infrared bands^[14,15].

The gas and dust in the ISM are in permanent interaction with radiation, turbulence, magnetic and gravitational fields, and accelerated particles^[16]. They are heated by stellar photons, originating from many stars (the so-called average interstellar radiation field), cosmic rays (energetic [\sim GeV] protons), and X-rays (emitted by local, galactic, and extragalactic hot gas). They also cool through a variety of line and continuum processes and the spectrum will depend on the local physical conditions.

2.2 Physical properties and chemical composition of molecular clouds

2.2.1 Physical properties

Understanding the physical properties of molecular clouds supposes the knowledge of properties of the whole ISM. Earlier models by McKee & Ostriker^[17] classified the ISM into three phases: (1) the *Cold Neutral Medium (CNM)* ($n > 10 \text{ cm}^{-3}$ and $T_K < 100 \text{ K}$ ^[18,19]), often referred to as **clouds**; (2) the *Warm Ionized Medium and Warm Neutral Medium (WIM and WNM)* ($n \sim 0.1 - 1 \text{ cm}^{-3}$ and temperatures of several thousands^[19,20]), which is sometimes considered as the boundary layers of the CNM, and (3) the *Hot Ionized Medium (HIM)* ($n < 0.01 \text{ cm}^{-3}$ and $T_K > 10^5 \text{ K}$ ^[19]), which is sometimes referred to as the **intercloud medium** or the **coronal gas**. As to Ferriere^[21], half of the interstellar mass is confined to discrete clouds occupying only $\sim 1 - 2\%$ of the interstellar volume. It can be roughly divided into three types: *the dark clouds*, *the diffuse clouds* and *the translucent clouds*. According to this author, the rest of the interstellar matter, spread out between the clouds, exist in three different forms: warm (mostly neutral) atomic, warm ionized, and hot ionized. In other words, the gas is organized in phases (cold molecular clouds, cool HI clouds, warm intercloud gas, and hot coronal gas) of which those objects are highly visible manifestations^[22]. Moreover, according to the physical conditions in the ISM, the gas is visibly present in a variety of distinct objects: HII regions, reflection nebulae, dark clouds, and supernova remnants^[6]. Table 2.1 presents six phases of the interstellar medium corresponding to a variety of differences of physical characteristics (temperature and density) of the different ISM environments. The physical information on the gas and dust could be inferred from molecular spectra. In particular, rotational and vibrational spectra illustrate much information about the density and temperature of the gas as well as its kinematics such as the collapse and rotation^[16,23].

Table 2.1 – The Interstellar gas phases.

Cloud type	T (K) ¹	Density ²	Indicators	Extinction ³
Coronal gas (Hot ionized medium)	10^6	10^{-2}	O VI-VIII, ...	
Intercloud H _I (Warm neutral medium)	$6 \times 10^3 - 10^4$	0.2-0.5	H I, O I, etc	0.1
Diffuse ionized gas (Warm ionized medium)	8×10^3	0.2-0.5	H II, O II-III, ...	1.0
Diffuse clouds (Atomic cold neutral medium)	30-150	1-1000-	H I, O I, etc	0.2
Dark clouds or Molecular clouds or Dense clouds (Molecular cold neutral medium)	<50	100-500	H ₂ , CO, etc	0.2 – 1
Protostellar cores (Molecular hot cores)	100-300	$10^4 - 10^6$	H ₂ , CO, etc	5- 10

From Kaiser^[6], Ehrenfreund and Cami^[24], Wooden et al.^[25], Klessen and Glover^[26],

As the relative abundances of isomers should depend strongly on the physical and chemical conditions in the interstellar medium, isomers act as tracers to elucidate temperature and density-dependent formation routes to extraterrestrial molecules^[6]. As shown in Table 2.1, at broad point of view the ISM gas could be distributed into six types of cloud environments:

1. **The coronal gas** or **Hot ionized medium (HIM)**. This ISM component is the result of supernovae (*in abbreviation: SN or SNe is a powerful and luminous stellar explosion that occurs during the last evolutionary stages of a massive star or when a white dwarf is triggered into runaway nuclear fusion*) exploding in the ISM, creating large, ionized bubbles filled with very hot gas ($T \sim 10^6$ K)^[17,26]. According to these two references, although the gas would eventually cool, the temperature dependence of the atomic cooling curve at high temperatures is such that the cooling time around $T = 10^6$ K is considerably longer than the cooling time in the temperature range $10^4 < T < 10^6$ K. Therefore, rather than this hot gas having a wide range of temperatures, one would instead expect to find most of it close to 10^6 K. This hot, ionized phase of the ISM has subsequently become known as the HIM. Generally speaking, it is a *hot* and *diffuse* component characterized by a temperature range $5.3 \leq \log T \leq 5.9$, a density range $-2.3 \leq \log n \leq -1.5$ with a pressure $p/k \leq 10^4 \text{cm}^{-3} \text{K}$ ^[27]. McKee and Ostriker^[17], in their self-consistent model of the local ISM, have demonstrated that 70% of interstellar space is filled with hot gas. They have found that this component occupies a much larger volume than the cold clouds—the filling factor being 0.2—but contains far less mass.
2. **The intercloud H_I** or **Warm neutral medium (WNM)**. The neutral hydrogen (H_I) exists in two stable phases, in pressure equilibrium with one another but also with the hot ionized medium: *the cold neutral medium (CNM)* at temperature $T < 300$ K, roughly $\sim 40 - 200$ K^[28] and the warm neutral medium (WNM) at temperature $T \sim 10^4$ K^[29]. The WNM, a warm diffuse medium, contributes to the emission but is extremely difficult to detect in absorption due to its low optical depth contrary to the dense phase (i.e., CNM), which has high 21 cm optical depth and gives rise to the narrow absorption features seen towards continuum sources. The latter is characterized by a number densities $n \sim 1 - 10 \text{cm}^{-3}$ whereas that of the former is $\sim 0.01 - 0.1 \text{cm}^{-3}$ ^[28]. These two H_I phases coexist with comparable thermal pressures but with radically different temperatures and densities, the primary cooling mechanism being the radiative de-excitation of collisionally excited fine-structure lines of metals in CNM and the onset of L_α cooling mechanism at about 8000 K resulting at a warm rarefied phase^[21]. The WNM fractional ionization ~ 0.1 is maintained by the very soft X-rays ($h\nu \sim 60$ eV) emitted by supernova remnants.
3. **Diffuse ionized gas** or **Warm ionized medium**. In their model of ISM component, McKee and Ostriker^[17] have subdivided the HIM into two regions, an *outer one* wherein the fractional ionization is ~ 0.7 maintained by hot B star warm ionized medium (WIM), and an *inner layer* of smaller volume (the WNM). By calculating the physical conditions of this component, the authors found a temperature $T \sim 8000$ K, a hydrogen density, $n \simeq 0.25 \text{cm}^{-3}$, a fractional ionization, $x \simeq 0.68$, a filling factor $f \approx 0.23$, a mean cloud radius of ≈ 2.1 pc and a mean column density of $\sim 0.22 \times 10^{19} \text{cm}^{-2}$.

The main ionization source and mechanism contributing to the WIM emission is *the photoionization* by OB stars (a unique source of energy sufficient to maintain the bulk ionization properties of the WIM)^[30]. In the Milky Way, OB stars provide $\gtrsim 10^{-4} \text{ergs cm}^{-2} \text{s}^{-1}$, or $\sim 15\%$ of the ionizing radiation output^[30]. Beside this heating mechanism which increases the electron temperature at low density (n_e) at a heating rate per unit volume proportional to n_e^2 , Reynolds et al.^[31] proposed an additional heating source with a rate per unit volume proportional to a lower power of n_e : *the dissipation of interstellar plasma turbulence* with a rate of $\sim 10^{-25} n_e \text{ergs cm}^{-3} \text{s}^{-1}$. According to the authors, if such source was present, it would dominate over photoionization heating in regions where $n_e \lesssim 0.1 \text{cm}^{-3}$, producing the observed increases in the $[S_{\text{II}}]/H_{\alpha}$ and $[N_{\text{II}}]/H_{\alpha}$ intensity ratios at large distances from the galactic midplane as well as accounting for the constancy of $[S_{\text{II}}]/[N_{\text{II}}]$, which is not explained by pure photoionization. They also provided an additional supplemental heating sources, such as *magnetic reconnection, cosmic rays, or photoelectric emission from small grains*, which could also account for these observed properties and which supply $\sim 10^{-5} \text{ergs s}^{-1}$ per square centimeter of the Galactic disk to the warm ionized medium.

4. **The Cold neutral medium (CNM).** So far, it has been seen that one of the three components of the ISM is the CNM. The CNM can be divided into numerous of cloud types, spanning a wide range of physical and chemical conditions^[32]. On one hand, the densest clouds, mostly protected against UV radiation from stars, are variously referred to as *dense clouds, dark clouds, or molecular clouds*. On the other hand, there are more tenuous clouds, fully exposed to starlight, and they are usually referred to as *diffuse clouds*, whereas clouds that fall in between these two extremes are often called *translucent clouds*. Vázquez-Semadeni et al.^[33] reported that the cloud formation process begins with the formation of transient, thin sheets of cold gas characterized by a *thicknesses* of ~ 0.05 pc, a *column densities* of $\sim 0.2 \times 10^{20} \text{ cm}^{-2}$, *temperatures* of ~ 20 K, and *line widths* of $\sim 1 \text{ km s}^{-1}$.

5. **Hot molecular cores (HMCs).** The physical structure of HMCs is not well known, and differs from source to source. Most sources have masses on the order of $10^3 M_{\text{d}\odot}$, and luminosities of the order of $10^5 L_{\odot}$, which is reprocessed by dust and mostly emitted in the far infrared. HMCs are compact (diameters ≤ 0.1 pc), dense ($n \geq 10^7 \text{ cm}^{-3}$), hot ($T \geq 100$ K), and dark ($A_{\text{V}} \geq 100 \text{ mag}$) molecular cloud cores^[34]. They are characterized by a rich chemistry observable in molecular line emission at (sub)mm wavelength^[35]. In fact, models of hot cores have shown that gas densities within these media typically fall in the $10^5 - 10^8 \text{ cm}^{-3}$ range, even though many single-point models adopt values of around 10^7 cm^{-3} ^[36]. Whereas warm cores are produced by low-mass protostars, high-mass protostars are more luminous than low-mass protostars, and heat the surrounding infalling core material (gas and dust) on protostellar disk to a greater extent and produce hot cores^[25].

Physical conditions of different clouds have been discussed in several works^[6,32,37,38]. For instance, diffuse clouds are characterized by typical number densities of $10^1 - 10^2 \text{ atoms cm}^{-3}$, average translational temperatures of the gas of $100 - 120$ K and contain up to a few thousand solar masses. They have a visual extinction of $A_{\text{V}} \leq 1 \text{ mag}$ and, consequently, the interstellar ultraviolet radiation easily penetrates them. UV photons play then a significant role in the chemistry of these clouds as they ensure photodissociation of molecules. Concerning translucent clouds which are thought to be the bridge between diffuse and dense structures, they are characterized by moderate number densities of $10^2 - 10^3 \text{ atoms cm}^{-3}$, relatively low kinetic temperatures of $50 - 100$ K compared to diffuse structures and present a visual extinction such that $1 \text{ mag} < A_{\text{V}} < 5 \text{ mag}$. The densest clouds are formed from low-density clouds and characterized by typical number densities of $10^2 - 10^4 \text{ atoms cm}^{-3}$ and low kinetic gas temperatures of only $10 - 15$ K. Concerning molecular abundance in different clouds, it has been pointed out that, in diffuse and translucent clouds, UV radiation penetrates easily so that it ensures the photodissociation of molecules. Thus, the formation of molecules is, in general, dominated by photochemistry and photoionization^[6]. Inside dense clouds, interstellar dust particles (i.e., submicrometer-sized silicate- and carbonaceous-based grain nuclei) shield complex molecules from the destructive short wavelength radiation field^[6], and the flux of the interstellar UV radiation field drops from $10^8 \text{ photons cm}^{-2} \text{ s}^{-1}$ to a residual flux of only $10^3 \text{ photons cm}^{-2} \text{ s}^{-1}$.

According to Solomon et al.^[39], the molecular clouds can be divided into two components: a *cold one with $T < 10$ K* and a *warm component, including many clouds with cores characterized by $T > 20$ K*. The authors pointed out that the cold clouds, which were priorly believed not to contain stars in spectral type than late B, are found to be smoothly distributed throughout the galactic disk. Moreover, the warm clouds, which are often thought to be among the largest and most massive, are associated with radio H_{II} regions and appear to be a spiral arm population^[40].

The distinction between different clouds may be stated in terms of the total column density of hydrogen through the cloud, given by^[41]:

$$N_{\text{H}} = \int [n(\text{H}) + 2n(\text{H}_2)] dl. \quad (2.1)$$

Diffuse clouds are then characterized by $N_{\text{H}} \lesssim 5 \times 10^{21} \text{ cm}^{-2}$ corresponding to a *visual extinction* $A_{\text{v}} \lesssim 3 \text{ mag}$ and *dense clouds* by $N_{\text{H}} \gtrsim 5 \times 10^{21} \text{ cm}^{-2}$ and $A_{\text{v}} \gtrsim 3 \text{ mag}$ ^[41]. The magnetic-field-influenced gravitational collapse of *diffuse clouds* forms *dark, dense molecular clouds* which are aptly known as stellar nurseries. Due to the absorption of most of the external UV radiation by the gas and dust, the interiors of dark, dense molecular clouds reach temperatures as low as 10 K, ensuring the incorporation of much of the gas-phase C, N, and O into *ice mantles* that coat the dust grains^[42]. Further, more localized, gravitational collapse of material onto a central dense core feeds the growth of a nascent protostar, which heats the inner regions of its surrounding envelope, creating the *hot* ($\sim 100 \text{ K}$), *dense* (number density $> 10^6$ molecules per cm^3 , optical depth $\sim 10^3$) physical conditions in which many complex interstellar molecules (e.g., methyl formate (HCOOCH_3)) are detected. For solar-type star formation, in particular, the protostar is found to be encircled by a thin, flat, rotating structure called a *protoplanetary disk*. Depending on the mass of the protostar, the transition from the cold core phase ($\sim 10 \text{ K}$) to a *hot core* or *corino* can take on the order of a million years^[42].

Table 2.2 – Some interstellar sources of molecules

Cloud type	Density(/ cm^3)	Temperature (K)	Salient molecular feature
Diffuse clouds			
Typical conditions	1000	50 -100	Some diatomic
Shocked regions		≤ 4000	CH^+
Translucent clouds	1000	10-50	Some polyatomic
Dense clouds			
Inter-core material	1000	~ 10	Some polyatomic
Quiescent cores	10^4	~ 10	Many polyatomic
<i>Low mass young-stellar objects</i>			
Starless cores (Collapse starting)	$10^4 - 10^6$	~ 10	Many polyatomic
Collapsing cores (Central object present)	$10^4 - 10^6$	~ 10	Depletion onto grains
Protoplanetary disks ¹	$\leq 10^{10}$	~ 30	Depletion onto grains
<i>High mass young-stellar objects</i>			
Hot molecular cores	10^6	100 – 300	Saturated molecules
Shocked regions ²	10^4	≤ 4000	Sputtering ³
Photo-dominated regions	10^4	100 – 1000	PAH's

From^[43]; ¹ *Protoplanetary disk*: It is a rotating circumstellar disc of dense gas and dust surrounding a young newly formed star. ² *Shocked regions* are regions whose gas is in turbulent motion associated with various outflows present in the region^[44]. ³ *Sputtering* is a physical process in which atoms in a solid-state (target) are released and pass into the gas phase by bombardment with energetic ions.

2.2.2 Interstellar molecular abundance

The majority of the volume of the interstellar medium is very hot ($T > 10\,000 \text{ K}$) and does not contain any molecules at all^[6]. Hence, any ISM environment among the ones presented in Table 2.1, except the fourth and fifth, is therefore not expected to contain molecules. In fact, Herbst^[43] has compiled the ISM environments where molecular species could be found. Table 2.2 presents the sources of molecules as presented by this author. Beside these two regions susceptible to contain molecules (diffuse and dark clouds), Kroto^[45] mentioned additional regions such as (1) *circumstellar shells*, (2) *stellar atmospheres* and *comets*. The vast variety of molecules, radicals, and ions detected so far in various regions of space are therefore not distributed homogeneously, but rather are confined to distinct environments.

As for Arumainayagam et al.^[42], the first detections of molecules (CH in 1937 and CN in 1940) in space appeared surprising because of the very harsh ISM conditions such as: (1) *low tem-*

peratures (10–100 K) that are usually thought to inhibit chemical synthesis, (2) *near zero pressures* (10^{-14} atm) that reduce reaction rates by lowering the molecular collision frequency, and (3) the *intense ionizing radiation* (including *cosmic rays with energies* $\sim 10^{21}$ eV) that is capable of destroying molecules. Few years before these discoveries, it was claimed that no known mechanism could account for the significant presence of extraterrestrial molecules^[46]. Table 2.3 contains the actually already detected molecules in the ISM or circumstellar shells by February, 2020 (<https://cdms.astro.uni-koeln.de/classic/molecules>). The overall already detected molecules in the ISM or Circumstellar Shells, as well as extragalactic (see the same website) molecules, but also not included molecule (see http://www.astrochymist.org/astrochymist_ism.html) account for more than 200 molecular species. By 2018, more than 204 individual molecular species, comprised of 16 different elements, had already been detected in diverse environments, ranging from nearby objects in our solar system to distant sources in the early universe^[23], including interstellar, circumstellar, extragalactic, protoplanetary disk, and exoplanetary environments by astronomical observations^[47]. By 2020, the number of confirmed detected molecular species shows that 224 molecules have been found in interstellar, circumstellar, extragalactic, protoplanetary disk, and exoplanetary environments^[48]. Most of the molecules already detected in space were identified based on their rotational transitions observed in the microwave and submillimeter part of the electromagnetic spectrum and the remaining proportion thanks to IR, visible (VIS) and ultraviolet (UV) observations.

As revealed in Table 2.3 (see also http://www.astrochymist.org/astrochymist_ism.html and http://www.astrochymist.org/astrochymist_ism.html), these molecules are of various kinds. Observation of this Table reveals that diatomic molecules formed with second- and third-row elements are particularly predominant. It is not thus surprising that most of molecules detected in space are composed of the cosmically abundant biogenic elements H, C, N, O and S, these atoms being the most abundant elements in the ISM. Likewise, it is clear that the more the number of atoms in a molecule increases, the more the number of molecules with this number of atoms already detected decreases. In fact, it has been found that the partition functions of larger molecules are large, making them much more difficult to be detected, even if they are present in large quantities^[49]. Another difficulty in searching for complex molecules arises from the fact that, for good astronomical sources, there are so many different molecules so that their fingerprints overlap, making them also difficult to disentangle. Moreover, the more the number of atoms in a molecule increases, generally, the more does the complexity of its spectrum and its spectrum becomes thus an indecipherable mush of lines^[50].

Among detected molecules, there are COMs especially prebiotic molecules with many functional groups such as sugar-like molecules (e.g., CH_2OHCHO ^[51]; alcohols (e.g., Vinyl alcohol $\text{CH}_2=\text{CHOH}$ ^[52], methyl alcohols [CH_3OH , CH_3OD , 13 CH_3OH]^[53]), $\text{CH}_3\text{OCH}_2\text{OH}$ ^[54] etc), ether (e.g., ethyl methyl ether $\text{CH}_3\text{OCH}_2\text{CH}_3$, dimethyl ether $((\text{CH})_3\text{O}$ ^[55]), alkenes (e.g., ethylene oxyd $\text{c}-\text{C}_2\text{H}_4\text{OH}$ ^[55,56]), amines (e.g., methyl amine CH_3NH_2 ^[57]), acids (e.g., CH_3COOH ^[58]), long carbon chain molecules (e.g., $\text{CH}_2\text{CH}-\text{CH}_3$ ^[59]), nitriles (e.g., HCN ^[60-62], HOCH_2CN ^[63], SiH_3CN ^[64], etc). The table also contains unsaturated COMs such as polyynes (e.g., HC_7N ou $\text{H}(\text{C}\equiv\text{C})_3\text{CN}$ ^[65], HC_9N ^[66], etc), fullerenes (e.g., C_{60} ^[67,68], C_{70} ^[68], C_{60}^+ ^[69]). Many among the molecular species in this table are well-known in the laboratory, but a great number is also constituted by quite unusual molecular species by terrestrial standards. The unusual species include positive molecular ions (e.g. HCO^+ , H_3O^+ , H_3^+ , HeH^+ ^[70], ArH^+ ^[71,72]), radicals (e.g., SH ^[73], C_6H ^[74], C_7H ^[75] C_8H and C_{10}H ^[76], C_3 ^[77], C_5 ^[78], etc), three-membered rings (e.g. C_3H , C_3H_2 ^[79]), isomers (e.g. HNC ^[62,80,81] and HCN ^[61,82]), anions (e.g., C_4H^- ^[83], C_6H^- ^[84], C_8H^- ^[76,85], C_3N^- ^[86] and C_5N^- ^[87], etc).

Amino acids are the essential molecular components of living organisms on Earth and have been widely identified in the ISM. However, whereas their spontaneous generation in the interstellar medium is possible, the proposed mechanisms for their spontaneous generation have been unable to account for their presence in Earth's early history^[88]. These molecules are found among the various tracers of organic materials in space (interstellar extinction, cometary spectra, planetary and meteoritic materials, etc). The diffuse interstellar bands (DIBs) may well represent a particularly

Table 2.3 – Molecules in the Interstellar Medium or Circumstellar Shells (as of 02/2020)

2 atoms	3 atoms	4 atoms	5 atoms	6 atoms	7 atoms	8 atoms	9 atoms	10 atoms	11 atoms	12 atoms	>12 atoms
H ₂	C ₃ ^{**}	c-C ₃ H	C ₅ ^{**}	C ₅ H	C ₆ H	CH ₃ C ₃ N	CH ₃ C ₄ H	CH ₃ C ₅ N	HC ₉ N	c-C ₆ H ₆ ^{**}	C ₆₀ ^{**}
AlF	C ₂ H	l-C ₃ H	C ₄ H	l-H ₂ C ₄	CH ₂ CHCN	HC(O)OCH ₃	CH ₃ CH ₂ CN	(CH ₃) ₂ CO	CH ₃ C ₆ H	n-C ₃ H ₇ CN	C ₇₀ ^{**}
AlCl	C ₂ O	C ₃ N	C ₄ Si	C ₂ H ₄ ^{**}	CH ₃ C ₂ H	CH ₃ COOH	(CH ₃) ₂ O	(CH ₂ OH) ₂	C ₂ H ₅ OCHO	i-C ₃ H ₇ CN	C ₆₀ ⁺
C ₂ [*]	C ₂ S	C ₃ O	l-C ₃ H ₂	CH ₃ CN	HC ₅ N	C ₇ H	CH ₃ CH ₂ OH	CH ₃ CH ₂ CHO	CH ₃ OC(O)CH ₃	C ₂ H ₅ OCH ₃	c-C ₆ H ₅ CN
CH	CH ₂	C ₃ S	c-C ₃ H ₂	CH ₃ NC	CH ₃ CHO	C ₆ H ₂	HC ₇ N	CH ₃ CHCH ₂ O			
CH ⁺	HCN	C ₂ H ₂ ^{**}	H ₂ CCN	CH ₃ OH	CH ₃ NH ₂	CH ₂ OHCHO	C ₈ H	CH ₃ OCH ₂ OH			
CN	HCO	NH ₃	CH ₄ ^{**}	CH ₃ SH	c-C ₂ H ₄ O	l-HC ₆ H ^{**}	CH ₃ C(O)NH ₂				
CO	HCO ⁺	HCCN	HC ₃ N	HC ₃ NH ⁺			C ₈ H ⁻				
CO ⁺	HCS ⁺	HCNH ⁺	HC ₂ NC	HC ₂ CHO	C ₆ H ⁻	CH ₂ CCHCN	C ₃ H ₆				
CP	HOC ⁺	HNCO	HCOOH	NH ₂ CHO	CH ₃ NCO	H ₂ NCH ₂ CN					
SiC	H ₂ O	HNCS	H ₂ CNH	C ₅ N	HC ₅ O	CH ₃ CHNH	CH ₃ NHCHO				
HCl	H ₂ S	HOCO ⁺	H ₅ C ₂ O	l-HC ₄ H ^{**}	HOCH ₂ CN	CH ₃ SiH ₃	HC ₇ O				
KCl	HNC	H ₂ CO	H ₂ NCN	l-HC ₄ N		H ₂ NC(O)NH ₂					
NH	HNO	H ₂ CN	HNC ₃ ^{**}	c-H ₂ C ₃ O							
NO	MgCN	H ₂ CS	SiH ₄								
NS	MgNC	H ₃ O ⁺	H ₂ COH ⁺	C ₅ N ⁻							
NaCl	N ₂ H ⁺	c-SiC ₂ ^{**}	C ₄ H ⁻	HNGHCN							
OH	N ₂ O	CH ₃	HC(O)CN	SiH ₃ CN							
PN	NaCN	C ₃ N ⁻	HNCNH								
SO	OCs	PH ₃	CH ₃ O	MgC ₄ H							
SiN	c-SiC ₂	HOCN	H ₂ NCO ⁺								
SiO	CO ₂ ^{**}	HSCN	NCCNH ⁺								
SiS	NH ₂ ^{**}	H ₂ O ₂	CH ₃ Cl								
CS	H ₃ ⁺ ^{**}	C ₃ H ⁺	MgC ₃ N								
HF	SiCN	HMgNC									
HD	AlNC	HCCO									
	SiNC	CNCN									
O ₂	HCP	HONO									
CF ⁺	CCP	MgC ₂ H									
	AlOH										
PO	H ₂ O ⁺										
AlO	H ₂ Cl ⁺										
OH ⁺	KCN										
CN ⁻	FeCN										
SH ⁺	HO ₂										
SH	TiO ₂										
HCl ⁺	C ₂ N										
TiO	Si ₂ C										
ArH ⁺	HS ₂										
N ₂	HCS										
	HSC										
NS ⁺	NCO										
HeH ⁺	CaNC										

See <https://cdms.astro.uni-koeln.de/classic/molecules>. * Detected through UV-VIS (electronic) spectrum.

** Detected through IR (vibrational) spectrum.

promising tracer for the presence of complex organics in the interstellar medium. DIBs are a large number of discrete, related, spectral features which are observed in the ultraviolet and visible parts of the interstellar extinction curve. DIBs are thought to represent a major player in understanding the organic content of the interstellar medium. The identification of the DIB carriers will provide essential information on prebiotic organics in the ISM^[89].

2.3 Interstellar chemistry

Due to the broad heterogeneity of temperatures ranging from 10 K to a few thousand Kelvins as well as to the extraordinary diversity of number densities extending over 8 orders of magnitude ($10^1 - 10^9 \text{ atoms cm}^{-3}$), the interstellar chemistry is undeniably expected to be diverse^[6]. While polyatomic molecules are a significant component of matter at temperatures below 4000 K, diatomic systems can survive to somewhat higher temperatures and may be found in environments with temperatures up to about 8000 K^[90]. Two basic sets of information such as *(i) the rate constant* and *(ii) the chemical reaction dynamics* are crucial to ascertain whether a chemical reaction is feasible in distinct interstellar environments^[6]. Hence, the former is fundamental in categorizing how *fast* a chemical reaction is (i.e., *kinetics*) whereas the latter concerns with the entrance and exit barriers, intermediates involved, reaction products, and the energy partition into translational and internal degrees of freedom. The kinetic measurements by Kaiser^[6] yielded compelling evidence that *atomic carbon, cyano, and ethynyl radicals* react rapidly with unsaturated hydrocarbon molecules even at ultralow temperatures.

The key point of interstellar chemistry is cloud opacity. If a cloud is transparent - a *diffuse cloud* characterized by a low optical depth¹ ($\tau \leq 1$) - then molecular lifetimes are limited by photodissociation by the ultraviolet radiation from stars. On the other hand, if a cloud is *opaque to starlight, i.e., with $\tau > 1$* , any formed molecules may be very long-lived^[27,45]. However, understanding the production mechanisms of the observed molecular species in the space has been an open question. Hence, even though the synthesis of simple molecules such as CO but also of simple hydrides like water and ammonia should be well explained by many viable gas-phase mechanisms, the interstellar formation mechanism for larger molecules has been a debate for many scientists in this domain^[41,42,91-100]. For instance, McNally^[92] suggested that interstellar molecules originate in the atmospheres of cool evolved stars from which they are expelled by stellar winds but this mechanism appears incapable to enrich the interstellar gas with molecules to a very large fraction. That is, even at an ejection velocity of 100 km s^{-1} a molecule travels only 10^{17} cm from its source during a typical lifetime of 10^{10} s ^[41]. Other authors thought that certain cool stars, notably IRC + 10216, are richly endowed with circumstellar molecules^[94]. But, if it was the case, several hundreds of such stars are losing mass at a rate of $10^{-5} M_{\odot}$ per year and such phenomena would be required to maintain the observed concentrations of heavy molecules in dark clouds of moderate size. Other molecular production possibilities were also suggested^[91,93]. Subsequently, new molecular production mechanisms have been proposed. This is the case of *gas phase* and *grain formation mechanisms*^[41]. A third mechanism had been introduced: *ice bulk* or *its surface*^[42,101]. In star forming regions, an icy mantle grows on dust particles from accretion of gas phase species on their surfaces^[101,102]. In fact, once a protostar is formed, the ices covering dust grains evaporate and many complex molecules which have been generated within the ices after extensive chemical reactions and thermal and energetic processing are released into the gas phase^[101,103,104].

A recent review by Arumainayagam et al.^[42] detailed these three molecular synthesis mechanisms: Reactions *(1) in gas-phase, (2) on bare dust grains* or *(3) in ice mantles*. This work showed that the **gas phase chemistry**, important in cold ($\sim 10 \text{ K}$) cores, could occur by as many as *nine different reaction mechanisms*^[42] such as : **cosmic-ray induced ioniza-**

1. *optical depth* or *optical thickness*, τ , which is a measure of transparency, is defined as the negative of the natural logarithm of transmission. There is the similarity between the definitions of optical depth ($\tau = -\log T$) and absorbance ($A = -\log_{10} T$).

tion, ion-neutral, neutral-neutral, radiative association, dissociative recombination, associative detachment, photodissociation, photoionization, photodetachment

The neutral-ion reactions was said to be the major chemical processes that produce observed neutral molecules in space cold regions^[5]. Kinetic energy of interstellar species being confined typically from 0.8 (diffuse clouds) to 0.08 kJ mol⁻¹ (dense clouds) on average, gas-phase reactions under thermodynamical equilibrium conditions in interstellar clouds should be exoergic or only slightly endoergic, exhibit little or no entrance barriers, and involve exit barriers which are lower in energy than the separated reactants. In addition, due to the low density of the interstellar cloud media, only two-body collisions (binary reactions) are relevant^[6].

Concerning the *grain chemistry*, four processes contribute to the composition and evolution of the observed interstellar ices in molecular clouds^[105]:

- (1) surface chemistry of species accreted on interstellar grains,
- (2) thermal processing of ice mantles driven by nearby newly formed stars,
- (3) energetic processing of ices by far-ultraviolet (FUV) photosensor particle bombardment.

Each of them has been claimed to be fundamental in the observational characteristics of interstellar ice mantles^[105-107].

Complex molecular species that cannot be created via gas reactions are mainly formed via grain chemistry^[101]. Nevertheless, because solid-state reactions often have *a barrier*, an energy input (thermal or other) is needed to overcome this barrier. In dense and cold regions where interstellar ice is formed, the production of complex organic molecules (COMs¹) can be induced by irradiation by the secondary UV radiation field, by permeating X-rays, or by charged particle bombardment by electrons or protons (Agúndez^[101] and references therein). In star-forming regions, the energy input can, however, be merely thermal and provided by Young Stellar Objects (YSOs). This thermal heating affects most of the volume of the material in hot cores and hot corinos, as well as a large part of the protoplanetary disk. Likewise, cometary ice is heated to a larger depth than UV photon penetration depths (Agúndez^[101] and references therein).

1. **Grain surface chemistry** model (surface + bulk) takes into account the different binding energies of the species on bare or icy surfaces and includes evaporation, photodissociation, and photodesorption² processes, which transform surface species either into other surface species or into gas-phase species^[109]. Grain surface chemistry is dominated by *hydrogenation* and *oxidation reactions* of simple species accreted from the gas phase. The CO chemistry is particularly relevant for the organic reservoir of interstellar ices^[105].

The key step in the surface chemistry of CO is hydrogenation to HCO which has an activation barrier of 1000 K and known to occur at low temperatures. The resulting radical HCO will react on a grain with H to form H₂CO^[105]. Subsequent reaction on grain with H lead to the formation of CH₃OH. The accreted C, N, and O can also lead to the formation of a variety of complex species such as HCONH₂, CH₃CH₂CO, CH₃OCH₃, etc.

2. **Thermal Processing** occurs when an ice mantle is heated to a temperature near its sublimation point. In fact, in a mixed molecular ice with components having similar concentrations but different sublimation temperatures, the evaporation of each component is largely regulated by its own sublimation behavior^[105] and thereafter return into gas phase^[110]. It has observed that thermal reactions are not limited by UV or cosmic rays fluxes or the scarcity of radicals on the surface because they involve only dominant mantle molecules and represent therefore an important step in the formation of COMs that constitute the primitive material of comets and asteroids^[111].
3. Photolysis is among the energetic processes to which planetary ices are continuously exposed where UV photons were shown to dominate the processing of ices in the outer layers of the surface^[112]. It has shown that in the outer shell, both *non-energetic (atom bombardment)* and *energetic (cosmic rays (CR) or induced UV photons)* formation routes on grain ices

1. Complex Organic Molecules (COMs) are organic molecules with more than six atoms^[23,108]

2. The chemical desorption process is the process that releases solid species into the gas phase, in astrochemical models^[109].

can result in the formation of COMs^[113]. The authors have also shown that in translucent clouds, hot cores, and proto-planetary disks, the *energetic processing* is much more relevant, that UV radiation fields are, particularly, much more intense than in dense cold quiescent regions.

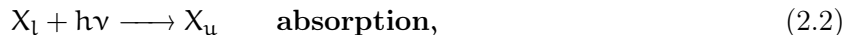
The molecular abundances in the interior regions of dense clouds are controlled by chemical reactions occurring in the gas phase and on grain surfaces but photo-dissociation and photoionization processes play a lesser role than in diffuse clouds as the penetration of ultraviolet radiation is sufficiently low^[114]. The detection of HCO^+ , CCH , N_2H^+ , and HNC clearly indicates that a flux of energy (i.e., *the cosmic rays*) may exist to maintain chemical disequilibrium in these regions. These cosmic rays (which are chiefly protons) produce an ionization rate per interstellar atom or molecule of around 10^{-17}sec^{-1} . Although this ionization rate is very low compared to photo-ionization in diffuse clouds, it is important in dark clouds^[114].

The gas-phase molecules and the solid dust grains play a very significant role in controlling the physics and chemistry. In fact, some molecules are formed on dust grain surfaces and, in addition to the absorption and scattering of starlight by dust, block starlight passing through interstellar clouds. Hence, dust extinction is a crucial parameter in modeling the chemistry of diffuse clouds. Except for the formation of H_2 which forms primarily on dust grain surfaces, the limited chemistry in the diffuse interstellar medium is essentially dominated by *gas phase reactions*, leading to the production of *small molecules* (including long-lived radicals such as CN). The magnetic-field-influenced gravitational collapse of diffuse clouds forms dark, dense molecular clouds which are aptly known as stellar nurseries. During the warm-up process (from $\sim 10\text{K}$ to 100K), the synthesis of complex organic molecules could occur via two mechanisms: (1) *barrierless radical-radical reactions* following the diffusion of non-thermally formed radicals (when the ice temperatures exceed $\sim 30\text{K}$), and (2) *purely thermal reactions* (e.g., $\text{NH}_3 + \text{CO}_2 \longrightarrow \text{NH}_2\text{COOH}$) which involve an activation barrier.

2.4 Radiative transitions

2.4.1 Spontaneous emission, absorption and stimulated emission

Consider an absorber X , i.e., *any* object with energy levels (atoms, ions, molecules, dust grains, ...). If the absorber is in any level l , there is a present radiation with photons having an energy equal to $E_u - E_l$, where E_l and E_u are the upper and lower level energies. The absorber can absorb a photon and undergo an *upward transition*:^[12]



where h is Planck's constant ($h = 6.6260693(11) \times 10^{-34}\text{J.s}$): $h\nu = E_u - E_l$.

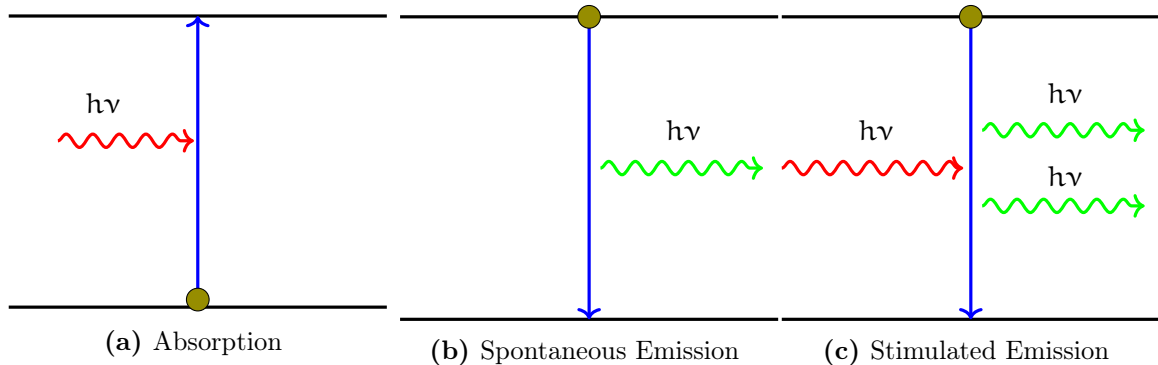


Figure 2.1 – Absorption, Spontaneous Emission and Stimulated emission.

Let n_l be the number density of absorbers X in level l . The rate per volume at which the absorbers absorb photons will be proportional to both the density of photons of the appropriate

energy and the number density n_l . Consequently, the rate of change of n_l due to *photoabsorption* in level l is given by:

$$\underbrace{\left(\frac{dn_u}{dt}\right)_{l \rightarrow u}}_{\text{populate the level } u} = - \underbrace{\left(\frac{dn_l}{dt}\right)_{l \rightarrow u}}_{\text{depopulate the level } l} = n_l B_{lu} u_\nu, \quad \nu = \frac{E_u - E_l}{h} \quad (2.3)$$

where u_ν is the radiation energy density per unit frequency, and B_{ul} is the *Einstein B coefficient* for the transition $l \rightarrow u$.

In the same way, an absorber X in an excited level u can decay to a lower level l with *emission of a photon*. This can happen in two ways:

$$X_u \longrightarrow X_l + h\nu, \quad \nu = (E_u - E_l)/h \quad \text{spontaneous emission}, \quad (2.4)$$

$$X_u + h\nu \longrightarrow X_l + 2h\nu, \quad \nu = (E_u - E_l)/h \quad \text{stimulated emission}, \quad (2.5)$$

Spontaneous emission is a random process, independent of the presence of a radiation field, with a probability per unit time A_{ul} , i.e., the *Einstein A coefficient*.

Stimulated emission occurs if photons of the *identical* frequency, polarization, and direction of propagation are already present, and the rate of stimulated emission is proportional to the density of these photons. Thus the total rate of depopulation of level u due to emission of photons is written as:

$$\underbrace{\left(\frac{dn_l}{dt}\right)_{u \rightarrow l}}_{\text{populate the level } l} = - \underbrace{\left(\frac{dn_u}{dt}\right)_{u \rightarrow l}}_{\text{depopulate the level } u} = n_u (A_{ul} + B_{ul}) u_\nu, \quad (2.6)$$

where the coefficient B_{ul} is the *Einstein B coefficient* for the downward transition $u \rightarrow l$. Through equations (2.3) and (2.6), we get three coefficients characterizing radiative transitions between the two levels u and l : A_{ul} , B_{ul} and B_{lu} . The coefficients B_{ul} and B_{lu} are related to A_{ul} by:

$$B_{ul} = \frac{c^3}{8\pi h \nu} A_{ul} \quad (2.7a)$$

$$B_{lu} = \frac{g_u}{g_l} B_{ul} = \frac{g_u}{g_l} \frac{c^3}{8\pi h \nu^3} A_{ul} \quad (2.7b)$$

where g_u and g_l are the statistical weights, i.e., the degeneracy factors of the upper and lower levels, respectively. From the equations (2.7a) and (2.7b), we see that the *strength* of stimulated emission (B_{ul}) and absorption (B_{lu}) are both found by A_{ul} and the ratio g_u/g_l .

The intensity of a radiation field is often characterized by a dimensionless quantity, the *photon occupation number* n_γ rather than absorption and stimulated emission in terms of the radiation energy density u_ν :

$$n_\gamma \equiv \frac{c^2}{2h\nu^3} I_\nu \quad \text{and} \quad \bar{n}_\gamma \equiv \frac{c^2}{2h\nu^3} \bar{I}_\nu = \frac{c^3}{8\pi h \nu^3} u_\nu \quad (2.8)$$

where the bar denotes averaging over directions. With this definition of \bar{n}_γ in (2.8), Equations (2.3) and (2.6) can be rewritten as:

$$\left(\frac{dn_l}{dt}\right)_{u \rightarrow l} = n_u \cdot A_{ul} \cdot (1 + \bar{n}_\gamma) \quad , \quad \text{and} \quad \left(\frac{dn_u}{dt}\right)_{l \rightarrow u} = n_l \cdot \frac{g_u}{g_l} A_{ul} \cdot \bar{n}_\gamma. \quad (2.9)$$

2.4.2 Absorption cross section

Let $\sigma_{lu}(\nu)$ be the *cross section for absorption of photons of frequency ν* resulting from the $l \rightarrow u$ transition. Knowing that photon density per unit frequency is just $u_\nu/h\nu$ and assuming that u_ν and $h\nu$ do not vary appreciably over the line profile of σ_{ul} , the absorption rate is then

$$\left(\frac{dn_u}{dt}\right)_{l \rightarrow u} = n_l \int d\nu \sigma_{lu}(\nu) c \frac{u_\nu}{h\nu} \approx n_l u_\nu \frac{c}{h\nu} \int d\nu \sigma_{lu}(\nu) \quad (2.10)$$

We get thus,

$$B_{lu} = \frac{c}{h\nu} \int d\nu \sigma_{lu}(\nu) \quad (2.11)$$

and (using equation (2.7b))

$$\int d\nu \sigma_{lu}(\nu) = \frac{g_u}{g_l} \frac{c^2}{8\pi\nu_{lu}^2} A_{ul}. \quad (2.12)$$

Relating then the monochromatic absorption cross section $\sigma_{lu}(\nu)$ to a normalized line profile ϕ_ν (see section 2.4.4):

$$\sigma_{lu}(\nu) = \frac{g_u}{g_l} \frac{c^2}{8\pi\nu_{lu}^2} A_{ul} \phi_\nu \quad \text{with} \quad \int \phi_\nu d\nu = 1. \quad (2.13)$$

The frequency dependence of the normalized line profile ϕ_ν is discussed bellow.

2.4.3 Oscillator strength

Strength of radiative transitions are often characterized by the Einstein A coefficient, A_{ul} . Identically, the *strength of an absorption transition* $l \rightarrow u$ can be characterized by the **oscillator strength** f_{lu} defined as:

$$f_{lu} \equiv \frac{m_e c}{\pi e^2} \int \sigma_{lu}(\nu) d\nu \quad (2.14)$$

The comparison of relations (2.12) and (2.14) shows that the Einstein A coefficient for spontaneous decay is related to the absorption oscillator strength of the upward transition by

$$A_{lu} = \frac{8\pi^2 e^2 \nu_{lu}^2}{m_e c^3} \frac{g_l}{g_u} f_{lu} = \frac{0.6670 \text{ cm}^2 \text{ s}^{-1}}{\lambda_{lu}^2} \frac{g_l}{g_u} f_{lu}. \quad (2.15)$$

The oscillator strength f_{ul} for a downward transition $u \rightarrow l$ is negative, and is defined by

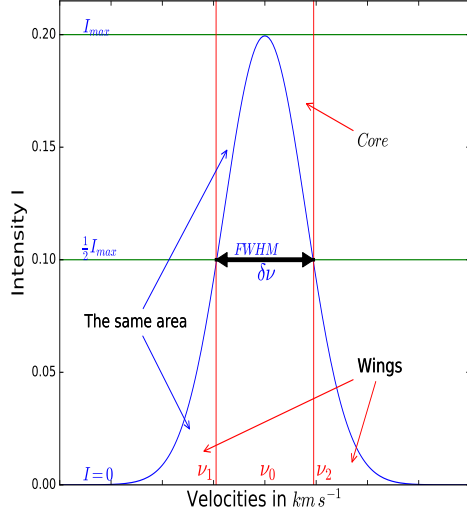
$$g_l f_{lu} = -g_u f_{ul}. \quad (2.16)$$

2.4.4 Widths and line profiles

Absorption or emission spectral lines are never strictly monochromatic, but always show an intensity distribution $I(\nu)$ around the central frequency $\nu_0 = (E_j - E_i)/h$ corresponding to a molecular transition with the energy difference $\Delta E = E_j - E_i$ between upper and lower levels. This intensity distribution is, in general, due to different mechanisms described below.

On the figure bellow, the function $I(\nu)$ in the vicinity of ν_0 is the *line profile*. The frequency interval $\delta\nu = |\nu_2 - \nu_1|$ between the two frequencies ν_2 and ν_1 verifying the relation $I(\nu_1) = I(\nu_2) = I(\nu_0)/2$ is called the *full-width at half-maximum* of the line (*FWHM*), also said in short, *linewidth* or *halfwidth* of the spectral line.

The natural linewidth of a spectral line is due to the Heisenberg uncertainty principle^[115]. According to this principle, there are limits on the accuracy with which two related physical quantities, such as *position* and *momentum*, or *energy* and *time*, can be measured:



$$\Delta x \Delta p \geq \hbar \quad (2.17a)$$

$$\Delta E \Delta t \geq \hbar \quad (2.17b)$$

where Δx and Δp are respectively, uncertainties in position and in momentum; ΔE and Δt , respectively, uncertainties in energy and lifetime, with $\hbar = h/2\pi$.

In general, three mechanisms are responsible to the line profile ϕ_ν :

1. Quantum mechanical uncertainty in the energy E of levels with finites lifetimes which determines the natural width of a line.
2. Collisional/pressure broadening, where collisions reduce the effective lifetime of a state and lead to broader lines.
3. Doppler or thermal broadening

2.4.4.1 Natural broadening

From the equation (2.17b), the relation

$$\Delta E \Delta t \sim \hbar \quad (2.18)$$

means that the longer the measurement time of the energy the accurate is the result or, conversely, the shorter the measurement period, the greater the uncertainty in the result value of the energy. In other words, short-lived states have large uncertainties in the energy. The equation (2.18) can be rewritten as

$$\Delta \nu \sim \frac{\Delta E}{h} \sim \frac{1}{2\pi \Delta t}, \quad (2.19)$$

knowing that $\Delta E = E_u - E_l = h\nu$. This equation shows that the lifetime Δt of an electron in an excited state corresponds to an uncertainty or spread in frequency $\Delta \nu$. Thus, a photon emitted in a transition from a E_u level to the ground state E_l will have a range of possible frequencies in $\Delta \nu$ given by (2.19). This effect is called *natural broadening*.

The *intrinsic* line profile is characterized by a normalized function $\phi(\nu)$ ^[12]:

$$\sigma^{\text{intr}}(\nu) = \frac{\pi e^2}{m_e c} f_{lu} \phi(\nu) \quad \text{with} \quad \int \phi(\nu) d\nu = 1 \quad (2.20)$$

The intrinsic line profile of an absorption line is approximated by a *Lorentzian* or *natural line profile function*:

$$\phi(\nu) = \frac{1}{16\pi^2} \frac{4\gamma_{ul}}{(\nu - \nu_{ul})^2 + \gamma_{ul}^2} = \frac{1}{\pi} \frac{\Delta \nu_N/2}{(\nu - \nu_{ul})^2 + (\Delta \nu_N/2)^2} \quad (2.21)$$

so that its linewidth (*FWHM*) is given by:

$$(\Delta \nu)_{\text{FWHM}}^{\text{intr}} = \Delta \nu_N = \frac{\gamma_{ul}}{2\pi} \quad (2.22)$$

with $\gamma_{ul} \equiv$ damping ratio. Far away from the line center, the function $\phi_\nu \propto \Delta\nu^{-2}$. In astrophysical situations, natural linewidth is not directly observed, except in the line wings in low-pressure (nebular) environments, decay being much slower than a gaussian line profile. In fact, other broadening mechanisms usually dominate it.

2.4.4.2 Collisional and pressure broadening

In dense gas regions, atoms and/or molecules are colliding frequently. These collisions reduce the lifetime of states further to a value smaller than the quantum mechanical lifetime. Consequently, if the frequency of collisions is ν_{col} , then one expects to get a *collisional linewidth* $\Delta\nu_{tot} \sim \nu_{col}$:

$$\phi(\nu) = \frac{1}{16\pi^2} \frac{\Gamma/4\pi^2}{(\nu - \nu_{ul})^2 + (\Gamma/4\pi^2)^2} = \frac{\Delta\nu_{tot}/2\pi}{(\nu - \nu_{ul})^2 + (\Delta\nu_{tot}/2\pi)^2} \quad (2.23)$$

where $\Gamma = \gamma + 2\nu_{col}$ and $\Delta\nu_{tot} = \Delta\nu + \frac{\nu_{col}}{\pi}$. Its profile still be a Lorentzian. Collisions dominate in high density environments.

2.4.4.3 Doppler or thermal broadening

Atoms/molecules in a gas have random motions that depend upon the temperature. For atoms of mass m , at temperature T , the typical speed is obtained from the equation between the kinetic and thermal energies:

$$\frac{1}{2}mV^2 = k_b T \quad (2.24)$$

where k_b is the Boltzmann's constant. The number of particles (atoms, for example) with a given velocity is given by *Maxwell's law*. Let V_x , V_y and V_z be the component of the velocity \vec{V} : $\|\vec{V}\|^2 = V_x^2 + V_y^2 + V_z^2$. The number of atoms dN within velocity interval dV_x (i.e., line of sight in the x direction) is given by:

$$dN(V_x) \propto \exp\left(-\frac{mV_x^2}{2k_b T}\right) dV_x \quad (2.25)$$

The distribution law for speeds has extra factor of V^2 :

$$dN(V) \propto V^2 \exp\left(-\frac{mV^2}{2k_b T}\right) dV \quad (2.26)$$

so that the most probable speed is such that:

$$V_{peak} = \sqrt{\frac{2k_b T}{m}} \quad \text{with} \quad V_{rms} = \sqrt{\langle V^2 \rangle} = \sqrt{\frac{3k_b T}{m}} \quad (2.27)$$

Considering then an atom moving with velocity V_x along the line of sight to the observer, the *Doppler shift* in frequency is given by:

$$\frac{\nu - \nu_0}{\nu_0} = \frac{V_x}{c} \quad (2.28)$$

Combine this equation (2.28) with the distribution of velocities (2.26), one gets:

$$\phi(\nu) = \frac{1}{\Delta\nu_D \sqrt{\pi}} \exp\left(-\frac{(\nu - \nu_0)^2}{(\Delta\nu_D)^2}\right) \quad (2.29)$$

so that the *Doppler width* of the line is:

$$\Delta\nu_D = \frac{\nu_0}{c} \sqrt{\frac{2k_b T}{m}} \quad (2.30)$$

The line profile in this case is *a gaussian*. When the gas has also large-scale (i.e. not microscopic) motions due to turbulence, those add to the width, so that:

$$\Delta v_D = \frac{v_0}{c} \left(\frac{2k_b T}{m} + V_{\text{turb}}^2 \right)^{1/2} \quad (2.31)$$

where V_{turb} is a measure of the turbulent velocity. Doppler/thermal broadening is important in many situations, e.g. in the spectra of stars; whereas turbulent component only matters when the temperature is very low/high velocity.

All these mechanisms could contribute simultaneously to the line broadening, but one or another could dominate on the remaining due to the environmental conditions.

2.5 References

- [1] G. Hinshaw, D. Larson, E. Komatsu, D. N. Spergel, C. Bennett, J. Dunkley, M. Nolta, M. Halpern, R. Hill, N. Odegard, et al. *Astrophys. J. Suppl. Ser.*, 208(2):19, 2013.
- [2] P. Collaboration, P. Ade, N. Aghanim, C. Armitage-Caplan, M. Arnaud, M. Ashdown, F. Atrio-Barandela, J. Aumont, C. Baccigalupi, A. Banday, et al. *Astron. Astrophys.*, 571: A16, 2014.
- [3] E. Herbst. *Annu. Rev. Phys. Chem.*, 46(1):27–54, 1995.
- [4] B. B. Ochsendorf. 2015.
- [5] S. Kwok. *Physics and chemistry of the interstellar medium*. University Science Books, 2007.
- [6] R. I. Kaiser. *Chem. Rev.*, 102(5):1309–1358, 2002.
- [7] J. A. Nuth III, S. B. Charnley, and N. M. Johnson. *Meteorites and the early solar system II*, 2:147–167, 2006.
- [8] S. Kwok. *Organic matter in the universe*. John Wiley & Sons, 2011.
- [9] A. Tielens. *J Rev. Mod. Phys.*, 85(3):1021, 2013.
- [10] P. Ehrenfreund and S. B. Charnley. *ARA&A*, 38(1):427–483, 2000.
- [11] P. Ehrenfreund and H. Fraser. Ice chemistry in space. In *Solid State Astrochemistry*, pages 317–356. Springer, 2003.
- [12] B. T. Draine. *Physics of the interstellar and intergalactic medium*, volume 19. Princeton University Press, 2010.
- [13] J. S. Mathis, W. Rumpl, and K. H. Nordsieck. *ApJ*, 217:425–433, 1977.
- [14] B. Draine and H. M. Lee. *ApJ*, 285:89–108, 1984.
- [15] B. Draine and A. Li. *ApJ*, 657(2):810, 2007.
- [16] S. Paron. *arXiv preprint arXiv:1803.02277*, 2018.
- [17] C. F. McKee and J. P. Ostriker. *ApJ*, 218:148–169, 1977.
- [18] C. Heiles and T. Troland. *Astrophys. J.*, 586(2):1067, 2003.
- [19] R. C. Kennicutt Jr and N. J. Evans. *Annu. Rev. Astron. Astrophys.*, 50:531–608, 2012.
- [20] D. P. Cox. *Annu. Rev. Astron. Astrophys.*, 43:337–385, 2005.
- [21] K. M. Ferriere. *J Rev. Mod. Phys.*, 73(4):1031, 2001.
- [22] A. G. Tielens. *The physics and chemistry of the interstellar medium*. Cambridge University Press, 2005.
- [23] E. Herbst and E. F. Van Dishoeck. *ARA&A*, 47:427–480, 2009.
- [24] P. Ehrenfreund and J. Cami. *Cold Spring Harb. Perspect. Biol.*, 2(12):a002097, 2010.
- [25] D. Wooden, S. Charnley, and P. Ehrenfreund. *Comets II*, pages 33–66, 2004.
- [26] R. S. Klessen and S. C. Glover. Physical processes in the interstellar medium. In *Star Formation in Galaxy Evolution: Connecting Numerical Models to Reality*, pages 85–249. Springer, 2016.
- [27] B. Turner and W. Burton. The large scale characteristics of the galaxy. In *IAU Symp. no. 84*, page 257. Reidel Dordrecht, 1979.
- [28] N. Kanekar, R. Subrahmanyam, J. N. Chengalur, and V. Safouris. *Mon. Not. R. Astron. Soc.*, 346(4):L57–L61, 2003.

- [29] G. Field, D. Goldsmith, and H. Habing. *ApJ*, 155:L149, 1969.
- [30] K. R. Sembach, J. C. Howk, R. S. Ryans, and F. P. Keenan. *ApJ*, 528(1):310, 2000.
- [31] R. Reynolds, L. Haffner, and S. Tufté. *Astrophys. J. Lett.*, 525(1):L21, 1999.
- [32] T. P. Snow and B. J. McCall. *Annu. Rev. Astron. Astrophys.*, 44:367–414, 2006.
- [33] E. Vázquez-Semadeni, D. Ryu, T. Passot, R. F. González, and A. Gazol. *ApJ*, 643(1):245, 2006.
- [34] H. Nomura and T. Millar. *A&A*, 414(2):409–423, 2004.
- [35] H. Beuther. *Proc. Int. Astron. Union*, 2(S237):148–154, 2006.
- [36] R. T. Garrod and S. L. Widicus Weaver. *Chem. Rev.*, 113(12):8939–8960, 2013.
- [37] G. Ferland, A. Fabian, and R. Johnstone. *Mon. Not. R. Astron. Soc.*, 266(2):399–411, 1994.
- [38] C. D. Wilson, C. E. Walker, and M. D. Thornley. *ApJ*, 483(1):210, 1997.
- [39] P. Solomon, D. Sanders, and A. Rivolo. *ApJ*, 292:L19–L24, 1985.
- [40] F. H. Shu, F. C. Adams, and S. Lizano. *ARA&A*, 25(1):23–81, 1987.
- [41] A. Dalgarno and J. Black. *Rep. Prog. Phys.*, 39(6):573, 1976.
- [42] C. R. Arumainayagam, R. T. Garrod, M. C. Boyer, A. K. Hay, S. T. Bao, J. S. Campbell, J. Wang, C. M. Nowak, M. R. Arumainayagam, and P. J. Hodge. *Chem. Soc. Rev.*, 48(8):2293–2314, 2019.
- [43] E. Herbst. *Int. Rev. Phys. Chem.*, 36(2):287–331, 2017.
- [44] L. Ziurys. Observations of shocked regions. In *Symposium-International Astronomical Union*, volume 150, pages 237–244. Cambridge University Press, 1992.
- [45] H. Kroto. *Int. Rev. Phys. Chem.*, 1(3):309–376, 1981.
- [46] A. S. Eddington. *Proc. R. Soc. Lond. A*, 111(759):424–456, 1926.
- [47] B. A. McGuire, A. M. Burkhardt, S. Kalenskii, C. N. Shingledecker, A. J. Remijan, E. Herbst, and M. C. McCarthy. *Science*, 359(6372):202–205, 2018.
- [48] B. A. McGuire. The 2020 census of interstellar, circumstellar, extragalactic, protoplanetary disk, and exoplanetary molecules: What are the pressing spectroscopic needs from the laboratory? International Symposium on Molecular Spectroscopy, 2020.
- [49] A. Belloche, R. Garrod, H. Müller, K. Menten, C. Comito, and P. Schilke. *A&A*, 499(1):215–232, 2009.
- [50] E. K. Wilson. *C&EN*, 84(18):33–34, 2006.
- [51] J. M. Hollis, F. J. Lovas, and P. R. Jewell. *Astrophys. J. Lett.*, 540(2):L107, 2000.
- [52] B. E. Turner and A. J. Apponi. *Astrophys. J. Lett.*, 561(2):L207, 2001.
- [53] C. Gottlieb, J. Ball, E. Gottlieb, and D. Dickinson. *ApJ*, 227:422–432, 1979.
- [54] B. A. McGuire, A. M. Burkhardt, C. N. Shingledecker, S. V. Kalenskii, E. Herbst, A. J. Remijan, and M. C. McCarthy. *Astrophys. J. Lett.*, 843(2):L28, 2017.
- [55] M. Ikeda, M. Ohishi, A. Nummelin, J. Dickens, P. Bergman, Å. Hjalmarsen, and W. M. Irvine. *ApJ*, 560(2):792, 2001.
- [56] J. Dickens, W. M. Irvine, M. Ohishi, M. Ikeda, S. Ishikawa, A. Nummelin, and Å. Hjalmarsen. *ApJ*, 489(2):753, 1997.
- [57] N. Fourikis, K. Takagi, and M. Morimoto. *ApJ*, 191:L139, 1974.
- [58] C. Xue, A. J. Remijan, C. L. Brogan, T. R. Hunter, E. Herbst, and B. A. McGuire. *ApJ*, 882(2):118, 2019.
- [59] N. Marcelino, J. Cernicharo, M. Agúndez, E. Roueff, M. Gerin, J. Martín-Pintado, R. Mauersberger, and C. Thum. *Astrophys. J. Lett.*, 665(2):L127, 2007.
- [60] A. Tokunaga, S. Beck, T. Geballe, J. Lacy, and E. Serabyn. *Icarus*, 48(2):283–289, 1981.
- [61] L. M. Ziurys and B. Turner. *ApJ*, 300:L19–L23, 1986.
- [62] S. Aalto, S. Garcia-Burillo, S. Muller, J. Winters, P. Van Der Werf, C. Henkel, F. Costagliola, and R. Neri. *A&A*, 537:A44, 2012.
- [63] S. Zeng, D. Quénard, I. Jiménez-Serra, J. Martín-Pintado, V. Rivilla, L. Testi, and R. Martín-Doménech. *MNRAS*, 484(1):L43–L48, 2019.
- [64] J. Cernicharo, M. Agúndez, L. V. Prieto, M. Guélin, J. Pardo, C. Kahane, C. Marka, C. Kramer, S. Navarro, G. Quintana-Lacaci, et al. *A&A*, 606:L5, 2017.

- [65] H. Kroto, C. Kirby, D. Walton, L. Avery, N. Broten, J. MacLeod, and T. Oka. *ApJ*, 219: L133–L137, 1978.
- [66] N. Broten, T. Oka, L. Avery, J. MacLeod, and H. Kroto. *ApJ*, 223:L105–L107, 1978.
- [67] W. W. Duley and A. Hu. *Astrophys. J. Lett.*, 745(1):L11, 2012.
- [68] J. Cami, J. Bernard-Salas, E. Peeters, and S. E. Malek. *Science*, 329(5996):1180–1182, 2010.
- [69] B. Foing and P. Ehrenfreund. *Nature*, 369(6478):296–298, 1994.
- [70] R. Güsten, H. Wiesemeyer, D. Neufeld, K. M. Menten, U. U. Graf, K. Jacobs, B. Klein, O. Ricken, C. Risacher, and J. Stutzki. *Nature*, 568(7752):357–359, 2019.
- [71] P. Schilke, D. A. Neufeld, H. S. Müller, C. Comito, E. A. Bergin, D. C. Lis, M. Gerin, J. H. Black, M. Wolfire, N. Indriolo, et al. *A&A*, 566:A29, 2014.
- [72] H. S. Müller, S. Muller, P. Schilke, E. A. Bergin, J. H. Black, M. Gerin, D. C. Lis, D. A. Neufeld, and S. Suri. *A&A*, 582:L4, 2015.
- [73] D. Neufeld, E. Falgarone, M. Gerin, B. Godard, E. Herbst, G. P. Des Forêts, A. Vasyunin, R. Güsten, H. Wiesemeyer, and O. Ricken. *A&A*, 542:L6, 2012.
- [74] H. Suzuki, M. Ohishi, N. Kaifu, S.-I. Ishikawa, and T. Kasuga. *Publ. Astron. Soc. Jpn.*, 38: 911–917, 1986.
- [75] M. Guélin, J. Cernicharo, M. Travers, M. McCarthy, C. Gottlieb, P. Thaddeus, M. Ohishi, S. Saito, and S. Yamamoto. *A&A*, 317:L1–L4, 1997.
- [76] A. J. Remijan, J. Hollis, F. J. Lovas, M. Cordiner, T. Millar, A. Markwick-Kemper, and P. Jewell. *Astrophys. J. Lett.*, 664(1):L47, 2007.
- [77] J. P. Maier, N. M. Lakin, G. A. Walker, and D. A. Bohlender. *ApJ*, 553(1):267, 2001.
- [78] P. F. Bernath, K. H. Hinkle, and J. J. Keady. *Science*, 244(4904):562–564, 1989.
- [79] J.-C. Loison, M. Agúndez, V. Wakelam, E. Roueff, P. Gratier, N. Marcelino, D. N. Reyes, J. Cernicharo, and M. Gerin. *Mon. Not. R. Astron. Soc.*, 470(4):4075–4088, 2017.
- [80] C. Vastel, J.-C. Loison, V. Wakelam, and B. Lefloch. *A&A*, 625:A91, 2019.
- [81] S. Nickerson, N. Rangwala, S. W. Colgan, C. DeWitt, X. Huang, K. Acharyya, M. Drozdovskaya, R. C. Fortenberry, E. Herbst, and T. J. Lee. *Astrophys. J.*, 907(1):51, 2021.
- [82] N. Brouillet, S. Muller, F. Herpin, J. Braine, and T. Jacq. *A&A*, 429(1):153–159, 2005.
- [83] J. Cernicharo, M. Guélin, M. Agúndez, K. Kawaguchi, M. McCarthy, and P. Thaddeus. *A&A*, 467(2):L37–L40, 2007.
- [84] H. Gupta, C. Gottlieb, M. McCarthy, and P. Thaddeus. *ApJ*, 691(2):1494, 2009.
- [85] S. Brünken, H. Gupta, C. Gottlieb, M. McCarthy, and P. Thaddeus. *Astrophys. J. Lett.*, 664 (1):L43, 2007.
- [86] P. Thaddeus, C. Gottlieb, H. Gupta, S. Brünken, M. McCarthy, M. Agúndez, M. Guélin, and J. Cernicharo. *ApJ*, 677(2):1132, 2008.
- [87] J. Cernicharo, M. Guélin, M. Agúndez, M. McCarthy, and P. Thaddeus. *Astrophys. J. Lett.*, 688(2):L83, 2008.
- [88] G. M. Caro, U. Meierhenrich, W. Schutte, B. Barbier, A. A. Segovia, H. Rosenbauer, W.-P. Thiemann, A. Brack, and J. Greenberg. *Nature*, 416(6879):403–406, 2002.
- [89] F. Salama. *Orig. Life Evol. Biosph.*, 28(4):349–364, 1998.
- [90] J. Tennyson. *Astronomical spectroscopy: an introduction to the atomic and molecular physics of astronomical spectra*, volume 2. World Scientific, 2010.
- [91] G. Herbig. *Proceedings in Mem. Soc. r. Sci. Liege*, 19:13, 1970.
- [92] D. McNally. Interstellar molecules: their formation and destruction. In *Advances in Atomic and Molecular Physics*, volume 8, pages 1–38. Elsevier, 1972.
- [93] E. Anders. *Molecules in the galactic environment* ed ma gordon and le snyder, 1973.
- [94] M. Morris. *ApJ*, 197:603–610, 1975.
- [95] M. Jin and R. T. Garrod. *Astrophys. J. Suppl. Ser.*, 249(2):26, 2020.
- [96] N. Inostroza, D. Mardones, J. Cernicharo, H. Zinnecker, J. Ge, N. Aria, P. Fuentealba, and C. Cardenas. *A&A*, 629:A28, 2019.
- [97] M. J. Abplanalp, S. Góbi, and R. I. Kaiser. *Phys. Chem. Chem. Phys.*, 21(10):5378–5393, 2019.

- [98] F. Vazart, D. Calderini, C. Puzzarini, D. Skouteris, and V. Barone. *J. Chem. Theory Comput.*, 12(11):5385–5397, 2016.
- [99] L. Reboussin, V. Wakelam, S. Guilloteau, and F. Hersant. *Mon. Not. R. Astron. Soc.*, 440(4):3557–3567, 2014.
- [100] M. D. Boamah, K. K. Sullivan, K. E. Shulenberger, C. M. Soe, L. M. Jacob, F. C. Yhee, K. E. Atkinson, M. C. Boyer, D. R. Haines, and C. R. Arumainayagam. *Faraday Discuss.*, 168:249–266, 2014.
- [101] M. Agúndez. Interstellar chemical models. In *Laboratory Astrophysics*, pages 219–232. Springer, 2018.
- [102] D. Whittet, P. Gerakines, J. Hough, and S. Shenoy. *ApJ*, 547(2):872, 2001.
- [103] K. I. Öberg, R. T. Garrod, E. F. Van Dishoeck, and H. Linnartz. *A&A*, 504(3):891–913, 2009.
- [104] P. Theulé, F. Duvernay, G. Danger, F. Borget, J. Bossa, V. Vinogradoff, F. Mispelaer, and T. Chiavassa. *Adv. Space Res.*, 52(8):1567–1579, 2013.
- [105] V. Mannings, A. P. Boss, and S. S. Russell. *Protostars and Planets IV*, 2000.
- [106] A. Tielens and D. Whittet. *Molecules in astrophysics: Probes and processes* ed ef van dishoeck, 1997.
- [107] W. Schutte, A. Boogert, A. Tielens, D. Whittet, P. Gerakines, J. Chiar, P. Ehrenfreund, J. Greenberg, E. Van Dishoeck, and T. De Graauw. *A&A*, 343:966–976, 1999.
- [108] V. Rivilla, M. Beltrán, R. Cesaroni, F. Fontani, C. Codella, and Q. Zhang. *A&A*, 598:A59, 2017.
- [109] S. Cazaux, M. Minissale, F. Dulieu, and S. Hocuk. *A&A*, 585:A55, 2016.
- [110] P. Ehrenfreund, L. d’Hendecourt, S. Charnley, and R. Ruiterkamp. *Journal of Geophysical Research: Planets*, 106(E12):33291–33301, 2001.
- [111] P. Theulé, J. A. Noble, and P. Ghesquière. Thermal reactivity dynamics in interstellar ice. In *Laboratory Astrophysics*, pages 149–155. Springer, 2018.
- [112] F. Salama. Uv photochemistry of ices. In *Solar System Ices*, pages 259–279. Springer, 1998.
- [113] K.-J. Chuang, G. Fedoseev, D. Qasim, S. Ioppolo, E. van Dishoeck, and H. Linnartz. *Mon. Not. R. Astron. Soc.*, 467(3):2552–2565, 2017.
- [114] E. Herbst and W. Klemperer. *Physics today*, 29(6):32–39, 1976.
- [115] V. B. Thomsen. *J. Chem. Educ.*, 72(7):616, 1995.

ELECTRONIC STRUCTURE CALCULATION

3.1 Born-Oppenheimer approximation

The *time-dependent Schrödinger equation* for a polyatomic system is

$$i\hbar \frac{\partial}{\partial t} \Psi(\mathbf{r}, \mathbf{R}, t) = \hat{\mathcal{H}} \Psi(\mathbf{r}, \mathbf{R}, t) \quad (3.1)$$

where the *molecular wave function* $\Psi(\mathbf{r}, \mathbf{R}, t)$ depends on the *electronic coordinates* \mathbf{r} , the *nuclear coordinates* \mathbf{R} in laboratory of space-fixed frame and time t . The hamilton operator $\hat{\mathcal{H}}$ in (3.1) can be written as:

$$\hat{\mathcal{H}} = \hat{\mathcal{T}} + \hat{\mathcal{V}} \quad (3.2)$$

where

$$\hat{\mathcal{T}} = -\frac{\hbar^2}{2m_e} \sum_{i=1}^{N1} \nabla_i^2 - \sum_{\alpha=1}^{N2} \frac{\hbar^2}{2M_\alpha} \nabla_\alpha^2 \quad (3.3a)$$

$$\hat{\mathcal{V}} = -\sum_{\alpha=1}^{N2} \sum_{i=1}^{N1} \frac{Z_\alpha e^2}{4\pi\epsilon_0 r_{\alpha i}} + \sum_{\alpha=1}^{N2} \sum_{\beta>\alpha}^{N2} \frac{Z_\alpha Z_\beta e^2}{4\pi\epsilon_0 R_{\alpha\beta}} + \sum_{i=1}^{N1} \sum_{j>i}^{N1} \frac{e^2}{4\pi\epsilon_0 r_{ij}} \quad (3.3b)$$

where i, j refer to electrons and α, β refer to nuclei. In atomic units, where $e = \hbar = m_e = 1$, $\frac{1}{4\pi\epsilon_0} = 1$ and $a_0 = 1$ (with m_e , the mass of the electron, and $a_0 = 4\pi\epsilon_0\hbar^2/(m_e e^2)$, the Bohr radius), the expression (3.3) becomes:

$$\hat{\mathcal{T}} = -\frac{1}{2} \sum_{i=1}^{N1} \nabla_i^2 - \sum_{\alpha=1}^{N2} \frac{1}{2M_\alpha} \nabla_\alpha^2 \quad (3.4a)$$

$$\hat{\mathcal{V}} = -\sum_{\alpha}^{N2} \sum_{i=1}^{N1} \frac{Z_\alpha}{r_{\alpha i}} + \sum_{\alpha}^{N2} \sum_{\beta>\alpha}^{N2} \frac{Z_\alpha Z_\beta}{R_{\alpha\beta}} + \sum_i^{N1} \sum_{j>i}^N \frac{1}{r_{ij}} \quad (3.4b)$$

Because in equation (3.4) for the hamiltonian operator, the time does not appear explicitly, a separation of variables according to space and time can be performed. Hence, the molecular wave function of the system takes the form:

$$\Psi(\mathbf{r}, \mathbf{R}, t) = \Phi(\mathbf{r}, \mathbf{R}) \cdot \psi(t) \quad (3.5)$$

By substituting equation (3.5) in equation (3.1), two differential equations are obtained: a *time-independent* and a *time-dependent* equations. The *time-independent Schrödinger equation* for the *spatial wave function* has the form:

$$\hat{\mathcal{H}}\Phi(\mathbf{r}, \mathbf{R}) = E\Phi(\mathbf{r}, \mathbf{R}) \quad (3.6)$$

where E is the *eigenvalue* of the hamiltonian operator and $\psi(\mathbf{r}, \mathbf{R})$ its eigenfunction. The obtained solution for the *time-dependent differential equation* is:

$$\psi(t) = e^{iEt/\hbar} \quad (3.7)$$

Let's now consider a system of axes centered on the center-of-mass (CM) of the molecule. In this center-of-mass reference, let's denote by $\mathbf{x}_1, \mathbf{x}_2, \dots, \mathbf{x}_{N1} \in \mathbb{R}^3$ and $\mathbf{X}_1, \mathbf{X}_2, \dots, \mathbf{X}_{N2} \in \mathbb{R}^3$ the new electronic and nuclear coordinates, respectively, with $N = N1 + N2$. In this reference, the CM of the whole system is given by the position operator:

$$\mathbf{R} = \frac{1}{M_T} \left(\sum_i^{N1} \mathbf{x}_i + \sum_{i=1}^{N2} M_i \mathbf{X}_i \right), \quad \text{with } M_T = N1 + \sum_{i=1}^{N2} M_i \quad (3.8)$$

Physically, this center-of-mass behaves like a free particle. The hamiltonian operator $\hat{\mathcal{H}}$ is therefore written as:

$$\hat{\mathcal{H}} = -\frac{1}{2M_T} \nabla_{\mathbf{R}}^2 + \hat{H} \quad (3.9)$$

where the first term is the *kinetic energy of the center-of-mass* T_{CM} . The second term is the *internal Hamiltonian* \hat{H} and is independent of the center-of-mass variables; it is *translationally invariant*. There are therefore *infinitely many possible choices of internal coordinates* that are unitarily equivalent, so that the form of \hat{H} is not determined uniquely, but whatever coordinates can be chosen and \hat{H} remains the same operator as in (3.9). The internal hamiltonian can be made explicitly by referring the particle coordinates to a point moving with the system, such as *the center-of-mass itself, the center-of-nuclear-mass or one of the moving particles*^[1-3]. The best choice is to take as origin of reference axes the center-of-nuclear-mass. In this case, there is a explicit separation between electrons and nuclei indices, contrary to the cases corresponding to the first two choices. There are then $N = (N1 + N2 - 1)$ translationally invariant coordinates $(\mathbf{x}_1, \mathbf{x}_2, \dots, \mathbf{x}_{N1}, \mathbf{X}_1, \mathbf{X}_2, \dots, \mathbf{X}_{N2-1})$. For $1 \leq i \leq N1$ and $1 \leq j \leq N2 - 1$, we have $\mu_{ij}^{-1} = M_i^{-1} + M_j^{-1}$, with $\mathbf{X} = (\mathbf{X}_1, \dots, \mathbf{X}_{N2-1})$ and $\mathbf{x} = (\mathbf{x}_1, \dots, \mathbf{x}_{N1})$, so that

$$\hat{H} = \hat{H}_N + \hat{H}_{el}, \quad (3.10)$$

given by:

$$\hat{H}_N = - \sum_{i=1, j>i}^{N2-1} \frac{1}{2\mu_{ij}} \nabla_{\mathbf{x}_i} \nabla_{\mathbf{x}_j} \quad (3.11)$$

and

$$\begin{aligned} \hat{H}_{el} = & -\frac{1}{2} \sum_{i=1}^{N1} \nabla_{\mathbf{x}_i}^2 - \frac{1}{2} \sum_{i=1, j>i}^{N1} \nabla_{\mathbf{x}_i} \cdot \nabla_{\mathbf{x}_j} \\ & \cdot - \sum_{i=1}^{N2-1} \sum_{j=1}^{N1} \frac{Z_i}{|\mathbf{x}_j - \mathbf{X}_i|} \\ & + \sum_{i=1, j>i}^{N1} \frac{1}{|\mathbf{x}_i - \mathbf{x}_j|} + \sum_{i=1, j>i}^{N2-1} \frac{Z_i Z_j}{|\mathbf{X}_i - \mathbf{X}_j|} \end{aligned} \quad (3.12)$$

The second term in equation (3.12) would vanish and the equation gets the familiar form as in equation (3.3). We therefore write the hamiltonian operator as below:

$$\hat{H} = \hat{T}_e(\mathbf{x}) + \hat{T}_N(\mathbf{X}) + \hat{V}_{eN}(\mathbf{x}, \mathbf{X}) + \hat{V}_{NN}(\mathbf{X}) + \hat{V}_{ee}(\mathbf{x}) \quad (3.13)$$

with $\hat{T}_e(\mathbf{x})$: the kinetic energy operator for electrons; $\hat{T}_N(\mathbf{X})$: the kinetic energy operator for nuclei; $\hat{V}_{NN}(\mathbf{X})$: the nuclei-nuclei interaction operator; $\hat{V}_{eN}(\mathbf{x}, \mathbf{X})$: nuclei-electrons interaction operator; $\hat{V}_{ee}(\mathbf{x})$: the electrons-electrons interaction operator. The equation (3.13) does not at all contain the translational part.

From molecular spectroscopy, it has been found that energy levels of the low-lying states, typically, of small polyatomic molecules an expansion in powers of κ^2 :

$$E_{nvj} \approx V_n^{(0)} + \kappa^2 E_{nv}^{(2)} + \kappa^4 E_{nvj}^{(4)} + \dots \quad (3.14)$$

where $V_n^{(0)}$ is the minimum value of the electronic energy which characterizes the molecule at rest, $E_{nv}^{(2)}$ is the energy of the nuclear vibrations, and $E_{nv}^{(4)}$ contains the rotational energy^[2,4].

After dropping the center-of-mass kinetic energy term, the equation (3.10) is similar with 3.3. However, there is a very fundamental difference between them which arises from the fact that with the center-of-nuclear-mass chosen as the electronic origin, H_{el} is *independent of the nuclear momentum operators*.

The resolution of the Schrödinger equation associated to the hamiltonian (3.6) can be simplified by using the so-called **Born-Oppenheimer approximation**. This method is based on two assumptions:

1. The nuclei are much heavier than electrons ($M_\alpha \gg m_e$) and, consequently, move very slowly in comparison with the electronic motion: $\hat{T}_N \ll \hat{T}_e$. The electronic part of the Schrödinger equation may therefore be solved under the condition that the nuclei are motionless. Consequently, the electronic energy may then be determined for many different fixed nuclear configurations.

By this assumption, the coordinates X do not change with the time for a given nuclear configuration. Consequently, the second term of the right side of the equation (3.13) vanishes:

$$\hat{T}_N(X) = - \sum_{j=1}^{N2-1} \frac{1}{2\mu_{ij}} \nabla_{x_i} \nabla_{x_j} \approx 0 \quad (3.15)$$

2. The nuclear part of the Schrödinger equation is solved by regarding the motion of the nuclei as taking place in the average potential field created by the fast-moving electrons.

According to the first assumption, the total wave function of a molecule can be broken into **its electronic** $\Phi_\kappa(\mathbf{r}, \bar{X})$ and **nuclear** $\chi_\nu(X)$ components:

$$\Phi(\mathbf{x}, X) = \Phi_\kappa(\mathbf{x}, \bar{X}) \chi(X) \quad (3.16)$$

However, the term corresponding to the nucleus-electron interaction, i.e., \hat{V}_{eN} , prevents a complete separation. For a given nuclear configuration, X is no longer a variable, but a *parameter*. Take, for example, $\bar{X} = X_{eq}$ corresponding to the equilibrium nuclear configuration. The Schrödinger equation becomes:

$$\left[\hat{H}_e + \hat{V}_{NN} \right] \Phi_\kappa(\mathbf{x}, X_{eq}) = E_\kappa \Phi_\kappa(\mathbf{x}, X_{eq}) \quad (3.17)$$

with the **purely electronic Hamiltonian** H_e given by:

$$\hat{H}_e = \hat{T}_e(\mathbf{x}) + \hat{V}_{eN}(\mathbf{x}, X_{eq}) + \hat{V}_{ee}(\mathbf{x}) \quad (3.18)$$

Due to the second hypothesis, the electronic hamiltonian operator including nuclear repulsion is:

$$\begin{aligned} \hat{H}_\kappa &= \hat{H}_e + \hat{V}_{nn}(X_{eq}) \\ &= \hat{H}_e + \hat{V}_{nn} \end{aligned} \quad (3.19)$$

so that for this nuclear configuration, the Schrödinger equation becomes:

$$\left[\hat{H}_e + \hat{V}_{NN} \right] \Phi_\kappa(\mathbf{x}, X_{eq}) = E_\kappa \Phi_\kappa(\mathbf{x}, X_{eq}) \quad (3.20)$$

with the **purely electronic hamiltonian** H_e given by:

$$\hat{H}_e = \hat{T}_e(\mathbf{x}) + \hat{V}_{eN}(\mathbf{x}, X_{eq}) + \hat{V}_{ee}(\mathbf{x}) \quad (3.21)$$

The energy E_κ in the equation (3.17) is the **electronic energy including internuclear repulsion**. The internuclear distances $X_{\alpha\beta}$ in $\hat{V}_{NN}(X)$ (see expression (3.4)) are not variables.

They are fixed at some constant value, $\chi_{e\mathbf{q}}$ in equations (3.17-3.23), for example. There are therefore *an infinite number of possible nuclear configurations*, and for **each of them** we may solve the electronic Schrodinger equation (3.6) and get a set of electronic wave functions and corresponding electronic energies; *each member of the set corresponds to a different molecular electronic state*^[5]. The electronic wave functions together with energies depend parametrically *on the nuclear configuration* characterized by $\psi_{\kappa} = \psi_{\kappa,\mathbf{n}}(\mathbf{q}_i, \mathbf{q}_\alpha)$ and $E_{\kappa} = E_{\kappa,\mathbf{n}}(\mathbf{q}_\alpha)$ (with \mathbf{n} representing the electronic quantum numbers). Moreover, we assume the eigenfunctions $\psi_{e\ell}$ form a complete **orthonormal set**:

$$\int \Phi_{\kappa\mathbf{m}}^* \Phi_{\kappa\mathbf{n}} d\mathbf{q} = \delta_{\mathbf{m}\mathbf{n}} \quad (3.22)$$

where $\delta_{\mathbf{m}\mathbf{n}} = 0$ if $\mathbf{m} \neq \mathbf{n}$ and $\delta_{\mathbf{m}\mathbf{n}} = 1$ if $\mathbf{m} = \mathbf{n}$.

Considering the second assumption of Born-Oppenheimer, the energy $E_{\kappa}(\mathbf{X})$ is used as a potential energy function to treat the nuclear motion. When the nuclei move, the electronic energy varies smoothly as a function of the parameters defining the nuclear configuration, and $E_{\kappa}(\mathbf{q}_\alpha)$ becomes, in effect, the potential energy for the nuclear motion. *The electrons act like a spring connecting the nuclei, as the internuclear distance changes, the energy stored in the spring changes.* Thus, the Schrödinger equation for nuclear motion is

$$\left[\hat{H}_{\mathbf{v}} + E_{\kappa}(\mathbf{X}) \right] \chi_{\kappa\mathbf{v}}(\mathbf{x}, \mathbf{X}) = E_{\kappa\mathbf{v}} \chi_{\kappa\mathbf{v}}(\mathbf{X}) \quad (3.23)$$

where the wave function $\chi_{\kappa\mathbf{v}}$ depends on the nuclear coordinates \mathbf{R} and on the electronic state κ . Each electronic state κ gives rise to a series of nuclear states, indexed by \mathbf{v} . The energy eigenvalue $E_{\kappa\mathbf{v}}$ in (3.23) is *the total energy of the molecule*, since the hamiltonian (3.23) includes operators for both nuclear energy and electronic energy. $E_{\kappa\mathbf{v}}$ is simply a number and does not depend on any coordinates. Remark that *for each electronic state for a molecule*, we must solve a different nuclear Schrödinger equation since E_{κ} differs from state to state.

It has been found that the total energy $E_{\kappa,\mathbf{v}}$ for an electronic state of a molecule is **approximately the sum of electronic, vibrational, and the rotational energies**:

$$E_{\kappa,\mathbf{v}} \approx E_{\text{elec}} + E_{\text{vib}} + E_{\text{rot}} \quad (3.24)$$

where E_{elec} is such that $E_{\text{elec}} = E_{\kappa}(\mathbf{x}_e)$.

3.2 Theory of molecular orbitals

It is known, from atomic orbitals theory, that the probability of finding the electron in the volume $d\tau$ (for atomic H, for example) is given by $\phi^2 d\tau$, with ϕ , a wave function representing the spatial distribution of the electron. That is, we may have $\int \phi^2 d\tau$. Let's start by a simplest molecule: H_2 .

Understanding then the bonding in H_2 , one may understand what is happening when the two atoms are approaching each other until *atomic orbitals interact*^[6]. In fact, when atoms, let's say A and B, get close enough to bond, their *atomic orbitals* reshape themselves and become a set of new orbitals that no longer belong to any one atom. They are orbitals for the entire molecule and are called *molecular orbitals*. The function describing the new electron distribution in the molecule, i.e., *molecular orbital* σ , is a *linear combination of atomic orbitals* (LCAOs) ϕ_A and ϕ_B :

$$\psi = c_1 \phi_A + c_2 \phi_B \quad (3.25)$$

Assuming the atomic orbitals ϕ_A and ϕ_B are normalized, one has:

$$(c_1)^2 + (c_2)^2 + 2c_1 c_2 \underbrace{\int \phi_A \phi_B d\tau}_S = \frac{1}{N^2} \quad (3.26)$$

The integral $\int \phi_A \phi_B d\tau$ is called the *overlap integral*, S , between the two wave functions ϕ_A and ϕ_B . The two wave functions *overlap* in the region between the two nuclei. The normalized wave function is therefore:

$$\psi = \frac{1}{\sqrt{(c_1)^2 + (c_2)^2 + 2c_1c_2S}} (c_1\phi_A + c_2\phi_B) \quad (3.27)$$

and its energy is given by:

$$\begin{aligned} E &= N^2 \int (c_1\phi_A + c_2\phi_B) \mathcal{H} (c_1\phi_A + c_2\phi_B) d\tau \\ &= \frac{(c_1)^2 \int \phi_A \mathcal{H} \phi_A d\tau + (c_2)^2 \int \phi_B \mathcal{H} \phi_B d\tau + 2c_1c_2 \int \phi_A \mathcal{H} \phi_B d\tau}{(c_1)^2 + (c_2)^2 + 2c_1c_2S} \end{aligned} \quad (3.28)$$

Let $H_{AA} = \int \phi_A \mathcal{H} \phi_A d\tau$, $H_{BB} = \int \phi_B \mathcal{H} \phi_B d\tau$ and $H_{AB} = H_{BA} = \int \phi_A \mathcal{H} \phi_B d\tau$. For a given atomic wave function and a given constant (i.e., constants H_{AA} , H_{BB} and H_{AB}) which will *minimize* the orbital energy E , the calculation of values for c_1 and c_2 is shown in Ballhausen and Gray^[6].

For $S < 1$ (knowing that $S = 1$ if nucleus 1 and nucleus 2 are together and $S = 0$ if they are infinitely separated), the calculation ends up to the two solutions below:

1. The case in which $H_{AA} = H_{BB}$:
 - an energy, *smaller* than $H_{AA} = H_{BB}$, called the ***bonding solution***; and
 - an energy, *larger* than $H_{AA} = H_{BB}$, called the energy of the ***antibonding solution***; and

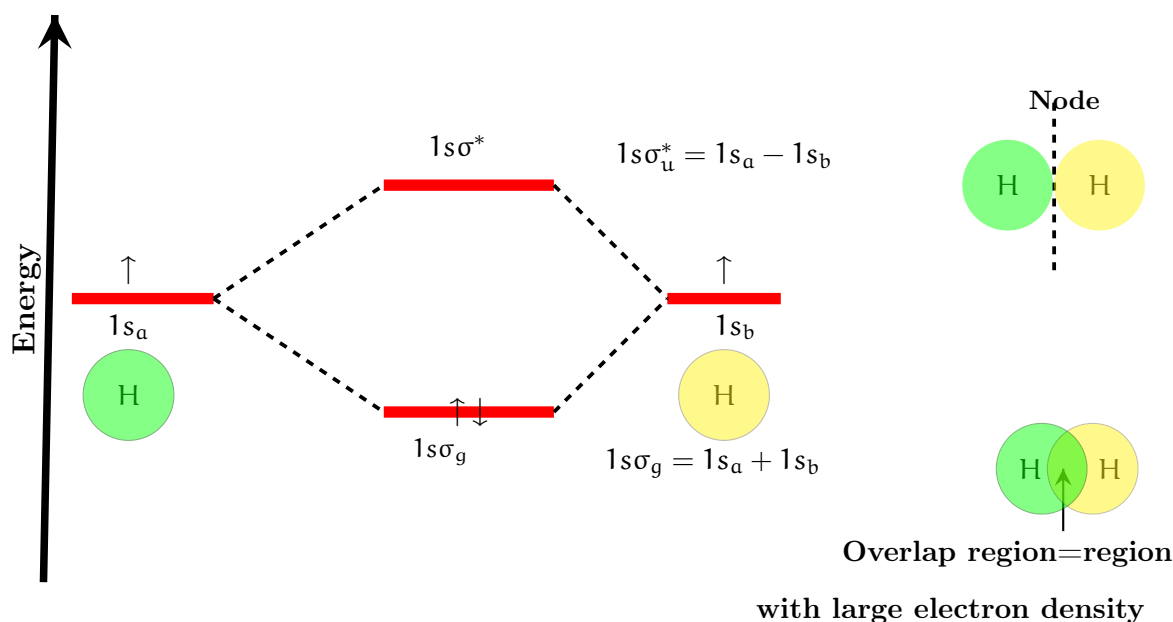


Figure 3.1 – Bonding and antibonding orbitals in the molecule formed by atom **A** and **B**.

The values for c_1 and c_2 are therefore

$$c_1 = -c_2 \left(\frac{H_{AB} - ES}{H_{AA} - E} \right) \quad \text{or} \quad c_1 = \left(\frac{H_{AA} - E}{H_{AB} - ES} \right) \quad (3.29)$$

with

$$(H_{AB} - ES)^2 = (H_{AA} - E)^2 \quad \text{or} \quad (H_{AB} - ES) = \pm(H_{AA} - E) \quad (3.30)$$

so that $c_2 = -c_1$ and $c_2 = c_1$; the two normalized wave functions are then

$$\frac{1}{\sqrt{2+2S}} (\phi_A + \phi_B) \quad (\text{low energy}) \quad \text{and} \quad \frac{1}{\sqrt{2-2S}} (\phi_A - \phi_B) \quad (\text{high energy}). \quad (3.31)$$

These coefficients for c_1 and c_2 are found in the condition $H_{AA} = H_{BB}$, i.e., the *symmetry condition*.

2. The general case, i.e., $H_{AA} \neq H_{BB}$ the resolution leads to:

$$E \approx \begin{cases} H_{AA} - \frac{H_{AB}^2}{H_{BB} - H_{AA}} \\ H_{BB} + \frac{H_{AB}^2}{H_{BB} - H_{AA}} \end{cases} \quad (3.32)$$

meaning that one solution gives an orbital a bit more stable than ψ_A and the other provides an orbital a little stable than ψ_B (see Figure 3.2).

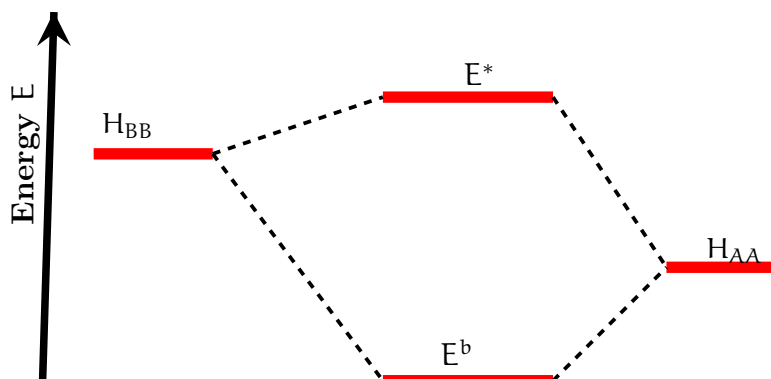


Figure 3.2 – Bonding and antibonding energy levels for $H_{BB} \gg H_{AA}$.

In the general case, the construction of orbitals in polyatomic molecule is based on *linear combination of atomic orbital* (LCAOs) method:

$$\psi_n = \sum_i c_{ni} \psi_i = c_{n1} \phi_1 + c_{n2} \psi_2 + c_{n3} \psi_3 + \dots \quad (3.33)$$

where ϕ s are the valence AOs of the atoms making up the molecules and c_{ni} the weighting coefficients that showing the number of each AO are in the MO.

Electrons in polyatomic systems (specially *s* and *p* electrons) may occupy *bonding*, *antibonding* or nonbonding molecular orbitals (MOs)^[7]. According to MO notation, bonding electrons are grouped into σ or π electrons if their wave functions or charge densities are rotationally symmetric with respect to or contain a nodal plane through the valence axis. *sigma* σ bonds are then formed by *s* – *s* overlaps and *2p* – *2p* (head to head), whereas, *pi* π bonds are formed by *2p* orbitals overlapping side-side. Electrons in antibonding orbitals are labelled with asterisks (σ^* or π^*). Similarly, unshared or nonbonding electrons (*orbitals on an atom that can't combine with any on the other*) are called **non-bonding** (*n*) electrons. The increasing electronic energy is in the order: $\sigma < \pi < n < \sigma^* < \pi^* < \text{Rydberg (R) states}$ ^[7].

Due to symmetry exclusion, the transitions between σ and π orbitals are excluded. The often observed transitions are therefore: $\sigma \rightarrow \sigma^*$, $\pi \rightarrow \pi^*$, $n \rightarrow \pi^*$ and $n \rightarrow \sigma^*$. However, the transitions $n \rightarrow \pi^*$ are also symmetry-forbidden, so their bands are very weak.

In general, the conditions for AOs to *interact* and *form* MOs are such that AOs that combine together to form MOs must have: (i) *the same symmetry*, (ii) *similar energy* and (iii) *spatial overlap*. Moreover, the electrons, in filling orbitals, *enter first the lowest orbital available*. In addition, the number of total atomic orbitals corresponds to the number of Molecular orbitals. This is the conservation of orbital bonding. MO follows also Hund's rule (electrons *spread out over orbitals of equal energy* before pairing up) and Pauli's exclusion principle (the *maximum number of electrons in an orbital is 2 of opposite spin*).

It is known that the energy change due to the transition between two states of energies E_n and E_{n+1} is given by:

$$\Delta E = E'' - E' = h\nu = hc/\lambda = hc\tilde{\nu} \quad (3.34)$$

where ν is the frequency of the electromagnetic radiation, c is the speed of light in the vacuum, λ is the wavelength of the radiation, E'' and E' are, respectively, the energies of the upper and lower states. Electrons can then be promoted from the ground state S_0 (it is usually a singlet (S)) to higher excited electronic states $\Sigma, \Pi, \Delta, \dots$

3.3 Variational principle

For a given molecule, the equation (3.6), with the hamiltonian given by the relation (3.13), has many acceptable eigenfunctions Ψ , each with a different associated eigenvalue E : $\{\Psi_i\}$ and $\{E_i\}$. These wave functions satisfy the normalization condition, i.e., they are orthonormal:

$$\iiint \Psi_j \Psi_i dx dy dz = \int \Psi_j \Psi_i d\mathbf{r} = \delta_{ij} \quad (3.35)$$

where $\delta_{ij} = 0$ if $i \neq j$ and $\delta_{ij} = 1$ if $i = j$. We then have

$$\int \Psi_i \mathbf{H} \Psi_j d\mathbf{r} = \int \Psi_j E_i \Psi_i d\mathbf{r} = E_i \delta_{ij} \quad (3.36)$$

Considering an arbitrary function Φ which is an eigenfunction in equation (3.6) and which is a linear combination of the Ψ_i , it can be written:

$$\Phi = \sum_i c_i \Psi_i \quad (3.37)$$

where, individual Ψ_i and c_i are unknown. Due to the normalization condition, we have:

$$\int \Phi^2 d\mathbf{r} = 1 = \int \sum_i c_i \Psi_i \sum_j c_j \Psi_j d\mathbf{r} = \sum_{ij} c_i c_j \int \Psi_i \Psi_j d\mathbf{r} = \sum_{ij} c_i c_j \delta_{ij} = \sum_i c_i^2 \quad (3.38)$$

Evaluating the energy associated with the wave function Φ , we have:

$$\begin{aligned} \int \Phi \mathcal{H} \Phi d\mathbf{r} &= \int \left(\sum_i c_i \Psi_i \right) \mathcal{H} \left(\sum_j c_j \Psi_j \right) d\mathbf{r} = \sum_{ij} c_i c_j \int \Psi_i \mathcal{H} \Psi_j d\mathbf{r} = \sum_{ij} c_i c_j E_j \delta_{ij} \\ &= \sum_i c_i^2 E_i \end{aligned} \quad (3.39)$$

Unfortunately, we still don't know the value of *any* of the quantities Φ , Ψ_i , c_i and, additionally, that of E_i . However, it is known that there must be a lowest energy value. Let us call that energy "*energy of the ground state*", E_0 . Combining then equations (3.38) and (3.39), we can write:

$$\int \Phi \mathcal{H} \Phi d\mathbf{r} - E_0 \int \Phi^2 d\mathbf{r} = \sum_i c_i^2 (E_i - E_0) \quad (3.40)$$

Assuming the coefficients to be real, $c_i^2 \geq 0$. By definition of E_0 , we have also $(E_i - E_0) \geq 0$. We have thus:

$$\int \Phi \mathcal{H} \Phi d\mathbf{r} - E_0 \int \Phi^2 d\mathbf{r} \geq 0 \quad (3.41)$$

which may be rearranged to give:

$$\frac{\int \Phi \mathcal{H} \Phi d\mathbf{r}}{\int \Phi^2 d\mathbf{r}} \geq E_0 \quad (3.42)$$

Knowing that the wave functions Φ are *normalized*, the denominator is given by $\int \Phi^2 d\mathbf{r} = 1$, so that:

$$\int \Phi \mathcal{H} \Phi d\mathbf{r} \geq E_0 \quad (3.43)$$

From the equation (3.43), it can be deduced that *looking for the best wave function to define the ground state of a system, find the optimal of such wave function by minimizing the expectation energy with the true Hamiltonian with respect to any free parameters. Lower expectation energies always indicate better solutions.* In other words, any approximate wave function is associated with an energy, which lies above or equals the exact energy, the equality holding only for the exact wave function.

3.4 ab initio methods

3.4.1 Hartree-Fock approximation

Hartree-Fock theory was developed to solve the electronic Schrödinger equation that results from the time-independent Schrödinger equation after Born-Oppenheimer approximation. Rewriting the equation (3.17) combined with (3.18), we get:

$$\left[\widehat{T}_e(\mathbf{r}) + \widehat{V}_{eN}(\mathbf{r}) + \widehat{V}_{ee}(\mathbf{r}) + \widehat{V}_{NN} \right] \Phi(\mathbf{r}, \mathbf{R}) = E_{el} \Phi(\mathbf{r}, \mathbf{R}) \quad (3.44)$$

where E_{el} are the energy eigenvalues and $\Phi(\mathbf{r}, \mathbf{R})$ the corresponding eigenstates, or wave functions, or orbitals, which must be *antisymmetric with respect to exchange of electronic coordinates in \mathbf{r}* and *symmetric or antisymmetric with respect to exchange of nuclear variables in \mathbf{R}* . In equation (3.44), \mathbf{r} et \mathbf{R} are electronic and nuclear coordinates, respectively, in the center-of-mass of the molecule, i.e., they are the same as the \mathbf{x} and \mathbf{X} coordinates in the section 3.1.

In the expression (3.44), $E_{el}(\mathbf{R})$ gives the *potential energy surface (PES)* from which some molecular properties, such as the equilibrium geometry and vibrational frequencies, etc, could be gotten^[8]. In fact, the solution of $\nabla E_{el}(\mathbf{R}) = 0$, i.e, the stationary problem, gives the *optimized geometry*^[9]. The electronic wave function $\Phi(\mathbf{r}, \mathbf{R}) = \Phi(\mathbf{r}, \mathbf{R}_{op})$ ($\mathbf{R} = \mathbf{R}_{op}$ being a constant for the optimized geometry or a parameter but not a variable) contains many useful information about molecular properties such as dipole (and multipole) moments, polarizability, etc^[8]. The electron-electron interaction term, i.e., $\widehat{V}_{ee}(\mathbf{r}, \mathbf{R}_{op})$, is a pair interaction and acts on pairs of electrons.

In the following, we will use, instead spatial coordinates \mathbf{r} , space-spin coordinates (\mathbf{x}_i) , i.e., beside the three spatial degrees of freedom, there is also an intrinsic spin coordinate, which we will call α or β . Spin coordinate (either α or β) is replaced by a generic spin coordinate ω , and the set of space-spin coordinates $\mathbf{x} = \{\mathbf{r}, \omega\}$ including space and spin coordinates. The notation for orbitals is changed from $\Phi(\mathbf{r}, \mathbf{R}_{op})$, a *spatial orbital*, to $\chi(\mathbf{x})$, a *spin orbital* such that $\chi(\mathbf{x}) = \varphi(\mathbf{r})\alpha(\omega)$ (i.e., the product of a spatial orbital and an electron spin eigenfunction). The wave function Φ becomes then:

$$\Phi(\mathbf{x}_1, \mathbf{x}_2, \dots, \mathbf{x}_N) = \prod_{i=1}^N \chi(\mathbf{x}_i) = \chi(\mathbf{x}_1)\chi(\mathbf{x}_2)\dots\chi(\mathbf{x}_N) \quad (3.45)$$

However, the approximation (3.45) has one major shortcoming: it fails to satisfy the *antisymmetry principle*, which states that a wave function describing fermions should be antisymmetric with respect to the interchange of any set of space-spin coordinates. The HF approximation allows to resolve this issue by using an *antisymmetrized many-electron wave function* in the form of Slater determinant:

$$\Phi_{HF}(\mathbf{x}_1, \mathbf{x}_2, \dots, \mathbf{x}_N) = \frac{1}{\sqrt{N!}} \begin{pmatrix} \chi_1(\mathbf{x}_1) & \chi_2(\mathbf{x}_1) & \dots & \chi_N(\mathbf{x}_1) \\ \chi_1(\mathbf{x}_2) & \chi_2(\mathbf{x}_2) & \dots & \chi_N(\mathbf{x}_2) \\ \vdots & \vdots & \ddots & \vdots \\ \chi_1(\mathbf{x}_N) & \chi_2(\mathbf{x}_N) & \dots & \chi_N(\mathbf{x}_N) \end{pmatrix} \quad (3.46)$$

The expression (3.46) ensures that the wave function changes sign when exchanging the coordinates of two of the electrons. The factor $1/\sqrt{N!}$ ensures the normalization. The wave function of the form (3.46) introduces a particle exchange and is called Hartree-Fock (HF) or *self-consistent field* (SCF). Hartree-Fock one-electron orbitals are not only normalized, but also mutually orthogonal: $\langle \chi_i | \chi_j \rangle = \delta_{ij}$, $i, j = 1, 2, \dots, N$. In a two-electron system, the expression (3.46) is rewritten as:

$$\Phi_{\text{HF}}(\mathbf{x}_1, \mathbf{x}_2) = \frac{1}{\sqrt{2}} \begin{pmatrix} \chi_1(\mathbf{x}_1) & \chi_2(\mathbf{x}_1) \\ \chi_1(\mathbf{x}_2) & \chi_2(\mathbf{x}_2) \end{pmatrix} \quad (3.47)$$

From this expression, if one tries to put two electrons in the same orbital at the same time, i.e., if $\chi_1 = \chi_2$, $\Phi_{\text{HF}}(\mathbf{x}_1, \mathbf{x}_2) = 0$. This condition corresponds to the *the exclusion principle of Pauli*, which is a consequence of the antisymmetry principle. The equation (3.47) could be written in the form:

$$\begin{aligned} \Phi_{\text{HF}} &= \frac{1}{\sqrt{2}} \begin{pmatrix} \varphi_a(1)\alpha(1) & \varphi_b(1)\alpha(1) \\ \varphi_a(2)\alpha(2) & \varphi_b(2)\alpha(2) \end{pmatrix} \\ &= \frac{1}{\sqrt{2}} [\varphi_a(1)\alpha(1)\varphi_b(2)\alpha(2) - \varphi_a(2)\alpha(2)\varphi_b(1)\alpha(1)] \end{aligned} \quad (3.48)$$

The discussion of one-electron and two-electron contributions to the energy found when the expression (3.47) is introduced in the expression for energy is made in book of Kohanoff^[9].

The *Hartree-Fock* energy is then written as:

$$E_{\text{HF}} = \sum_{i=1}^N E_{ii} + \frac{1}{2} \sum_{i=1}^N \sum_{j=1}^N (J_{ij} - K_{ij}) + V_{\text{nn}}, \quad (3.49)$$

where E_{ii} is the one-electron contribution to the energy in *Hartree self-consistent field* (HSCF) approximation given by: $E^{(1)} = \sum_{i=1}^N \int \chi_i^*(1) \hat{h}_1(1) \chi_i(1) d\mathbf{x}_1 = \sum_{i=1}^N E_{ii}$; J_{ij} and K_{ij} are respectively, the *Coulomb* integrals of the Hartree method given by $J_{ij} = E_{ijij}^{(2)} = \int \int \chi_i^*(i) \chi_j^*(j) \hat{v}_2(i, j) \chi_i(i) \chi_j(j) d\mathbf{x}_i d\mathbf{x}_j$ and the terms of the second class, called *exchange* integrals, and written as $K_{ij} = E_{ijji}^{(2)} = \int \int \chi_i^*(i) \chi_j^*(j) \hat{v}_2(k, l) \chi_i(j) \chi_j(i) d\mathbf{x}_i d\mathbf{x}_j$

The expression (3.49), in terms of the eigenvalues of the Fock operator

$$\varepsilon_i = E_{ii} + \sum_{j=1}^N (J_{ij} - K_{ij}), \quad (3.50)$$

becomes:

$$E_{\text{HF}} = \sum_{i=1}^N \varepsilon_i - \frac{1}{2} \sum_{i=1}^N \sum_{j=1}^N (J_{ij} - K_{ij}) + V_{\text{nn}}, \quad (3.51)$$

For *closed shell* systems, i.e., with even number of electrons and therefore with equal numbers for each projection, the two spin orbitals with the same orbital part and different spin part contribute with the same energy. The coulomb contribution to the energy is $2 \sum_{i=1}^{N/2} \sum_{j=1}^{N/2} J_{ij}$. The factor two arises due to that there are four equal contributions in the double sum: $(i \uparrow, j \uparrow)$, $(i \uparrow, j \downarrow)$, $(i \downarrow, j \uparrow)$, $(i \downarrow, j \downarrow)$. This argument holds also for the exchange term, but for this case, integrals with the same projection are excluded and then only two terms are surviving: $(i \uparrow, j \downarrow)$ and $(i \downarrow, j \uparrow)$. Consequently, for closed shell systems,

the Hartree-Fock energy can be written as:

$$\begin{aligned}
E_{\text{HF}}^{\text{cs}} &= 2 \sum_{i=1}^{N/2} E_{ii} + \frac{1}{2} \sum_{i=1}^N \sum_{j=1}^N (2J_{ij} - K_{ij}) + V_{\text{nn}} \\
&= 2 \sum_{i=1}^{N/2} \varepsilon_i - \frac{1}{2} \sum_{i=1}^N \sum_{j=1}^N (2J_{ij} - K_{ij}) + V_{\text{nn}} \\
&= \sum_{i=1}^{N/2} (\varepsilon_i + E_{ii}) + V_{\text{nn}}, \tag{3.52}
\end{aligned}$$

Unlike Hartree approach, the Hartree-Fock approximation takes into account the non-locality. The HF approximation limitation is that many-body wave function (see Ref.^[9]) is not often well-represented by a single Slater determinant. The main missing component is the *electronic correlation*, i.e., the HF takes into account the average effect of electron repulsion, but not the explicit electron-electron interaction^[10]. The electron-correlation problem, i.e., the manner the dynamics of each electron is affected by the others, has been found to be the single largest source of error in quantum chemical computations^[11]. Due to the central field approximation, the energies from HF calculations are always greater than the exact energy and tend to a limiting value called the *Hartree-Fock limit* when the basis set is improved^[10].

3.4.2 Post-Hartree-Fock methods

The important limitation of Hartree-Fock methods is the absence of the electron correlation due to the fact that the interactions between electrons are treated in an average way (see the section (3.4.1)). It has been reported that the HF wave function accounts for $\approx 99\%$ of the total energy E_{tot} , so that the difference $E_{\text{tot}} - E_{\text{HF}}$ is called the *correlation energy*. The *Post-Hartree-Fock methods* were developed in the aim at improving the used many-electron wave function. In these methods, the electron correlation (e.i., how the dynamics of each electron is affected by the others) is corrected in different ways depending on the methods used. There are then methods^[9]:

- i) that use the combinations of several Slater determinants as static (and dynamic) correlations,
- ii) that introduce correlation perturbatively above the HF solution, and
- iii) that are based on correlated wave functions.

The *static correlation* arises from the near degeneracies in valence or active orbitals and is associated with the multireference nature of the system, whilst the *dynamical correlation* arises from non-valence or external orbitals^[12]. In other words, while the static correlation corresponds to configurations which are nearly degenerate with respect to the reference Slater determinant, the dynamical correlation arises from the mixing of Hartree-Fock state with higher-order excited states^[11]. The static correlation corresponds then to correction of deficiencies arising from the use of the *single-reference approximation*, i.e., the use of a single Slater determinant in representing the state of a system. Recalling that the Hartree-Fock approximation relies on single-reference approximation in addition to the two assumptions in Born-Oppenheimer approximation.

The HF wave function is the best single-determinant that can be constructed. Any approach aiming at introducing correlation is likely to take as starting point the HF wave function. The best strategy is to introduce a small number of determinants that produce a large impact at the energy level.

Considering then a multi-determinant wave function for an N-electrons system, it is possible to construct *a linear combination of a finite number ND of Slater determinants*:

$$\Phi(\mathbf{x}_1, \dots, \mathbf{x}_N) = C_0 \Phi_0(\mathbf{x}_1, \dots, \mathbf{x}_N) + \sum_{i=1}^{\text{ND}} C_i \Phi_i(\mathbf{x}_1, \dots, \mathbf{x}_N), \quad (3.53)$$

where $\Phi_0 = \Phi_{\text{HF}}$ is the HF solution for the electronic ground state. Φ_0 corresponds then to the N electrons occupying the energetically lowest N spin orbitals $\{\varphi_i(\mathbf{r}), i = 1, \dots, N\}$, i.e., the N/2 lowest spacial orbitals, each one occupied by a *spin up* and a *spin down* electron for closed shell systems. Φ_i are other determinants corresponding to excited states. In this correction, the larger ND is, the better is correlation introduced. In other words, Φ_i correspond to the determinants in which *one (or 2 or 3,...)* electron has (have) been promoted from *any of the occupied states* to *any of the unoccupied states*. If *one* electron is promoted, the determinant is said **single excitation** or simply **single** and denoted by S. Likewise, determinants in which two electrons have been promoted from occupied to empty one-electron orbitals are called **double (D)**, if three electrons are promoted, the determinant is called a **triple (T)** and when four are promoted, it is called **quadruple (Q)**, etc.

3.4.2.1 Configuration interaction (CI)

This method consists in introducing in the expansion (3.53) the Slater determinants constructed with the occupied and unoccupied one-electron orbitals of the HF Hamiltonian. The expansion coefficients C_i are optimized to minimize the total energy. The CI wave function in terms of singles, doubles, triples, etc, is:

$$\Phi_{\text{CI}} = C_0 \Phi_{\text{HF}} + \sum_{i=1} C_i^{\text{S}} \Phi_i^{\text{S}} + \sum_{i=1} C_i^{\text{D}} \Phi_i^{\text{D}} + \sum_{i=1} C_i^{\text{T}} \Phi_i^{\text{T}} + \dots \quad (3.54)$$

The problem consists then in finding the set of coefficients C_i that makes the energy:

$$E_{\text{CI}} = \int \dots \int \Phi_{\text{CI}}^*(\mathbf{x}_1, \dots, \mathbf{x}_N) \hat{\mathcal{H}} \Phi_{\text{CI}}(\mathbf{x}_1, \dots, \mathbf{x}_N) d\mathbf{x}_1 \dots d\mathbf{x}_N \quad (3.55)$$

minimal. Φ_{CI} are *normalized*: $\sum_{i=1} C_i^2 = 1$. The coefficients C_i are determined by a variational optimization of the expectation value of the electronic energy^[13]:

$$E_{\text{CI}} = \min_{\mathbf{c}} \frac{\langle \mathbf{C} | \hat{\mathcal{H}} | \mathbf{C} \rangle}{\langle \mathbf{C} | \mathbf{C} \rangle} \iff \mathbf{H}\mathbf{C} = E_{\text{CI}}\mathbf{C} \quad (3.56)$$

where \mathbf{H} is the Hamiltonian matrix with elements given by $H_{ij} = \langle i | \hat{\mathcal{H}} | j \rangle$ and \mathbf{C} is the matrix containing the expansion coefficients C_i . The method in which all available determinants are included in the calculation is said **full CI**^[9]. Due to the expensive cost (in computing time) of this last, most common CI methods correspond to those in which expansion is truncated at some levels of excitations. There are then *CISD method* for which the truncation in expansion is done at level of doubles, *CISDT* which includes triples, the highest practically used being that includes quadruples (CISDTQ). This latter is quite close to full CI and is very expensive.

3.4.2.2 Multi-configurational methods: MCSCF and MRCI

To overcome the limitation of constructing the determinants in the CI expansion with fixed HF one-electron eigenstates, the determinants are allowed to be variationally optimized together with the expansion coefficients. The method used is called *Multi-configuration self-consistent field (MCSCF)*. No advantage over standard CI, except in the case of wave functions that require singly instead of doubly occupied spin orbitals for which the HF solution is qualitatively incorrect.

The number of configurations to include in optimization procedure is easy, but the big problem is how to choose these configurations. A robust approach is the *complete active space self-configuration field (CASSCF)* in which the selection of configurations is done by dividing the one-electron orbitals into *active* and *inactive* spaces. Orbitals in active space, i.e., a fraction of highest-lying occupied states such those occupied by the valence electrons, are used to construct all possible configurations by allowing excitations to a few low-lying unoccupied orbitals. The determinants corresponding to these configurations are then together with the expansion coefficients variationally optimized.

A multi-configuration wave function with optimized orbitals and occupancies, i.e., a wave function in which the electronic excitations of all the determinants have to be included, can be used as a reference for a CI calculation. These methods are called *multi-reference configuration interaction (MRCI)*. In these methods, the cost of the calculation is increased by a factor equal to the number of configurations.

3.4.2.3 Perturbative methods

According to the *perturbation theory*, the full Hamiltonian of a system is expressed as the sum of a reference Hamiltonian ($\hat{\mathcal{H}}_0$), i.e., the unperturbed electronic Hamiltonian and a series of (time-independent) perturbations, e.g. $\hat{\mathcal{P}}_1, \hat{\mathcal{P}}_2$, for linear and quadratic operators:

$$\hat{\mathcal{H}} = \hat{\mathcal{H}}_0 + \lambda \hat{\mathcal{P}}_1 + \lambda^2 \hat{\mathcal{P}}_2, \quad (3.57)$$

where λ determines the strength. The exact solution of the Schrödinger equation is

$$\hat{\mathcal{H}}_0 \Phi_i^{(0)} = E_i^{(0)} \Phi_i^{(0)}, \quad i = 0, 1, 2, \dots, \infty \quad (3.58)$$

where $\Phi_i^{(0)}$ are the unperturbed eigenstates and E_i^0 the corresponding energies. The full Schrödinger equation is given by:

$$\hat{\mathcal{H}} \Phi_i = E_i \Phi_i, \quad i = 0, 1, 2, \dots, \infty \quad (3.59)$$

where the eigenstates and eigenvalues, expanded in powers of λ are, respectively, given by:

$$\Phi_i = \Phi_i^{(0)} + \lambda \Phi_i^{(1)} + \lambda^2 \Phi_i^{(2)} + \dots \quad \text{and} \quad E_i = E_i^{(0)} + \lambda E_i^{(1)} + \lambda^2 E_i^{(2)} + \dots \quad (3.60)$$

with the first order correction to the energy, i.e., the expectation value of the perturbation in the unperturbed eigenstates is:

$$E_i^{(1)} = \langle \Phi_i^{(0)} | \hat{\mathcal{P}}_1 | \Phi_i^{(0)} \rangle, \quad (3.61)$$

and the first order correction to the eigenfunctions is obtained as:

$$\Phi_i^{(1)} = \sum_{j \neq i} \frac{\langle \Phi_j^{(0)} | \hat{\mathcal{P}}_1 | \Phi_i^{(0)} \rangle}{E_i^{(0)} - E_j^{(0)}}. \quad (3.62)$$

The second order correction to the energy is

$$E_i^{(2)} = \langle \Phi_0^{(0)} | \hat{\mathcal{P}}_2 | \Phi_0^{(0)} \rangle + \sum_{j \neq 0} \frac{\langle \Phi_0^{(0)} | \hat{\mathcal{P}}_1 | \Phi_j^{(0)} \rangle \langle \Phi_j^{(0)} | \hat{\mathcal{P}}_1 | \Phi_0^{(0)} \rangle}{E_0^{(0)} - E_j^{(0)}}. \quad (3.63)$$

Among these methods, there is:

- The **Møller-Plesset theory** for which the (linear term of) perturbation to the unperturbed electronic Hamiltonian is:

$$\hat{\mathcal{P}}_1 = \frac{1}{2} \sum_{i \neq j} \hat{v}_2(i, j) - \sum_{ij} \left(\hat{g}_{ij} - \hat{\mathcal{K}}_{ij} \right). \quad (3.64)$$

This theory is called the *Møller-Plesset* (MP) perturbation theory^[14]. The first order energy is given by:

$$E_{\text{MP1}} = E_{\text{MP}}^{(0)} + E_{\text{MP1}}^{(1)} = \underbrace{\sum_{i=1}^N \varepsilon_i}_{\text{Unperturbed energies}} + \underbrace{\frac{1}{2} V_{ee} - V_{ee}}_{\text{Perturbation}} = \sum_{i=1}^N \varepsilon_i - \frac{1}{2} V_{ee} = E_{\text{HF}} \quad (3.65)$$

with $V_{ee} = \langle \Phi_k^0 | \sum_{i \neq j} \hat{v}_2(i, j) | \Phi_k^0 \rangle \equiv$ electronic energy, i.e., expectation value for the two body Coulomb operator in $\Phi_k^{(0)}$. The first correction correspond to the second order (MP2) and the first energy correction is:

$$E_{\text{MP}}^{(2)} = \sum_{\mu < \nu = N_{\text{occ}} + 1}^{\text{ND}} \sum_{i < j = 1}^{N_{\text{occ}}} \frac{\left| \langle \Phi_k^{(0)} | \hat{\mathcal{P}}_1 | \Phi_k^{i-j\mu\nu} \rangle \right|^2}{E_k^{(0)} - E_2^{ij\mu\nu}}, \quad (3.66)$$

where electrons in the unperturbed many-body state k occupying the orbital i and j are promoted to the empty orbitals μ and ν . The sum

$$E_{\text{MP2}} = \underbrace{E_{\text{MP}}^{(0)} + E_{\text{MP}}^{(1)}}_{E_{\text{MP}}} + E_{\text{MP}}^{(2)} \quad (3.67)$$

is known as *MP2 energy*. The MP2 approximation consists then of stopping the perturbative expansion for the energy to the level 2 while the correction for the wave function is stopping at first order.

There are also high orders in perturbation expansion such as MP3 whose energy is found using the first order corrected wave functions, MP4, etc.

- The **Coupled clusters (CC)** is another method of correcting the problem of electron correlation introduced in HF approximation by using the infinite-order perturbation theory^[15]. This method consists of including an infinite number of terms of a certain class and discarding all other terms of other type in the quantum many-body perturbation expansion^[16–18]. To do so, it uses a non-linear parametrization of the wave function, i.e., an exponential ansatz of cluster operators for the many-electron wave function^[15], given by as:

$$\Phi_{\text{CC}} = e^{\hat{\mathcal{T}}} \Phi_0 = \left(1 + \hat{\mathcal{T}} + \frac{\hat{\mathcal{T}}^2}{2!} + \frac{\hat{\mathcal{T}}^3}{3!} + \dots \right) \Phi_0 \quad (3.68)$$

where $\Phi_0 = \Phi_{\text{HF}}$ is a single Slater determinant constructed from the HF one-electron orbitals that best approximates the ground state energy of a many-electron system. $\hat{T} = \hat{T}_1 + \hat{T}_2 + \dots + \hat{T}_N$ is an operator acting on HF wave function to generate all the excited Slater determinants up to a certain order. The first term is:

$$\hat{T}_1 \Phi_k^{(0)} = \sum_{\mu=\text{N}_{\text{occ}}+1}^{\text{ND}} \sum_{i=1}^{\text{N}_{\text{occ}}} t_i^\mu \Phi_k^{i\mu}, \quad (3.69)$$

whereas the second term:

$$\hat{T}_2 \Phi_k^{(0)} = \sum_{\mu < \nu = \text{N}_{\text{occ}}+1}^{\text{ND}} \sum_{i < j = 1}^{\text{N}_{\text{occ}}} t_{ij}^{\mu\nu} \Phi_k^{ij\mu\nu}, \quad (3.70)$$

includes double excitations, etc. If $\hat{T} = \hat{T}_2$, the coupled cluster wave function is limited to connected *double excitations* (CCD), if $\hat{T} = \hat{T}_1 + \hat{T}_2$, it is referred to coupled cluster singles and doubles (CCSD) approximation, if $\hat{T} = \hat{T}_1 + \hat{T}_2 + \hat{T}_3$, is referred to singles, doubles and triples (CCSDT) approximation and if $\hat{T} = \hat{T}_1 + \hat{T}_2 + \hat{T}_3 + \hat{T}_4$ termed as singles, doubles, triples and quadruples (CCSDTQ) approximation. However, the inclusion of the inclusion of higher-than-doubly excited clusters, such as the triexcited and quadruply excited \hat{T}_3 and \hat{T}_4 components, is very expensive^[19]. This problem has been circumvented, for instance, by the use of perturbative approximations for the wave function^[19], which results in combining the coupled cluster singles and doubles and a perturbative triple to yield CCSD(T) method or the combination of the coupled cluster singles, doubles and triples and a perturbative quadruple to give the CCSDT(Q) methods.

3.4.3 Density functional theory (DFT)

Unlike the HF and post-HF, which are wave function based methods, the central quantity in DFT is the electron density. Regardless the number of electrons in a system, the density is always 3 dimensional. Thus, an important advantage of electron density over the wave function is the reduced dimensionality, allowing to be applied to much larger systems. The electron density is defined as the integral over the spin coordinates of all electrons and over all but one of the spatial variables ($\mathbf{x} \equiv \mathbf{r}, \mathbf{s}$)^[20]:

$$\rho(\mathbf{r}) = N \int \dots \int |\Phi(\mathbf{x}_1, \mathbf{x}_2, \dots, \mathbf{x}_N)|^2 d\mathbf{s}_1 d\mathbf{x}_1 d\mathbf{x}_2 \dots d\mathbf{x}_N \quad (3.71)$$

where $\rho(\mathbf{r})$ determines the probability of finding any of the N electrons within a volume element \mathbf{x} . It is an observable, which can be measured experimentally, and is such that:

$$\rho(\mathbf{r} \rightarrow \infty) = 0 \quad (3.72a)$$

$$\int \rho(\mathbf{r}) d\mathbf{r} = N \quad (3.72b)$$

Thus, in DFT method, the molecular energy is then determined from the electron density $\rho(\mathbf{x}, \mathbf{y}, \mathbf{z})$ rather from a wave function, which is the central quantity in HF and post-HF methods^[21]. Likewise, in DFT, the interest quantity is a functional whereas it is a function in HF and post-HF methods. A *functional* maps a function into a number. The area under a curve is functional of the function that defines the curve between two points. In other words, whereas a function takes a value of a variable or variables and defines a single

number from those variables, a functional takes a function and defines a single number from the function^[22]. The DFT is based on two fundamental mathematical theorems (see section 3.4.3.1) demonstrated by Kohn & Hohenberg^[23] and the set of equations by Kohn & Sham (section 3.4.3.2).

3.4.3.1 The Hohenberg-Kohn theorem

Theorem 1: *The external potential $v_{\text{ext}}(\mathbf{r})$ ¹ is (to within a constant) a unique functional of $\rho(\mathbf{r})$, since, in turn $v_{\text{ext}}(\mathbf{r})$ fixes $\hat{\mathcal{H}}$, the full many particle ground state is a unique functional of $\rho(\mathbf{r})$ ^[24].*

The proof for this theorem can be found in the work by Hohenberg and Kohn^[23]. Given then a **ground-state wave function** Φ for a given potential $v_{\text{ext}}(\mathbf{r})$ is a functional of ρ , i.e., $\Phi[\rho]$, Hohenberg and Kohn defined the **universal functional density**:

$$F[\rho] = \langle \Phi[\rho] | \hat{T} + \hat{U}_{ee} | \Phi[\rho] \rangle \quad (3.73)$$

and the **total electronic energy functional**:

$$E[\rho] = F[\rho] + \int v_{\text{ext}}(\mathbf{r})\rho(\mathbf{r})\mathbf{d}\mathbf{r} \quad (3.74)$$

so that the ground state energy (E_0), can be calculated from the variational principle^[21]:

$$\rho_0(x, y, z) \longrightarrow E_0 \implies E_0 = F[\rho_0] = E[\rho_0] \quad (3.75)$$

where^[20]:

$$F[\rho] = \underbrace{\min}_{\Phi \rightarrow \rho} \langle \Phi | \hat{T} + \hat{V}_{ee} | \Phi \rangle, \quad (3.76)$$

or, in other words, the ground state electronic energy is^[25]:

$$\begin{aligned} E_0 &= \underbrace{\min}_{\Phi} \langle \Phi | \hat{T} + \hat{U}_{ee} + \hat{V}_{ne} | \Phi \rangle \\ &= \underbrace{\min}_{\rho} \underbrace{\min}_{\Phi \rightarrow \rho} \langle \Phi | \hat{T} + \hat{U}_{ee} + \hat{V}_{ne} | \Phi \rangle \\ &= \underbrace{\min}_{\rho} \left\{ \underbrace{\min}_{\Phi \rightarrow \rho} \langle \Phi | \hat{T} + \hat{U}_{ee} | \Phi \rangle + \int \underbrace{v_{\text{ext}}(\mathbf{r})}_{=V_{ne}} \rho(\mathbf{r}) \mathbf{d}\mathbf{r} \right\} \\ &= \underbrace{\min}_{\rho} \left\{ F[\rho] + \int v_{\text{ext}}(\mathbf{r})\rho(\mathbf{r})\mathbf{d}\mathbf{r} \right\} \end{aligned} \quad (3.77)$$

with the minimum taken over all Φ that give the density ρ .

Theorem 2: *Any trial electron density function will give an energy higher than (or equal to, if it were exactly the true electron density function) the true ground state energy:*

$$E_v[\rho] \equiv \int v_{\text{ext}}(\mathbf{r})\rho(\mathbf{r})\mathbf{d}\mathbf{r} + F[\rho] \geq E_0 \quad (3.78)$$

where E_v is the variational energy which is a functional of the density. This means that $\Phi[\rho]$ is the ground state of a potential with ρ as its ground state density so that $E_0 = E_v[\rho_0]$ verifying $E_0 < E_v[\rho]$ for any $\rho \neq \rho_0$, is the ground state energy. The proof is found in Kohanoff^[9], Hohenberg and Kohn^[23].

1. By *External potential*, one wants to say the *nuclear potential*, as the nuclei are *external* if one concentrates his attention on the electrons^[21].

3.4.3.2 Kohn-Sham (KS) equations

The most and fundamental difficult in DFT is the direct approximation of the universal functional $F[\rho]$ ^[25]. In 1960s, Kohn and Sham^[26] proposed to decompose the functional $F[\rho]$ into two terms:

$$F[\rho] = T_s[\rho] + E_{\text{HXC}}[\rho]. \quad (3.79)$$

The first term in (3.79), $T_s[\rho]$, is the *non-interacting kinetic-energy functional*, whereas the second term, E_{HXC} , is called the *Hartree exchange-correlation functional*. The kinetic-energy functional for a non-interacting electrons system is defined as^[25]:

$$T_s[\rho] = \underbrace{\min}_{\Phi \rightarrow \rho} \langle \Phi | \hat{T} | \Phi \rangle = \langle \Phi[\rho] | \hat{T} | \Phi[\rho] \rangle \quad (3.80)$$

where $\Phi \rightarrow \rho$ indicates that the minimization is performed over normalized single-determinant wave functions Φ which yield the density $\rho = \rho_{\uparrow} + \rho_{\downarrow}$ ^[27]. The minimizing single-determinant wave function, denoted by $\Phi[\rho]$, is called the *KS wave function*. The Hartree exchange-correlation functional $E_{\text{HXC}}[\rho]$ can be written as

$$E_{\text{HXC}}[\rho] = E_{\text{H}}[\rho] + E_{\text{XC}}[\rho], \quad (3.81)$$

with $E_{\text{H}}[\rho]$, the Hartree functional given by:

$$E_{\text{H}}[\rho] = \frac{1}{2} \iint \frac{\rho(\mathbf{r}_1)\rho(\mathbf{r}_2)}{|\mathbf{r}_1 - \mathbf{r}_2|} d\mathbf{r}_1 d\mathbf{r}_2, \quad (3.82)$$

which represents the classical electrostatic repulsion energy for the charge distribution $\rho(\mathbf{r})$, and $E_{\text{XC}}[\rho]$, the exchange-correlation energy functional to approximate. For a system of electronic density $\rho(\mathbf{r})$, which is slowly varying, this expression can be given by^[23,26]:

$$E_{\text{HXC}}[\rho] = \int \rho(\mathbf{r}) \varepsilon_{\text{XC}}(\rho(\mathbf{r})) d\mathbf{r} \quad (3.83)$$

where $\varepsilon_{\text{XC}}(\rho)$ is the exchange and correlation per electron of a uniform electron gas of density ρ . However, in general case, this functional is decomposed into the *exchange energy functional* E_{X} and the *correlation energy functional* E_{C} :

$$E_{\text{XC}}[\rho] = E_{\text{X}}[\rho] + E_{\text{C}}[\rho] \quad (3.84)$$

where

$$E_{\text{X}}[\rho] = \langle \Phi[\rho] | \hat{U}_{ee} | \Phi[\rho] \rangle, \quad (3.85)$$

and

$$E_{\text{C}}[\rho] = \langle \Psi[\rho] | \hat{T} + \hat{U}_{ee} | \Psi[\rho] \rangle - \langle \Phi[\rho] | \hat{T} + \hat{U}_{ee} | \Phi[\rho] \rangle = T_{\text{c}}[\rho] + U_{\text{c}}[\rho]. \quad (3.86)$$

where

$$T_{\text{c}}[\rho] = \langle \Psi[\rho] | \hat{T} | \Psi[\rho] \rangle - \langle \Phi[\rho] | \hat{T} | \Phi[\rho] \rangle$$

and

$$U_{\text{c}}[\rho] = \langle \Psi[\rho] | \hat{U}_{ee} | \Psi[\rho] \rangle - \langle \Phi[\rho] | \hat{U}_{ee} | \Phi[\rho] \rangle$$

are, respectively, the kinetic and potential contributions. Recalling that Φ is single determinant wave function and Ψ a many-body wave function. The single determinant Φ is constructed from a set of N orthonormal occupied spin-orbitals $\psi_i(\mathbf{x})_{i=1,\dots,N}$ defined as

$\psi_i(\mathbf{x}) = \phi_i(\mathbf{r})\chi_{\sigma_i}(\sigma)$, where $\phi_i(\mathbf{r})$ is a spatial orbital and $\chi_{\sigma_i}(\sigma) = \delta_{\sigma_i, \sigma}$ is a spin function.

The total electronic energy, in terms of orbitals, is rewritten as:

$$E[\{\phi_i\}] = \sum_{i=1}^N \int \phi_i^*(\mathbf{r}) \left(-\frac{1}{2}\nabla^2 + v_{ne}(\mathbf{r}) \right) \phi_i(\mathbf{r}) d\mathbf{r} + E_{\text{HXC}}[\rho] \quad (3.87)$$

and the density as:

$$\rho(\mathbf{r}) = \sum_{i=1}^N |\phi_i(\mathbf{r})|^2 \quad (3.88)$$

The minimization over orbitals $\{\phi_i\}$ keeping the orbitals orthonormalized is achieved using the Lagrangian:

$$\mathcal{L}[\{\phi_i\}] = E[\{\phi_i\}] - \sum_{i=1}^N \varepsilon_i \left(\int \phi_i^*(\mathbf{r}) \phi_i(\mathbf{r}) d\mathbf{r} - 1 \right) \quad (3.89)$$

where ε_i is the Lagrange multiplier associated with the normalization of $\phi_i(\mathbf{r})$. The Lagrangian must be *stationary* with respect to the variations of the orbitals $\phi_i(\mathbf{r})$:

$$\frac{\delta \mathcal{L}}{\delta \phi_i^*(\mathbf{r})} = 0 \quad (3.90)$$

Using the chain rule for a functional $F[f]$ of a function $f(x)$ for a functional $F[f]$ of a function $f[g](x)$:

$$\delta F[f] = \frac{\delta F[f]}{\delta f} \frac{\delta f}{\delta x} dx \quad \text{and} \quad \frac{\delta F}{\delta g(x)} = \int \frac{\delta F}{\delta f(x')} \frac{\delta f(x')}{\delta g(x)} dx', \quad (3.91)$$

we find for the functional derivative of the Lagrangian:

$$0 = \frac{\delta \mathcal{L}}{\delta \phi_i^*(\mathbf{r})} = \left(-\frac{1}{2}\nabla^2 + v_{ne}(\mathbf{r}) \right) \phi_i(\mathbf{r}) + \frac{\delta E_{\text{HXC}}[\rho]}{\delta \phi_i^*(\mathbf{r})} - \varepsilon_i \phi_i(\mathbf{r}) \quad (3.92)$$

The calculation of $\frac{\delta E_{\text{HXC}}[\rho]}{\delta \phi_i^*(\mathbf{r})}$ using the chain rule results in:

$$\frac{\delta E_{\text{HXC}}[\rho]}{\delta \phi_i^*(\mathbf{r})} = \int \frac{\delta E_{\text{HXC}}[\rho]}{\delta \rho(\mathbf{r}')} \frac{\delta \rho(\mathbf{r}')}{\delta \phi_i^*(\mathbf{r})} d\mathbf{r}' = v_{\text{HXC}}(\mathbf{r}) \phi_i(\mathbf{r}) \quad (3.93)$$

where $\delta \rho(\mathbf{r}')/\delta \phi_i^*(\mathbf{r}) = \phi_i(\mathbf{r})\delta(\mathbf{r} - \mathbf{r}')$ has been used. $v_{\text{HXC}}(\mathbf{r})$ is the *Hartree-exchange-correlation potential*. One ends up then at the *KS equations*:

$$\left(-\frac{1}{2}\nabla^2 + v_{ne}(\mathbf{r}) + v_{\text{HXC}}(\mathbf{r}) \right) \phi_i(\mathbf{r}) = \varepsilon_i \phi_i(\mathbf{r}) \quad (3.94)$$

where the orbitals $\phi_i(\mathbf{r})$ are called the *KS orbitals* and ε_i are the *KS orbital energies*.

3.4.3.3 Hybrid density functional theory

Hybrid schemes combining elements of the HF method and of the KS procedure of DFT have become very popular to calculate the molecular properties^[28]. Hybrid approach was introduced by Becke^[29] with the aim of exploiting the obvious strengths of each partner. In fact, the HF–KS hybrid schemes should be used in order to improve the approximations for the pertinent correlation functionals^[28]. Local density functionals for E_C cannot repair the fundamental defects of the Hartree-Fock approximation in molecular bonds, and consequently, even though local E_C functionals model short-range features such as interelectronic

cusps, they cannot simulate multiconfiguration mixing^[29–31]. Density-functional theory employing the local-density approximation (LDA), either in an all-electron formalism^[32,33] or using the pseudopotential plane-wave approach^[34–36] has been used in the literature beside HF approximation theory^[37]. The introduction of the generalized gradient approximation (GGA) in density-functional theory calculations is used as improvement over the LDA in the computation of a substantial amount of molecular properties^[37].

The starting point in this hybridization theory, has been the adiabatic connection formula introduced by Becke^[29], who showed that the exchange-correlation can be expressed by^[27,29]:

$$E_{XC}^{\text{hyb}} = \frac{1}{2} (E_X + E_{XC,\lambda=1}^{\text{DFA}}), \quad (3.95)$$

where E_X is the *exact exchange energy* and DFA, a density functional approximation that uses the *local spin density* (LSD) approximation for $E_X + E_{XC,\lambda=1}^{\text{DFA}}$. The $\lambda = 0$ corresponds to the KS noninteracting system, i.e., to the KS exchange-correlation.

Furthermore, the exchange-correlation for a *three-parameter hybrid* is written as^[27,38]:

$$E_{XC}^{\text{hyb}} = E_{XC}^{\text{LSD}} + \alpha_0(E_X - E_X^{\text{LSD}}) + \alpha_X(E_X^{\text{GGA}} - E_X^{\text{LSD}}) + \alpha_C(E_C^{\text{GGA}} - E_C^{\text{LSD}}) \quad (3.96)$$

where $\alpha_0 = 0.20$, $\alpha_X = 0.72$, and $\alpha_C = 0.81$. $E_{XC}^{\text{GGA}} = \int d^3r f(\rho \uparrow, \rho \downarrow, \nabla_{\rho \uparrow}, \nabla_{\rho \downarrow})$ is a generalized gradient approximation, and $E_{XC}^{\text{LSD}} = \int d^3r f(\rho \uparrow, \rho \downarrow, 0, 0)$ is its local spin density (LSD). There exist also the hybrid meta-generalized gradient approximations (mGGAs): M06L, M06, M06-2X and M06-HF. The General formula for hybrid meta-generalized gradient approximation is:

$$E_{XC}^{\text{hyb}} = \frac{X}{100} E_X^{\text{HF}} + \left(1 - \frac{X}{100}\right) E_X^{\text{DFT}} + E_C^{\text{DFT}} \quad (3.97)$$

where E_X^{HF} is the nonlocal Hartree-Fock (HF) exchange energy, X is the percentage of Hartree-Fock exchange in the hybrid functional, E_X^{DFT} is the local DFT exchange energy, and E_C^{DFT} is the local DFT correlation energy. Each of the above listed functionals has a different amount of exact exchange: M06-L which is fully local has no HF exchange and cannot be therefore considered as hybrid, M06 has 27% HF exchange, M06-2X 54% and M06-HF 100%. This is, for example, the *double-hybrid DFT* (B2PLYP)^[39]

3.4.4 Gaussian-n (G_n) theory

The Gaussian-n theories (G_n)^[40–44] are methods developed with the goal of approaching exact molecular energies using a set of calculations based mainly on *ab initio* molecular orbital theory with different levels of accuracy and basis sets^[45]. A composite approach, wherein a very high-level correlation method [such as quadratic configuration interaction theory (QCISD)(T) and coupled cluster theory (CCSD)(T)] based on a moderate-sized basis set (e.g., 6-31G(d)) combined with energies from lower level calculations (such as MP4 and MP2) with much larger basis sets is used in these methods, in addition to the *higher level correction* (HLC) to estimate the energy^[45]. Reduced versions for G_n theories are also used with the aim a either reducing the computational expense of the calculations [e.g., with *reduced order perturbation theory* that uses Møller-Plesset perturbation theory: G2(MP2)^[46], G3(MP2)^[47], G4(MP2)^[44]], or replacing the QCISD(T) which is not available in the quantum chemistry codes used by some research groups or which is used for some theoretical reasons (as, often, there is no improvement with respect to QCISD(T) energy) or used for occasional cases where the QCISD(T) method yields a poor energy^[47]. Another

G₃ theory variant, G3//B3LYP or G3B3, using B3LYP density functional theory [B3LYP/6-31G(d)] for the geometries and zero-point energies calculations was introduced by Baboul et al.^[48]. In fact, for 299 energies assessed using G3B3, these authors found that this level of theory presents an average absolute deviation from experiment of 0.99 kcal/mol, compared to 1.01 kcal/mol for G3 theory. The improvement was, especially, observed for some cases where MP2 theory is deficient for geometries.

Beside the Gn theories, there are *Complete basis set* (CBS) methods of Petersson and coworkers for computing very accurate energies^[49–51,51–55] and their modified versions such as the CBS-4 [HF/3-21G(d) for geometries and frequencies], the *complete basis set-quadratic Becke 3* (CBS-QB3) [B3LYP/6-311G(2d,d,p) for geometries and frequencies], the *complete basis set-quadratic configuration interaction, incorporates atomic pair natural orbital (APNO) basis sets* (CBS-QCI/APNO) [QCISD/6-311G(d,p) for geometries and frequencies]^[56].

3.4.5 Basis sets

A *basis set* is, commonly, a collection of vectors which defines a space in which a problem is solved. In quantum chemistry, a *basis set* denotes a set of (nonorthogonal) one-particle functions used to build molecular orbitals^[21,57]. A central technique is the molecular orbitals (MO) approach, where MOs are expressed as a *linear combination of atomic orbitals (LCAO)*, i.e., the wave function parameterized in terms of Slater determinants composed of one-electron orbitals, each one being a product of a spatial and a spin function^[58,59]. In fact, on computer, the calculation of the mathematical form of the MOs is impossible, and the problem is rather reduced to the calculation of MO expansion coefficients in terms of the Atomic orbital (AO) basis functions^[59], i.e., the *basis sets*:

$$\psi(\mathbf{r}) = \sum_{\alpha=1}^{N_{\text{BF}}} G_{\alpha}(\mathbf{r}) C_{\alpha i} \quad (3.98)$$

where $\psi(\mathbf{r})$ are molecular (spatial) orbital, $G_{\alpha}(\mathbf{r})$, a (fixed) basis function and $C_{\alpha i}$ a coefficient. A wide variety of functions were used in the literature to expand MOs. These include Slater functions, Gaussian functions, plane waves, wavelets, numerical basis functions, etc^[60]

3.4.5.1 Slater type functions

For hydrogen-like systems, Slater functions or *Slater-Type Orbitals (STOs)* (i.e., one-electron like hydrogen AOs) are very suitable for expanding MOs because they have the correct shape *near the nucleus* but also *afar from the nucleus* as they decay like $e^{-\alpha r}$. Cartesian STOs can be written in the form^[57,61]:

$$\Phi_{\mathbf{k}\mathbf{m}\mathbf{n}}^{\text{STO}}(x, y, z) = N x^k y^m z^n e^{-\zeta r} \quad (3.99)$$

where N is a normalization constant; \mathbf{k} , \mathbf{m} and \mathbf{n} control the angular momentum $L = k + m + n$. The parameter ζ controls the *width of the orbital*, i.e., large ζ gives *tight function*, whereas small ζ yields *diffuse function*. In spherical polar coordinates, STOs are defined as

$$\Phi_{nlm}^{\text{STO}}(x, y, z) = N r^{n-1} e^{-\zeta r} Y_{lm}(\theta, \phi) \quad (3.100)$$

with l and m are angular momentum quantum numbers. STO's are more accurate and have correct short- and long-range behavior. However, the cusp at the nucleus is only correct for particular linear combinations of Slater orbitals, but also it takes longer to compute integrals using them^[57,61].

3.4.5.2 Gaussian type functions

The 1s orbital of the H atom, $e^{-\zeta r}$, gives rise to difficult integrals. In order to circumvent this issue, *Gaussian-Type Orbitals (GTOs)* are used, even for the 1s.

Cartesian Gaussian orbitals are defined as

$$\phi_{kmn}^{\text{GTO}}(x, y, z) = N x^k y^m z^n e^{-\zeta r^2} \quad (3.101)$$

The linear combinations of these can again be used to form spherical polynomials of definite angular momentum.

$$\phi_{nlm}^{\text{GTO}}(r, \theta, \varphi) = N r^{2n-2-l} e^{-\zeta r^2} \quad (3.102)$$

In quantum chemistry, a single Gaussian function is called a *primitive Gaussian function*, or *primitive GTO (Gaussian Type Orbital)*. Spherical and Cartesian functions are the same for up to $l = 1$ (p-functions) but differ for $l = 2$ or higher. One basis function (STO, GTO or CGTO) for each AO in the atom is referred to as minimal basis set.

In practice, a linear combination of n primitive GTO's are used to mimic a STO's. They are called *Contracted Gaussians (CGs)*. They then attempt to approximate Slater-type orbitals (STOs) by n primitive Gaussians. The simplest kinds of these are referred to as STO-nG (STO-1G, STO-2G, STO-3G). The STO-nG basis set were found unsatisfactory due to the fact that they only include one CG per atomic orbital. The valence electrons play an important role in the bonding process. The use of more than one CG per valence electron allow improving the basis sets. Basis sets of this kind are called *split valence basis sets* as the description of valence orbitals are split into two or more basis functions: *e.g.* **DZ** (double zeta), **TZ** (triple zeta), **QZ** (quadruple zeta). This is achieved by adding *one CG per core atomic orbital and more than one for the valence atomic orbitals*.

The small split valence basis set and the most economical one is the **3-2G** basis set. In this basis set, the non-valence electrons are described by single basis functions composed of 3 CG; *each valence electron is described by two basis functions*: the first of these basis functions is composed of two primitive GTOs while the second consists of a single uncontracted primitive GTO. In John Pople notation, the split valence basis sets are written as $X - YZg$ ^[62], where X represents the *number of primitive gaussians* comprising each core atomic orbital basis functions, Y and Z indicate that the valence orbitals are formed by two basis functions, the first one composed of a linear combination of Y primitive GTO, the other composed of a linear combination of Z primitive GTOs. In general, *two numbers* after the hyphens implies that this basis set is a **split-valence double-zeta basis set**; *three, four numbers, ...*, such as $X - YZWg$, $X - YZWVg$, etc, imply a **split-valence triple-, quadruple-zeta basis sets**, etc.

Moreover, increasing the number of CGs per atomic orbital does not also guarantee the good quality of the basis set. Thus, other types of CGs need to be included:

- *Polarisation functions* in order to enhance the *flexibility* of atoms to form chemical bonds in any direction and hence improve calculated molecular structures are included. This is done by using the CGs of angular momentum higher than in the valence orbitals of each atom.
e.g.: 3-21G*, 6-31G*, 6-31G**, DVP, TZP, cc-pVDZ, cc-pVTZ
- CGs which extend further from the nucleus than the atomic orbitals. These *diffuse functions* are used to improve the predicted properties of species with extended electronic densities such as anions or molecules forming hydrogen bonds.
e.g.: 4-31+G, 6-31+G, 6-31++G, 6-311++G.

Balanced basis sets include both polarisation and diffuse functions. Examples: 6-31+G**, 6-311++G*, aug-cc-pVTZ. MOs obtained using the basis sets described above are solutions

of the Kohn-Sham equations only within the *function space* of the basis set used. To improve the quality of a basis set, the number of CGs to use must be increased. Any molecular orbital can be represented exactly by *complete basis set*. Nevertheless, complete basis sets tend to have an infinite number of functions and are, consequently, not practical for calculations. Complete basis set are therefore estimated by systematically increasing the number of basis functions and extrapolating to an infinite-size basis set.

e.g: cc-pVDZ, cc-pVTZ, cc-pVQZ.

3.5 Gaussian software

3.5.1 Introduction

Gaussian is a computer program that can be used by many scientists such as chemists, physicists, chemical engineers, biochemists, and others. It has been designed to utilize fundamental laws of quantum mechanics to predict properties of molecules and reactions. It predict then molecular energies and structures, energies and structures of transition states, molecular orbitals, spectroscopic data (NMR, IR, UV, Raman, etc), reaction pathways, multipole moments, electron affinities and ionization potentials, bond and reaction energies, atomic charges, and much more advanced calculations. It has been released in 1970 by John Pople and his research group at Carnegie-Mellon University as Gaussian 70^[63,64]. It has been continuously updated since then and the latest version in the Gaussian series of programs is Gaussian16.

Among the several Gaussian program features and capabilities, only some of them are explored in this thesis to compute and analyze the studied molecular structures, UV-VIS, vibrational and rotational spectra, as well as their thermochemistry with the aim of providing sufficient material necessary in the search and characterization of these molecular compounds in the ISM. In the use of Gaussian software, the computation of different properties is achieved using *keywords* (see Gaussian 09w tutorial^[65]). For instance, the computation of IR frequencies and some rotational constants including centrifugal ones, are invoked using the *keyword "Freq=vibrot"*. The starting point is getting the *optimized structure*, i.e., structure corresponding to *minimum energy* in the Figure 3.3. All other properties (***spectroscopic properties*** such UV-VIS, IR, Raman, Rotational spectra; ***thermodynamic properties*** such as proton affinity, Gibbs free, enthalpy and entropy energies, etc) are calculated from this structure. The molecular spectroscopic and thermodynamic properties, but also all quantities computed by Gaussian programs depend on the theoretical method used, since each one has its form of approximating the resolution of the Schrödinger equation (see sections 3.4.1 and 3.4.2).

When a molecule interact with light, it does not absorb all light that comes its way, but only with light that carries the right amount of energy to promote the molecule from one discrete energy level to another^[66]. In other words, the molecule absorbs a photon of energy E that can promote it from one rotational, vibration or electronic level of energy to another, and/or contributes to translational motions:

$$E = h\nu = \Delta E_{\text{trans}} + \Delta E_{\text{elect}} + \Delta E_{\text{vib}} + \Delta E_{\text{rot}} \quad (3.103)$$

More specifically, light of *infrared frequencies* can only promote molecules from one vibrational energy level to another. Light of *microwave wavelengths*, having low frequencies, can only promote molecules from one rotational energy level to another. Similarly, *visible and ultraviolet lights*, much more energetic, promote the redistribution of electrons in a molecule such that the electronic potential energy of the molecule is changed (see Figure 3.3).

3.5.2 Electronic transitions

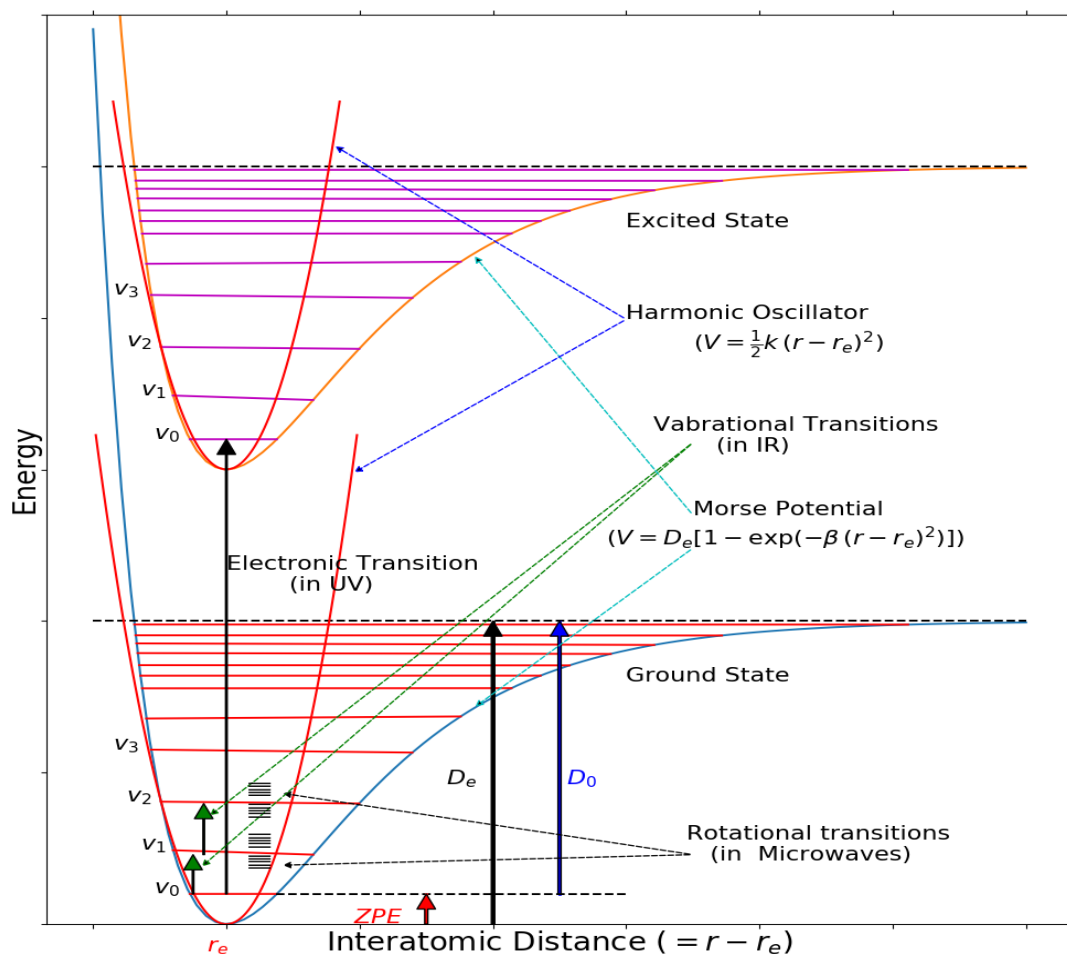


Figure 3.3 – Schematic view of the adiabatic potential curve (Electrical potential energy versus the internuclear separation).

As shown in the section 3.1, by first approximation the electronic energy corresponding to the pure electronic energy E_e is such that

$$\hat{H}_{el}\psi = E_{el}\psi, \quad (3.104)$$

where the hamiltonian \hat{H}_e is given by the equation (3.18), its eigenfunction ψ in the equation (3.17) and E_e given by:

$$E_e = T_e + V = T_e + V_e + V_{eN} \quad (3.105)$$

However, as shown at Figure 3.3, at each electronic energy state corresponds many discrete vibrational levels; at each one of these later corresponds also an infinity number of rotational energy levels. Thus, vibrational and rotational motions being for nuclei, the potential under which electrons move includes also the repulsion between nuclei, so that the electronic energy E_{el} is the eigenvalue of the hamiltonian (3.19):

$$E_{el} = T_e + V_e + V_{eN} + V_{NN} \quad (3.106)$$

or^[67]

$$E_{\text{el}} = E_e + E_{\text{vr}} \quad (3.107)$$

where E_{vr} is the vibrational-rotational energy.

3.5.3 Molecular vibrations

Vibrations in molecules can be excited through two physical mechanisms: the absorption of light quanta and the inelastic scattering of photons^[68]. Vibrational spectroscopy includes several different techniques, the most essential of which are mid-infrared (IR), near-IR, and Raman spectroscopy. Both mid-IR and Raman spectroscopy provide characteristic fundamental vibrations that are employed for the elucidation of molecular structure^[69]. In fact, Infrared and Raman spectroscopy are two of the most widely used techniques for the determination of molecular structure and for the identification of compounds^[70]. Vibrational spectra can reveal significant structural features of complex organic materials^[71]. Whereas *IR spectroscopy* is based on the absorption of photons with energy matching the difference of energies between the low and up levels of energy, the *Raman spectroscopy* is founded on the *scattering mechanism* where a portion of the incident photons is scattered inelastically such that the energy of the scattered photons $h\nu_{\text{R}}$ differs from that of the incident photons ($h\nu_0$)^[68]:

$$h\nu_{\text{r}} = h\nu_{\text{f}} - h\nu_{\text{i}} \quad (\text{an IR transition}) \quad (3.108\text{a})$$

$$h\nu_0 - h\nu_{\text{R}} = h\nu_{\text{f}} - h\nu_{\text{i}} \quad (\text{a Raman transition}) \quad (3.108\text{b})$$

In the expression (3.108a), i.e., in IR spectroscopy, the molecule is irradiated by a *polychromatic light* in which some of the photons have energies $h\nu_{\text{R}}$ that correspond to the difference of energy between f and i levels. In contrast, in the expression (3.108b), i.e., in the Raman spectroscopy, the excitation of molecular vibrations requires monochromatic irradiation (photons of energy $h\nu_0$). The main information in vibrational spectroscopy are found in the energies of the vibrational transitions and the strength of the band intensities

The mid- and far-infrared wavelength ranges are extremely rich in spectral features, many of which probe unique species which cannot be observed at any other wavelength^[72]. This is the cases of symmetric molecules like CH_4 and C_2H_2 which have no dipole moment and thus cannot be observed through rotational transitions at millimeter wavelengths. Likewise, fundamental vibrational transitions of important molecules such as H_2O , CH_4 , C_2H_2 , HCN and CO_2 occur at mid-infrared wavelengths.

3.5.3.1 Theory of molecular IR spectra

Consider, first, the vibration of a diatomic molecule, often assimilated to an *harmonic oscillator*. The potential energy deriving from the restoring force can be expressed as

$$V = \frac{1}{2}kq^2, \quad (3.109)$$

which is represented in Figure 3.3 (in red).

In fact, the big challenge in vibrational spectroscopy had been to find the correct potential energy, which represents the harmonic oscillator, that given by the expression (3.109) being far from the true one for diatomic vibrations. One of the most general potential forms, denoted as the Dunham potential^[73], is a *Taylor series expansion about the*

equilibrium position (r_e) (Figure 3.3):

$$V(r) = V(r_e) + \left. \frac{dV}{dr} \right|_{r_e} (r - r_e) + \frac{1}{2} \left. \frac{d^2V}{dr^2} \right|_{r_e} (r - r_e)^2 + \dots \quad (3.110)$$

By choosing the bottom of the well as the zero energy, we have $V(r_e) = 0$. Likewise, the expansion of $V(r)$ about the minimum at r_e leads to

$$\left. \frac{dV}{dr} \right|_{r_e} (r - r_e) = 0. \quad (3.111)$$

Therefore, it remains that:

$$V(r) = \frac{1}{2} \left. \frac{d^2V}{dr^2} \right|_{r_e} (r - r_e)^2 + \frac{1}{6} \left. \frac{d^3V}{dr^3} \right|_{r_e} (r - r_e)^3 + \dots, \quad (3.112)$$

which can be written as:

$$V(r) = \frac{1}{2} k(r - r_e)^2 + \frac{1}{6} k_3(r - r_e)^3 + \frac{1}{24} k_4(r - r_e)^4 + \dots \quad (3.113)$$

where $k_n = \left. \frac{d^n V}{dr^n} \right|_{r_e}$ with $k = k_2$. Terms of degrees greater than 2 are negligible so that, retaining the leading one, i.e., $\frac{1}{2} k(r - r_e)^2$, we retrieve the expression (3.109).

From quantum theory, a molecule has only *discrete vibrational energy levels* characterized by the quantum number v so that:

$$E_v = \left(v + \frac{1}{2} \right) \frac{h}{2\pi} \sqrt{\frac{k}{\mu}} = \left(v + \frac{1}{2} \right) h\nu \quad (3.114)$$

with $v = 0, 1, 2, 3, \dots$ and $\nu = \frac{1}{2\pi} \sqrt{\frac{k}{\mu}}$ where $\mu = \frac{m_1 m_2}{m_1 + m_2}$ is the reduced mass. The energy $E_0 = \frac{1}{2} h\nu$ is called the *zero point energy (ZPE)*. The vibrational energy levels are uniformly spaced and the vibrational terms expressed in wavenumber are given:

$$G(v) = \left(v + \frac{1}{2} \right) \omega; \quad \omega = \frac{h}{2\pi c} \sqrt{\frac{k}{\mu}} \quad (3.115)$$

The parabolic potential well in Figure 3.3 is not a good representation of the force felt by diatomic molecules. A popular function that represents the best this force is the **Morse potential** (see the same figure) given by:

$$V = D_e (1 - e^{-\beta q})^2 \quad (3.116)$$

where D_e is the *depth of the potential well* and β , a *measure of the curvature at the bottom of the well*. Unlike the harmonic oscillator, the Morse potential, asymptotically, approaches the *dissociation limit* $V(r) = D$ as $r \rightarrow \infty$. Another advantage is that, for a Morse potential, the Schrödinger equation can be solved analytically. The corresponding vibrational terms, including centrifugal terms are^[74,75]:

$$G(v) = \omega_e \left(v + \frac{1}{2} \right) - \omega_e x_e \left(v + \frac{1}{2} \right)^2 + B_e J(J+1) - D_e (J(J+1))^2 - \alpha_e \left(v + \frac{1}{2} \right) J(J+1) \quad (3.117)$$

where $G(v)$ and all spectroscopic constants are in cm^{-1} . Moreover, the spectroscopic constants in equation (3.117) are expressed as:

$$\omega_e = \beta \left(\frac{Dh \times 10^2}{2\pi^2 c \mu} \right)^{\frac{1}{2}}, \quad \omega_e \chi_e = \frac{h\beta^2 \times 10^2}{8\pi^2 c \mu}, \quad B_e = \frac{h \times 10^{-2}}{8\pi^2 \mu r_e^2 c},$$

$$D_e = \frac{4B_e^3}{\omega_e^2}, \quad \text{and} \quad \alpha_e = \frac{6(\omega_e \chi_e B_e^3)^{1/2}}{\omega_e} - \frac{6B_e^2}{\omega_e} \quad (3.118)$$

recalling that D_e in (3.118) is not to be confused with D_e , depth of the potential well; the former a centrifugal constant. In these expressions, χ_e is a small positive dimensionless constant of the order of ~ 0.01 and $\chi_e \omega_e$ is called the *anharmonicity*^[76]. It measures the extent of anharmonic behaviour of the oscillator. Excluding rotations ($J = 0$), the expression (3.117) becomes:

$$G(v) = \omega_e \left(v + \frac{1}{2} \right) - \omega_e \chi_e \left(v + \frac{1}{2} \right)^2 \quad (3.119)$$

where $G(v)$ is the customary symbol for the vibrational energy levels. In this expression, the second term is an *anharmonic correction* to the first one, i.e., the vibrational energy levels corresponding to the harmonic oscillator.

Transition from the ground state ($v = 0$) to higher energy levels require energies:

$$\Delta E = E_v - E_0 = \omega_e v - \omega_e \chi_e v(v + 1). \quad (3.120)$$

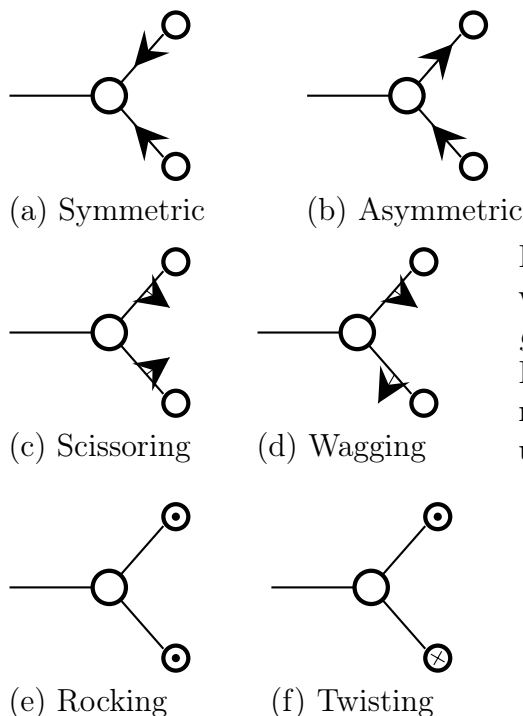
The transition from $v = 0 \rightarrow v = 1$ is called the ***fundamental transition***. A given normal molecular vibration is IR active if at least one component of the electric dipole moment of the molecule changes during this vibration. That is, the value of a dipole moment derivative, taken at the equilibrium must differ from zero^[77]:

$$\left(\frac{\partial \mu_i}{\partial Q_k} \right)_0 \neq 0 \quad (3.121)$$

For diatomic molecules of the type XY the dipole moment goes through a maximum as the internuclear distance changes from zero to infinity, the position of the maximum being different from the equilibrium distance. The dipole moment derivative can then be positive or negative, but still being different from zero and the vibration becomes thus IR active.

For *polyatomic molecules*, difficulties in the solutions of vibrational problem appear. All the atoms participate in the vibrations of a polyatomic molecule and the difficulties in these molecules arise from the fact that there are couplings between various vibrational modes, this coupling being described using *normal modes*^[78]. A normal mode is an independent motion in a molecule which occurs without disturbing or causing perturbation to any other modes. At each mode is associated a certain symmetry, consequently, group theory is an essential tool in the determination of what symmetries corresponding to different normal modes and in the prediction of whether, the modes are *IR active* and/or *Raman active*. In a molecule with n atoms, there are $3n$ *degrees of motional freedom*, each atom having *three degrees of freedom* as it can move independently along each of the three axes of a Cartesian coordinate system. Among the $3n$ degrees of freedom, six do not change the distance between atoms and can, consequently, be removed from the set. These are the *three degrees* corresponding to the *translational* (x, y, z) of the center of mass (they consist to the motion of all atoms simultaneously in the same direction parallel to the axes of the Cartesian coordinate system) and three (or *two* for linear molecules) describing *rotations* about the principal axes of the inertial ellipsoid of the molecule, i.e., those associated with

the rotational motion of the molecules as a whole (θ, ϕ, χ). The remaining $3N - 6$ (or $3N - 5$ for linear molecules) degrees are motions which change the lengths of the chemical bonds and the angles between atoms. Since bonds in molecules are elastic, periodic motions occur. They then correspond to the $3N - 6$ (or $3N - 5$ for linear molecules) *normal modes*.



These $3N - 6$ ($3N - 5$ for linear molecules) include stretching modes and bending deformations. For instance, the figure beside presents (a) a *symmetric* and (b) an *asymmetric* stretching modes.

Likewise, the same figure shows bending modes which can be classified into (c) *scissoring*, (d) *wagging*, (e) *rocking* and (f) *twisting* bending modes. Like in diatomic molecules, in polyatomic molecules, a vibrational mode is IR active if molecular dipole moment varies during the vibration.

That is, the vibrational transition $\nu_k \rightarrow \nu_i$ is IR active if at least one of the three vectors components $[\mu_x]_{fi}^k \neq 0$. In other words, a transition between two energy levels is generally accompanied by emission or absorption of radiation if the dipole moment of the transition, i.e., *transition moment* is different from zero:

$$\begin{aligned} \mu_{fi} &= \langle \psi_f | \hat{\mu} | \psi_i \rangle \neq 0 \\ &= \int \psi_f^* \hat{\mu} \psi_i d\tau \end{aligned} \quad (3.122)$$

3.5.3.2 Molecular Raman transitions

Molecules with no permanent dipole moment do not have pure rotational spectrum. Moreover, molecular vibrational motion for which there is no oscillation of dipole do not have IR absorption or emission spectra. In fact, for a molecule in order to show infrared absorptions its electric dipole moment must change during the vibration. This is the selection rule for infrared spectroscopy^[79]. *Raman spectroscopy* can then be used in the determination of rotational and vibrational level spacings, and hence determination of bond lengths and force constants for such molecules^[79]. This technique can, for instance, be used to study rotational energy levels for molecules inaccessible by *Microwave Spectroscopy* as they lack permanent dipole moment such as H_2 , O_2 , N_2 , etc.

Beside being absorbed and emitted by atoms and molecules, photons may also be *scattered*. Scatterings may be *elastic*. In such kind of scatterings, the molecule state remains the same and unchanged. They are called *Rayleigh scatterings*. Another kind of scatterings is that of *inelastic scatterings* which leave the molecule in a different quantum state. These are called *Raman scatterings*.

The scattered radiation can reveal much about the physical and chemical properties of the sample^[80]. In Raman process, an incident photon can lose some of its energy to the molecule or gain some from it, and so leaves the molecule with a lower or a higher frequency, respectively (see Figure 3.4): the lower frequency components of the scattered radiation are

called the *Stokes lines* and the higher frequency components are called the *anti-Stokes lines*^[81].

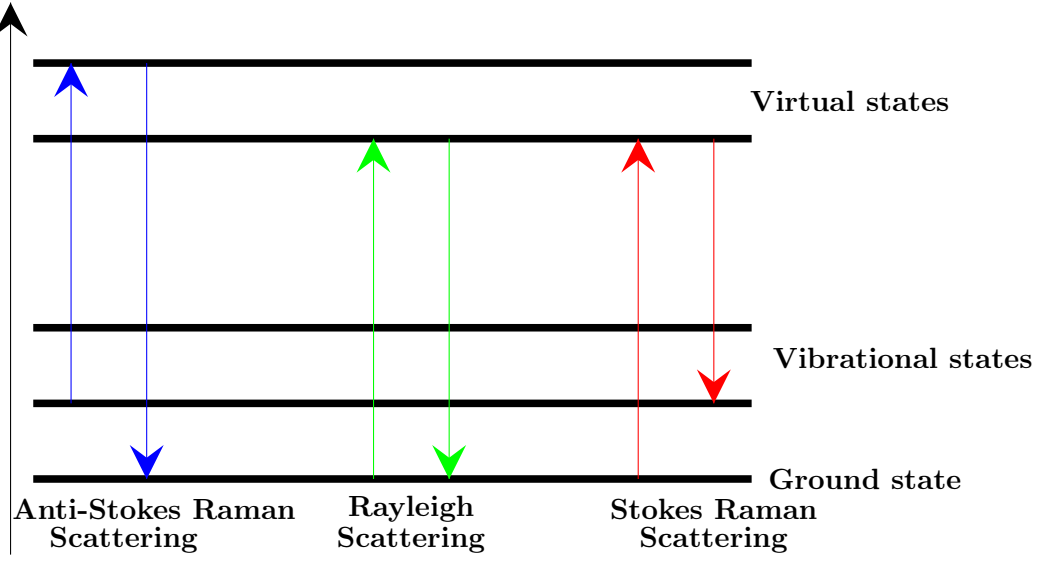


Figure 3.4 – Elastic and inelastic scatterings

The shifted frequency is given:

$$\nu_{\text{shift}} = \nu_0 \pm \nu_{\text{molecule}} \quad (3.123)$$

where ν_0 is the frequency of the incident radiation and ν_{molecule} , an internal frequency corresponding to rotational, vibrational, or electronic transitions within a molecule. From classical model point of view, when an *electric field* \mathcal{E} is applied to a molecule, its *charge distribution* is distorted following the Coulomb's law. Thus, the applied electric field induces a *dipole moment* in the molecule whose magnitude varies linearly with the strength of the electric field \mathcal{E} for weak fields:

$$\mu = \alpha \mathcal{E} \quad (3.124)$$

where the proportionality constant α is called the *polarizability* and is a characteristic of the molecule which is a measure of how easy it is to distort the charge distribution of the molecule.

Stokes and Anti-Stokes components appear when $\Delta\alpha \neq 0$, so the molecule must be *anisotropically polarizable*. The *gross selection rule* for pure vibrational Raman is that *the polarizability of the molecule must change as the molecule vibrates*.

The Raman intensity can be given by:

$$I = Kl\alpha^2\omega^4 \quad (3.125)$$

where K is a constant, l is the laser power (if a laser is used), α the polarizability and ω the frequency of the incident radiation. In terms of Raman activities (S_i) calculated with the gaussian 09 package, relative Raman intensities (I_i) can be calculated using the following relation^[82]:

$$I_i = \frac{f(\nu_0 - \nu_i)^4 S_i}{\nu_i [1 - \exp(-hc\nu_i/kT)]} \quad (3.126)$$

where ν_0 is the exciting frequency (in cm^{-1}) (in this work, we have used the excitation frequency $\nu_0 = 9398.5\text{cm}^{-1}$, which corresponds to the wavelength of 1064 nm of a Nd:YAG

laser^[83]), ν_i the vibrational wave number of the i^{th} normal mode, h , c and k are fundamental constants, and f is a suitably chosen common normalization factor for all peak intensities.

Unlike the IR spectroscopy, a change of the polarization potential, i.e., deformation of the electron cloud, is necessary for a molecule to exhibit a Raman effect. The intensity of the scattered light is dependent on the amount of the polarization potential change^[80].

3.5.4 Molecular rotations

Rigid rotor

At first approximation a molecule is regarded as a rigid body specified by atomic positions expressed in Cartesian coordinates (x, y, z) with origin defined as the center of mass of the molecule. The derivation of the quantum mechanical properties of molecular rotors, including their microwave spectra, begins with the classical expressions for the angular momenta and rotational energy.

According to the classical mechanics, the angular momentum of a rigid system of particles is written as^[84,85]:

$$\mathbf{P} = \mathbf{I} \cdot \boldsymbol{\omega} \quad (3.127)$$

where $\boldsymbol{\omega}$ is the angular velocity and \mathbf{I} , the moment of inertia tensor.

The classical kinetic energy of rotation for the molecule can then be written as:

$$E_{\text{rot}} = \frac{1}{2} (\omega_x, \omega_y, \omega_z) \begin{pmatrix} I_{xx} & I_{xy} & I_{xz} \\ I_{yx} & I_{yy} & I_{yz} \\ I_{zx} & I_{zy} & I_{zz} \end{pmatrix} \begin{pmatrix} \omega_x \\ \omega_y \\ \omega_z \end{pmatrix} \quad (3.128)$$

where ω_i is the angular velocity around the i^{th} axis and the I_{ii} are components of the *principal moments of inertia*.

The origin of the coordinate system being chosen at the center of mass, this choice allows the total kinetic energy to be written as the sum of the kinetic energy of translational motion of the center of mass plus the kinetic energy of the motion relative to the center of mass. The translational and rotational motions can hence be treated separately.

If the x , y , and z axes are appropriately chosen, the products of inertia become zero. Such axes can be found by diagonalizing the moment of inertia tensor:

$$\begin{vmatrix} I_{xx} - I & I_{xy} & I_{xz} \\ I_{yx} & I_{yy} - I & I_{yz} \\ I_{zx} & I_{zy} & I_{zz} - I \end{vmatrix} = 0 \quad (3.129)$$

The three roots I of the equation (3.129) are *the principal moments of inertia* along the principal axes which are denoted \mathbf{a} axis, \mathbf{b} axis, and \mathbf{c} axis. The angular momentum components, along these axes, are then $P_i = I_i \omega_i$, ($i = \mathbf{a}, \mathbf{b}, \mathbf{c}$) so that the rotational kinetic energy becomes:

$$\begin{aligned} E_{\text{rot}} &= \frac{1}{2} I_a \omega_a^2 + \frac{1}{2} I_b \omega_b^2 + \frac{1}{2} I_c \omega_c^2 \\ &= \frac{1}{2} \left(\frac{P_a^2}{I_a} \right) + \frac{1}{2} \left(\frac{P_b^2}{I_b} \right) + \frac{1}{2} \left(\frac{P_c^2}{I_c} \right) \end{aligned} \quad (3.130)$$

where

$$P^2 = P_a^2 + P_b^2 + P_c^2 \quad (3.131)$$

The operator can be written as

$$\mathbf{P}^2 = -\hbar^2 \left\{ \left(\frac{1}{\sin \theta} \right) \left(\frac{\partial}{\partial \theta} \right) \left[\sin \theta \left(\frac{\partial}{\partial \theta} \right) \right] + \frac{1}{\sin^2 \theta} \left(\frac{\partial^2}{\partial \phi^2} \right) \right\} \quad (3.132)$$

The wave function is, therefore, represented by spherical harmonics. The relative values of principal moments of inertia allow to classify molecules into four categories:

1. If $I_b = I_c = I$ and $I_a \approx 0$, there is no rotation around the \mathbf{a} axis. Molecules with such elements of principal moments of inertia are called **linear molecules**. This is the case of all diatomic and polyatomic linear molecules.
2. Beside linear molecules, there are nonlinear polyatomic ones with moments of inertia are such that: $I_a \leq I_b \leq I_c$ with $I_c = I_{\text{max}}$ and $I_a \neq 0$. These molecules are classified into three main groups:
 - **Spherical top molecules:** For these molecules, the principal moments of inertia are such that $I_a = I_b = I_c$.
 - **Symmetric top molecules:** They can be subdivided into two groups: Prolate tops and Oblate tops. For these molecules, one of the principal axes of inertia must lie along the molecular axis of symmetry and the principal moments of inertia which have their axes perpendicular to this axis are equal.
 - a) **Prolate tops:** Prolate top molecules are molecules such that $I_a < I_b = I_c$. The axis of least moment of inertia, i.e., \mathbf{a} , lies along the symmetry axis.
 - b) **Oblate tops:** Oblate top molecules are molecules such that $I_a = I_b < I_c$. The axis of the greatest moment of inertia, i.e., \mathbf{c} , lies along the symmetry axis.
 - **Asymmetric top molecules:** They are molecules for which the three moments of inertia are different from each other ($I_a < I_b < I_c$). Some molecules are strictly asymmetric tops but have two nearly equal moments of inertia:
 - a) $I_a < I_b \approx I_c$: These molecules are called *near prolate asymmetric tops*.
 - b) $I_a \approx I_b < I_c$: They are *near oblate asymmetric tops*.

Rotational spectra of asymmetric top molecules

As discussed above, asymmetric top molecules are molecules whose three principal moments of inertia are different from one another. Most nonlinear molecules found in interstellar clouds belong to this class^[84]. In defining the rotational constants, the identification of molecular principle inertial axes \mathbf{a} , \mathbf{b} and \mathbf{c} to \mathbf{x} , \mathbf{y} and \mathbf{z} is made so that $I_a < I_b < I_c$ or so that the molecular rotational constants are such that $A > B > C$, with $A = \hbar/8\pi^2 I_a$, $B = \hbar/8\pi^2 I_b$ and $C = \hbar/8\pi^2 I_c$.

When $I_b \rightarrow I_c$, the prolate symmetric top is approached whereas when $I_b \rightarrow I_a$, the oblate symmetric top is approached. A parameter which is a measure of the rotor asymmetry^[85] is defined from rotational constants by:

$$\kappa = \frac{2B - A - C}{A - C} \quad (3.133)$$

The value $\kappa = -1$ and $\kappa = +1$ correspond to the prolate and oblate tops, respectively, whereas $\kappa = 0$ corresponds to the most asymmetric top. There are therefore six possibilities as described by^[86] leading to I^r , I^l , II^r , II^l , III^r and III^l representations., where I^r , II^r and

Table 3.1 – Possibilities of representation for an asymmetric molecule

Type	I ^r	I ^l	II ^r	II ^l	III ^r	III ^l
x	b	c	c	a	a	b
y	c	b	a	c	b	a
z	a	a	b	b	c	c
F	$\frac{1}{2}(\kappa - 1)$	0	$\frac{1}{2}(\kappa + 1)$	$\frac{1}{2}(\kappa - 1)$	0	$\frac{1}{2}(\kappa + 1)$
G	1	κ	-1	1	κ	-1
H	$-\frac{1}{2}(\kappa - 1)$	1	$\frac{1}{2}(\kappa - 1)$	$\frac{1}{2}(\kappa + 1)$	-1	$-\frac{1}{2}(\kappa - 1)$

III^r are the three permutations of the right-handed **a**, **b** and **c** axes and I^l, II^l and III^l, those that correspond to the left-handed **a**, **b** and **c** axes as given in Table 3.1^[85,86]:

In quantum mechanics, the hamiltonian describing the rotation of a rigid asymmetric body is given by

$$\mathcal{H} = AP_a^2 + BP_b^2 + CP_c^2 \quad (3.134)$$

with A, B and C) defined as above. To facilitate the calculation of energy levels, this hamiltonian can be written as^[85,86]

$$\mathcal{H} = \frac{1}{2}(A + C)P^2 + \frac{1}{2}(A - C)\mathcal{H}(\kappa) \quad (3.135)$$

where $\mathcal{H}(\kappa)$ is a reduced hamiltonian given by

$$\mathcal{H}(\kappa) = P_a^2 + \kappa P_b^2 - P_c^2, \quad (3.136)$$

$P^2 = P_a^2 + P_b^2 + P_c^2$ and κ the asymmetry parameter given by the equation (3.133). Reduced energies, i.e., eigenvalues of $\mathcal{H}(\kappa)$ depend only on the inertial asymmetry parameter κ and are not on the individual rotational constants.

Unlike the hamiltonian for symmetric rotor, the hamiltonian for asymmetric rotor is such that the Schrödinger wave equation cannot be solved directly. Nevertheless, the general *asymmetric rotor wave functions* may be represented by a linear combination of symmetric rotor functions:

$$\psi_{J\tau M} = \sum_{J,K,M} a_{JKM} \psi_{J,K,M} \quad (3.137)$$

where the function $\psi_{J,K,M}$ can be expressed in terms of *Euler angles* ϕ , θ and χ as follows:

$$\psi_{J,K,M} = \Theta_{J,K,M} e^{iK\phi} e^{iM\chi} \quad (3.138)$$

with

$$\Theta_{J,K,M} e^{iK\phi} e^{iM\chi} = N_{J,K,M} \left(\sin \frac{\theta}{2} \right)^{|K-M|} \left(\cos \frac{\theta}{2} \right)^{|K+M|} F \left(\sin^2 \frac{\theta}{2} \right) \quad (3.139)$$

$F(\sin^2 \theta/2)$ being a hypergeometric series and $N_{J,K,M}$ a normalizing factor satisfying the condition:

$$N_{J,K,M}^2 \int \psi_{J\tau M} \psi_{J\tau M}^* d\tau = 1 \quad (3.140)$$

The reduced energies eigenvalue of the reduced hamiltonian (3.136) are $(2J + 1)$ solutions of the secular equation

$$\left| \mathbf{E}(\kappa) - \mathbf{I}\lambda \right| = 0 \quad (3.141)$$

so that the total rotational energy for a particular level is given by

$$E = \frac{1}{2}(A + C)J(J + 1) + \frac{1}{2}(A - C)E_{J\tau}(\kappa) \quad (3.142)$$

The nonvanishing matrix elements of $\mathbf{E}(\kappa)$, i.e., $E_{J\tau}(\kappa)$ (with $\tau = K_{-1} - K_{+1}$) are given by:

$$E_{K,K} = (J, K, M | \mathcal{H}(\kappa) | J, K, M) = F[J(J + 1) - K^2] + GK^2 \quad (3.143a)$$

$$E_{K,K\pm 2} = (J, K, M | \mathcal{H}(\kappa) | J, K \pm 2, M) = H[f(J, K \pm 1)]^{1/2} \quad (3.143b)$$

where

$$f(J, K \pm 1) = \frac{1}{4}[J(J + 1) - K(K \pm 1)][J(J + 1) - (K \pm 1)(K \pm 2)] \quad (3.143c)$$

where

$$E_{K,K} = E_{-K,-K} \quad E_{K,K+2} = E_{K+2,K} = E_{-K,-K-2} = E_{-K-2,-K} \quad (3.143d)$$

where F, G and H are given in Table 3.1.

3.5.5 Molecular thermodynamic properties

The thermodynamic quantities calculated from Gaussian program are, in general linked to spectroscopic properties of the molecules. In fact, calculated quantities, either entropy, energy, heat capacity, etc depend on contributions from *translational*, *electronic*, *rotational* and *vibrational motion* through their **partition components** $q(V, T)$ ^[87].

The partition function contribution to the *entropy*, *internal energy* and *volume constant heat capacity* are^[87],

$$\begin{aligned} S &= R + R \ln(q(V, T)) + RT \left(\frac{\partial \ln q}{\partial T} \right)_V = R \ln \left((q(V, T)e) + RT \left(\frac{\partial \ln q}{\partial T} \right)_V \right) \\ &= R \left(\ln(q_t q_e q_r q_v e) + T \left(\frac{\partial \ln q}{\partial T} \right)_V \right) \end{aligned} \quad (3.144a)$$

$$E = Nk_B T^2 \left(\frac{\partial \ln q}{\partial T} \right)_V \quad (3.144b)$$

$$C_V = \left(\frac{\partial \ln E}{\partial T} \right)_{N,V}, \quad (3.144c)$$

respectively. It is these three equations which are used to derive the final expressions used to calculate the different components of the thermodynamic quantities printed out by *Gaussian*. Considering an ideal gas: $PV = NRT = \left(\frac{n}{N_A} N_A k_B T\right)$ and $V = \frac{k_B T}{P}$, the contributions from:

— *the translational*:

$$q_t = \left(\frac{2\pi m k_B T}{h^2} \right)^{3/2} V = \left(\frac{2\pi m k_B T}{h^2} \right)^{3/2} \frac{k_B T}{P} \quad (3.145)$$

so that

$$S_t = R \left(\ln(q_t e) + T \left(\frac{3}{2T} \right) \right) = R \left(\ln(q_t) + 1 + \frac{3}{2} \right) \quad (3.146)$$

since $(\partial \ln q_t / \partial T)_V = 3/2T$.

$$E_t = Nk_B T^2 \left(\frac{\partial \ln q_t}{\partial T} \right)_V = RT^2 \left(\frac{3}{2T} \right) = \frac{3}{2}RT \quad (3.147)$$

and

$$C_t = \left(\frac{\partial \ln E}{\partial T} \right)_{N,V} = \frac{3}{2}R. \quad (3.148)$$

— *the electronic motion:*

$$q_e = \omega_0 e^{-\epsilon_0/k_B T} + \omega_1 e^{-\epsilon_1/k_B T} + \omega_2 e^{-\epsilon_2/k_B T} + \dots \quad (3.149)$$

where ω is the degeneracy of the energy level and ϵ_n , the energy of the n^{th} level. *Gaussian* assumes that the first electronic excitation energy is much greater than $k_B T$, consequently, the *first and higher excited states* are assumed to be inaccessible at any temperature. Setting the energy of the ground state to zero, the electronic partition function is simply $q_e = \omega_0$,

The entropy due to electronic motion is therefore:

$$S_e = R \left(\ln q_e + T \left(\frac{\partial \ln q_e}{\partial T} \right) \right) = T (\ln q_e + 0) \quad (3.150)$$

As there is no temperature dependent term in this partition function component, both the electronic, the internal thermal energy and heat capacity *due to electronic motion are zero.*

— *the rotational motion:*

This contribution depends on the configuration such: single atoms, linear polyatomic molecules or non-linear polyatomic molecules.

For instance, for single atom, $q_r = 1$ and is independent of the temperature. Consequently, the contributions of rotation to either entropy, the internal energy and heat capacity are zero.

For a nonlinear polyatomic molecule, the rotational partition function is:

$$q_r = \frac{\sqrt{\pi}}{\tau} \left(\frac{T^{3/2}}{(\Theta_{r,x} \Theta_{r,y} \Theta_{r,z})^{1/2}} \right) \quad (3.151)$$

so that:

$$S_r = R \left(\ln(q_r) + T \left(\frac{\partial \ln q_r}{\partial T} \right)_V \right) = R \left(\ln(q_r) + \frac{3}{2} \right) \quad (3.152a)$$

$$E_r = RT^2 \left(\frac{\partial \ln q_r}{\partial T} \right)_V = RT^2 \left(\frac{3}{2T} \right)_V = \frac{3}{2} RT \quad (3.152b)$$

$$C_r = \left(\frac{\partial E_r}{\partial T} \right)_V = \frac{3}{2} R \quad (3.152c)$$

According to these equations, the average contribution to the internal thermal energy from each rotational degree of freedom is $RT/2$, while its contribution to C_r is $R/2$.

— *the vibrational motion:*

The contributions from vibrational motions to the partition function, entropy, internal energy and constant volume heat capacity are composed of a sum (or product) of the contributions from each vibrational mode, say, M . Therefore, each of the $3N - 6$ (or $3N - 5$ for linear molecules) modes has its characteristic vibrational temperature: $\Theta_{v,M} = h\nu_M/k_B$. There are two ways of choosing the *zero of energy*, and, consequently, two ways of calculating the partition function: either *the bottom of the internuclear potential energy well*, or *the first vibrational level*. *Gaussian* use the first way. In this case, the contribution to the partition function from a given vibrational mode is:

$$q_{v,M} = \frac{e^{-\Theta_{v,M}/2T}}{1 - e^{-\Theta_{v,M}/T}} \quad (3.153)$$

so that the overall vibrational partition function becomes:

$$q_v = \prod_M = \frac{e^{-\Theta_{v,M}/2T}}{1 - e^{-\Theta_{v,M}/T}} \quad (3.154)$$

The total vibrational contributions to internal energy, entropy and volume constant heat capacity are therefore:

$$\begin{aligned} S_v &= R \left(\ln(q_v) + T \left(\frac{\partial q_v}{\partial T} \right)_v \right) \\ &= R \sum_M \left(\frac{\Theta_{v,M}/T}{e^{\Theta_{v,M}/T} - 1} - \ln(1 - e^{-\Theta_{v,M}/T}) \right) \end{aligned} \quad (3.155a)$$

$$E_v = RT^2 \left(\frac{\partial \ln q_v}{\partial T} \right)_v = R \sum_M \Theta_{v,M} \left(\frac{1}{2} + \frac{1}{e^{\Theta_{v,M}/T} - 1} \right) \quad (3.155b)$$

For then a nonlinear molecule, the Zero-point corrected energy can be approximated by:

$$E(T) = E_r(T) + E_t(T) + \text{ZPE} + E_v + E_e \quad (3.156)$$

According to the relations (3.152b and (3.147), both E_r and E_t equal to $\frac{3}{2}R$. E_v can usually be neglected compared to the Zero-point energy (ZPE), and $E_e = 0$.

Considering then the reaction of protonation:



the proton affinity is defined as the negative of the reaction enthalpy at 298.15K

$$\begin{aligned} P(A) &= -\Delta_r H = \Delta H + RT \\ &= - \left[\left(\sum H_{\text{elc}}(\text{products}) - \sum H_{\text{elc}}(\text{reactants}) \right) + (\text{ZPE}(\text{products}) - \text{ZPE}(\text{reactants})) \right] + RT \end{aligned} \quad (3.158)$$

Calculating the energy change in going from the *reactants* (A^- and H^+) to *products* (AH), E_r remains constant since the proton does not possess rotational kinetic energy and the translational energy of the proton contributes with $-\frac{3}{2}RT$ so that:

$$P(A) = -\Delta H_{\text{elc}} - \Delta \text{ZPE} + \frac{5}{2}RT \quad (3.159)$$

with

$$\Delta H_{\text{elc}} = \Delta H_{\text{elc}}(AH) - \Delta H_{\text{elc}}(A^-) \quad (3.160)$$

3.6 References

- [1] B. T. Sutcliffe and R. G. Woolley. *PCCP*, 7(21):3664–3676, 2005.
- [2] B. T. Sutcliffe and R. G. Woolley. *TJ. Chem. Phys*, 137(22):22A544, 2012.
- [3] T. Jecko. *J. Math. Phys.*, 55(5):053504, 2014.
- [4] M. Born and R. Oppenheimer. *Annalen der physik*, 389(20):457–484, 1927.
- [5] I. N. Levine et al. *Molecular spectroscopy*. Wiley, 1975.
- [6] C. A. Ballhausen and H. B. Gray. *Molecular orbital theory: an introductory lecture note and reprint volume*. WA Benjamin, Inc., 1965.

- [7] H. Förster. Uv/vis spectroscopy. In *Characterization I*, pages 337–426. Springer, 2004.
- [8] C. D. Sherrill. *School of Chemistry and Biochemistry Georgia Institute of Technology*, 2000.
- [9] J. Kohanoff. *Electronic structure calculations for solids and molecules: theory and computational methods*. Cambridge University Press, 2006.
- [10] D. C. Young et al. *WileyInterscience New York*, 2001.
- [11] C. L. Benavides-Riveros, N. N. Lathiotakis, and M. A. Marques. *PCCP*, 19(20):12655–12664, 2017.
- [12] D. Ghosh. *ecommons Cornell University*, 2010.
- [13] T. Helgaker, P. Jorgensen, and J. Olsen. *Molecular electronic-structure theory*. John Wiley & Sons, 2014.
- [14] C. Møller and M. S. Plesset. *Phys. Rev.*, 46(7):618, 1934.
- [15] I. Y. Zhang and A. Grüneis. *Front. Mater.*, 6:123, 2019.
- [16] R. J. Bartlett. *Annu. Rev. Phys. Chem.*, 32(1):359–401, 1981.
- [17] R. J. Bartlett. *J. Phys. Chem. A*, 93(5):1697–1708, 1989.
- [18] R. J. Bartlett and M. Musiał. *J Rev. Mod. Phys.*, 79(1):291, 2007.
- [19] K. Kowalski and P. Piecuch. *J. Chem. Phys.*, 113(1):18–35, 2000.
- [20] R. O. Jones and O. Gunnarsson. *J Rev. Mod. Phys.*, 61(3):689, 1989.
- [21] E. Lewars. *Introduction to the theory and applications of molecular and quantum mechanics*, page 318, 2003.
- [22] D. Sholl and J. A. Steckel. *Density functional theory: a practical introduction*. John Wiley & Sons, 2011.
- [23] P. Hohenberg and W. Kohn. *Phys. Rev.*, 136(3B):B864, 1964.
- [24] W. Koch and M. C. Holthausen. *A chemist’s guide to density functional theory*. John Wiley & Sons, 2015.
- [25] J. Toulouse. *Sorbonne Université and CNRS*, 2019.
- [26] W. Kohn and L. J. Sham. *Phys. Rev.*, 140(4A):A1133, 1965.
- [27] J. P. Perdew, M. Ernzerhof, and K. Burke. *J. Chem. Phys.*, 105(22):9982–9985, 1996.
- [28] A. Görling and M. Levy. *J. Chem. Phys.*, 106(7):2675–2680, 1997.
- [29] A. D. Becke. *J. Chem. Phys.*, 98(2):1372–1377, 1993.
- [30] R. Colle and O. Salvetti. *J. Chem. Phys.*, 79(3):1404–1407, 1983.
- [31] R. Colle and O. Salvetti. *J. Chem. Phys.*, 93(1):534–544, 1990.
- [32] M. Weinert, E. Wimmer, and A. J. Freeman. *Physical Review B*, 26(8):4571, 1982.
- [33] C. Hu, O. Sugino, and Y. Tateyama. *J. Chem. Phys.*, 131(11):114101, 2009.
- [34] V. Milman, B. Winkler, J. White, C. Pickard, M. Payne, E. Akhmatkaya, and R. Nobes. *Int. J. Quantum Chem.*, 77(5):895–910, 2000.
- [35] A. Soon, T. Söhnel, and H. Idriss. *Surf. Sci.*, 579(2-3):131–140, 2005.
- [36] J. Tan, Y. Li, and G. Ji. *Computational materials science*, 58:243–247, 2012.
- [37] C. Stampfl and C. Van de Walle. *Physical Review B*, 59(8):5521, 1999.
- [38] A. D. Becke. *J. Chem. Phys.*, 98(492):5648–5652, 1993.
- [39] S. Grimme and F. Neese. *J. Chem. Phys.*, 127(15):154116, 2007.
- [40] J. A. Pople, M. Head-Gordon, D. J. Fox, K. Raghavachari, and L. A. Curtiss. *J. Chem. Phys.*, 90(10):5622–5629, 1989.
- [41] L. A. Curtiss, C. Jones, G. W. Trucks, K. Raghavachari, and J. A. Pople. *J. Chem. Phys.*, 93(4):2537–2545, 1990.
- [42] L. A. Curtiss, K. Raghavachari, G. W. Trucks, and J. A. Pople. *J. Chem. Phys.*, 94(11):7221–7230, 1991.
- [43] L. A. Curtiss, K. Raghavachari, P. C. Redfern, V. Rassolov, and J. A. Pople. *J. Chem. Phys.*, 109(18):7764–7776, 1998.

- [44] L. A. Curtiss, P. C. Redfern, and K. Raghavachari. *J. Chem. Phys.*, 127(12):124105, 2007.
- [45] L. A. Curtiss, P. C. Redfern, and K. Raghavachari. *Wiley Interdiscip. Rev. Comput. Mol. Sci.*, 1(5):810–825, 2011.
- [46] L. Curtis, K. Raghavachari, and J. Pople. *J. Chem. Phys.*, 98:1293–1298, 1993.
- [47] L. A. Curtiss, P. C. Redfern, K. Raghavachari, V. Rassolov, and J. A. Pople. *J. Chem. Phys.*, 110(10):4703–4709, 1999.
- [48] A. G. Baboul, L. A. Curtiss, P. C. Redfern, and K. Raghavachari. *J. Chem. Phys.*, 110(16):7650–7657, 1999.
- [49] M. R. Nyden and G. Petersson. *J. Chem. Phys.*, 75(4):1843–1862, 1981.
- [50] a. Petersson, A. Bennett, T. G. Tensfeldt, M. A. Al-Laham, W. A. Shirley, and J. Mantzaris. *J. Chem. Phys.*, 89(4):2193–2218, 1988.
- [51] G. Petersson, T. G. Tensfeldt, and J. Montgomery Jr. *J. Chem. Phys.*, 94(9):6091–6101, 1991.
- [52] J. Montgomery Jr, J. Ochterski, and G. Petersson. *J. Chem. Phys.*, 101(7):5900–5909, 1994.
- [53] J. W. Ochterski, G. A. Petersson, and J. A. Montgomery Jr. *J. Chem. Phys.*, 104(7):2598–2619, 1996.
- [54] J. A. Montgomery Jr, M. J. Frisch, J. W. Ochterski, and G. A. Petersson. *J. Chem. Phys.*, 110(6):2822–2827, 1999.
- [55] J. A. Montgomery Jr, M. J. Frisch, J. W. Ochterski, and G. A. Petersson. *J. Chem. Phys.*, 112(15):6532–6542, 2000.
- [56] G. A. Petersson. Complete basis set models for chemical reactivity: from the helium atom to enzyme kinetics. In *Quantum-mechanical prediction of thermochemical data*, pages 99–130. Springer, 2001.
- [57] C. D. Sherrill. *School of Chemistry and Biochemistry, Georgia Institute of Technology*, 2017.
- [58] B. Nagy and F. Jensen. *Rev. Comput. Chem.*, 30:93–149, 2017.
- [59] C. Skylaris. *Univ. Southampton*, 1989.
- [60] J. VandeVondele and J. Hutter. *J. Chem. Phys.*, 127(11):114105, 2007.
- [61] E. R. Davidson and D. Feller. *Chem. Rev.*, 86(4):681–696, 1986.
- [62] R. Ditchfield, W. J. Hehre, and J. A. Pople. *J. Chem. Phys.*, 54(2):724–728, 1971.
- [63] W. Hehre, W. Lathan, R. Ditchfield, M. Newton, and J. Pople. *Quantum Chemistry Program Exchange*, 236, 1970.
- [64] J. Pople and D. Smith. Theoretical models for chemistry. In *Energy, Structure and Reactivity: Proceedings of the 1972 Boulder Summer Research Conference on Theoretical Chemistry*, pages 51–61. Wiley New York, 1973.
- [65] A. Tomberg. *An introduction to computational chemistry using G09W and Avogadro software*, pages 1–36, 2013.
- [66] D. C. Harris and M. D. Bertolucci. *Symmetry and spectroscopy: an introduction to vibrational and electronic spectroscopy*. Courier Corporation, 1989.
- [67] G. Herzberg. *Electronic spectra and electronic structure of polyatomic molecules*, volume 2. Krieger Publishing Company, 1991.
- [68] F. Siebert and P. Hildebrandt. *Vibrational Spectroscopy in Life Science*, pages 11–61, 2008.
- [69] P. Larkin. *Infrared and Raman spectroscopy: principles and spectral interpretation*. Elsevier, 2017.
- [70] D. Lin-Vien, N. B. Colthup, W. G. Fateley, and J. G. Grasselli. *The handbook of infrared and Raman characteristic frequencies of organic molecules*. Elsevier, 1991.

- [71] D. W. Mayo, F. A. Miller, and R. W. Hannah. *Course notes on the interpretation of infrared and Raman spectra*. John Wiley & Sons, 2004.
- [72] E. F. Van Dishoeck. *ARA&A*, 42, 2004.
- [73] J. Dunham. *Phys. Rev.*, 41(6):721, 1932.
- [74] C. H. Townes and A. L. Schawlow. *Microwave spectroscopy*. Courier Corporation, 2013.
- [75] P. F. Bernath. *Spectra of atoms and molecules*. Oxford university press, 2020.
- [76] M. Strekalov. *Chem. Phys. Lett.*, 439(1-3):209–212, 2007.
- [77] J. Chalmers and P. Griffiths. *Handbook of Vibrational Spectroscopy, 5 volumes set*. Wiley, 2002.
- [78] V. Gupta. *Principles and applications of quantum chemistry*. Academic Press, 2015.
- [79] B. Stuart. *Kirk-Othmer encyclopedia of chemical technology*, 2000.
- [80] S. Candefjord. *Combining a resonance and a Raman sensor: towards a new method for localizing prostate tumors in vivo*. Luleå tekniska universitet, 2007.
- [81] P. W. Atkins and R. S. Friedman. *Molecular quantum mechanics*. Oxford university press, 2011.
- [82] K. Parivathini, K. Settu, and A. Claude. 2017.
- [83] P. M. Wojciechowski and D. Michalska. *SAA*, 68(3):948–955, 2007.
- [84] S. Yamamoto. *Introduction to Astrochemistry: Chemical Evolution from Interstellar Clouds to Star and Planet Formation*. Springer, 2017.
- [85] W. Gordy, R. L. Cook, et al. *Microwave molecular spectra*. Wiley, 1984.
- [86] G. W. King, R. Hainer, and P. C. Cross. *J. Chem. Phys.*, 11(1):27–42, 1943.
- [87] J. W. Ochterski. *Gaussian Inc*, 1:19, 2000.

MOLECULAR STRUCTURE, IR, RAMAN AND UV-VIS SPECTRA OF 2-CYANO- THIOPHENE AND 3-CYANOTHIOPHENE

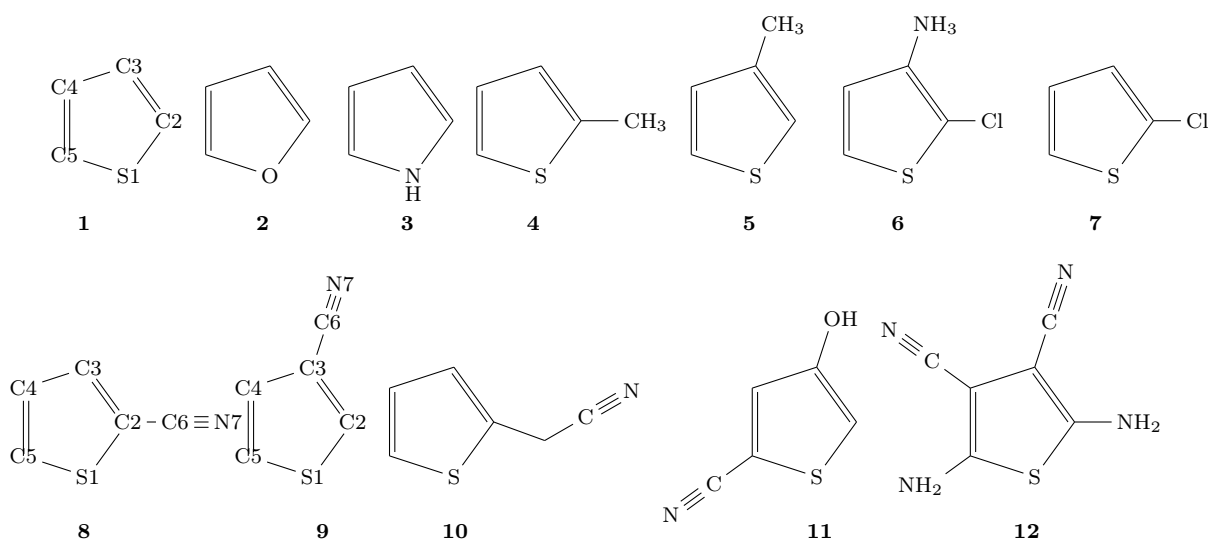
4.1 Introduction

In astrochemistry, along with often partial experimental data, theoretical predictions are of paramount importance in the characterization of molecular properties involving high resolution data for new compounds. In fact, the advances of new observatories such as the Atacama Large Millimeter/ Submillimeter Array (ALMA)^[1] and Stratospheric Observatory for Infrared Astronomy (SOFIA)^[2] need both reliable theoretical and experimental data in the search of new molecular species in space. From the first report of the presence of molecules in space, i.e., in 1940^[3] up to now, more than 230 organic and inorganic molecular species have been found in the planetary atmospheres, in comets and in the interstellar medium (ISM) of galaxies^[4-6]. Most of them were detected by dint of their microwave emissions (e.g., CN^[7], CF^[8], CNSi^[9], HSCN^[10], C₂HNO^[11], C₆H₃N^[12], ...), by means of their infrared emissions (e.g., CH₃^[13], C₂H₄ and C₄H₂^[14],...), but also on the basis of the UV emission (e.g., C₂^[15], N₂^[16], ...). Of the molecular species found in the ISM environment, a large number contains the cyano group R-C≡N^[17-19].

A search for simple aromatic molecules that are believed to give rise to a common emission feature commonly referred to as the unidentified infrared (UIR), including several polycyclic aromatic nitrogen heterocycles and nitriles, has recently been conducted by McGuire and coworkers^[20]. Their investigation has resulted in the detection of benzonitrile (c - C₆H₅CN) on the basis of its rotational transitions in the cold core Taurus Molecular Cloud 1 (TMC-1), which has long been known to display a rich chemistry dominated by unsaturated carbon-chain molecules such as the cyanopolyynes (HC_nN with, n = odd number)^[20,21]. Before the detection of this molecule, the only six-membered aromatic molecule whose interstellar detection had been well established is benzene (C₆H₆)^[22,23]. Regarding the five-membered cycle such as thiophene, the analysis of insoluble organic matter (IOM) and hydrothermally treated IOM extracted from two carbonaceous chondrites such as Murchison and Allende, revealed a non-negligible proportion of thiophene in those materials^[24]. Moreover, through the investigation of isotopic abundance in IOM, it has been argued that the D and ¹⁵N isotope excess observed in it indicates that it has an ISM origin^[25-27]. Likewise, many other theories about IOM formation and its probable origin have been proposed, but both converged to its ISM origin^[24-28]. Thiophene, its methyl substituted derivatives (2- and 3-methylthiophene) and many other sulfur-bearing compounds are among organic compounds recently observed in 3-billion-year-old mudstones at Gale crater on Mars^[29]. However, none among thiophene and its substituted derivative was reported yet by astrochemists or astrophysicists in the ISM. In this context, the recent detection of benzonitrile opens a new avenue for the search of five-and/or six-membered aromatic rings, including

thiophene and its substituted derivatives. For their detection, both relevant experimental and theoretical data are needed.

In recent years, thiophene derivatives have attracted much attention of researchers due to their various chemical and physical properties allowing a great range of applications, either acting as anticancer and anti-tumor agents^[30–33], as conducting^[34], electronic and optoelectronic materials^[35–38], etc. Particularly, nitrile substituted thiophenes have shown very potent in vitro and in vivo anthelmintic activities against *Haemonchus contortus*^[39]. They have also shown very high qualities for light emitting diodes (LEDs) due to the cyano group which increases the photoluminescence (PL) and electroluminescence (EL)^[40,41]. Moreover, the thermochemistry of substituted thiophene-carbonitrile derivatives has been explored^[42]. A survey of the available literature shows however a few studies con-



Scheme 4.1 – Chemical structures of **1** (thiophene), **2** (furan), **3** (pyrrole), **4** (2-methylthiophene), **5** (3-methylthiophene), **6** (2-chloro-3-nitrothiophene), **7** (2-chloro-thiophene), **8** (2-cyanothiophene [2CNT]), **9** (3-cyanothiophene [3CNT]), **10** (2-(5-bromothiophen-2-yl)acetonitrile), **11** (5-Cyano-3-hydroxythiophene) and **12** (2,5-diaminothiophene-3,4-dicarbonitrile)

ducted on 2-cyanothiophene and 3-cyanothiophene (**CNT**, cf. Scheme 4.1: compounds **8** and **9**), especially about their structural and spectroscopic properties. Cataliotti et al.^[43] conducted a FT-IR and FT-Raman investigation on **8** in both the solid and liquid states. In this chapter, a frequency assignment was performed, but no potential energy distribution (PED) was attempted in order to emphasize the contribution of each fundamental frequency at a particular band position. Aleksanyan et al.^[44] experimentally analyzed the IR spectra for both **8** and **9** to explore the effects of the nature and position of the CN substituent on the vibrational spectra. Apart from that the number of fundamental frequencies observed was limited, no frequency assignment was carried out. Microwave spectra were reported for **8**^[45], **9**^[46], ³⁴S– and ¹⁵N-3CNT^[47]. The number of rotational lines observed and assigned experimentally, that of hyperfine quadrupole splittings found are also limited. While Boig et al.^[48] have studied the UV-VIS spectrum of **8**, no UV-VIS spectrum of **9** is known. Furthermore, experimental geometric parameters are also lacking in the literature. Previous attempts about their structures (compounds **8**^[45] and **9**^[46]) proposed more than two sets of parameters for each compound. To the best of our knowledge, only one theoretical study was reported so far on CNT. Solc and co-workers^[49] in their theoretical work on the structure, electronic properties and the photophysics of some substituted thiophenes investigated

the influence of the substitution of H by CN groups at different sites of a thiophene and terthiophene rings. Concerning structures, they conclude that, considering thiophene and terthiophene, there is bond contraction for the α substitution and bond elongation in case of β substitution. Regarding excitation energy, these authors found that a CN group located in the α -position causes a larger bathochromic shift than a CN group in the β . Apart from the works stated above, no study on vibrational or rotational spectra is reported yet.

In this context, the main purpose in this chapter is the computation of IR, Raman and UV-VIS spectra for cyanothiophenes (expected to be detected in ISM) in attempt to supplement the incomplete spectroscopic data from the literature. Another purpose is establishment of correction schemes in order to make reliable predicted properties. To achieve these goals, accurate geometrical parameters are proposed, while fundamental vibrational frequencies for both 2CNT and 3CNT and their deuterated species are predicted and assigned on basis of the PED. In addition, the UV-VIS spectra of these molecules are also investigated. We provide with a consistent set of spectroscopic data which are expected to be valuable in the search of new species in the ISM, and also in other experimental studies.

4.2 Computational details

Geometrical parameters for different molecular properties calculations are determined using the method described in a previous work^[50] and references therein. Following this method, geometries are first fully optimized using the analytical gradient procedures applying different methods including the Hartree-Fock (HF), second order Møller-Plesset perturbation-theory (MP2)^[51], Becke’s three parameter hybrid exchange functional^[52] with a correlation functional proposed by Lee, Yang and Parr^[53] (B3LYP) and highly parameterized empirical exchange correlation function (M06-2X)^[54] and numerical-gradient method at the third-order perturbation (MP3) level, implemented in Gaussian 09 package^[55]. One-electron basis sets including the 6-31G(d), 6-31G(d,p), 6-311G(d,p), 6-31+G(d), 6-31+G(d,p) and 6-311++G(d,p) are employed. Rotational constants computed at different levels of theory are compared with available experimental results in order to calibrate the computed results and thereby to select a good level of theory. The M06-2X/6-31G(d,p) method appears to show the best results compared to the others.

In order to obtain an improved and reliable set of geometrical parameters, the method is firstly applied on **1** whose experimental geometrical data are available in the literature. It is thereafter applied on its substituted nitrile derivatives (compounds **8** and **9**). Geometrical parameters are obtained from computational levels mentioned above, in conjunction with empirical corrections for systematic errors on the computed values of bond distances and angles. The empirical correction for each geometrical parameter at each level of theory is determined from the values calculated for similar compounds whose experimental data are well established. Thereafter, the best predicted geometries are obtained after an empirical adjustment based on the variations of rotational constants with respect to the bond lengths variations following the procedure reported in the above mentioned work^[50].

Fundamental vibrational frequencies are computed using density functional theory with the M06-2X functional and the 6-31G(d,p) basis set. The lack of imaginary frequency in calculated wavenumbers indicates that their geometries correspond to energy minima. However, fundamental harmonic frequencies computed by popular quantum chemistry models often deviate from the corresponding experimental ones due to the use of finite basis sets, these models neglect the anharmonicity effects and incomplete incorporation of electron correlation^[56]. This is also due to the neglect of relativistic effects and non-Born-Oppenheimer behavior. In order to obtain improved fundamental vibrational frequencies, a correction

scheme which makes use of experimental data of similar molecules is used as described in earlier papers^[50]. However, because experimental data for fundamental frequencies for similar molecular species are not sufficient in the literature, we use another scaling method. It has been demonstrated that the use of scaled quantum mechanics force field (SQMFF) method in scaling down the fundamental frequencies calculated at DFT functional leads to better results^[57,58]. We therefore tested this method and its results agree well with experiment, when available. The M06-2X/6-31G(d,p) calculated wavenumbers from the best computed geometries are corrected for systematic calculation errors using the SQMFF. By this method, force constants, in cartesian force constant matrix, generated by Gaussian 09 package are scaled down using multiple selective scaling factors in order to produce the experimental frequencies. In the present work, this task is achieved using the MOLVIB program 8.0^[59,60]. Internal force constants f_{ij} are then transformed according to the relation^[57,61]: $f'_{ij} = \sqrt{S_i S_j} f_{ij}$, where, S_i and S_j denote the scaling factors. Owing to the fact that **9** does not have enough experimental data for this end and that **8** and **9** are isomers, the relationship between the experimental and calculated frequency for **8** at the used level of theory and for a particular mode of vibration holds also for **9**. That is valid for the ratio $\nu_{\text{exp}}^i / \nu_{\text{cal}}^i$, where the superscript i denotes the vibration mode, ν_{exp}^i and ν_{cal}^i the experimental and calculated frequencies of vibrational modes, respectively. For similar modes, the above ratio for **8** is expected to be the same for **9**. This is ensured by the transferability of scaling factors between similar molecules introduced by Pulay^[57,61]. This allows us to derive the near-experimental vibrational wavenumbers used for **9**. Thereafter, calculated vibrational frequencies are scaled down to (re)produce experimental results. In parallel, during the scaling process using MOLVIB, the potential energy distribution (PED) for the different modes of vibration are also computed.

4.3 Results and discussion

4.3.1 Molecular geometry

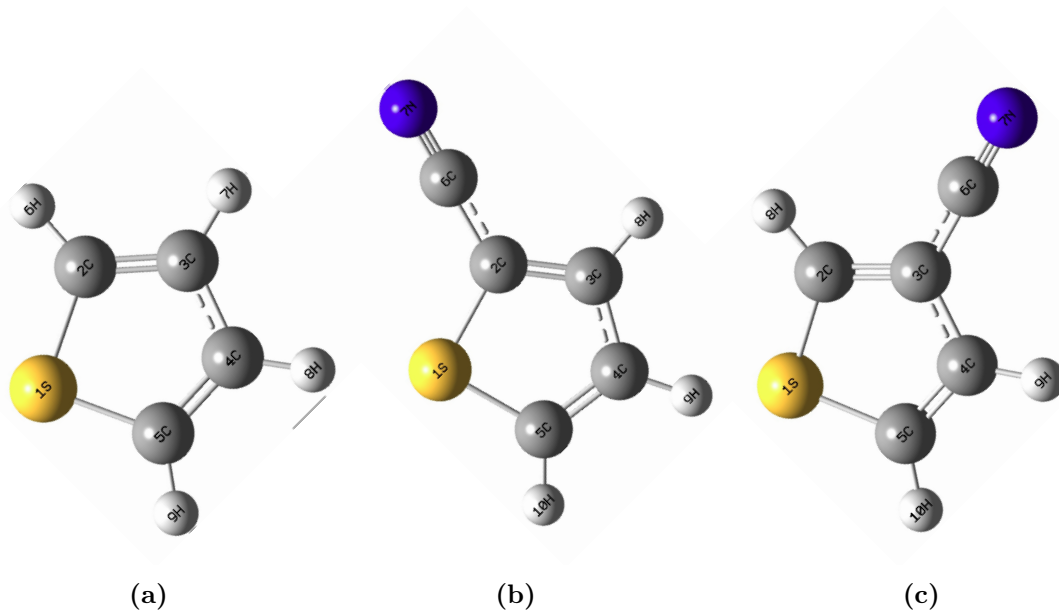


Figure 4.1 – M06-2X/6-31G(d,p) optimized geometries for (a) thiophene, (b) 2CNT and (c) 3CNT; yellow: S, gray=C, blue=N and light gray=H

Geometrical parameters and rotational constants of **1** calculated at ten levels are

given in Table A.1. The differences between the experimental results and those given in Table A.1 with standard deviations for geometrical parameters are given in Table A.2. Likewise, geometrical parameters and rotational constants of **8** and **9** calculated at the same levels as for **1** are given in Table A.3 and Table A.4, respectively. From Table A.2, the variations in geometrical parameters at the different levels, as calculated with various basis sets, are relatively small. Larger standard deviations are observed in cases of HF and B3LYP, the largest one being that of 0.015 Å for HF/6-31G(d). Significant deviations are observed, in particular, for SC and CC bond lengths. For instance, the SC bond length is significantly overestimated by HF, MP3 and B3LYP; the largest variations with respect to the experimental value being observed at the B3LYP functional ($\Delta\text{SC} = 0.022$ Å). It is important to note that all methods overestimate the SC bond length; a minor variation being observed in case of MP2/6-31G(d,p) ($\Delta\text{SC} = 0.003$ Å). In contrast, all levels underestimate the C=C bond length (except for MP2), but also the C-C bond length (except for HF and MP3). For instance, the values $\text{Calc} - \text{Exp} < 0$ for all methods, but those associated to MP2 for C=C. The variations of C-H bond lengths are small; they are relatively large at HF level ($\Delta\text{CH} = 0.007$ Å). In general, bond angle variations are small, but they differ also from level to level. Comparison of standard deviations indicates that the HF and B3LYP show larger standard deviations ($\sigma = 0.015$ Å at HF and $\sigma = 0.011$ Å at B3LYP). Conversely, the MP3/6-311G(d,p) level ($\sigma = 0.005$ Å) gives good geometrical parameters followed by the MP2 and M06-2X methods for different basis sets used ($\sigma = 0.006$ Å). These results agree well with our expectation for that the MP3, being superior than MP2, it is expected to yield more accurate geometrical parameters than the latter.

Regarding rotational constants, very large deviations with respect to experimental values are observed for all levels considered, with smaller deviations for the M06-2X, especially, with the 6-31G(d,p) basis set (cf Table A.2). Indeed, the comparison between levels of theory with low standard deviations in geometrical parameters such as MP2/6-31G(d,p), MP3/6-311G(d) and M06-2X/6-31G(d,p) for **1** is done: $|\Delta A|(\text{MP3}) = 14.32$ MHz, $|\Delta A|(\text{MP2}) = 37.28$ MHz, $|\Delta A|(\text{M06} - 2\text{X}) = 0.93$ MHz; $|\Delta B|(\text{MP3}) = 49.67$ MHz, $|\Delta B|(\text{MP2}) = 29.81$ MHz and $|\Delta B|(\text{M06} - 2\text{X}) = 8.05$ MHz; $|\Delta C|(\text{MP3}) = 18.75$ MHz, $|\Delta C|(\text{MP2}) = 3.33$ MHz and $|\Delta C|(\text{M06} - 2\text{X}) = 1.68$ MHz. These deviations show that although MP3/6-311G(d) gives good geometrical parameters ($\sigma = 0.005$ Å), its rotational constants have larger deviation with respect to experiment, especially for B (49.67 MHz smaller than the experimental value). By these deviations, the M06-2X functional reproduces fairly good A constant (0.93 MHz smaller than the experimental results). It also reproduces also good results for both B and C constants, the larger deviation being observed for B (8.05 MHz larger than experiment). Overall, the M06-2X/6-31G(d,p) level gives the best results. Consequently, geometrical and rotational parameters calculated at this level are taken as references.

In order to identify the factors responsible for the discrepancies observed between theoretical and experimental rotational constants, the sensitivities of the rotational constants of thiophene with respect to changes in geometrical parameters are analysed. The results presented in Table A.5 show that the A constant is markedly sensitive to variations of both S-C, C=C and C-C bond lengths and S-C=C, C=C-C bond angles, with a relatively low sensitivity to the C-H bond length variation. The B constant is also considerably sensitive to the S-C and C=C bond length and S-C=C bond angle variations. The C-C variation does not affect it much as it does for the A constant. We note that the variation of the C-H bond length in α -position does not at all affect the value of B, whereas that in β -position dimly affects. Likewise, the behaviour of the C constant is similar to that of B, except that the sensitivity to bond length variations is relatively lower as compared to that in B, and

Table 4.1 – Experimental and achieved geometries for **1**, **8** and **9** after empirical adjustments to some geometrical parameters (distances in Å^o, angles in °).

Compound	1 ^{a,b}			8 ^b	9 ^b
	Exp	Calc	Calc-Exp		
Bond lengths					
S1 - C2	1.7140	1.7186	0.0046	1.7247	1.7135
S1 - C5	1.7140	1.7186	0.0046	1.7096	1.7266
C2 - C3	1.3696	1.3702	0.0006	1.3715	1.3684
C3 - C4	1.4232	1.4235	0.0003	1.4130	1.4279
C4 - C5	1.3696	1.3702	0.0006	1.3715	1.3578
C2/C3 - C6	-	-	-	1.4270	1.4315
C6 - N7	-	-	-	1.1560	1.1550
C2/C3 - H6/H8	1.0776	1.0780	0.0004	1.0825	-
C3/C2 - H7/H8	1.0805	1.0821	0.0016	-	1.0802
C4 - H8/H9	1.0805	1.081	0.0016	1.0825	1.0819
C5 - H9/H10	1.0776	1.0780	0.0004	1.0780	1.0802
Bond Angles					
S1 - C2 - C3	111.47	111.39	-0.08	112.32	111.47
S1 - C5 - C4	111.47	111.39	-0.08	111.88	112.09
C2 - S1 - C5	92.17	92.11	-0.06	91.20	91.63
C2 - C3 - C4	112.45	112.56	0.11	112.35	112.80
C3 - C4 - C5	112.45	112.56	0.11	112.25	111.80
C2/C3 - C6 - N7	-	-	-	179.74	179.84
S1-C2-H6/H8	119.85	120.23	0.38	-	121.19
C4-C3-H7/H8	124.27	124.20	-0.07	122.66	-
C4-C3-C6	-	-	-	-	123.6
C3-C2-C6	-	-	-	126.9	-
C3-C4-H8/H9	124.27	124.20	-0.07	124.23	124.47
S1 -C5-H9/H10	119.85	120.28	0.43	119.80	121.19

^a From Ref. [62]

^b The numbering scheme used is that of Figure 4.1.

that it is sensitive to C–H bond length variations.

Thereby, an improved computed molecular structure for **1** is obtained using an empirical correction scheme described in work by Riggs et al. [50]. Average corrections for each of the bond lengths and bond angles are obtained from similar molecular compounds with experimental data as shown in Table A.6, that include **2** [63], **3** [64], **4** [65], **5** [66], **6** [67] and **7** [68]. These corrections are then used to derive predictions of corresponding parameters for **1**. Comparison between obtained parameters (Table A.6) with existing values in the literature shows the following: the value found for C=C and C-C, i.e., 1.372 and 1.421 Å, respectively, are exactly the values found by a combined use of electron diffraction, vibrational spectroscopy, microwave spectroscopy and DFT (referred hereafter as EDVM) [69]. The value of C=C is also closer to that found by a microwave study [62] (MW) with a difference of +0.002 Å, but that of C-C is smaller than the MW one ($\Delta C3C4 = -0.001$ Å). Calculated values for C-H bond lengths are slightly smaller than those found by EDVM (difference of -0.002 Å for C2-H6 and 0.003 Å for C3-H7). They are lightly a bit larger than those found by MW ($\Delta C2H6 = 0.005$ Å, $\Delta C3H7 = 0.004$ Å). Likewise, the S-C value is also closer but smaller than the MW result ($\Delta SC = 0.001$ Å). The C=C-C and C-C-H bond angles are also closer to their values from MW study (difference of 0.6° and 0.0°, respectively).

The final best predicted parameters (in Table 4.1) are obtained after an empirical adjustment based on the variations of rotational constants with respect to bond length and bond angle variations as presented in Table A.5. These final results turn out to be in very good agreement with MW results (RMS = 0.0023 Å for bond lengths and $\approx 0.2^\circ$ for bond angles). The rotational constants as well as the dipole moment values (Table 4.2) are also in good agreement with experiment.

Table 4.2 – Experimental *vs* calculated rotational constants (with empirical corrections), and dipole moments (M06-2X/6-31G(d,p)).

	compound 1		compound 8		compound 9	
	Exp. ^a	Calc	Exp. ^b	Calc	Exp. ^c	Calc
A (MHz)	8041.770	8041.456	5402.387	5402.443	7115.180	7115.536
B (MHz)	5418.120	5417.404	1816.253	1816.251	1491.299	1491.039
C (MHz)	3235.770	3236.812	1358.614	1359.274	1232.535	1232.725
μ_a (Debye)		0.5707	4.470	4.575	4.090	4.011
μ_b (Debye)		0.000	0.736	-0.792	0.560	-0.587
μ_c (Debye)		0.0000	0.000	0.000	0.000	0.000
μ_{tot} (Debye)	0.55 ^d (0.53 ^e)	0.5707	4.53	4.643	4.13	4.053

^a From Ref. [70], ^b From Ref. [71], ^c From Ref. [46],

^d From Ref. [66], ^e From Ref. [72].

The agreement between these final results and the experiment is emphasized by the agreement between calculated and experimental results for other properties such as IR as shown in Table A.7.

The same approach is subsequently applied on compounds **8** and **9**. Variations of rotational constants with respect to variations of geometrical parameters are given in Table A.5 for both these compounds. As shown in Table A.8 and Table A.9 for **8** and **9**, respectively, the corrections determined for their parent **1** are maintained for the ring and C-H bond lengths. For the remaining bond lengths and angles (C-C6 and C \equiv N bond lengths and bond angles containing these bond lengths), three additional species are used in finding the corrections, namely **10**^[73], **11**^[74] and **12**^[75]. Likewise, empirical adjustments based on the variations of rotational constants with respect to bond lengths and angles variations presented in Table A.5 lead to calculated geometrical structures presented in Table 4.1 and rotational constants and dipole moments given in Table 4.2. As for **1**, geometrical parameters computed by this method for **8** and **9** (Table 4.1) should be in good agreement with experiment ones if th latter exists.

Unlike the behaviour observed in **1** regarding the variation of rotational constants with respect to the variation of geometrical parameters, only the A constant is found to be highly sensitive to S-C and C=C bond lengths (Table A.5) for both compound **8** and **9**. Overall, from Table 4.1 and Table 4.2, there is an agreement between available experimental and calculated results for all quantities related to compounds **1**. Calculated geometrical structures for both cyanothiophene compounds **8** and **9** are, consequently, expected to be accurate and reliable.

Table A.11 presents the deviations of calculated results including empirical corrections (in Table 4.1 for geometrical parameters and Table 4.2 for rotational constants) from original quantum chemical ones (cfr Table A.1 for **1**, Table A.3 for **8** and Table A.4 for **9**). This Table shows that changes in geometrical parameters due to the correction process are low for **1**, **8** and **9** in general, but particularly low for **9**. The largest variation in geometrical parameters for **9** is 0.0026 Å, i.e., a elongation of 0.0026 Å for S1C5 and a contraction of 0.0026 Å for C2=C3. The largest bond length variations for **1** and **8** are elongation of 0.0072 Å for C2=C3 and C4=C5 in case of **8**; elongation of 0.0073 Å in case of **1**. Regarding bond angle variations, the larger variation is observed for the compound **8**, i.e., 0.62° for S1C5C4. The larger variation for **1** and **9** is $\approx 0.40^\circ$ (an increase $\Delta\text{CSC} = 0.41^\circ$ and a decrease $\Delta\text{CSC} = -0.37^\circ$ for **1** and **9**, respectively). Nevertheless, from Table A.9, it is clear that empirical corrections have produced remarkable improvement of rotational constants. The larger variation is a decrease $\Delta A = -18.01$ MHz for **8** followed by a n

increase $\Delta A = 14.08$ MHz for **9**. The larger variation of B is observed for **1** (7.33 MHz), while that of C is observed for **8** (3.55 MHz). It should be noted that for all parameters, larger variations are observed for **8**.

4.3.2 Effects of CN substitution in α - and β -position in compound **1**

For **1**, the two S-C bond lengths are equal ($S1C2 = S1C5 = 1.719$ Å), as well as the two C=C bond lengths ($C2C3 = C4C5 = 1.370$ Å). The substitution of a H-atom in the α -position of the thiophene ring **1** by a CN group elongates the S1-C2 ($\Delta S1C2 = 0.006$ Å) and C=C ($\Delta C2C3 = \Delta C4C5 = 0.0013$ Å) bond lengths, whereas the S1-C5 and the C3-C4 bond lengths are contracted (i.e., contraction of 0.0090 and 0.0105 Å, respectively). We notice, in contrast, an elongation of S1-C5 ($\Delta S1C5 = 0.0126$ Å) and C3-C4 ($\Delta C3C4 = 0.0047$ Å) bond lengths but also a contraction of S1-C2 ($\Delta S1C2 = 0.0005$ Å) and C=C ($\Delta C2C3 = 0.0012$ Å, $\Delta C4C5 = 0.0118$ Å) bond lengths caused by a CN group at β -position. In general, we notice perturbations of geometrical parameters due to the substitution of H by CN-group at α and β -positions of the aromatic ring, respectively. Standard deviations $\sigma = 0.0057$ Å and $\sigma = 0.016$ Å for bond lengths are found for α and β H substitution respectively, whereas they are 0.81 and 0.70° for bond angles in the same order. Nevertheless, our results contrast with earlier findings, especially for SC bond lengths. In fact, Solc et al.^[49] calculated (using B3LYP/6-31G(d) and MP2/6-31G(d)) the bond variations produced by introduction of one or many CN groups at different sites of thiophene ring. Contrary to our results, they found S1C2 bond contraction and a S1C5 bond elongation for the α substitution and a S1C2 contraction in case of β substitution.

The small changes in geometrical parameters induced by the introduction of a CN group at α - or β -position produce a decrease of all rotational constants. The constant A is considerably decreased upon substitution at the α position ($\Delta A = 2637.4$ MHz, $\Delta B = 3601.9$ MHz and $\Delta C = 1877.2$ MHz) whereas both B and C greatly decrease when the CN group is introduced at the β position ($\Delta A = 926.59$ MHz, $\Delta B = 3926.8$ MHz and $\Delta C = 2003.2$ MHz).

Substitution of H by CN at these positions decreases also the dipole moments (cfr Table 4.2). Contrary to previous results of Solc et al.^[49], our results as well as the experimental ones show that **8** exhibits larger dipole moment than **9**, whereas according to the above mentioned reference, it is **9** that exhibits a larger dipole moment than **8**.

4.3.3 Vibrational Frequencies and Assignment

As shown in Table 4.3 (for **8**) and Table 4.4 (for **9**), their 24 normal modes are distributed into two symmetry representations of the C_s point group:

$$\Gamma_{3N-6} = 17 A' (\text{in-plane}) + 7 A'' (\text{out-of-plane}).$$

Each of these Tables presents available experimental and calculated (scaled and unscaled) vibrational frequencies and the scaling factor for each mode of vibration. As shown by these Tables, these scaling factors span the range 0.94 - 1.0, except the modes at 2226 and 2236 cm^{-1} for **8** and **9**, respectively, for both scaling factors are 0.914. From these Tables, there is a good agreement between available experimental and corrected frequencies. The RMS for frequencies decreases in fact from 93 cm^{-1} for the unscaled frequencies to 10 cm^{-1} after scaling process for **8**. This agreement is emphasized by that observed also for **1** (Table A.12) taken as reference. For the latter, the RMS decreases from 97 cm^{-1} for the unscaled frequencies to 5 cm^{-1} for the scaled counterparts. The larger RMS obtained for **8** may be ascribed to the fact that we are comparing experimental frequencies recorded in the liquid state^[43] to the calculated gas phase ones. An agreement between calculated fundamental

Table 4.3 – Experimental vs M06-2X/6-31G(d,p) calculated (from geometry with empirical corrections) frequencies (cm^{-1}) for **8** and corresponding scaling factors.

Numbering	Symmetry	Exp.				Calculated ^e		
		IR ^a	Raman ^a	IR ^b	Raman ^b	Unscaled	IR ^c	Scaling fac.R ^d
In-plane								
ν_1	A'	3112	3111	-	-	3320	3132	0.9430
ν_2	A'	3098	3101	-	3093	3275	3088	0.9430
ν_3	A'	3086	3091	-	-	3260	3075	0.9431
ν_4	A'	2225	2223	-	2224	2433	2226	0.9144
ν_5	A'	1514	1512	1511	1510	1610	1532	0.9517
ν_6	A'	1416	1415	1412	1414	1498	1414	0.9436
ν_7	A'	1353	1352	1349	1351	1411	1353	0.9587
ν_8	A'	1235	1234	1228	1228	1266	1232	0.9731
ν_9	A'	1160	1160	1150	-	1202	1134	0.9437
ν_{10}	A'	1078	1080	1054	1076	1108	1073	0.9682
ν_{11}	A'	1041	1045	1040	1040	1078	1043	0.9668
ν_{13}	A'	857	860	856	857	894	865	0.9666
ν_{15}	A'	754	751	720	-	775	746	0.9619
ν_{17}	A'	668	-	-	-	708	681	0.9601
ν_{20}	A'	507	-	504	-	522	510	0.9762
ν_{21}	A'	487	-	486	-	497	483	0.9708
ν_{23}	A'	-	-	170	-	147	145	0.9845
Out-of-plane								
ν_{12}	A''	915	902	912	911	949	913	0.9616
ν_{14}	A''	844	-	-	-	877	838	0.9557
ν_{16}	A''	686	688	-	-	733	700	0.9540
ν_{18}	A''	568	-	564	-	596	575	0.9640
ν_{19}	A''	526	-	525	-	551	526	0.9546
ν_{22}	A''	418	415	415	-	424	408	0.9624
ν_{24}	A''	-	-	-	-	145	136	0.9401

^a From Ref.^[43] (liquid state); ^b From Ref.^[44]; ^c Fundamental frequencies scaled using the SQMFF method; ^d Individual scaling factors; ^e Intensities are provided in Table 4.7.

frequencies and the experiment is expected for **9**. A further analysis of calculated IR spectra is carried out in terms of PED. The PED analysis has the advantage of being more accurate and allowing a quantitative description of the contribution of movement of a given group of atoms in a normal mode^[76]. In other words, the advantage results in the fact that the energy of each vibration mode is represented as a sum of contributions from particular internal coordinates^[77].

A detailed frequency assignment for both CNT compounds, where the contribution of each vibrational mode and the molecular atoms involved is presented in Table 4.5 for **8** and Table 4.6 for **9**. As it can be seen in these two tables, all vibrational modes, except for the C-H stretching ones, are mixed modes and the dominant mode contributes for less than 90% to the corresponding vibration. Table 4.7 presents the calculated frequencies, infrared intensities, Raman activities and intensities for both compounds **8** and **9**. Figures 4.2a and 4.2b illustrate their simulated gas phase IR spectra and Figures 4.2c and 4.2d their Raman spectra. The results in both the Figure 4.2 and Table Table 4.7 show the most intense

Table 4.4 – Experimental vs M06-2X/6-31G(d,p) calculated (from geometry with empirical corrections) frequencies (cm^{-1}) for **9** and corresponding scaling factors.

Numbering	Symmetry	Exp.		Calculated ^e		
		IR ^a	Raman ^a	Unscaled	IR ^c	Scaling fac.R ^d
In-plane						
ν_1	A'	-	3120	3304	3125	0.9461
ν_2	A'	-	-	3301	3123	0.9461
ν_3	A'	-	3096	3274	3097	0.9461
ν_4	A'	-	2232	2446	2236	0.9141
ν_5	A'	1510	1513	1624	1546	0.9521
ν_6	A'	1404	1403	1511	1423	0.9418
ν_7	A'	1370	1372	1444	1381	0.9568
ν_8	A'	1220	1223	1256	1222	0.9728
ν_9	A'	1125	1156	1190	1148	0.9645
ν_{10}	A'	1085	1085	1114	1084	0.9737
ν_{11}	A'	926	933	962	924	0.9605
ν_{13}	A'	-	-	900	855	0.9499
ν_{15}	A'	790	765	829	800	0.9649
ν_{17}	A'	-	646	658	633	0.9615
ν_{20}	A'	-	487	494	482	0.9752
ν_{21}	A'	-	463	490	468	0.9537
ν_{23}	A'	-	174	151	144	0.9513
Out-of-plane						
ν_{12}	A''	872	874	927	893	0.9633
ν_{14}	A''	-	828	851	807	0.9474
ν_{16}	A''	700	-	725	689	0.9513
ν_{18}	A''	-	-	650	624	0.9591
ν_{19}	A''	-	520	554	531	0.9592
ν_{22}	A''	-	-	443	433	0.9788
ν_{24}	A''	-	-	146	143	0.9812

^a From Ref.^[43] (liquid state); ^b From Ref.^[44]; ^c Fundamental frequencies scaled using the SQMFF method; ^d Individual scaling factors; ^e Intensities are provided in Table 4.7.

infrared bands at 2226 and 700 cm^{-1} for **8** and at 2236 and 800 cm^{-1} for **9**. The band centered at 700 cm^{-1} for **8** and at 800 cm^{-1} for **9** are predominant with respect to those found at 2226 and 2236 cm^{-1} , respectively, for the two compounds. The IR intensities are 73.39 and 41.29 $\text{km} \cdot \text{mol}^{-1}$ for the former and for the latter, respectively, in case of **8**.

Table 4.5 – Potential energy distribution for **8**

Frequency (cm^{-1})	PED (%)	Mode	Atoms ¹				PED (%)	Mode	Atoms ¹			
			h	k	l	m			h	k	l	m
In - plane modes												
3132	97%	νCH	5	10	0	0						
3088	70%	νCH	3	8	0	0	28%	νCH	4	9	0	0
3075	69%	νCH	4	9	0	0	29%	νCH	3	8	0	0
2226	88%	$\nu\text{C}\equiv\text{N}$	6	7	0	0	12%	νCC	2	6	0	0
1532	39%	$\nu\text{C}=\text{C}$	2	3	0	0	18%	$\nu\text{C}=\text{C}$	4	5	0	0
	11%	δCCH	4	3	8	0	7%	δCCH	3	4	9	0

(Continued)

Table 4.5 – (Continued)

Frequency (cm^{-1})	PED (%)	Mode	Atoms ¹				PED (%)	Mode	Atoms ¹			
			h	k	l	m			h	k	l	m
1414	6%	νCC	2	6	0	0	6%	δCCH	2	3	8	0
	31%	νCC	3	4	0	0	18%	$\nu\text{C}=\text{C}$	4	5	0	0
	14%	δCCH	5	4	9	0	11%	δCCH	3	4	9	0
1353	6%	δCCH	2	3	8	0	18%	δCCH	4	5	10	0
	24%	$\nu\text{C}=\text{C}$	4	5	0	0						
	18%	$\nu\text{C}=\text{C}$	2	3	0	0						
1232	6%	νCC	2	6	0	0	17%	δSCH	1	5	10	0
	24%	δCCH	2	3	8	0	18%	δCCH	4	3	8	0
	10%	δCCH	5	4	9	0	9%	$\nu\text{C}=\text{C}$	2	3	0	0
1135	8%	δCCH	4	5	10	0	8%	δCCH	3	4	9	0
	35%	νCC	2	6	0	0	18%	νSC	1	2	0	0
	9%	νCC	3	4	0	0	5%	δSCC	1	2	3	0
1073	5%	$\nu\text{C}=\text{C}$	4	5	0	0	25%	δSCH	1	5	10	0
	25%	δCCH	4	5	10	0						
	13%	δCCH	5	4	9	0						
1043	10%	δCCH	3	4	9	0	13%	$\nu\text{C}=\text{C}$	4	5	0	0
	33%	νCC	3	4	0	0	22%	δCCH	4	3	8	0
	12%	δCCH	2	3	8	0	8%	δCH	3	4	9	0
865	7%	δHCC	5	4	9	0	18%	δSCC	1	5	4	0
	42%	νSC	1	5	0	0						
	14%	δCCC	3	4	5	0						
746	6%	δCCH	3	4	9	0	9%	δSCH	1	5	10	0
	38%	νSC	1	5	0	0	26%	νSC	1	2	0	0
	11%	δCCC	2	3	4	0	10%	δCCC	3	4	5	0
681	22%	νSC	1	2	0	0	16%	νSC	1	5	0	0
	12%	δCSC	5	1	2	0	10%	νCC	2	6	0	0
	9%	δSCC	6	2	1	0	6%	δSCC	1	5	4	0
510	38%	δCCN	2	6	7	0	15%	δCCC	6	2	3	0
	13%	νSC	1	2	0	0	10%	δCSC	5	1	2	0
	7%	δSCC	1	2	6	0	14%	νSC	1	2	0	0
483	38%	νCC	2	6	7	0						
14%	δSCC	1	2	3	0							
145	6%	δCSC	5	1	2	0	7%	δCCN	2	6	7	0
	55%	δCCN	2	6	7	0	6%	δSCC	6	2	1	0
	21%	δCCC	6	2	3	0	23%	δSCC	6	2	1	0
Out - of - plane modes												
913	30%	γHCCH	8	3	4	9	26%	γHCCH	9	4	5	10
	10%	γHCCS	9	4	5	1	8%	γCCCH	2	3	4	9
	7%	γCCCH	8	3	4	5	6%	γCCCH	8	3	4	5
838	22%	γHCCH	9	4	5	10	20%	γCCCH	6	2	3	8
	15%	γHCCC	8	3	4	5	14%	γSCCH	1	2	3	8
	9%	γCCCH	3	4	5	10	21%	γCSCH	2	1	5	10
700	34%	γCCCH	3	4	5	10						
16%	γHCCS	9	4	5	1							
575	32%	γCCN	0	2	6	7	14%	γCCCC	5	4	3	2
	13%	γCCCC	1	2	3	4	7%	γCCCH	8	3	4	5
	7%	γSCCH	1	2	3	8	7%	γCCCS	3	4	5	1
526	59%	γCCN	0	2	6	7	9%	γCCCS	3	4	5	1
	6%	γCCCC	4	3	2	6	5%	γCCSC	4	5	1	2
	408	61%	γCCN	0	2	6	7	10%	γCSCH	5	1	2
136	8%	γCCSC	4	5	1	2	7%	γCCCC	5	4	3	2
	43%	γCCN	0	2	6	7	22%	γCCCC	4	3	2	6
	16%	γCSCH	5	1	2	6	14%	γCCCH	6	2	3	8

¹ See scheme 1 for atom numbering.

ν : stretching, δ : in-plane bending and γ : out-of-plane bending modes.

Table 4.6 – Potential energy distribution for **9**

Frequency (cm^{-1})	PED (%)	Mode	Atoms ¹				PED (%)	Mode	Atoms ¹			
			h	k	l	m			h	k	l	m
In - plane modes												
3125	82%	νCH	5	10	0	0	9%	νCH	2	8	0	0

(Continued)

Table 4.6 – (Continued)

Frequency (cm^{-1})	PED (%)	Mode	Atoms ¹				PED (%)	Mode	Atoms ¹			
			h	k	l	m			h	k	l	m
	8%	νCH	4	9	0	0						
3123	90%	νCH	2	8	0	0	8%	νCH	5	10	0	0
3097	90%	νCH	4	9	0	0	9%	νCH	5	10	0	0
2236	87%	$\nu\text{C}\equiv\text{N}$	6	7	0	0	12%	νCC	3	6	0	0
1546	29%	$\nu\text{C}=\text{C}$	2	3	0	0	28%	$\nu\text{C}=\text{C}$	4	5	0	0
	10%	δCCH	9	4	3	0	8%	νCC	3	6	0	0
1423	39%	$\nu\text{C}=\text{C}$	4	5	0	0	29%	$\nu\text{C}=\text{C}$	2	3	0	0
	5%	δSCH	10	5	1	0	5%	νCC	3	6	0	0
1381	39%	νCC	3	4	0	0	10%	δCCH	10	5	4	0
	10%	$\nu\text{C}=\text{C}$	2	3	0	0	9%	δCCH	9	4	5	0
	6%	δSCH	10	5	1	0						
1222	15%	δCCH	10	5	4	0	15%	δCCH	9	4	5	0
	14%	δCCH	8	2	3	0	12%	δSCH	10	5	1	0
	12%	δCCH	9	4	3	0	7%	δCCH	9	4	5	0
1148	30%	δSCH	8	2	1	0	24%	δCCH	8	2	3	0
	21%	νCC	3	6	0	0	6%	νCC	3	4	0	0
1084	21%	δCCH	9	4	3	0	20%	δCCH	9	4	5	0
	20%	δCCH	10	5	4	0	17%	δSCH	10	5	1	0
	8%	$\nu\text{C}=\text{C}$	4	5	0	0						
924	18%	νCC	3	6	0	0	14%	δCCC	3	4	5	0
	12%	δSCH	10	5	1	0	12%	νCC	3	4	0	0
	8%	$\nu\text{C}=\text{C}$	2	3	0	0	7%	δCCS	4	5	1	0
855	71%	νSC	1	2	0	0	9%	δSCC	1	2	3	0
	7%	δSCH	8	2	1	0						
807	64%	νSC	1	5	0	0	11%	δCCS	4	5	1	0
	5%	νCC	3	4	0	0						
633	30%	νSC	1	5	0	0	23%	δCSC	5	1	2	0
	11%	δCCS	4	5	1	0	8%	νCC	3	6	0	0
	6%	δCCC	3	4	5	0						
531	51%	δCCN	3	6	7	0	18%	δCCC	6	3	4	0
	14%	δCCC	6	3	2	0						
468	36%	νCC	3	6	0	0	15%	νSC	1	2	0	0
	10%	δCCC	3	4	5	0	8%	δSCC	1	2	3	0
	7%	δCSC	5	1	2	0						
144	53%	δCCN	3	6	7	0	20%	δCCC	6	3	2	0
	20%	δCCC	6	3	4	0						
Out - of - plane modes												
893	45%	γCCCH	9	4	5	10	14%	γSCCH	9	4	5	1
	13%	γCCCH	6	3	4	9	11%	γCCCH	2	3	4	9
	6%	γCCCH	3	4	5	10	5%	γCCCH	2	1	5	10
800	36%	γCCCH	8	2	3	6	21%	γCCCH	8	2	3	4
	17%	γCSCH	5	1	2	8	5%	γCCCH	3	4	5	10
689	28%	γCCCH	3	4	5	10	17%	γCSCH	2	1	5	10
	12%	γCCCH	8	2	3	4	8%	γSCCH	9	4	5	1
	8%	γCCCH	6	3	4	9	8%	γCSCH	5	1	2	8
624	39%	γCCN	0	3	6	7	11%	γCCCC	2	3	4	5
	9%	γCSC	1	2	3	4	9%	γCCCH	2	3	4	9
	8%	γCCCH	8	2	3	4	6%	γSCCC	1	2	3	4
482	56%	γCCN	0	3	6	7	13%	γSCCC	3	4	5	1
	8%	γCCSC	4	5	1	2	7%	γCCCC	5	4	3	6
	5%	γCCCC	2	3	4	5						
433	53%	γCCN	0	3	6	7	13%	γSCCC	1	2	3	4
	12%	γCSCC	5	1	2	3	8%	γCCSC	4	5	1	2
143	41%	γCCN	0	3	6	7	15%	γSCCC	1	2	3	6
	12%	γCCCC	5	4	3	6	8%	γCCCH	6	3	4	9
	7%	γCCN	3	6	7	0	6%	CCCH	8	2	3	6

¹ See scheme 1 for atom numbering.

ν : stretching, δ : in-plane bending and γ : out-of-plane bending modes.

They are 61.85 and 34.96 km. mol^{-1} in the same order for **9**. In both **8** and **9**, these bands correspond to the CH out-of-plane deformations and to the $\text{C}\equiv\text{N}$ stretching modes, respectively: the most IR intense band corresponding to the out-of-plane bending CH mode with a $\text{PED}\approx 82\%$ for **8** and $\text{PED}\approx 79\%$ for **9**. The bands corresponding to the stretching $\text{C}\equiv\text{N}$ modes correspond to **88** and **87%** as PED for **8** and **9**, respectively.

Table 4.7 – M06-2X/6-31G(d,p) calculated frequencies (cm^{-1}), infrared intensities (km. mol^{-1}) and Raman activities ($\text{\AA}^4/\text{amu}$) and Raman intensities ($\times 10^{-24} \text{F}^2 \cdot \text{m}^{-1} \cdot \text{kg}^{-1}$) for compounds **8** and **9**.

compound 8				compounds 9			
Freq.	IR ¹ int.	Ram. Activ	Ram. Int. ¹	Freq.	IR int(1).	Ram. Activ	Rama. Int ¹
3132	2.90	140.46	13.80	3125	1.31	175.89	6.83
3088	0.22	133.36	13.66	3123	7.41	36.76	1.43
3075	1.56	94.77	9.83	3097	1.39	80.97	3.23
2226	41.29	323.25	76.72	2236	34.96	270.48	24.95
1532	0.04	14.31	7.14	1546	0.74	26.86	5.18
1414	18.68	103.82	59.57	1423	13.05	40.71	9.08
1353	5.77	51.59	31.91	1381	8.55	4.98	1.17
1232	12.74	5.09	3.67	1222	2.50	4.57	1.31
1134	16.31	1.73	1.42	1148	3.84	17.64	5.60
1073	1.20	14.91	13.39	1084	3.01	3.50	1.21
1043	4.61	1.51	1.42	924	8.76	3.56	1.58
913	0.46	2.21	2.54	893	0.00	0.70	0.33
865	19.11	4.07	5.05	855	23.37	3.30	1.64
838	6.12	2.30	2.99	807	5.22	11.26	6.08
746	0.38	6.79	10.45	800	61.85	1.16	0.64
700	73.39	2.85	4.81	689	12.79	4.27	2.89
681	1.78	14.13	24.81	633	0.95	6.36	4.87
575	3.67	1.26	2.82	624	22.07	0.84	0.66
526	4.93	2.44	6.20	531	0.39	2.23	2.20
510	1.57	2.27	6.03	482	1.38	6.04	6.87
483	1.79	3.86	11.12	468	0.02	6.21	7.36
408	0.32	3.68	13.58	433	2.31	1.21	1.61
145	3.39	4.44	88.14	144	5.02	3.71	29.28
136	1.09	0.34	7.44	143	3.02	0.12	0.92

¹ No available experimental intensities for both IR and Raman spectra.

Moreover, in both these two compounds, the first three higher bands are not mixed and correspond, exclusively, to the out-of-plane CH-bending modes. This is, for instance, the cases of 913, 838 and 700 cm^{-1} where the bending CH contributions are 87, 80 and 82 % for **8**, and 893, 800 and 689 cm^{-1} with bending CH contributions of 84, 78 and 81 % for **9**. At lower wavenumbers, the contribution of this mode is somewhat trifling: $\text{PED} < 15\%$. It is worthy noting that IR bands are stronger for **8** than for **9**. Whereas, they are almost only the two quoted IR strong bands in **8**, there exist two other relatively strong bands in case of **9** with intensities approaching that of the one centered at 800 cm^{-1} . This is the case of the one is centered at 855 cm^{-1} , predominately due to S–C stretching modes ($\text{PED} \approx 71\%$ and the one centered at 624 cm^{-1} , mainly due to the out-of-plane C–C \equiv N. Either for **8** or **9**, the Raman spectra are dominated by the C \equiv N stretching mode of vibration and the in-plane C–C \equiv N deformation centered, respectively. The two vibrational modes appear, respectively, at 2225 and 145 cm^{-1} in case of **8** and at 2236 and 144 cm^{-1} in **9**. As shown in Table 4.7, the Raman intensities are 76.72 and $88.14 \times 10^{-24} \text{F}^2 \text{m}^{-1} \text{kg}^{-1}$, respectively, for **8**; 24.95 and $29.28 \times 10^{-24} \text{F}^2 \text{m}^{-1} \text{kg}^{-1}$, respectively, for **9**. Like the IR intensities, Raman bands are stronger for **8** than in case of **9**.

In their work on vibrational spectra of push–pull molecules, Dell et al.^[78] have reported a peculiar feature in vibrational spectroscopy for the studied systems. Their results have revealed that, contrary to generally accepted rule of thumb according to which what

Table 4.8 – Calculated frequencies (cm^{-1}), infrared intensities (km. mol^{-1}) and Raman activities ($\text{\AA}^4/\text{amu}$) and Raman intensities ($\times 10^{-24} \text{F}^2 \cdot \text{m}^{-1} \cdot \text{kg}^{-1}$) for deuterated forms of **8** and **9**

deuterated 8				deuterated 9			
Freq.	IR int.	Ram. Activ	Ram. Int.	Freq.	IR int.	Ram. Activ	Rama. Int
2304	39.45	287.16	24.76	2313	33.65	246.82	21.09
2293	2.58	97.36	8.49	2292	1.80	88.71	7.74
2262	0.29	48.32	4.35	2280	4.36	20.45	1.81
2241	1.50	44.89	4.12	2254	1.72	35.30	3.20
1501	3.33	38.97	7.92	1512	2.66	28.31	5.68
1383	24.28	122.76	28.77	1401	21.05	42.90	9.84
1260	1.98	15.17	4.15	1326	1.15	12.88	3.24
1142	16.36	4.73	1.52	1041	1.33	5.86	2.17
1001	2.70	2.87	1.12	980	4.95	2.32	0.94
856	7.56	12.08	5.98	853	2.23	15.30	7.62
768	1.31	4.12	2.38	777	0.82	4.08	2.32
765	0.10	1.93	1.13	752	18.22	3.72	2.22
744	9.43	0.96	0.58	750	4.24	4.56	2.73
706	0.27	6.49	4.24	739	0.85	0.66	0.40
674	0.01	0.63	0.44	668	10.83	2.17	1.54
656	2.46	9.86	7.17	603	2.29	4.81	3.95
514	42.82	0.61	0.63	541	1.39	0.35	0.33
509	6.13	1.73	1.81	525	43.40	1.26	1.26
498	2.33	2.07	2.24	520	0.55	2.11	2.14
478	1.07	4.17	4.79	464	0.01	5.84	7.00
439	0.04	0.55	0.71	436	0.97	5.16	6.79
398	1.72	3.84	5.79	403	0.10	0.25	0.37
140	3.57	4.63	38.47	150	3.10	0.05	0.37
135	1.35	0.10	0.89	140	5.01	3.69	30.73

¹ No available experimental intensities for both IR and Raman spectra.

is strong in the infrared is weak in the Raman and vice versa, the most prominent features of the Raman spectrum are also strongly active in the infrared. This finding agrees well with our observation regarding the $\text{C}\equiv\text{N}$ stretching mode. Either for deuterated forms or non-deuterated ones, the mode of vibration is strongly active both in IR and Raman.

It is known that the intensities of infrared bands are proportional to the dipole moment changes accompanying vibrational motion^[79,80]. Typically, it has been established that the fluctuations in the changes accompanying the vibrational distortions are associated with changes in length and orientation of the separate bonds^[80]. The results reveal that introduction of a cyano-group in α and β position of the aromatic ring of **1** increases both the IR and Raman intensities, except for the in-plane and out-of-plan CH modes containing C=C bond length as well as stretching modes. This is, the case of the band centered at 712 cm^{-1} for which the C–C=C–H mode contributes at $\approx 30\%$, the S–C=C–H mode at $\approx 28\%$ and the C=C–C–H mode at $\approx 22\%$.

Table 4.9 – Potential energy distribution for the deuterated form of **8**

Frequency (cm^{-1})	PED (%)	Mode	Atoms ¹				PED (%)	Mode	Atoms ¹			
			h	k	l	m			h	k	l	m
In - plane modes												

(Continued)

Table 4.9 – (Continued)

Frequency (cm^{-1})	PED (%)	Mode	Atoms ¹				PED (%)	Mode	Atoms ¹			
			h	k	l	m			h	k	l	m
In - plane modes												
2304	87%	$\nu\text{C}\equiv\text{N}$	6	7	0	0	11%	νCC	3	6	0	0
2293	82%	νCD	5	10	0	0	12%	νCD	4	9	0	0
2262	68%	νCD	3	8	0	0	20%	νCD	4	9	0	0
	8%	νCD	5	10	0	0						
2241	64%	νCD	4	9	0	0	27%	νCD	3	8	0	0
	7%	νCD	5	10	0	0						
1501	54%	$\nu\text{C}=\text{C}$	2	3	0	0	12%	νCC	2	6	0	0
	10%	$\nu\text{C}=\text{C}$	4	5	0	0						
1383	38%	$\nu\text{C}=\text{C}$	4	5	0	0	14%	νCC	10	3	4	0
	32%	$\nu\text{C}=\text{C}$	2	3	0	0						
1260	30%	νCC	3	4	0	0	13%	$\nu\text{C}=\text{C}$	4	5	0	0
	8%	δCCD	4	5	10	0	8%	$\nu\text{C}=\text{C}$	2	3	0	0
	6%	νSC	3	6	0	0						
1142	37%	νCC	2	6	0	0	25%	νSC	1	2	0	0
	7%	δCCC	3	2	6	0	6%	$\nu\text{C}=\text{C}$	2	3	0	0
	6%	δCCC	3	4	5	0	5%	δSCC	1	2	3	0
1001	18%	νSC	1	5	0	0	14%	δCCD	5	4	9	0
	14%	δCCD	4	5	10	0	11%	δCCD	2	3	8	0
	10%	δCCD	4	3	8	0	10%	δCCD	3	4	9	0
856	18%	δCCD	4	3	8	0	13%	νSC	1	5	0	0
	11%	νCC	3	4	0	0	10%	δCCD	4	5	10	0
	8%	δCCD	2	3	8	0	6%	δCCD	3	4	9	0
768	24%	δSCD	1	5	10	0	16%	δCCD	4	5	10	0
	16%	δCCD	5	4	9	0	13%	δCCD	3	4	9	0
	10%	δCCD	4	3	8	0	9%	δCCD	2	3	8	0
744	19%	νSC	1	5	0	0	18%	δCCD	1	5	10	0
	17%	δCCD	3	4	9	0	9%	δSCC	1	5	4	0
	8%	δCCD	2	3	8	0	8%	δCCD	4	3	8	0
706	34%	νSC	1	5	0	0	15%	δCCC	3	4	5	0
	12%	δCCC	2	3	4	0	11%	δCCD	5	4	9	0
	9%	νSC	3	4	5	0	7%	δCCD	2	3	8	0
656	26%	νSC	1	2	0	0	10%	δCSC	2	1	5	0
	9%	δSCC	1	2	6	0	8%	νCC	2	6	0	0
	8%	δCCD	4	5	10	0	6%	$\nu\text{C}=\text{C}$	2	3	0	0
498	35%	δCCN	3	6	7	0	20%	νSC	1	2	0	0
	14%	δCCC	3	2	6	0	11%	δSCC	1	2	6	0
	5%	δCSC	2	1	5	0						
478	37%	νCC	2	6	0	0	18%	δSCC	1	2	3	0
	11%	δCSC	2	1	5	0	7%	νSC	1	2	0	0
140	62%	δCCN	3	6	7	0	19%	δSCC	1	2	4	0
	17%	δCCC	3	2	6	0						
Out - of - plane modes												
765	27%	γDCCD	8	3	4	9	17%	γCCCD	1	5	4	9
	12%	γCCCD	6	2	3	8	10%	γCCCC	2	3	4	5
	8%	γCCCS	3	4	5	1	7%	γSCCC	1	2	3	4
674	30%	γDCCD	9	4	5	10	20%	γCCCD	6	2	3	8
	10%	γCCCD	2	3	4	9	7%	γCCN	0	2	6	7
	6%	γCCCD	8	3	4	5	6%	γSCCC	1	2	3	8
514	44%	γCCN	0	2	6	7	14%	γSCCD	1	2	3	8
	9%	γDCCD	8	3	4	9	6%	γCCCD	5	4	3	8
509	34%	γSCCD	1	5	4	9	21%	γCCCD	2	3	4	9
	9%	γCSCD	2	1	5	10	9%	γCCCS	3	4	5	1
	8%	γDCCD	8	3	4	9	5%	γCSCC	2	1	5	4
439	22%	γCCN	0	2	6	7	16%	γCSCD	2	1	5	10
	15%	γDCCD	9	4	5	10	9%	γCCCD	6	2	3	8
	8%	γSCCD	1	2	3	8	7%	γCCCD	2	3	4	5
398	60%	γCCN	0	2	6	7	8%	γCSCD	2	1	5	10
	7%	γCSCC	5	1	2	3	6%	γCSCC	2	1	5	4
135	52%	γCCN	0	2	6	7	19%	γCCCC	6	2	3	4
	14%	γSCCC	5	1	2	6	11%	γCCCD	6	23	3	8

¹ See scheme 1 for atom numbering.

ν : Stretching, δ : In-plane bending γ : Out-of-plane bending.

This band is brighter than corresponding ones in **8** and **9**. Moreover, the **8** shows higher IR and Raman intensities than **9**. It should be noted also that the comparison of

Table A.13, Table 4.5 and Table 4.6 shows that, whereas CH modes in α or β sites (i.e., in **2** and **5** or in **3** and **4** positions, respectively) of the thiophene ring contribute equally at a particular IR frequency for **1**, each of the CH modes in **8** and **9** has a frequency where it mainly contributes. For example, the C₂–H and C₅–H modes of vibrations contributes both at 3118 cm⁻¹ with 47% for each one and at 3116 cm⁻¹ also with 48% for each one. In contrast, C₅–H contributes with 97% at 3132 cm⁻¹, C₃–H at 3089 cm⁻¹ (70%) and C₄–H at 3075 cm⁻¹ with 69% for **8**.

For the first time, the deuterated forms of both **8** and **9** are investigated. According to Peeters et al.^[81], knowledge on deuterated compounds is important for the ISM chemical and environmental comprehension. Deuterium isotopes provide us with a powerful tool to distinguish processes occurring at low temperatures in the ISM from those occurring in high-temperature environments. Table 4.8 presents the calculated frequencies, infrared intensities, Raman activities and intensities for both deuterated **8** and **9** forms, whereas Figures 4.3a and 4.3b plot their simulated gas phase IR spectra and Figures 4.3c and 4.3d their Raman spectra. As in cases of non-deuterated forms, the most prominent IR bands correspond to the out-of-plane CD deformations and C≡N stretching modes. These modes appear, respectively, at 514 (36 %) and 2304 cm⁻¹ (87 %) for the deuterated **8**; at 525 (78 %) and 2313 cm⁻¹ (87 %) for the deuterated **9**. Nevertheless, in case of deuterated **8**, the contribution of the out-of-plane C≡N mode dominates the out-of-plane CH mode. Regarding the Raman spectra, it is worthy mentioning that the strongest bands correspond to the in-plane C–C≡N bending modes at 140 cm⁻¹ with 62 % and 55 % as contributions, respectively, for deuterated **8** and deuterated **9**. they are followed by the C≡N stretching modes both in the two compounds. These are shown, on one hand, in Figures 4.3c and 4.3d and, on the other hand, in Table 4.8 and Table 4.9 (for deuterated **8**) and Table 4.10 (for deuterated **9**).

4.3.3.1 C-H and C-D vibrational modes.

Previous studies investigated the C-H stretching modes for five-membered cyclic compounds (**1**, **2**, **3**, selenophene, tellurophone)^[82–85]. This mode was found mainly to occur in the range of 3030 – 3162 cm⁻¹ but that of the gas-phase for **1** were found typically in the region of 3086 – 3126 cm⁻¹^[82,84]. Table 4.5 and Table A.13 show a good agreement between our present results and these prior findings. For example, three peaks are identified at 3132 (97 %), 3088 (99 %) and 3075 cm⁻¹ (98 %) for **8** and at 3125 (99 %), 3123 (98 %) and 3097 cm⁻¹ (99 %) for **9**.

This assignment of C-H stretching mode agrees well with its experimental observations at 3112, 3098 and 3086 cm⁻¹ and those at 3111, 3101 and 3091 cm⁻¹ in the IR and Raman spectra of **8**^[43]. It had also been pointed out that the stretching modes involving hydrogen atom do not occur in the region below 1650 cm⁻¹^[86]. This observation also correlates with our results because no C-H stretching modes is indeed found in this region.

The C-H in-plane bending vibrations appear in the range of 900 – 1500 cm⁻¹^[87,88]. In this chapter, these vibrational modes are predicted at 1532 (24 %), 1414 (31 %), 1353 (35 %), 1232 (68 %), 1073 (73 %), 1043 (49 %) and 864.58 cm⁻¹ (15 %) in case of **8**. For **9**, they occur at 1546 (10 %), 1423 (6%), 1382 (23%), 1222 (68%), 1148 (47%) and at 1084 cm⁻¹. A careful analysis of our results shows that these modes of deformation have roughly large contribution, whether in **8** or **9**, in the range 1250 – 1020 cm⁻¹.

Table 4.10 – Potential energy distribution for the deuterated form of **9**

Frequency (cm^{-1})	PED (%)	Mode	Atoms ¹				PED (%)	Mode	Atoms ¹			
			h	k	l	m			h	k	l	m
In - plane modes												
2313	87%	$\nu\text{C}\equiv\text{N}$	6	7	0	0	11%	νCC	3	6	0	0
2292	65%	νCD	5	10	0	0	27%	νCD	4	9	0	0
2280	94%	νCD	2	8	0	0						
2254	68%	νCD	4	9	0	0	30%	νCD	5	10	0	0
1512	35%	$\nu\text{C}=\text{C}$	2	3	0	0	25%	$\nu\text{C}=\text{C}$	4	5	0	0
	11%	νCC	3	6	0	0	5%	δCCD	9	4	3	0
1401	38%	$\nu\text{C}=\text{C}$	4	5	0	0	32%	$\nu\text{C}=\text{C}$	2	3	0	0
	14%	νCC	10	3	4	0						
1326	42%	νCC	3	4	0	0	16%	νCC	3	6	0	0
	8%	$\nu\text{C}=\text{C}$	2	3	0	0						
1041	22%	νCC	3	4	0	0	18%	δCCD	10	5	4	0
	13%	δCCD	9	4	5	0	12%	νSC	1	5	0	0
	8%	δSCD	10	5	1	0						
979	29%	νCC	3	4	0	0	24%	δCCD	8	2	3	0
	18%	δSCD	8	2	1	0	8%	νCC	3	4	0	0
853	21%	νCC	3	4	0	0	13%	δCCD	9	4	3	0
	9%	νSC	1	5	0	0	8%	δCCC	2	3	4	0
	7%	νSC	1	2	0	0	7%	δSCC	1	2	3	0
776.95	24%	δCCD	10	5	4	0	21%	δSCD	10	5	1	0
	21%	δSCD	9	4	5	0	18%	δCCD	9	4	3	0
752	35%	νSC	1	2	0	0	32%	δSCD	8	2	1	0
	16%	δCCD	8	2	3	0	5%	δSCC	1	2	3	0
750	35%	νSC	1	5	0	0	32%	δSCD	10	5	1	0
	16%	δCCS	4	5	1	0	5%	δCCD	9	4	3	0
	16%	δCCC	3	4	5	0						
603	27%	νSC	1	5	0	0	21%	δCSC	5	1	2	0
	9%	δCCS	4	5	1	0	7%	δCCD	8	2	3	0
	6%	νSC	1	2	0	0	5%	νCC	3	6	0	0
520	52%	δCCN	3	6	7	0	16%	δCCC	6	3	4	0
	13%	δCCC	6	3	2	0						
464	35%	νCC	3	6	0	0	13%	νSC	1	2	0	0
	11%	δCCC	2	3	4	0	9%	δSCC	1	2	3	0
	7%	δCSC	5	1	2	0						
140	55%	δCCN	3	6	7	0	22%	δCCC	6	3	4	0
	22%	δCCC	6	3	2	0						
Out - of - plane modes												
739	28%	γDCCD	9	4	5	10	18%	γCCCD	6	3	4	9
	10%	γCCCC	2	3	4	5	8%	γSCCD	9	4	5	1
	8%	γCCN	2	3	4	5	8%	γSCCD	3	4	5	1
668	23%	γCCCD	8	2	3	6	17%	γCCCD	9	4	5	10
	14%	γCCN	0	3	6	7	9%	γCCCD	3	4	5	10
	7%	γCCCD	8	2	3	4	5%	γSCCC	1	2	3	4
541	14%	γCCCD	8	2	3	4	9%	γCSCD	5	1	2	8
	14%	γCCN	0	3	6	7	9%	γCCCD	3	4	5	10
	6%	γCCCD	8	2	3	4	9%	γSCCC	1	2	3	4
525	23%	γSCCD	9	4	5	1	18%	γCCCD	3	4	5	10
	17%	γCCCD	2	3	4	9	16%	γCCN	0	3	6	7
	13%	γCSCD	2	1	5	10	7%	γCCCD	6	3	4	9
436	53%	γCCN	0	3	6	7	10%	γCCCS	3	4	5	1
	6%	γCCSC	4	5	1	2	5%	γCCCC	5	4	3	6
	5%	γCCCC	5	4	3	6						
403	49%	γCCN	0	3	6	7	12%	γCCCS	1	2	3	4
	11%	γCSCC	5	1	2	3	6%	γCCCC	4	5	1	2
150	40%	γCCN	3	6	7	0	21%	γCCCC	5	4	3	6
	16%	γSCCC	1	2	3	6	11%	γCCCD	6	3	4	9
	9%	γCCCD	8	2	3	6						

¹ See scheme 1 for atom numbering.

ν : Stretching, δ : In-plane bending γ : Out-of-plane bending.

According to Balachandran et al.^[87] the CH out-of-plane bending deformations appear in the wavenumber range $800 - 1000\text{ cm}^{-1}$. From another work by Louarn et al.^[89], it was pointed out that the range of $600 - 1000\text{ cm}^{-1}$ is a complex region that likely contains

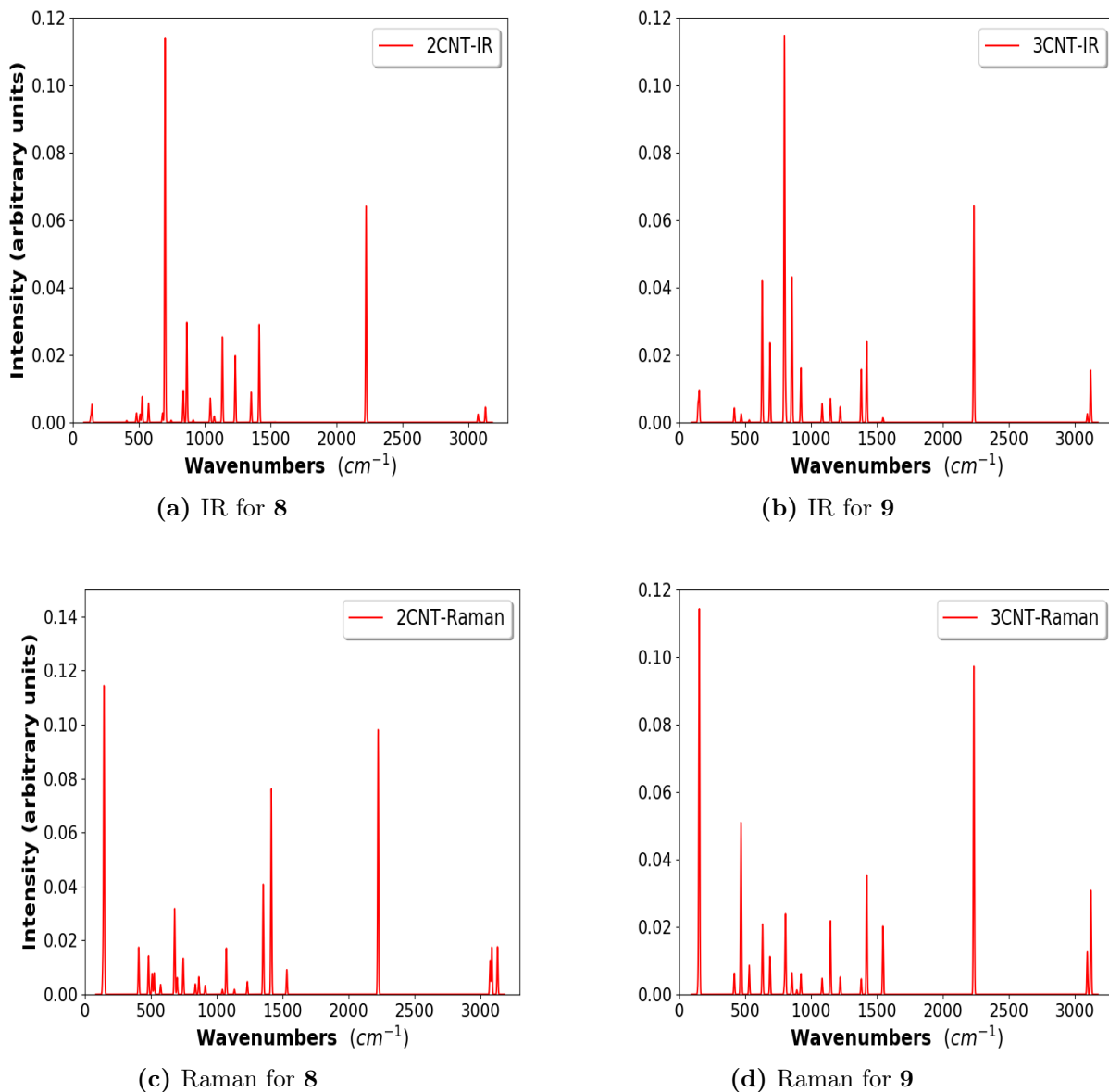


Figure 4.2 – M06-2X/6-31G(d,p) computed gas phase IR spectra (Figures 4.2a for **8** and 4.2b for **9**) and Raman spectra (Figures 4.2c for **8** and 4.2d for **9**).

both in-plane and out-of-plane modes. Our results lend support for this interpretation. Indeed, the out-of-plane modes are found predominantly in the region between 600 cm^{-1} and 1000 cm^{-1} . As shown in Table 4.5, the out-of-plane CH modes are centered at 919 , 833 and 692 cm^{-1} with 87, 80 and 83% as PED, respectively for **8**. Outside of the range quoted above, this mode appears at 574 and 131 cm^{-1} with only 14% as PED. Table 4.6 also shows this kind of modes predicted at 893 , 800 and 689 cm^{-1} with 89, 79, 81 and 18% as PED for **9**. Some in-plane deformations are also observed in this region.

Replacement of H by D, as expected, decreases the frequency of C-H stretching mode. These modes in both aromatic and aliphatic compounds are experimentally observable in the range $2000 - 2500\text{ cm}^{-1}$, i.e., in $4 - 5\mu\text{m}$ ^[81]. It was also found that the aromatic CD stretching mode occurs at $4.40\mu\text{m}$ and bending CD modes associated with PAHs in the range of $9 - 18\mu\text{m}$ ^[90]. Our results are quite consistent with these previous findings. Indeed, for the deuterated form of **8** (Table 4.9), the CD stretching modes are predicted to vibrate

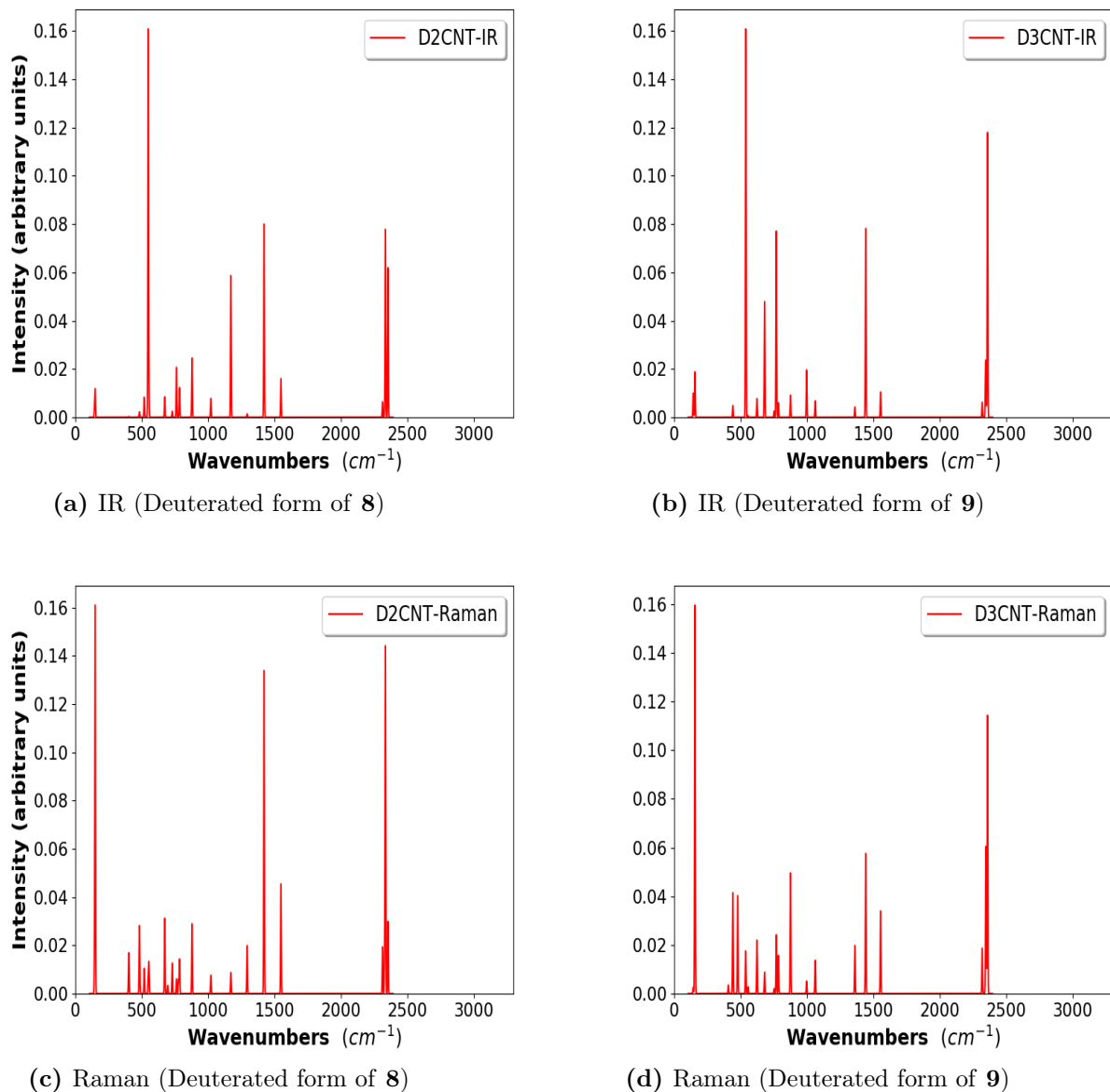


Figure 4.3 – M06-2X/6-31G(d,p) computed gas phase IR spectra (Figures 4.3a for deuterated **8** and 4.3b for deuterated **9**) and Raman spectra (Figures 4.3c for deuterated **8** and 4.3d for deuterated **9**).

at 2293, 2262 and 2241 cm^{-1} (i.e., 4.40–4.46 μm). For deuterated **9** (Table 4.10), they are determined at 2292, 2280 and 2254 cm^{-1} (i.e., 4.36–4.40 μm). The in-plane CD modes appear in the range of 706-1001 cm^{-1} or 9.99–14.16 μm for **8** and in the range of 750-1041 cm^{-1} or 9.61–13.33 μm for **9**. Similarly, the out-of-plane CD modes are mainly determined in the range of 493-765 cm^{-1} or 13.07–20.27 μm for **8** and 525-739 cm^{-1} or 13.53–19.06 μm for **9**. From Figure 4.3, the comparison of IR and Raman results shows that, while the band corresponding to the in-plane $\text{CC}\equiv\text{N}$ modes are the strongest ones both in deuterated **8** and **9** Raman spectra, they are almost the weakest in their IR spectra. The same figure reveals also that the strong bands both in IR and Raman spectra are those corresponding to the CD stretching modes in both deuterated **8** and **9**, but also those corresponding to the $\text{C}=\text{C}$ stretching mode for **8**.

4.3.3.2 C=C and C-C modes of vibration.

Many literature works ascribe the region of $1300 - 1600 \text{ cm}^{-1}$ to the C=C and C-C stretching modes^[89], more precisely the region of $1500 - 1530 \text{ cm}^{-1}$ corresponds to the C=C and 1445 cm^{-1} to the C-C. In-plane and out-of-plane bending vibrations of CC group occur in lower regions of $50 - 360 \text{ cm}^{-1}$ with very weak force constants^[91]. In previous experimental work by Cataliotti et al.^[43], the C=C stretching modes in liquid state of **8** were observed at 1510 and 1416 cm^{-1} and at 1512 and 1415 cm^{-1} for the IR and Raman spectra, respectively. The C-C stretching modes are observed at 1354 cm^{-1} and 1352 cm^{-1} in IR and Raman spectra, respectively.

The ring C=C stretching mode is computed to be centered at 1533 (57%) and 1411 cm^{-1} (29%) (cf. Table 4.5 and Table 4.6), the contributions being lower than 20% below this frequency for **8**. For **9**, they are found at 1546 (57%) and 1423 cm^{-1} (68%) with very small contribution (8%) at 1084 and 924 cm^{-1} . The ring $\nu\text{C} - \text{C}$ modes were experimentally observed at 1354 (IR) and 1352 cm^{-1} (Raman) in liquid state of **8**. In our present results, these modes are predicted at 1414 (31%), 1135 (9%) and 1043 cm^{-1} (33%) for **8** and at 1381 (39%), 1148 (6%), 924 (12%) and 807 cm^{-1} (5%) for **9**.

The out of ring C-C stretching mode (i.e., C-CN) was experimentally observed at 2225 (2223) and 1160 (1159) cm^{-1} in IR (Raman) spectrum of **8**. This mode appears at 2226 (12%), 1135 (35%) and at 483 cm^{-1} (38%) for **8**. It emerges also at 2236 (12%), 1148 (21%), 924 (18%) and 468 cm^{-1} (36%) in **9**. Our calculated results are therefore in good agreement with previous experimental findings whether for the C=C or C-C vibrational modes.

4.3.3.3 S-C modes of vibrations

The vibrational bands of the S-C group were predicted to be found in the region $245 - 1035 \text{ cm}^{-1}$ with variable intensities both in aliphatic and aromatic sulfides^[91]. For instance, in a previous work by Singh et al.^[92], the SC stretching mode was assigned to 609 , 754 , 840 , and 873 cm^{-1} . These stretching and in-plan modes are located predominantly in the above quoted region. For instance, the S-C stretching modes are predicted at 865 (42%), 746 (64%) and 681 cm^{-1} (38%) in **8**; at 855 (71%), 807 (64%) and 633 (30%) and 468 cm^{-1} (15%) for **9**.

4.3.3.4 C \equiv N vibrations.

The characteristic C \equiv N stretching mode of vibration is easily identified in the range of $2270 - 2210 \text{ cm}^{-1}$ ^[93]. Moreover, it has been reported that unsaturated or aromatic nitriles in which the double bond or ring is adjacent to C \equiv N group, absorb more strongly in infrared region than saturated compounds, and the related band occurs at somewhat lower frequency, near 2230 cm^{-1} ^[94]. This assertion correlates well with our observation as mentioned above. In fact, either for deuterated forms or non-deuterated ones, but also either for IR or Raman spectra, our results reveal that the stretching mode C \equiv N gives rise to the second strongest band after the out-of-plane deformation CH (IR).

For Raman spectra, both the first, i.e., the in-plane bending mode (C \equiv N) and the stretching mode (C \equiv N) are related to the C \equiv N, this latter being adjacent to a double bond and a ring in an aromatic compound. This vibrational mode was also observed at 2225 cm^{-1} .^[43] In the present work, this mode is predicted at 2226 cm^{-1} (88%) for **8** and at 2236 cm^{-1} (89%) for **9**. Both values are consistent with the theoretical results found by Coruh et al.^[93] at B3LYP/6-311++G(d,p) (2224 and 2236 cm^{-1}) but also to their FT-

Table 4.11 – Lowest valence excited singlet states of **1**, **8** and **9** obtained using the TD-DFT (M06-2X/6-31G(d,p) method).

State	E_{exc}	λ_{abs}	f	Transition		
compound 1						
$S_1(A_1)$	6.19	200.17	0.10	H - 1 \rightarrow L (84%)	:	$\pi \rightarrow \pi^*$
$S_2(B_2)$	6.20	200.12	0.09	H \rightarrow L (91%)	:	$\pi \rightarrow \pi^*$
compound 8						
$S_1(A')$	5.44	226.20	0.20	H - 1 \rightarrow L (11%)	:	$\pi \rightarrow \pi^*$
				H \rightarrow L (84%)	:	$\pi \rightarrow \pi^*$
				H - 1 \rightarrow L (81%)	:	$\pi \rightarrow \pi^*$
$S_2(A')$	5.85	211.84	0.13	H \rightarrow L (12%)	:	$\pi \rightarrow \pi^*$
compound 9						
$S_1(A')$	5.56	210.40	0.16	H - 1 \rightarrow L (77%)	:	$\pi \rightarrow \pi^*$
				H \rightarrow L (12%)	:	$\pi \rightarrow \pi^*$
$S_2(A')$	5.64	209.09	0.06	H - 1 \rightarrow L (12%)	:	$\pi \rightarrow \pi^*$
				H \rightarrow L (83%)	:	$\pi \rightarrow \pi^*$

H: HOMO (Highest Occupied Molecular Orbital), L: LUMO (Lowest Unoccupied Molecular Orbital), E_{exc} : Excitation energy (in eV), λ_{abs} : Absorption wavelength (in nm). Only electronic transitions with contributions ≥ 10 are considered.

Raman results (2231 cm^{-1}). There is thus a very good agreement between the present results and previous experimental results. Table 4.6 and Figures 4.2a and 4.2b (IR), as well as Figures 4.2c and 4.2d (Raman) show that these bands, both in **8** and **9**, are characterized by high intensities, whether in IR or Raman spectrum. The in-plane and out-of-plane ring-C \equiv N modes are highly contaminated with neighboring modes and do not, consequently, have characteristic frequency. In fact, the in-plane ring-C \equiv N modes are found at 510 (38%) and 145 cm^{-1} (55%) for the **7**; at 531 (51%) and 144 cm^{-1} (53%) in case of **8**. Likewise, the out-of-plane ring-C \equiv N modes are predicted at 574 (32%), 524 (59%), 410 (61%) and 131 cm^{-1} (43%) for **8** and at 624 (39%), 482 (56%), 433 (53%) and 143 cm^{-1} (34%) for **9**.

4.3.4 UV-VIS spectra

For a prediction of electronic spectra of the molecules considered, we first carry out time-dependent density functional theory (TD-DFT) calculations for the non-substituted parent compound **1**. The M06-2X functional in conjunction with the 6-31G(d,p) basis set is used for this purpose, using the predicted geometries (with empirical correction). Similar computations are subsequently performed for both compounds **8** and **9**. The frontier orbitals are an important indicator for the determination of the way a molecule interact with other species because the gap between HOMO and LUMO characterizes the molecular chemical stability^[87]. A molecule with a small frontier orbital gap (the gap between HOMO and LUMO) is more polarizable and is generally associated with higher chemical reactivity and lower kinetic stability. For this reason, the frontier orbital gap for the molecules considered are tabulated. We find the frontier energy gaps of 6.1, 5.4 and 5.8 eV for **1**, **8** and **9**, respectively. The energy difference between the two optimized structures of **8** and **9** is about 3 kJ/mol . The electronic transitions within frontier orbitals are also involved in elementary electronic absorption and emission processes. Concerning the polycyclic aromatic compounds (PACs), including PAHs that refers exclusively to compounds containing

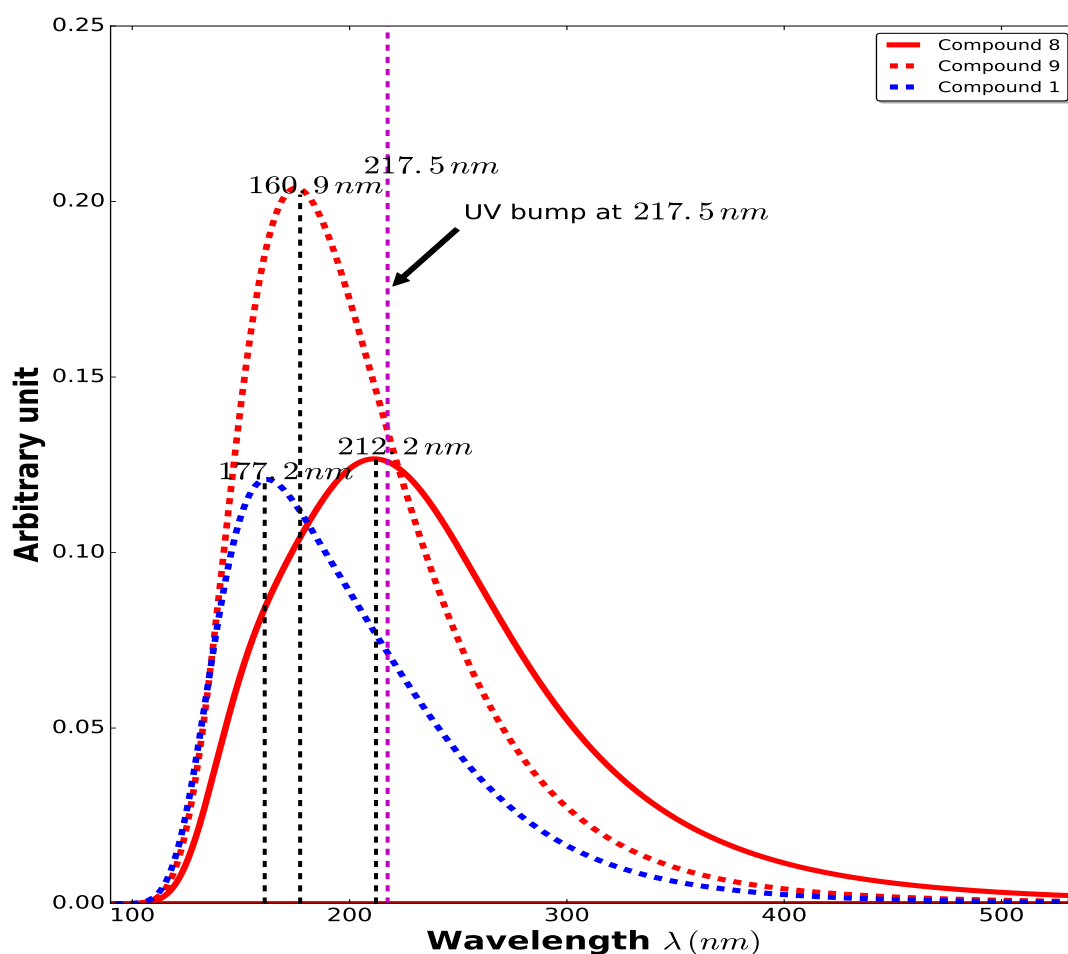


Figure 4.4 – Gas phase computed UV-Visible spectrum of compounds **1**, **8** & **9** using TD-M06-2X/6-31G(d,p).

only carbon and hydrogen^[95], it has been found that these compounds are carriers of the interstellar UV bump, i.e., a local extinction maximum, at $4.6 \mu\text{m}^{-1}$ (217.5 nm)^[96,97].

It has also been stated that this bump is due to the $\pi \rightarrow \pi^*$ electronic transitions of the delocalized electrons in sp^2 hybridized carbon bonds in carbon clusters^[96,98]. Figure 4.4 plots the stimulated gas phase UV-visible spectra of **1**, **8** and **9**. The maximum absorption for these compounds, especially that of **8** ($\lambda_{\text{max}} = 216 \text{ nm}$) is closer to the interstellar UV bump. Table 4.11 gives the lowest-lying valence excited singlet states. It shows also the main molecular orbitals (with contributions $\geq 10\%$) involved in the electronic transitions. From this Table, only electronic transitions between HOMO – 1 and LUMO and/or between HOMO and LUMO contribute significantly to UV-VIS spectra. These molecular orbitals are presented on Figure 4.5. From this figure, it is clear that all the orbitals are of π -type. It is therefore confirmed that all electronic transitions involve π electrons, the $\pi \rightarrow \pi^*$ transitions. It is worthy noting that no experimental data about these results are available yet.

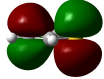
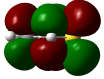

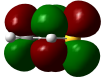
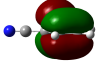
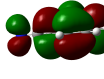
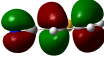
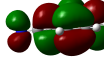
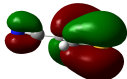
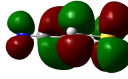
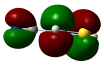
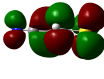
Compound	Molecular Orbitals	
Thiophene	 <p>HOMO - 1</p>	<p>→</p>  <p>LUMO</p>
	 <p>HOMO</p>	<p>→</p>  <p>LUMO</p>
2CNT	 <p>HOMO - 1</p>	<p>→</p>  <p>LUMO</p>
	 <p>HOMO</p>	<p>→</p>  <p>LUMO</p>
3CNT	 <p>HOMO - 1</p>	<p>→</p>  <p>LUMO</p>
	 <p>HOMO</p>	<p>→</p>  <p>LUMO</p>

Figure 4.5 – Plots of main Molecular Orbitals involved in the electronic transitions.

4.4 Summary

Quantum chemical calculations on the structures and basic spectroscopic properties, including geometrical parameters and rotational constants, IR, Raman and UV-VIS spectra were carried out for both cyanothiophene compounds **8** and **9** with the aim of providing some basic information for the detection of these molecules that are of great astrophysical interest. Following the empirical corrections for systematic deficiencies of methods and basis sets to adjust geometrical parameters, the molecular geometry for the parent thiophene **1** was determined and an excellent agreement with experiment achieved. An agreement between the available experimental and calculated values for the fundamental vibrational frequencies of the parent compound **1** was also fulfilled. The same strategy was subsequently used for both cyano derivatives **8** and **9**. Geometrical parameters and thereby the rotational constants of two cyanothiophene derivatives have thus been obtained. In the present work i) reliable molecular geometries are provided, ii) a complete description of both IR and Raman spectra made, including IR frequency assignment on the basis of PED analysis, iii) both IR and Raman spectra for deuterated derivatives are predicted, iv) electronic UV-VIS spectra for both **8** and **9** are predicted **8**, being expected to absorb the interstellar in the UV region at 218 nm, the main electronic transitions are elucidated and corresponding Molecular Orbitals plotted, v) IR and Raman spectral bands for all the fundamental vibrational modes, including C-D modes, are identified and assigned. We would hope that these predicted results are helpful to assist astrophysicists and astrochemists in the experimental search of these aromatic species in the interstellar space.

4.5 References

- [1] L. Pagani, E. Bergin, P. Goldsmith, G. Melnick, R. Snell, and C. Favre. 2019.
- [2] A. Krabbe. Sofia telescope. In *Airborne Telescope Systems*, volume 4014, pages 276–282. International Society for Optics and Photonics, 2000.
- [3] A. McKellar. *Publ. Astron. Soc. Pac.*, 52(307):187–192, 1940.
- [4] C. P. Endres, S. Schlemmer, P. Schilke, J. Stutzki, and H. S. Müller. *J. Mol. Spectrosc.*, 327:95–104, 2016.
- [5] H. S. Müller, F. Schlöder, J. Stutzki, and G. Winnewisser. *J. Mol. Struct.*, 742(1-3): 215–227, 2005.
- [6] H. S. Müller, S. Thorwirth, D. Roth, and G. Winnewisser. *A&A*, 370(3):L49–L52, 2001.
- [7] K. Jefferts, A. Penzias, and R. Wilson. *ApJ*, 161:L87, 1970.
- [8] D. A. Neufeld, P. Schilke, K. M. Menten, M. G. Wolfire, J. H. Black, F. Schuller, H. S. Müller, S. Thorwirth, R. Güsten, and S. Philipp. *A&A*, 454(2):L37–L40, 2006.
- [9] M. Guélin, S. Muller, J. Cernicharo, A. Apponi, M. McCarthy, C. Gottlieb, and P. Thaddeus. *A&A*, 363:L9–L12, 2000.
- [10] D. Halfen, L. M. Ziurys, S. Brünken, C. Gottlieb, M. McCarthy, and P. Thaddeus. *Astrophys. J. Lett.*, 702(2):L124, 2009.
- [11] A. J. Remijan, J. Hollis, F. Lovas, W. D. Stork, P. Jewell, and D. Meier. *Astrophys. J. Lett.*, 675(2):L85, 2008.
- [12] L. E. Snyder, J. Hollis, P. Jewell, F. J. Lovas, and A. Remijan. *ApJ*, 647(1):412, 2006.
- [13] H. Feuchtgruber, F. Helmich, E. Van Dishoeck, and C. Wright. *Astrophys. J. Lett.*, 535 (2):L111, 2000.
- [14] J. Cernicharo, A. M. Heras, J. R. Pardo, A. Tielens, M. Guélin, E. Dartois, R. Neri, and L. Waters. *Astrophys. J. Lett.*, 546(2):L127, 2001.
- [15] F. H. Chaffee, B. L. Lutz, J. H. Black, P. A. V. Bout, and R. L. Snell. Rotational

- fine structure lines of interstellar C₂ toward ζ persei. In *Symposium-International Astronomical Union*, volume 87, pages 263–267. Cambridge University Press, 1980.
- [16] D. C. Knauth, B. Andersson, S. R. McCandliss, and H. W. Moos. *Nature*, 429(6992): 636, 2004.
- [17] D. McNaughton, M. K. Jahn, M. J. Travers, D. Wachsmuth, P. D. Godfrey, and J.-U. Grabow. *Mon. Not. R. Astron. Soc.*, 476(4):5268–5273, 2018.
- [18] S. Bteich, B. Tercero, J. Cernicharo, R. Motiyenko, L. Margulès, and J.-C. Guillemin. *A&A*, 592:A43, 2016.
- [19] R. Hudson and M. Moore. *Icarus*, 172(2):466–478, 2004.
- [20] B. A. McGuire, A. M. Burkhardt, S. Kalenskii, C. N. Shingledecker, A. J. Remijan, E. Herbst, and M. C. McCarthy. *Science*, 359(6372):202–205, 2018.
- [21] B. A. McGuire, A. M. Burkhardt, C. N. Shingledecker, S. V. Kalenskii, E. Herbst, A. J. Remijan, and M. C. McCarthy. *Astrophys. J. Lett.*, 843(2):L28, 2017.
- [22] M. Matsuura, A. Zijlstra, F. Molster, S. Hony, L. Waters, F. Kemper, J. Bowey, H. Chihara, C. Koike, and L. Keller. *ApJ*, 604(2):791, 2004.
- [23] J. Cernicharo, A. M. Heras, A. Tielens, J. R. Pardo, F. Herpin, M. Guélin, and L. Waters. *Astrophys. J. Lett.*, 546(2):L123, 2001.
- [24] M. Bose, R. Root, and S. Pizzarello. *Meteorit. Planet. Sci.*, 52(3):546–559, 2017.
- [25] F. Robert and S. Epstein. *Geochim. Cosmochim. Acta*, 46(1):81–95, 1982.
- [26] J. Kerridge and S. Chang. *Meteoritics*, 18:323, 1983.
- [27] J. Yang and S. Epstein. *Nature*, 311(5986):544, 1984.
- [28] L. Remusat, F. Palhol, F. Robert, S. Derenne, and C. France-Lanord. *Earth Planet. Sci. Lett.*, 243(1-2):15–25, 2006.
- [29] J. L. Eigenbrode, R. E. Summons, A. Steele, C. Freissinet, M. Millan, R. Navarro-González, B. Sutter, A. C. McAdam, H. B. Franz, D. P. Glavin, et al. *Science*, 360(6393):1096–1101, 2018.
- [30] G. Cai, S. Wang, L. Zhao, Y. Sun, D. Yang, R. Lee, M. Zhao, H. Zhang, and Y. Zhou. *Molecules*, 24(1):192, 2019.
- [31] L. Zhao and W.-W. Liao. *Org. Chem. Front.*, 5:801–805, 2018. doi: 10.1039/C7QO01000A. URL <http://dx.doi.org/10.1039/C7QO01000A>.
- [32] M. Aleksić, B. Bertoša, R. Nhili, S. Depauw, I. Martin-Kleiner, M.-H. David-Cordonnier, S. Tomić, M. Kralj, and G. Karminski-Zamola. *Eur. J. Med. Chem.*, 71:267–281, 2014.
- [33] V. Manikandamathavan, M. Thangaraj, T. Weyhermuller, R. Parameswari, V. Punitha, N. N. Murthy, and B. U. Nair. *Eur. J. Med. Chem.*, 135:434–446, 2017.
- [34] G. Hadziioannou and P. Van Hutten. *Semiconducting polymers*. Wiley Online Library, 2000.
- [35] S. Li, J. Yan, C.-Z. Li, F. Liu, M. Shi, H. Chen, and T. P. Russell. *J. Mater. Chem. A*, 4(10):3777–3783, 2016.
- [36] Y. Patil and R. Misra. *The Chemical Record*, 2018.
- [37] C. Rost, S. Karg, W. Riess, M. A. Loi, M. Murgia, and M. Muccini. *Appl. Phys. Lett.*, 85(9):1613–1615, 2004.
- [38] M. Halik, H. Klauk, U. Zschieschang, G. Schmid, S. Ponomarenko, S. Kirchmeyer, and W. Weber. *Advanced Materials*, 15(11):917–922, 2003.
- [39] I. C. Gonzalez, L. N. Davis, and C. K. Smith II. *Bioorg. Med. Chem. Lett.*, 14(15): 4037–4043, 2004.
- [40] S. Cheylan, A. Fraleoni-Morgera, J. Puigdollers, C. Voz, L. Setti, R. Alcubilla, G. Badenes, P. Costa-Bizzarri, and M. Lanzi. *Thin Solid Films*, 497(1-2):16–19, 2006.
- [41] F. Hide, Y. Greenwald, F. Wudl, and A. Heeger. *Synth. Met.*, 85(1-3):1255–1256, 1997.

- [42] M. A. R. da Silva and A. F. L. Santos. *J. Chem. Thermodyn.*, 40(2):225–231, 2008.
- [43] R. S. Cataliotti, F. Antolini, A. Morresi, F. Santinelli, and S. Santini. *J. Raman Spectrosc.*, 19(6):423–428, 1988.
- [44] V. Aleksanyan, N. Magdesieva, Y. K. Yur’ev, et al. *J. Struct. Chem.*, 7(1):36–41, 1967.
- [45] T. Avirah, T. Malloy Jr, and R. L. Cook. *J. Mol. Struct.*, 29(1):47–52, 1975.
- [46] J. Wiese and D. H. Sutter. *Z. Naturforsch.*, 32(8):890–896, 1977.
- [47] J. Wiese, R. Schwarz, and D. Sutter. *Z. Naturforsch.*, 35(7):770–772, 1980.
- [48] F. S. Boig, G. W. Costa, and I. Osvar. *J. Org. Chem.*, 18(7):775–778, 1953.
- [49] R. Solc, V. Lukeš, E. Klein, M. Griesser, and A.-M. Kelterer. *J. Phys. Chem. A*, 112(43):10931–10938, 2008.
- [50] N. V. Riggs, L. Radom, M. Winnewisser, B. P. Winnewisser, M. Birk, et al. *Chem. Phys.*, 122(2):305–315, 1988.
- [51] J. A. Pople, J. S. Binkley, and R. Seeger. *Int. J. Quantum Chem.*, 10(S10):1–19, 1976.
- [52] A. D. Becke. *J. Chem. Phys.*, 98(7):5648–5652, 1993.
- [53] C. Lee, W. Yang, and R. G. Parr. *Phys. Rev. B*, 37(2):785, 1988.
- [54] Y. Zhao and D. G. Truhlar. *Theor. Chem. Acc.*, 120(1-3):215–241, 2008.
- [55] M. J. Frisch, G. Trucks, H. Schlegel, G. Scuseria, M. Robb, J. Cheeseman, G. Scalmani, V. Barone, B. Mennucci, G. Petersson, et al. *Inc.: Wallingford, CT*, 2009.
- [56] J. P. Merrick, D. Moran, and L. Radom. *J. Phys. Chem. A.*, 111(45):11683–11700, 2007.
- [57] G. Rauhut and P. Pulay. *J. Phys. Chem. A*, 99(10):3093–3100, 1995.
- [58] P. M. Kozłowski, M. Z. Zgierski, and P. Pulay. *Chem. Phys. Lett.*, 247(4-6):379–385, 1995.
- [59] T. Sundius. *J. Mol. Struct.*, 218:321–326, 1990.
- [60] T. Sundius. *Vib. Spectrosc.*, 29(1-2):89–95, 2002.
- [61] P. Pulay, G. Fogarasi, G. Pongor, J. E. Boggs, and A. Vargha. *J. Am. Chem. Soc.*, 105(24):7037–7047, 1983.
- [62] B. Bak, D. Christensen, L. Hansen-Nygaard, and J. Rastrup-Andersen. *J. Mol. Spectrosc.*, 7(1-6):58–63, 1961.
- [63] B. Bak, D. Christensen, W. B. Dixon, L. Hansen-Nygaard, J. R. Andersen, and M. Schottländer. *J. Mol. Spectrosc.*, 9:124–129, 1962.
- [64] U. Nygaard, J. T. Nielsen, J. Kirchheiner, G. Maltesen, J. Rastrup-Andersen, and G. O. Sørensen. *J. Mol. Struct.*, 3(6):491–506, 1969.
- [65] M. Tanabe, N. Kuze, H. Fujiwara, H. Takeuchi, and S. Konaka. *J. Mol. Struct. THEOCHEM*, 372(2-3):173–180, 1995.
- [66] T. Ogata and K. Kozima. *J. Mol. Spectrosc.*, 42(1):38–46, 1972.
- [67] D. M. Kovtun, I. V. Kochikov, and Y. I. Tarasov. *J. Mol. Struct.*, 1100:311–317, 2015.
- [68] Y. Jin, X. Li, Y. Zheng, Q. Gou, Z. Xia, and G. Feng. *SAA*, 218:136–141, 2019.
- [69] I. Kochikov, Y. I. Tarasov, V. Spiridonov, G. Kuramshina, D. Rankin, A. Saakjan, and A. Yagola. *J. Mol. Struct.*, 567:29–40, 2001.
- [70] U. Kretschmer, W. Stahl, and H. Dreizler. *Z. Naturforsch.*, 48(5-6):733–736, 1993.
- [71] J. Wiese, L. Engelbrecht, and H. Dreizler. *Z. Naturforsch.*, 32(2):152–155, 1977.
- [72] A. Fouda. *Monatshefte für Chemie/Chemical Monthly*, 117(2):159–165, 1986.
- [73] T. M. Pappenfus, T. L. Wood, J. L. Morey, W. D. Wilcox, and D. E. Janzen. *Acta Crystallogr. E*, 74(2):189–192, 2018.
- [74] A. J. Blake, B. A. Clark, H. Gierens, R. O. Gould, G. A. Hunter, H. McNab, M. Morrow, and C. C. Sommerville. *Acta Crystallogr. Sect. B Struct. Sci.*, 55(6):963–974, 1999.
- [75] C. J. Ziegler and V. N. Nemykin. *Acta Crystallogr. Sect. E Struct. Rep. Online*, 68(9):o2693–o2693, 2012.

- [76] M. H. Jamróz. *SAA*, 114:220–230, 2013.
- [77] H. Rostkowska, L. Lapinski, and M. J. Nowak. *Vib. Spectrosc.*, 49(1):43–51, 2009.
- [78] M. Del Zoppo, M. Tommasini, C. Castiglioni, and G. Zerbi. *Chem. Phys. Lett.*, 287(1-2):100–108, 1998.
- [79] S. Califano. *J. Chem. Phys.*, 36(4):903–909, 1962.
- [80] B. Galabov, B. Nikolova, and W. J. Orville-Thomas. *Croat. Chem. Acta*, 57(5):1145–1164, 1984.
- [81] E. Peeters, L. Allamandola, C. Bauschlicher Jr, D. Hudgins, S. Sandford, and A. Tielens. *ApJ*, 604(1):252, 2004.
- [82] M. Rico, J. Orza, and J. Morcillo. *SAA*, 21(4):689–719, 1965.
- [83] R. Cataliotti and G. Paliani. *Can. J. Chem.*, 54(15):2451–2457, 1976.
- [84] T. Klots, R. Chirico, and W. Steele. *SAA*, 50(4):765–795, 1994.
- [85] J. S. Kwiatkowski, J. Leszczyński, and I. Teca. *J. Mol. Struct.*, 436:451–480, 1997.
- [86] K. Gdula, M. Barczak, and P. Borowski. *Annales UMCS Chemia*, 67(1-2):131–153, 2012.
- [87] V. Balachandran, A. Janaki, and A. Nataraj. *SAA*, 118:321–330, 2014.
- [88] D. G. Irayadian, S. J. Vedhagiri, M. Govindarajan, and K. Parimalad. 2018.
- [89] G. Louarn, J. Buisson, S. Lefrant, and D. Fichou. *J. Phys. Chem. A*, 99(29):11399–11404, 1995.
- [90] K. D. Doney, A. Candian, T. Mori, T. Onaka, and A. Tielens. *A&A*, 586:A65, 2016.
- [91] N. Issaoui, H. Ghalla, F. Bardak, M. Karabacak, N. A. Dlala, H. Flakus, and B. Oujia. *J. Mol. Struct.*, 1130:659–668, 2017.
- [92] D. K. Singh, S. K. Srivastava, A. K. Ojha, and B. Asthana. *J. Mol. Struct.*, 892(1-3):384–391, 2008.
- [93] A. Coruh, F. Yilmaz, B. Sengez, M. Kurt, M. Cinar, and M. Karabacak. *Struct. Chem.*, 22(1):45–56, 2011.
- [94] H. Oturak, N. KINAYTÜRK, M. Topuz, N. Kutlu, E. Kaynaker, P. Talip, and Y. Sert. *Acta Physica Polonica, A.*, 132(3), 2017.
- [95] D. M. Hudgins. *Polycyclic Aromat. Compd.*, 22(3-4):469–488, 2002.
- [96] K. Gadallah, H. Mutschke, and C. Jäger. *A&A*, 528:A56, 2011.
- [97] M. Steglich, C. Jäger, G. Rouillé, F. Huisken, H. Mutschke, and T. Henning. *Astrophys. J. Lett.*, 712(1):L16, 2010.
- [98] V. Mennella, L. Colangeli, A. Blanco, E. Bussoletti, S. Fonti, P. Palumbo, and H. Mertins. *ApJ*, 444:288–292, 1995.

ROTATIONAL SPECTRA AND HYPERFINE STRUCTURES OF 2-CYANOTHIOPHENE AND 3-CYANOTHIOPHENE

5.1 Introduction

Up to now, more than 210 organic and inorganic molecular species have been found in the planetary atmospheres, comets and the interstellar medium (ISM) of galaxies^[1,2], and most of them were identified on the basis of their microwave and/or infrared emissions. A non-negligible number of them contain the cyano ($C\equiv N$) group^[3] and were detected in the ISM and circumstellar environments thanks to their rotational emission spectra. Recently detected nitriles include glycolonitrile ($HOCH_2CN$)^[4], Z-cyanomethanimine ($z-HNCHCN$)^[5], isocyanogen ($CNCN$)^[6], benzonitrile ($c-C_6H_5CN$)^[2], silyl cyanide (SiH_3CN)^[7,8], protonated cyanogen ($NCCNH^+$)^[9], cyanomethylidyne (CCN)^[10], isopropyl cyanide (C_3H_7CN)^[11], the long cyanopolyne ($HC_{11}N$)^[12], etc.

Extensive laboratory and/or observational studies were carried out in order to understand the role of nitriles in kinematic or temperature probes in different ISM environments and to search for new molecular species. These studies concern molecules from the most simple such as methyl cyanide ($CH_3C\equiv N$)^[13-16], vinyl cyanide ($CH_2CHC\equiv N$)^[13,17], to complex ones such as cyanodiacetylene ($HC_4C\equiv N$)^[13], ethyl cyanide ($CH_3CH_2C\equiv N$)^[13,18-20], isopropyl cyanide ($i-C_3H_7C\equiv N$)^[11,21], cyanides of the serie $((HC\equiv C)_n-C\equiv N)$ ^[9,22,23], with n in range 0–5, the serie $(CH_3(C\equiv C)_n-C\equiv N)$ ^[24] with $n = 0-2$, cyanoallene ($CH_2CCHC\equiv N$)^[25] and aromatic derivatives such as benzonitrile ($c-C_6H_5CN$)^[2,26]. The latter was recently detected via its gas-phase rotational transitions in the cold core Taurus Molecular Cloud 1 (TMC-1) which is known to display a rich chemistry dominated by unsaturated carbon-chain molecules such as the cyanopolyynes (HC_nN , $n = \text{odd number}$)^[2,26]. Benzonitrile has a six-membered ring and is the second compound of the six-membered cycle detected in space in general, and in the ISM and circumstellar environment in particular, after the earlier detection of benzene (C_6H_6) via its bending mode ν_4 in the proto-planetary nebula CRL 618^[27]. Beside, the very recently detected five-membered ring, cyanocyclopentadiene ($c-C_5H_5CN$)^[28], no five-membered ring else molecular species was detected in the interstellar medium yet.

Aromatic molecules and their substituted derivatives (heterocyclic or not) constitute an important component of the ISM^[29,30]. Of them, heterocyclic molecules are six-membered and five-membered with one or more carbon atoms substituted by a nitrogen atom and/or either oxygen or sulfur atoms. Aromatic heterocyclic molecules have astrobiological relevance as precursors of nucleobases^[31]. Small heterocyclic five-membered rings have been detected in carbonaceous meteorites^[32]. For instance, benzofurans, a type of O-heterocycle, have been detected in the Yamato-791198 meteorite, whereas N-heterocycles have been detected in carbonaceous chondrites, including Orgueil, Murchison, Murray, and LON 94102 (nuevo2015n and references therein). S-heterocycles, such as benzothiophene, have been also

detected in the Murchison carbonaceous chondrite^[33]. Moreover, in a recent work by^[34], thiophene and its methyl substituted derivatives (2- and 3-methylthiophene) and many other sulfur-bearing compounds were observed in samples of Mudstones gathered from Gale crater on Mars by gas chromatography - mass spectrometry (GC-MS) analysis. The parent thiophene was also identified in Murchison and Orgueil meteorites^[33,35]. The analysis of insoluble organic matter (IOM) from two carbonaceous chondrites such as Murchison and Allende pointed out a non-negligible proportion of thiophene in those materials^[36]. Through investigation of isotopic abundance in IOM, the D and ¹⁵N excesses observed in it indicate that thiophene has an ISM origin^[37-39]. Many other studies also supported the likely ISM origin of IOM; the recent among them being that of^[36]. Moreover, Lattelais et al.^[40] reported that pyrrole, furan and thiophene are unambiguously the most stable isomers of the C₄H₅N, C₄H₄O and C₄H₄S families, respectively, at the 10 – 50 K temperatures of the ISM. Heterocyclic molecules and their hydrogen substituted derivatives may then exist in different ISM environments. However, no ISM detection of one of these heterocyclic compounds or their substituted derivatives is formally confirmed yet by astrochemists or astrophysicists.

According to the work by Martin et al.^[20], sulfur is depleted in regions where it is expected to be abundant, especially around young stellar objects where already detected S-bearing species account for only 0.1% of its estimated cosmic abundance. It has then recently been suggested that not yet detected gas-phase sulfur-bearing molecules should play a key role in the observed sulfur depletion^[41] when one compares its cosmic values throughout the diffuse and translucent stages of an interstellar molecular cloud, and its atomic and molecular gas-phase constituents toward lines of sight containing higher-density environments^[42]. Therefore, as no S-substituted heterocyclic molecule was yet detected in the ISM environment, these molecular species are likely interstellar targets. Isomeric forms of molecular species are of interest in astrochemistry because they can help constrain the chemical processes leading to their formation and depletion, whether they occur in the gas phase or on the surfaces of dust particles^[43].

It has been demonstrated that hyperfine splitting plays an important role in ISM physics. Indeed, a hyperfine splitting allows the measurement of optical depths of molecular lines, an estimation of molecular column densities without assumptions about the beam filling factor^[44]. The same report shows also that hyperfine splitting can be used in deriving the kinematic structure of clouds from observations of molecular line profiles. Moreover, hyperfine coupling splittings are of particular importance in ISM chemistry because some of molecular species identified in the ISM are revealed by their hyperfine structures^[2,45].

Thanks to the availability of new facilities with high angular resolution and high sensitivity such as the Atacama Large Millimeter/Submillimeter Array (ALMA)^[46], new molecular species are expected to be discovered in a variety of universe environments. Rotational data (including nuclear quadrupole hyperfine information for nuclei with $I \geq 1$ and non-zero quadrupole moments) for not yet detected compounds are very valuable for these observatories for the detection and identification of new compounds.

For this purpose, a quantum chemical investigation of ¹⁴N quadrupole hyperfine structures of 2-cyanothiophene (**8**) and 3-cyanothiophene (3CNT) (cf. Scheme 4.1) and their ³³S isotopologues (i.e., ³³S-3 C¹⁵NT and ³³S-2 C¹⁵NT), as well as deuterated species (3 C¹⁵NT-2D and 2 C¹⁵NT-3D, where 3D \equiv H bonded to C3 is substituted by ²H and 2D \equiv H bonded to C2 is substituted by ²H) was carried out. Of these quadrupolar nuclei, only ¹⁴N quadrupole hyperfine structures were previously studied for **8**^[47,48] and **9**^[49]. Nonetheless, through these two works, only χ_+ ($=(\chi_{bb} + \chi_{cc})$) values were unambiguously found; the χ_- ($=(\chi_{bb} - \chi_{cc})$) being set to zero for **9**^[49], whereas its determination had been unsuccessful

for **8**^[47]. That is, no χ_{aa} , χ_{bb} , χ_{cc} and χ_{ab} values for the ¹⁴N nucleus either for **8** or **9** were yet reported. Moreover, for the first time, the ³³S and D quadrupole hyperfine structures for **8** and **9** are investigated.

The current work is expected to supplement the existing data for the ¹⁴N quadrupole hyperfine nuclei within **8** and **9** and to provide new data for hyperfine structures for the remaining studied isotopologues. These results are intended to be of great importance for astrophysicists in the search for new species in the ISM.

5.2 Computational details

The method for the determination of the geometrical parameters for **8** and **9** is described in our previous work^[50] (see Chapter 4). From calculated rotational parameters for **8**, **9** and some of their isotopologues computed at M06-2X/6-31G(d,p) level of theory (including the empirical corrections), the rotational spectra were computed using the SPFIT/SPCAT package^[51] for J up to 100 and at different temperatures. The "assignments" of rotational transitions as well as the analysis of quadrupole hyperfine splittings are also done using the SPFIT/SPCAT. The input files for SPFIT are generated using the ASFIT program of the ASFIT/ASROT package from PROSPE web site^[52,53]. In order to keep valuable data, we employ a strength cut off for intensities to account for the decreasing sensitivity of experimental instrumentation with increasing frequency or to capture lines with comparable transition dipole moments, as proposed by^[54]

$$10^{\text{LOGINT}} > 10^{\text{LOGSTR0}} + (\nu/300 \text{ GHz})^2 \times 10^{\text{LOGSTR1}}$$

where ν is the frequency in nm^2MHz units at 300 K. The two-dimensionless constants LOGSTR0 and LOGSTR1 were set to -9 and -7 , respectively as suggested by Coudert et al.^[55]. The selection rule selection rule for the rotational quantum number J gives rise certain series of blanchs: $\Delta J = +1$ (R blanch), $\Delta J = 0$ (Q blanch) and $\Delta J = -1$ (P blanch). The selection rules for asymmetric top molecules depend to the components of the molecular dipole moments μ_a , μ_b and μ_c along the molecular three principle inertial axes since, in order to have a rotational spectrum, a molecule must hold a permanent dipole moment. For non vanishing dipole moment, every nonvanishing dipole moment component yields a set of rotational transitions obeying certain selection rules corresponding to the dipole moment components: a-type selection rules, b-type selection rules and c-type selection rules. The a-type selection rule is : $\Delta K_a = 0(\pm 2, \pm 4, \dots)$ and $\Delta K_c = \pm 1(\pm 3, \pm 5, \dots)$; for b-type, we have: $\Delta K_a = \pm 1(\pm 3, \pm 5, \dots)$ and $\Delta K_c = \pm 1(\pm 3, \pm 5, \dots)$ and for c-type: $\Delta K_a = \pm 1(\pm 3, \pm 5, \dots)$ and $\Delta K_c = 0(\pm 2, \pm 4, \dots)$.

5.3 Results and discussion

5.3.1 Molecular geometry

The structural shapes of **8** and **9** are shown on the Figure 4.1 and the geometrical parameters summarized in Table 4.1. Table 5.1 presents the M06-2X/6-31G(d,p) best predicted structures (with empirical corrections) of some selected isotopologues of **9** and 2CN (¹⁵N⁻, ³³S⁻, ³⁴S-3CNT and ¹⁵N⁻, ³³S⁻, ³⁴S-2CNT). Calculated asymmetry parameters κ ^[56,57] for **8**, **9** and their isotopologues (i.e., $\kappa = -0.783, -0.762, -0.774, -0.918, -0.907$ and -0.912 for ³³S-2C¹⁵NT, 2C¹⁵NT-3D, **8**, ³³S-3C¹⁵NT, 3C¹⁵NT-2D and **9**, respectively) are presented in Table 5.2 and Table 5.3. These values show that all the compounds investigated are *near prolate* asymmetric molecules, with asymmetry parameter closer to that of a prolate top ($\kappa = -1$). From these results, it can be seen that **8** and its isotopologues species

Table 5.1 – M06-2X/6-31G(d,p) best predicted after empirical corrections structures of **9** and **8** isotopologues (distances in Å^o, angles in °)

9 isotopologues ¹				8 isotopologues ¹			
Parameters	¹⁵ N–3 CNT	³³ S–3 CNT	³⁴ S–3 CNT	Parameters	¹⁵ N– 8	³³ S– 8	³⁴ S– 8
Bond lengths				Bond lengths			
S1 - C2	1.7134	1.7130	1.7130	S1 - C2	1.7252	1.7252	1.7252
S1 - C5	1.7264	1.7260	1.7260	S1 - C5	1.7144	1.7144	1.7144
C2 - C3	1.368	1.3684	1.3684	C2 - C3	1.3715	1.3715	1.3715
C3 - C4	1.4280	1.4279	1.4279	C3 - C4	1.4131	1.4131	1.4131
C4 - C5	1.3684	1.3578	1.3578	C4 - C5	1.3715	1.3715	1.3715
C3 - C6	1.4313	1.4320	1.4315	C2 - C6	1.4269	1.4269	1.4269
C6 - N7	1.1560	1.1550	1.1550	C6 - N7	1.1570	1.1570	1.1570
C2 - D8	1.0802	1.0802	1.0802	C3 - D8	1.0825	1.0825	1.0825
C4 - D9	1.0819	1.0819	1.0819	C4 - D9	1.0821	1.0821	1.0821
C5 - D10	1.0802	1.0802	1.0802	C5 - D10	1.0806	1.0806	1.0806
Bond angles				Bond angles			
S1 - C2 - C3	111.469	111.471	111.471	S1 - C2 - C3	111.859	111.859	111.859
S1 - C5 - C4	112.096	112.098	112.098	S1 - C5 - C4	112.166	112.166	112.166
C2 - S1 - C5	91.640	91.648	91.648	C2 - S1 - C5	91.207	91.207	91.207
C2 - C3 - C4	112.910	112.905	112.905	C2 - C3 - C4	112.346	112.346	112.346
C3 - C4 - C5	111.884	111.879	111.879	C3 - C4 - C5	112.423	112.423	112.423
C3 - C6 - N7	179.576	179.579	179.578	C2 - C6 - N7	179.853	179.853	179.853
C4-C3-C6	124.006	124.009	124.009	S1 -C2-C6	121.235	121.235	121.235
S1 -C2-D8	121.195	121.196	121.197	C4-C3-D8	125.028	125.028	125.028
C3-C4-D9	123.644	123.649	123.648	C3-C4-D9	124.200	124.200	124.200
S1 -C5-D10	119.963	119.965	119.9650	S1 -C5-D10	119.826	119.826	119.826

¹ The atoms numbering order is shown on the scheme 1

are more asymmetric than **9** and its isotopologues compounds. These values compared to that of thiophene, i.e., $\kappa = 0.092$ (Table A.14), are less asymmetric than thiophene whose value approaches that of the most asymmetric ($\kappa = 0$). Note that, unlike the other species, thiophene tends to be oblate. Compound **8**, **9** and their isotopologues correspond all to the representation I^r (with $I_a < I_b < I_c$ so that $I_z < I_x < I_y$ with $x \leftarrow b, y \leftarrow c$ and $z \leftarrow a$) and to the C_s point group. Their parent, thiophene, belongs to the C_{2v} point group. The analysis of results in Table 5.2 and Table 5.3, reveals that, whether for **8** and **9**, the studied deuterated forms are more asymmetric than all the corresponding investigated species.

5.3.2 Microwave spectra

5.3.2.1 Rotational parameters and dipole moments.

The calculated rotational parameters are given in Table 5.2 for **8**, ³³S-2 C¹⁵NT and 2C¹⁵NT-3D and Table 5.3 for **9**, ³³S-3 C¹⁵NT and 3C¹⁵NT-2D. It is of common knowledge that only molecules with a permanent dipole moment show rotational spectra. Calculated principal inertial axes dipole moment components are found to be $\mu_a = 4.58$ D, $\mu_b = -0.79$ D, $\mu_c = 0$ for **8** (Table 5.2) and $\mu_a = 4.01$ D, $\mu_b = -0.59$ D, $\mu_c = 0$ in case of **9** (Table 5.3). Their calculated total dipole moments are $\mu_{\text{tot}} = 4.642$ D and $\mu_{\text{tot}} = 4.053$ D, respectively. These results are in good agreement with the experimental data for **8** ($\mu_{\text{tot}} = 4.51$ D^[59] and $\mu_{\text{tot}} = 4.47$ D^[59]) and for **9** ($\mu_{\text{tot}} = 4.13$ D^[49]). The results show that total dipole moments for isotopologues ³³S-2 C¹⁵NT, ³³S-3 C¹⁵NT, 2C¹⁵NT-3D and 3C¹⁵NT-2D are very closer to those of their parent molecules. The same results reveal that no c-type transitions should be expected, all μ_c components being equal to zero. Principle inertial moments are also provided in the same tables. Values of these physical parameters show that components along x and y , i.e., I_x and I_y (or, I_b and I_c) are greater in **9** and its isotopologues

Table 5.2 – Experimental and M06-2X/6-31G(d,p) calculated rotational parameters for **8**, ^{33}S - $2\text{C}^{15}\text{NT}$ and $2\text{C}^{15}\text{NT-3D}$ (a deuterated form of **8**).

	8			$^{33}\text{S-}2\text{C}^{15}\text{NT}$	$2\text{C}^{15}\text{NT-3D}^3$
	Exp ¹	Exp ²	Calc	Calc.	Calc
A(MHz)	5401.350	5402.387	5402.345	5326.958	5094.386
B(MHz)	1816.260	1816.253	1816.263	1756.844	1758.817
C(MHz)	1358.640	1358.614	1359.275	1321.131	1307.430
Δ_J (kHz)	0.172	-0.092	0.112	0.107	0.106
Δ_K (kHz)	19.900	-6.683	4.140	4.092	4.068
Δ_{KJ} (kHz)	1.868	2.889	0.173	0.101	0.163
δ_J (kHz)	0.018	0.098	0.038	0.036	0.038
δ_K (kHz)	1.700	-4.852	0.592	0.578	0.534
μ_a (Debye)	4.510	4.470	4.575	4.572	4.573
μ_b (Debye)	0.860	0.736	-0.787	-0.809	-0.801
μ_c (Debye)	0.000	0.000	0.000	0.000	0.000
μ_{tot} (Debye)	4.591	4.53	4.642	4.643	4.643
I_{aa} (amu \AA^2)	93.565		93.548	94.872	99.203
I_{bb} (amu \AA^2)	278.251		278.253	287.662	287.340
I_{cc} (amu \AA^2)	371.972		371.800	382.536	386.543
χ_{aa} (MHz)			-3.810	-26.906	-0.043
χ_{bb} (MHz)			2.328	3.512	0.155
χ_{cc} (MHz)			1.482	23.393	-0.112
χ_{ab} (MHz)			0.483	-7.801	0.119
χ_+ (MHz)		4.04 \pm 0.16	3.810	26.905	0.036
χ_- (MHz)			0.845	-19.881	0.267
κ			-0.774	-0.783	-0.762

¹ From Ref. [47]; ² From Ref. [48]; ³ $2\text{C}^{15}\text{NT-3D}$ indicates that the H atom bonded to C3 (i.e., H8) is replaced by ^2H (see Figure 4.1 for the numbering scheme).

than in **8** and its isotopologues. The opposite is observed for the z components, i.e., values for I_z (I_a) are lower in the former than in the latter. Moreover, in each set, components for the commonly stables compounds are lower than those for their isotopologues. For instance, components for **8** or **9** are lower than those for $^{33}\text{S-}2\text{C}^{15}\text{NT}$ and $2\text{C}^{15}\text{NT-}2\text{D}$ (Table 5.2) or $^{33}\text{S-}3\text{C}^{15}\text{NT}$ and $3\text{C}^{15}\text{NT-}2\text{D}$ (Table 5.3). Furthermore, value components for $2\text{C}^{15}\text{NT-}2\text{D}$ or $3\text{C}^{15}\text{NT-}2\text{D}$ are greater than $^{33}\text{S-}2\text{C}^{15}\text{NT}$ or $^{33}\text{S-}3\text{C}^{15}\text{NT}$ (see the same tables). Taking into account the relationship between line intensity, linestrength and dipole moment components for a given temperature^[54], it is obvious that the rotational spectra of different molecular species are dominated by strong a-type transitions and weak b-type transitions. Moreover, from dipole moment components, both a-type and b-type transitions of **8** are expected to be stronger than those of **9**. The same conclusions are expected to be drawn between rotational transitions of **8** and **9** isotopologues, **8** isotopologues dipole moments being greater than those for **9**.

5.3.2.2 Rotational spectra.

Table 5.4 presents both calculated and available experimental rotational transitions and their corresponding frequencies (in MHz) for **9**, **8** and thiophene. A very accurate prediction and an excellent agreement between experimental and predicted spectra is achieved, except for the line $10_{46} \leftarrow 10_{37}$ for **9**, experimentally found at 39835.700 MHz^[49] and predicted, in this work, at 39853.474 MHz, i.e., with a deviation $\nu_{\text{Calc}} - \nu_{\text{Exp}} = 17.774$ MHz. When this line is excluded, the calculation of standard deviations ends up to RMS=0.049 MHz. It is evaluated at 0.275MHz for **8**. Concerning the thiophene, the experimental tran-

Table 5.3 – Experimental and M06-2X/6-31G(d,p) calculated rotational parameters for **9**, ^{33}S - $3\text{C}^{15}\text{NT}$ and $3\text{C}^{15}\text{NT-2D}$ (deuterated form of **9**).

	9		$^{33}\text{S-}3\text{C}^{15}\text{NT}$	$3\text{C}^{15}\text{NT-2D}^2$
	Exp ¹	Calc	Calc.	Calc
A(MHz)	7115.180	7115.536	7086.222	6711.333
B(MHz)	1491.299	1491.039	1432.737	1446.650
C(MHz)	1232.535	1232.725	1191.776	1190.116
Δ_{J} (kHz)	0.043	0.046	0.043	0.043
Δ_{K} (kHz)	1.97	3.518	3.697	2.426
Δ_{KJ} (kHz)	1.028	0.964	0.912	0.968
δ_{J} (kHz)	0.0089	0.010	0.009	0.010
δ_{K} (kHz)	0.670	0.693	-0.100	0.674
μ_{a} (Debye)	4.090	4.011	4.010	4.012
μ_{b} (Debye)	0.560	-0.587	-0.592	-0.576
μ_{c} (Debye)	0.000	0.000	0.000	0.000
μ_{tot} (Debye)	4.130	4.053	4.053	4.053
I_{aa} (amu \AA^2)	71.050	71.025	71.319	75.302
I_{bb} (amu \AA^2)	338.988	338.944	352.738	349.344
I_{cc} (amu \AA^2)	410.155	409.970	424.056	424.647
χ_{aa} (MHz)		-3.813	-2.262	-0.080
χ_{bb} (MHz)		2.157	-19.480	0.196
χ_{cc} (MHz)		1.657	21.747	0.117
χ_{ab} (MHz)		0.553	14.561	-0.073
χ_{+} (MHz) ³	4.12 \pm 0.06	3.814	2.267	0.313
χ_{-} (MHz) ⁴	0.000	0.500	-41.227	0.079
κ		-0.912	-0.918	-0.907

¹ From Ref. [49]; ² $3\text{C}^{15}\text{NT-2D}$ indicates that the H atom bonded to C2 (i.e., H8) is replaced by

²H (see Figure 4.1 for the numbering scheme); ³ $\chi_{+} = \chi_{\text{bb}} + \chi_{\text{cc}}$; ⁴ $\chi_{-} = \chi_{\text{bb}} - \chi_{\text{cc}}$.

sitions marked with asterisks in Table 5.4 are not theoretically reproduced in this work. When these transitions are excluded, we find a smaller error $\text{RMS} \approx 0.086\text{MHz}$, whereas this RMS value increases up to 7.486 MHz, when they are included. Figure 5.1 presents simulated spectra for **8** (in red color), **9** (green color) and thiophene (blue color) at $T = 10\text{K}$. As expected, the thiophene with a total dipole moment almost equals to zero $\mu_{\text{tot}} = 0.571\text{D}$ has spectral line intensities very low compared to those of **8** and **9**. Its spectrum is thus too weak to appear in front of **8** and **9** spectra (with $\mu_{\text{tot}} = 4.053\text{D}$ and $\mu_{\text{tot}} = 4.642\text{D}$, respectively).

Detailing the computed spectra at a temperature $T = 300\text{K}$, especially, in the frequency range under study ($3 - 300\text{GHz}$ or $1\text{mm} - 10\text{cm}$) and for J up to 100, 5820 a-type rotational lines are identified for thiophene. A further analysis of these lines shows that 2571 among them are of ^aR-type and 3249 of ^aQ-type transitions. No ^aP-type transitions found to fulfil the intensity cutoff condition. We expect to find stronger transitions for $\Delta K_{-1} = 0$ and $\Delta K_{-1} = \pm 1$. However, due to its low $\mu_{\text{tot}} = \mu_{\text{a}}$ dipole moment, as shown in Table A.14, all these transitions exhibit very low intensities, recalling that the line intensity strongly depends on the line strength value and the dipole moment components, through the factor ${}^x\text{S}_{\text{fi}}\mu_{\chi}^2$ (where i and f are initial and final states, respectively, and μ_{χ} , the dipole moment component along an axis χ)^[54].

Regarding **8**, about 40987 rotational transitions are identified and assigned in the same conditions as above. Among them, 20530 lines are of the a-type, whereas, the remaining 20457 ones are of b-type. Relying on its dipole moment components (Table 5.2), the predicted spectrum of **8** should contain strong a-type transitions and b-type weak ones. As a matter of fact, the 20530 a-type transitions are grouped into 5460 ^aP-, 4583 ^aQ- and

Table 5.4 – Comparison of experimental and calculated (using calculated rotational parameters in Table 5.2) rotational transitions and their corresponding frequencies ν (in MHz) for **9**, **8** and thiophene

3CNT				8			
Transition ^a	$\nu_{\text{exp}}^{\text{b}}$	ν_{cal}	$\nu_{\text{calc}} - \nu_{\text{exp}}$	Transition ^a	$\nu_{\text{exp}}^{\text{c}}$	ν_{cal}	$\nu_{\text{calc}} - \nu_{\text{exp}}$
4 ₁₄ ← 3 ₁₃	10360.955	10360.887	-0.068	3 ₁₃ ← 2 ₁₂	8813.580	8813.565	-0.015
4 ₀₄ ← 3 ₀₃	10808.667	10808.668	0.001	3 ₀₃ ← 2 ₀₂	9362.600	9362.529	-0.071
4 ₁₃ ← 3 ₁₂	11394.832	11394.827	-0.005	3 ₂₂ ← 2 ₂₁	9524.150	9524.569	0.419
4 ₃₁ ← 3 ₂₂	39684.917	39684.917	0.000	3 ₂₁ ← 2 ₂₀	9687.110	9686.663	-0.447
4 ₃₂ ← 3 ₂₁	39639.960	39640.070	0.110	3 ₁₂ ← 2 ₁₁	10184.150	10184.122	-0.028
5 ₁₅ ← 4 ₁₄	12935.946	12935.955	0.009	3 ₃₁ ← 2 ₂₀	28583.180	28583.368	0.188
5 ₀₅ ← 4 ₀₄	13447.532	13447.575	0.043	3 ₃₀ ← 2 ₂₁	28626.490	28626.744	0.254
5 ₁₄ ← 4 ₁₃	14225.926	14225.900	-0.025	4 ₁₄ ← 3 ₁₃	11708.570	11708.583	0.013
6 ₁₆ ← 5 ₁₅	15501.884	15501.879	-0.005	4 ₀₄ ← 3 ₀₃	12307.400	12307.352	-0.048
6 ₁₅ ← 5 ₁₄	17044.135	17044.183	0.048	4 ₁₃ ← 3 ₁₂	13525.070	13525.268	0.198
6 ₃₄ ← 6 ₂₅	28924.770	28924.706	-0.064	5 ₁₅ ← 4 ₁₄	14573.020	14573.157	0.137
7 ₀₇ ← 6 ₀₆	18607.678	18607.688	0.010	5 ₀₅ ← 4 ₀₄	15136.840	15137.039	0.199
7 ₂₆ ← 6 ₂₅	18999.006	18999.006	-0.000	5 ₁₄ ← 4 ₁₃	16813.370	16813.480	0.110
7 ₆₁ ← 6 ₆₀	19090.700	19090.695	-0.005	6 ₁₅ ← 6 ₁₆	9421.100	9421.329	0.229
7 ₅₂ ← 6 ₅₁	19097.433	19097.399	-0.034	6 ₅₂ ← 5 ₅₁	19152.070	19151.588	-0.482
7 ₂₅ ← 6 ₂₄	19457.790	19457.715	-0.075	6 ₅₁ ← 5 ₅₀	19152.070	19151.633	-0.437
7 ₁₆ ← 6 ₁₅	19846.074	19846.080	0.006	6 ₃₄ ← 5 ₃₃	19215.810	19215.625	-0.185
7 ₁₇ ← 6 ₀₆	21567.419	21567.407	-0.012	6 ₃₃ ← 5 ₃₂	19340.400	19340.442	0.042
8 ₁₈ ← 7 ₁₇	20603.020	20603.005	-0.015	6 ₁₅ ← 5 ₁₄	20027.360	20027.394	0.034
8 ₀₈ ← 7 ₀₇	21128.545	21128.540	-0.005	6 ₂₄ ← 5 ₂₃	20035.740	20035.682	-0.058
8 ₂₇ ← 7 ₂₆	21684.306	21684.299	-0.007	7 ₁₆ ← 7 ₁₇	12353.200	12353.547	0.347
8 ₇₁ ← 7 ₇₀	21816.941	21816.921	-0.020	7 ₀₇ ← 6 ₀₆	20561.190	20561.391	0.201
8 ₆₂ ← 7 ₆₁	21822.904	21822.909	0.005	7 ₁₇ ← 6 ₀₆	21199.660	21200.314	0.654
8 ₂₆ ← 7 ₂₅	22345.263	22345.289	0.026	7 ₂₆ ← 6 ₂₅	21908.810	21908.759	-0.051
8 ₁₇ ← 7 ₁₆	22627.461	22627.467	0.006	7 ₄₄ ← 6 ₄₃	22423.150	22423.104	-0.046
8 ₁₈ ← 7 ₀₇	23562.613	23562.724	0.111	7 ₄₃ ← 6 ₄₂	22435.990	22435.824	-0.166
8 ₂₇ ← 8 ₁₈	22057.226	22057.179	-0.047	8 ₁₈ ← 7 ₁₇	22990.070	22989.970	-0.100
8 ₃₆ ← 8 ₂₇	29242.617	29242.586	-0.031	8 ₁₈ ← 7 ₀₇	23628.450	23628.893	0.443
9 ₈₁ ← 8 ₈₀	24543.122	24543.101	-0.021	8 ₄₅ ← 7 ₄₄	25673.160	25672.841	-0.319
9 ₇₂ ← 8 ₇₁	24548.659	24548.652	-0.007	8 ₄₅ ← 8 ₃₆	26594.390	26593.689	-0.701
9 ₁₉ ← 8 ₀₈	25571.786	25571.786	0.000	8 ₅₄ ← 8 ₄₅	34088.820	34089.103	0.283
9 ₀₉ ← 8 ₁₈	21182.199	21182.168	-0.031	9 ₂₇ ← 9 ₂₈	8870.200	8870.000	-0.200
10 ₀₁₀ ← 9 ₀₉	26079.562	26079.578	0.016	9 ₄₆ ← 8 ₄₅	28934.620	28934.351	-0.269
10 ₉₁ ← 9 ₉₀	27269.214	27269.200	-0.014	9 ₄₅ ← 8 ₄₄	29015.260	29015.041	-0.219
10 ₂₉ ← 9 ₁₈	38820.194	38820.168	-0.026	9 ₂₇ ← 8 ₂₆	30451.290	30451.199	-0.091
10 ₄₆ ← 10 ₃₇	39835.700	39853.474	17.774	10 ₂₈ ← 10 ₂₉	11856.850	11856.950	0.100
10 ₁₉ ← 10 ₁₁₀	13925.416	13925.316	-0.100	12 ₃₉ ← 12 ₃₁₀	7305.140	7304.923	-0.217
13 ₁₂₁ ← 12 ₁₂₀	35446.781	35446.786	0.005	13 ₃₁₀ ← 13 ₃₁₁	10156.050	10156.256	0.206
13 ₁₁₂ ← 12 ₁₁₁	35451.698	35451.711	0.013				
13 ₁₁₂ ← 12 ₁₁₁	36056.942	36056.937	-0.005				
13 ₃₁₀ ← 12 ₃₉	36080.816	36080.807	-0.009				
14 ₁₃₁ ← 13 ₁₃₀	38172.338	38172.349	0.011				
15 ₁₁₄ ← 15 ₁₁₅	28124.106	28124.332	0.226				
17 ₁₁₆ ← 17 ₁₁₇	34056.248	34056.127	-0.121				
20 ₂₁₈ ← 20 ₂₁₉	28702.487	28702.478	-0.009				
Thiophene ^d							
1 ₀₁ ← 0 ₀₀	8654.041	8653.918	-0.123	2 ₁₂ ← 1 ₁₁	15125.590	15125.443	-0.147
2 ₁₁ ← 1 ₁₀	19490.534	19490.380	-0.154	3 ₁₂ ← 3 ₁₃	12833.981	12833.968	-0.013
3 ₁₃ ← 2 ₁₂	22202.321	22202.290	-0.031	3 ₀₃ ← 2 ₀₂	23044.130	23044.091	-0.039
3 ₂₂ ← 2 ₂₁	25962.050	25962.096	0.046	4 ₂₂ ← 4 ₂₃	9061.310	9061.346	0.036
4 ₁₃ ← 4 ₁₄	20212.550	20212.556	0.006	6 ₃₃ ← 6 ₃₄	11099.734	11099.697	-0.037
7 ₄₃ ← 7 ₄₄	6139.040*	6139.035	-0.005	9 ₅₄ ← 9 ₅₅	6958.820*	6958.544	-0.276
11 ₆₅ ← 11 ₆₆	7605.258*	7604.475	-0.783	15 ₈₇ ← 15 ₈₈	8475.693*	8472.996	-2.697
17 ₉₈ ← 17 ₉₉	8737.352*	8733.180	-4.172	19 ₁₀₉ ← 19 ₁₀₁₀	8903.731*	8897.709	-6.022
21 ₁₁₀ ← 21 ₁₁₁₁	8987.693*	8979.435	-8.258	23 ₁₂₁₁ ← 23 ₁₂₁₂	9000.604*	8989.725	-10.879
25 ₁₃₁₂ ← 25 ₁₃₁₃	8952.582*	8938.702	-13.880	27 ₁₄₁₃ ← 27 ₁₄₁₄	8852.656*	8835.414	-17.242
29 ₁₅₁₄ ← 29 ₁₅₁₅	8708.901*	8687.957	-20.944				

^a $J'_{K-K_+} \leftarrow J''_{K-K_+}$; ^b [47]; ^c [49]; ^d [58].

* Frequencies measured by WG-MWFT [58]

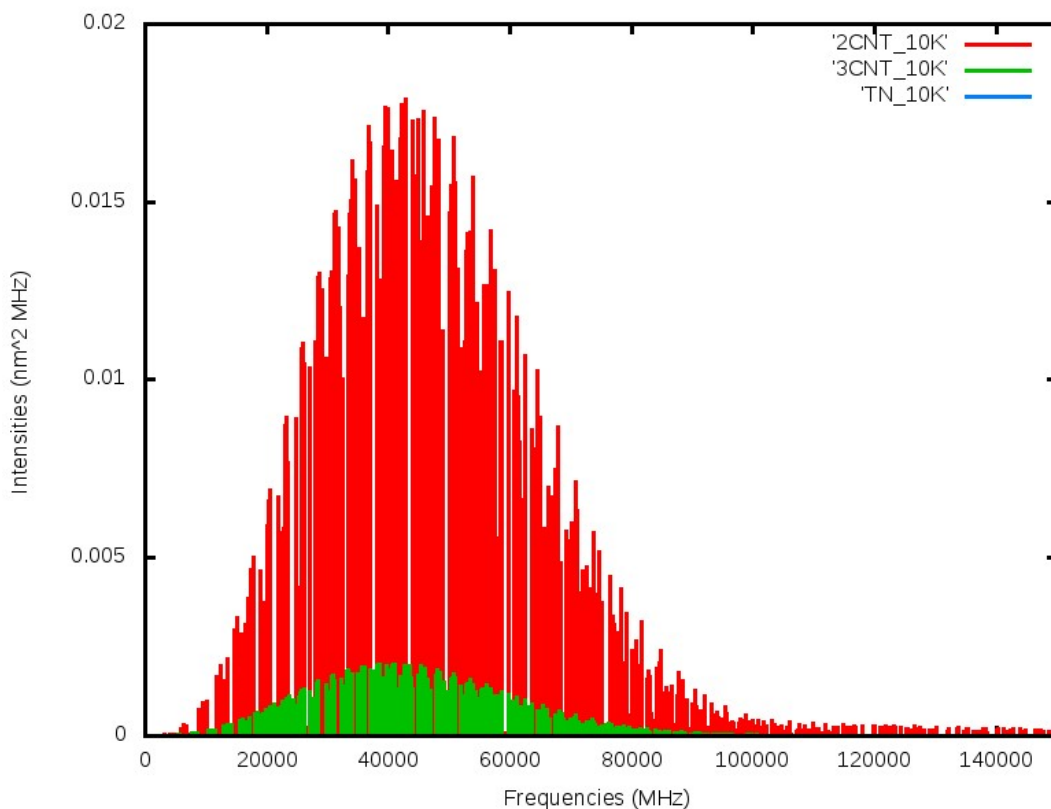


Figure 5.1 – Simulated rotational spectra for **8** (in red color), **9** (green color) and thiophene (blue color) at temperature $T = 10$ K.

10487 aR -type transitions. Likewise, the 20457 b -type transitions are grouped into 7074 bP -, 6093 bQ - and 7290 bR -type transitions. As expected, Table 5.2b reveals that all the b -type transitions are weak. Concerning the 5460 aP - transitions, as shown by their low absorption coefficients ($< 10^{-8} \text{cm}^{-1}$), they are also very weak. Likewise, 1609 aR -type transitions characterized by $|\Delta K_{-1}| \geq 2$, and $|\Delta K_{+1}| \geq 1$ are also, as b -type and aP -type transition, weak. Only aR -type transitions characterized by $\Delta K_{-1} = 0$ and $|\Delta K_{+1}| = \pm 1$ are strong lines (almost all of them have $|\Delta K_{+1}| = 1$). We identify 8878 lines of this type for **8**.

Finally, concerning **9**, 17575 lines are predicted in the domain and conditions quoted above. The spectrum of this molecule **9** presents strong a -type and weak b -type transitions. The 17575 transitions are then grouped into 10672 a -type and 6903 b -type transitions. As in case of **8**, the strongest lines are of aR -type transitions characterized by $\Delta K_{-1} = 0$ and $|\Delta K_{+1}| = \pm 1$. This is the case for 9068 lines, the remaining 98 aR -type lines, as well as 1506 aQ -type, being weak. No P -type lines fulfilling the cutoff line strength condition are identified. In general, whether for **8** and **9**, computed spectra are characterized by stronger a -type and weaker b -type. No b -type transitions were identified among the stronger lines found in section 5.3.2.4 (see Table 5.5 - Table 5.7 and Table 5.10 - Table 5.12).

5.3.2.3 Isotopic analysis

The increased sensitivity and high spectral resolution of millimeter telescopes allow an increasing number of isotopically substituted molecules in the interstellar medium to be detected^[60]. The microwave spectral data for different isotopologues are very valuable, especially, in searching for new species in the universe. In fact, the isotopic species that should be concerned by the study are ^{34}S , ^{33}S , ^{13}C , ^{14}C , ^{15}N and ^2H (or D).

Studies on isotopic abundance in ISM were performed^[61–64]. For instance, the comparison between terrestrial isotopic abundance and that of the star IRC + 10216 performed with Kahane and his/her coworkers^[62] has shown that $^{28}\text{Si}/^{29}\text{Si}=19.6$ (earth) and 18.7 in the star, $^{28}\text{Si}/^{30}\text{Si}=29.8$ (earth) and 28.6 in the star, $^{32}\text{S}/^{34}\text{S}=22.5$ (earth) and 20.2 in the star, $^{32}\text{S}/^{33}\text{S}=125$ (earth) and 100 in the star, $^{34}\text{S}/^{33}\text{S}=5.5$ (earth) and 5.7 in the star, $^{12}\text{C}/^{13}\text{C}=89$ (earth) and 47 in the star, $^{14}\text{N}/^{15}\text{N}=277$ (earth) and >4400 in the star.

The D/H ratio was found to be in the range 1.26 – 1.49 in the different terrestrial environments while it can reach 10.90 in the atmosphere of Mars^[65]. From these results, it can be seen that the isotopic abundance on the earth differs significantly from that in the space for nitrogen. It is almost the same for sulfur. Whereas, the N isotopic composition varies by no more than 2%, it can reach 500% in the solar system^[66]. The survey of the literature shows that the $^{14}\text{N}/^{15}\text{N}$ ratio is in the range 100– ~ 5000 in the different ISM environments (see Wampfler et al.^[67] and references therein).

A deep analysis of rotational spectra of isotopologues and isotopomers at the same time and same conditions as quoted above would yield a huge amount of results that we cannot deal with. Consequently, we now investigate some of them, especially, species containing only one quadrupolar nucleus, i.e., $^{15}\text{N}^-$, $^{33}\text{S}^-$, $^{34}\text{S}-3\text{CNT}$ and $^{15}\text{N}^-$, $^{33}\text{S}^-$, $^{34}\text{S}-2\text{CNT}$. Beside this set, rotational spectra of $^{34}\text{S}-$ and $^{15}\text{N}-3\text{CNT}$ for which experimental rotational constants and a small number of rotational lines are available in the literature are also analyzed and the results compared with the experimental data. Table 5.2 and Table 5.3 list predicted rotational parameters (rotational and centrifugal distortion constants, dipole moment components, inertial principal moment components and nuclear quadrupole coupling constants) for $^{33}\text{S}-3\text{CNT}$; $^{34}\text{S}-$, $^{15}\text{N}-$, $^{33}\text{S}-2\text{CNT}$ and deuterated forms, recalling that experimental data are not yet available.

Microwave spectra for $^{34}\text{S}-$, $^{15}\text{N}-3\text{CNT}$ are simulated and a comparison to experimental results is done for transitions having experimental data as shown in Table A.15. From this table, a good agreement between calculated and experimental results is again achieved with a $\text{RMS} = 0.072 \text{ MHz}$ for $^{34}\text{S}-3\text{CNT}$ and $\text{RMS} = 0.029 \text{ MHz}$ in case of $^{15}\text{N}-3\text{CNT}$. Considering all calculated rotational transitions, we obtain 20598 lines for ($^{15}\text{N}-3\text{CNT}$) and 13465 lines for $^{34}\text{S}-3\text{CNT}$. The 20598 of $^{15}\text{N}-3\text{CNT}$ are grouped into 11525 **a**-type and 5270 **b**-type lines whereas the 13465 lines of $^{34}\text{S}-3\text{CNT}$ are subdivided into 8192 **a**-type and 5273 **b**-type lines. As for their parent molecule, both $^{34}\text{S}-3\text{CNT}$ and $^{15}\text{N}-3\text{CNT}$ spectra are dominated by stronger **a**-type, especially, $^{\text{a}}\text{R}$ -type lines characterized by $|\Delta K_{-1}| = 0$, and $|\Delta K_{+1}| = \pm 1$. (i.e., 6801 lines for $^{34}\text{S}-3\text{CNT}$ and 9661 in case of $^{15}\text{N}-3\text{CNT}$). Their rotational spectra have comparable peak intensity (comparable absorption coefficients $\alpha_{\text{m}} = 1.90 \times 10^{-5} \text{ cm}^{-1}$ for $^{15}\text{N}-3\text{CNT}$ and $\alpha_{\text{m}} = 1.92 \times 10^{-5} \text{ cm}^{-1}$ for $^{34}\text{S}-3\text{CNT}$) and, consequently, of comparable intensity with their parent molecule **9**. The $^{\text{a}}\text{Q}$ -type and $^{\text{b}}\text{Q}$ -type transitions ($^{\text{b}}\text{R}-$, $^{\text{b}}\text{Q}$ -type transitions, as well as $^{\text{a}}\text{R}$ -type transitions with $|\Delta K_{-1}| > 2$) are weak for both isotopologues. A high chance of detectability for these two compounds is again expected at high values J, around the same range of frequency.

5.3.2.4 Hyperfine structure analysis and optimum region of detectability.

The hyperfine spectra of **9** and **8** at different temperatures (i.e., at 8.6, 10, 30 and 150 K) are shown on Figures 5.2a and 5.2b, respectively. The analysis of hyperfine spectra for these molecular species and their isotopologues is done taking into account the environmental conditions of the place in the ISM where they are likely to be observed. In fact, the investigated species are all unstaturated aromatic compounds with a number of atoms greater than six. They are then classified among complex organic molecules. Complex

Table 5.5 – Strongest microwave lines with corresponding hyperfine splitting components for **8** at 8.6, 9.375, 10.0 and 30.0 K.

Transition	ν_{cal} (MHz)	Est.Err ¹ (MHz)	Int. ²	Transition	ν_{cal} (MHz)	Est.Err ¹ (MHz)	Int. ²
T=8.6 K							
12 _{2,10} ← 11 _{2,9}	40018.3118	0.2821	19.3370	13 _{2,11} ← 12 _{2,10}	42933.1484	0.4533	0.1053
	40018.4548	0.2911	21.0300		42933.3901	0.4748	17.6890
	40018.4711	0.2925	17.7790		42933.5660	0.4854	19.1130
	40018.8551	0.3709	0.1353		42933.5821	0.4866	16.3710
13 _{2,11} ← 12 _{2,10}	42933.1484	0.4533	0.1139	13 _{2,11} ← 12 _{2,10}	42933.7904	0.5351	0.1053
	42933.3901	0.4748	19.1420		40017.8781	0.2769	0.1226
	42933.5660	0.4854	20.6820		40018.3118	0.2821	17.5310
	42933.5821	0.4866	17.7150		40018.4548	0.2911	19.0660
14 _{0,14} ← 13 _{0,13}	42933.7904	0.5351	0.1140	15 _{0,15} ← 14 _{0,14}	40018.4711	0.2925	16.1190
	39412.7583	1.4593	0.0984		40018.8551	0.3709	0.1226
	39414.9464	1.3206	19.1900		42127.2362	1.8073	0.0783
	39414.9815	1.3189	17.8600		42129.4683	1.6717	17.5440
14 _{1,14} ← 13 _{1,13}	39414.9904	1.3185	20.6190	15 _{1,15} ← 14 _{1,14}	42129.4982	1.6702	16.4070
	39417.3384	1.2794	0.0984		42129.5064	1.6699	18.7590
	39401.1737	1.4572	0.0984		42131.8902	1.6147	0.0783
	39403.3673	1.3180	19.1760		42120.7039	1.8055	0.0783
13 _{2,11} ← 12 _{2,10}	39403.3996	1.3164	17.8460	26 ← 25	42122.9390	1.6697	5.6100
	39403.4088	1.3161	20.6030		72026.2831	10.2955	5.3980
	39405.7625	1.2771	0.0983		72026.2864	10.2953	5.8303
					72026.2812	10.2961	5.6100
T=10.0 K							
13 _{2,11} ← 12 _{2,10}	42933.1484	0.4533	0.0985	26 ← 25	72026.2908	10.2955	5.3980
	42933.3901	0.4748	16.5520		72026.2941	10.2954	5.8303
	42933.5660	0.4854	17.8840		69307.2611	9.0717	5.5901
	42933.5821	0.4866	15.3180		69307.2714	9.0712	5.3705
15 _{0,15} ← 14 _{0,14}	42933.7904	0.5351	0.0985	26 ← 25	69307.2750	9.0710	5.8186
	42127.2362	1.8073	0.0739		69307.2756	9.0718	5.5901
	42129.4683	1.6717	16.5610		69307.2859	9.0712	5.3705
	42129.4982	1.6702	15.4880		69307.2895	9.0710	5.8186
15 _{1,15} ← 14 _{1,14}	42129.4982	1.6702	15.4880	27 ← 26	74745.4553	11.6258	5.5813
	42129.5064	1.6699	17.7080		74745.4642	11.6253	5.3781
	42131.8902	1.6147	0.0739		74745.4673	11.6251	5.7922
12 _{2,10} ← 11 _{2,9}	40017.8781	0.2769	0.1132	22 ← 21	73746.3879	2.2719	5.5338
	40018.3118	0.2821	16.1880		73746.5130	2.2796	5.7917
	40018.4548	0.2911	17.6060		73746.5200	2.2801	5.2873
	40018.4711	0.2925	14.8840				
12 _{2,10} ← 11 _{2,9}	40018.4711	0.2925	14.8840	21 ← 20			
	40018.8551	0.3709	0.1132				

Est.Err¹: Estimated error for calculated frequency from observed one; Int.²: intensity of the line (in $\times 10^{-3} \text{ nm}^2 \text{ MHz}$).

Table 5.6 – Selected strongest line transitions and the corresponding hyperfine splitting components of **9** at different temperatures.

Transition	V _{cat}			Transition	V _{cat}		
	Int. ²	Est.Err ¹	T=8.6 K		Int. ²	Est.Err ¹	T=9.375 K
13 ₁₁₂ ← 12 ₁₁₁	13 ← 13	0.0943	36056.3602	0.0649	0.0902	38617.5850	14 ← 14
	13 ← 12	0.0472	36056.9342	10.9080	0.0604	38618.2354	14 ← 13
	14 ← 13	0.0512	36057.0106	11.7860	0.0647	38618.3171	15 ← 14
	12 ← 11	0.0520	36057.0128	10.0950	0.0653	38618.3191	13 ← 12
	12 ← 12	0.0831	36057.6348	0.0649	0.0773	38619.0197	13 ← 13
14 ₁₁₃ ← 13 ₁₁₂	14 ← 14	0.0902	38617.5850	0.0560	0.2675	38286.7770	15 ← 15
	14 ← 13	0.0604	38618.2354	10.9520	0.0800	38288.5190	15 ← 14
	15 ← 14	0.0647	38618.3171	11.7670	0.0804	38288.5541	14 ← 13
	13 ← 12	0.0653	38618.3191	10.1920	0.0805	38288.5597	16 ← 15
	13 ← 13	0.0773	38619.0197	0.0563	0.2880	38290.4209	14 ← 14
14 ₀₁₄ ← 13 ₀₁₃	14 ← 14	0.2532	35843.6866	0.0557	0.0941	41135.3166	15 ← 15
	14 ← 13	0.0631	35845.3809	10.8590	0.0762	41136.0488	15 ← 14
	13 ← 12	0.0633	35845.4227	10.1060	0.0807	41136.1332	16 ← 15
	15 ← 14	0.0633	35845.4286	11.6670	0.0814	41136.1357	14 ← 13
	13 ← 13	0.2713	35847.2477	0.0557	0.0836	41136.9200	14 ← 14
15 ₀₁₅ ← 14 ₀₁₄	15 ← 15	0.2675	38286.7770	0.0483	0.0943	36056.3602	13 ← 13
	15 ← 14	0.0800	38288.5190	10.8090	0.0472	36056.9342	13 ← 12
	14 ← 13	0.0804	38288.5541	10.1080	0.0512	36057.0106	14 ← 13
	16 ← 15	0.0805	38288.5597	11.5570	0.0520	36057.0128	12 ← 11
	14 ← 14	0.2880	38290.4209	0.0483	0.0831	36057.6348	12 ← 12
T=10.0 K							
14 ₁₁₃ ← 13 ₁₁₂	14 ← 13	0.0604	38618.2354	9.3514	0.4080	70930.8993	25 ← 24
	15 ← 14	0.0647	38618.3171	10.0480	0.4091	70930.9266	26 ← 25
	13 ← 12	0.0653	38618.3191	8.7029	0.4092	70930.9272	24 ← 23
15 ₁₁₄ ← 14 ₁₁₃	15 ← 14	0.0762	41136.0488	9.3922	0.4632	73615.2134	26 ← 25
	16 ← 15	0.0807	41136.1332	10.0430	0.4648	73615.2488	27 ← 26
	14 ← 13	0.0814	41136.1357	8.7835	0.4649	73615.2497	25 ← 24
15 ₀₁₅ ← 14 ₀₁₄	15 ← 14	0.0800	38288.5190	9.3220	0.3577	68192.8840	24 ← 23
	14 ← 13	0.0804	38288.5541	8.7179	0.3584	68192.9027	25 ← 24
	16 ← 15	0.0805	38288.5597	9.9678	0.3584	68192.9030	23 ← 22
16 ₀₁₆ ← 15 ₀₁₅	16 ← 15	0.1004	40735.4680	9.3210	0.6682	70255.7442	28 ← 27
	15 ← 14	0.1008	40735.4976	8.7538	0.6684	70255.7518	27 ← 26
	17 ← 16	0.1009	40735.5029	9.9247	0.6684	70255.7541	29 ← 28

Est.Err¹ : Estimated error (in MHz) for calculated frequency from observed one; Int.² : intensity of the line (in $\times 10^{-3} \text{ nm}^2 \text{ MHz}$).

Table 5.7 – Hyperfine structures for deuterated $2\text{C}^{15}\text{NT} - \text{d}_3$ and $3\text{C}^{15}\text{NT} - \text{d}_2$; for $^{33}\text{S} - 2\text{C}^{15}\text{NT}$ and $^{33}\text{S} - 2\text{C}^{15}\text{NT}$ at 10.0 K.

Transition	ν_{calc} (MHz)	Est.Err ¹ (MHz)	Int. ²	Transition	ν_{calc} (MHz)	Est.Err ¹ (MHz)	Int. ²
	$2\text{C}^{15}\text{NT} - \text{d}_3$					$3\text{C}^{15}\text{NT} - \text{d}_2$	
$13_{2,11} \leftarrow 12_{2,10}$	41338.4341 41338.4693 41338.4702	0.0880 0.0880 0.0880	0.0896 13.9350 16.2690		39725.6274 39725.6573 39725.6580	0.1447 0.1447 0.1447	0.0387 8.1064 9.2086
	41338.4780 41338.5170	0.0880 0.0880	15.0570 0.0896	$15_{1,14} \leftarrow 14_{1,13}$		0.1447 0.1447	8.6682 0.0387
$15_{0,15} \leftarrow 14_{0,14}$	40535.8008 40535.8666 40535.8668	0.2660 0.2660 0.2660	0.0679 16.2560 14.2170		37309.4025 37309.4396 37309.4404	0.1122 0.1122 0.1122	0.0440 7.9853 9.2189
	40535.8681 40535.9297	0.2660 0.2660	15.2030 0.0679	$14_{1,13} \leftarrow 13_{1,12}$		0.1122 0.1122	8.5801 0.0440
$15_{1,15} \leftarrow 14_{1,14}$	40530.8980 40530.9639 40530.9641	0.2657 0.2657 0.2657	0.0678 16.2490 14.2120		39325.6626 39325.7148 39325.7148	0.0000 0.3045 0.3045	0.0339 9.1939 8.1093
	40530.9653 40531.0271	0.2657 0.2657	15.1970 0.0678	$16_{0,16} \leftarrow 15_{0,15}$		0.3045 0.0000	8.6347 0.0339
	$^{33}\text{S} - 2\text{C}^{15}\text{NT}$					$^{33}\text{S} - 3\text{C}^{15}\text{NT}$	
$13_{2,11} \leftarrow 12_{2,10}$	41700.3344 41704.7914 41704.7921	0.0891 0.0891 0.0891	0.1076 11.5470 12.4820		39748.9164 39749.1145 39749.1541	0.1383 0.1383 0.1384	0.0593 0.0794 9.1870
	41705.1473 41705.1480 41705.3304	0.0891 0.0891 0.0891	10.6840 13.4900 0.1433	$15_{1,14} \leftarrow 14_{1,13}$		0.1384 0.1383 0.1383	8.5897 9.8254 8.0319
	41709.6060	0.0891	0.1076		39750.0669	0.1384	0.0600
$15_{0,15} \leftarrow 14_{0,14}$	40962.3584 40962.4209 40962.4407	0.2645 0.2645 0.2645	11.6430 12.4530 10.8860		37294.6591 37295.4107 37295.5031	0.1099 0.1099 0.1099	0.0679 0.0902 9.0937
	40962.5032 40963.4406	0.2645 0.2645	13.3170 0.1077	$14_{1,13} \leftarrow 13_{1,12}$		0.1099 0.1099 0.1099	8.4602 9.7723 7.8719
$15_{1,15} \leftarrow 14_{1,14}$	40954.7553 40954.8180 40954.8349	0.2642 0.2642 0.2642	11.6380 12.4480 10.8810		37296.1548 37296.9989	0.1100 0.1100	0.0675 0.0675
	40954.8977 40955.8380	0.2642 0.2642	13.3100 0.1076	$16_{0,16} \leftarrow 15_{0,15}$		0.3007 0.3006 0.3006	0.0521 8.5468 9.1027

Est.Err¹: Estimated error for calculated frequency from observed one; Int.²: intensity of the line (in $\times 10^{-3} \text{nm}^{-2} \text{MHz}$)

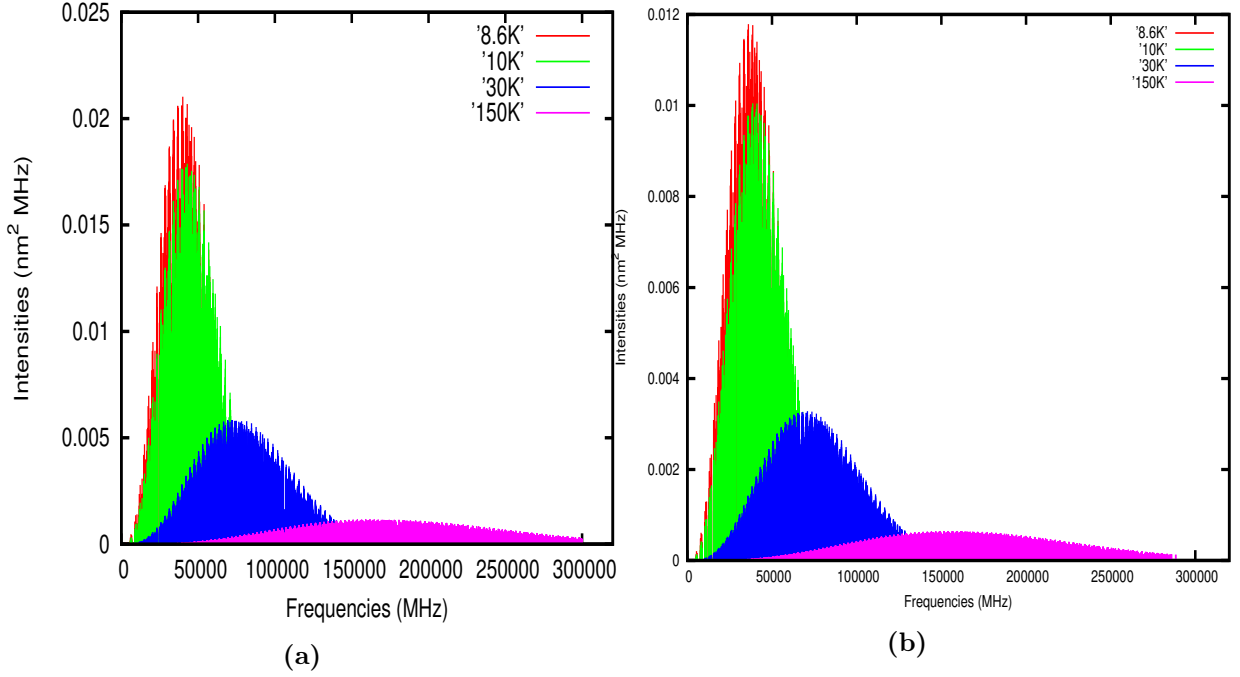


Figure 5.2 – Rotational spectra of **8** (5.2a) and **9** (5.2b) for temperatures $T = 8.6$ (red), 10.0 (green), 30.0 (blue) and 150.0 K (magenta color).

organic species have been widely detected in hot cores embedded in high-mass star forming regions, but also in low-mass hot corinos where their formation towards warm sources is well reproduced by the so-called *warm-up scenario*^[68]. More specifically, the molecular compounds in this study are therefore likely to be observed in cold dense regions like the TMC-1 ($T \sim 10$ K) which is known to be rich in unsaturated complex molecular species^[69]. The temperature in cold cores is evaluated at $T \simeq 8.6$ K to $T \simeq 10$ K^[70]. Unsaturated complex species are also found in the so-called *lukewarm corino* L1527 ($T \approx 30$ K) which is known also to contain significant abundances of complex molecules, including negative molecular ions^[69].

As then shown by the figures quoted above, the line intensity decreases with the increase of the temperature whereas the frequency coverage region increases with the temperature. Indeed, results in these figures show that, for $T = 10$ K, for example, the frequency coverage is up to ≈ 100000 MHz ≈ 100 GHz, whereas for $T = 30$ K, the frequency coverage reaches up to ≈ 300 GHz. Regarding the relationship between the line intensity and the temperature, the same results reveal that the line intensity at $T = 10$ K, for example, is about 20 times that at $T = 150$ K. Concerning the peak intensities for the investigated temperatures, the results that they are located in the region around 40 GHz for temperatures ranging from 8.6 – 10 K and for values of J around 15. Table 5.5 and Table 5.6 present strongest transitions at different temperatures ($T = 8.6, 9.375, 10.0$ and 30.0 K) for **8** and **9**, respectively. For temperatures around 30 K, the maximum peak intensity is found around 71 GHz and for J around 22 (Figure 5.2a and Table 5.5 for **8** ; Figure 5.2b and Table 5.6 for **9**). Likewise, the comparison of results in Figures 5.2a and 5.2b shows that transition lines are stronger for **8** than of **9** . In the same way, line intensities for isotopologues and for each of the two species were compared as shown on Figure 5.3 and in Table 5.7. From Figures 5.3a and 5.3b, one can see that the brightest lines for each isotopologue appear in the same region of frequency as the brightest ones for its parent. Moreover, whereas, line intensities

are remarkably different for different temperature in case of **8** isotopologues, the difference is not noticeable for **9** isotopologues. Furthermore, the results in Table 5.7 show that, at temperatures prevailing in the cold cores, where the species are expected to be found, most intense lines correspond to J in the range 12 – 17 and in the frequency range 36 – 43 GHz both for **8**, **9** and the investigated isotopologues.

Table 5.8 – Experimental and computed hyperfine splittings for **8**

$J'_{K_{-1}K_{+1}} \leftarrow J''_{K_{-1}K_{+1}}$	cal ¹ F' \leftarrow F''	exp ² F' \leftarrow F''	Int. ³	ν_{cal}	Δ_1 ⁴	ν_o ⁵	ν_{exp} ⁶	Δ_2 ⁷
$7_{61} \leftarrow 6_{60}$	8 \leftarrow 7	8 \leftarrow 7	5.6470	22338.0030	-0.3802	22338.3832	22338.6820	-0.2988
	7 \leftarrow 6		4.8647	22338.1775	-0.2057			
	9 \leftarrow 8		6.5398	22338.6200	0.2368			
	6 \leftarrow 5	6 \leftarrow 5	4.1922	22338.7946	0.4114			
and								
$7_{62} \leftarrow 6_{61}$	8 \leftarrow 7		5.6470	22338.0008	-0.3802	22338.3810	22337.7040	0.6770
	7 \leftarrow 6	7 \leftarrow 6	4.8647	22338.1754	-0.2056			
	9 \leftarrow 8		6.5398	22338.6178	0.2368			
	6 \leftarrow 5		4.1922	22338.7924	0.4114			
$9_{81} \leftarrow 8_{80}$	10 \leftarrow 9	10 \leftarrow 9	9.2348	28712.2775	-0.3034	28712.5809	28712.8800	-0.2991
	9 \leftarrow 8		8.2396	28712.3898	-0.1911			
	11 \leftarrow 10		10.3397	28712.7892	0.2083			
	8 \leftarrow 7	8 \leftarrow 7	7.3539	28712.9015	0.3206			
and								
$9_{82} \leftarrow 8_{81}$	10 \leftarrow 9		9.2348	28712.2775	-0.3034	28712.5809	28712.0700	0.5109
	9 \leftarrow 8	9 \leftarrow 8	8.2396	28712.3897	-0.1912			
	11 \leftarrow 10		10.3397	28712.7892	0.2083			
	8 \leftarrow 7		7.3539	28712.9015	0.3206			
$10_{91} \leftarrow 9_{90}$	11 \leftarrow 10	11 \leftarrow 10	11.2763	31899.3835	-0.2748	31899.6583	31899.9340	-0.2757
	10 \leftarrow 9		10.1817	31899.4764	-0.1819			
	12 \leftarrow 11		12.4797	31899.8544	0.1961			
	9 \leftarrow 8	9 \leftarrow 8	9.1956	31899.9474	0.2891			
and								
$10_{92} \leftarrow 9_{91}$	11 \leftarrow 10		11.2763	31899.3835	-0.2748	31899.6583	31899.1110	0.5473
	10 \leftarrow 9	10 \leftarrow 9	10.1817	31899.4764	-0.1819			
	12 \leftarrow 11		12.4797	31899.8544	0.1961			
	9 \leftarrow 8		9.1956	31899.9474	0.2891			
$11_{92} \leftarrow 10_{91}$	12 \leftarrow 11	12 \leftarrow 11	25.9641	35109.1188	-0.2028	35109.3216	35109.6360	-0.3144
	11 \leftarrow 10		23.6703	35109.1799	-0.1417			
	13 \leftarrow 12		28.4653	35109.4724	0.1508			
	10 \leftarrow 9	10 \leftarrow 9	21.5836	35109.5335	0.2119			
and								
$11_{93} \leftarrow 10_{92}$	12 \leftarrow 11		25.9641	35109.1188	-0.2028	35109.3216	35109.1630	0.1586
	11 \leftarrow 10	11 \leftarrow 10	23.6703	35109.1799	-0.1417			
	13 \leftarrow 12		28.4653	35109.4724	0.1508			
	10 \leftarrow 9		21.5836	35109.5335	0.2119			
$11_{101} \leftarrow 10_{100}$	12 \leftarrow 11	12 \leftarrow 10	13.4570	35086.3477	-0.2191	35086.5668	35086.8810	-0.3142
	11 \leftarrow 10		12.2682	35086.4259	-0.1409			
	13 \leftarrow 12		14.7534	35086.7837	0.2169			
	10 \leftarrow 9	11 \leftarrow 9	11.1866	35086.8620	0.2952			
and								
$11_{102} \leftarrow 10_{101}$	12 \leftarrow 11		13.4570	35086.3477	-0.2191	35086.5668	35086.2010	0.3658
	11 \leftarrow 10	11 \leftarrow 10	12.2682	35086.4259	-0.1409			
	13 \leftarrow 12		14.7534	35086.7837	0.2169			
	10 \leftarrow 9		11.1866	35086.8620	0.2952			

¹cal & ²exp: calculate & experimental hyperfine components; ³Int: Intensities in $\times 10^{-7} \text{ nm}^2 \text{ MHz}$;

⁴ $\Delta_1 = \nu_{\text{cal}} - \nu_o$ in ; ⁵ ν_o : hypothetical unsplit line frequency (in MHz); ⁶ ν_{exp} : experimental frequency components (in MHz) from^[47]; ⁷ $\Delta_2 = \nu_o - \nu_{\text{exp}}$.

Isotopic species that should be concerned by this quadrupole hyperfine study are ³⁴S, ³³S, ¹³C, ¹⁴C, ¹⁵N and ²H. However, only nuclei characterized by a spin $I \geq 1$ and a nonzero quadrupole moment could cause hyperfine quadrupole splittings and give rise to a hyperfine structure in each rotational transition. For the thiophenes considered, this should be the case for ¹⁴N ($I = 1$), ²H ($I = 1$) and ³³S ($I = 3/2$), ¹³C being not concerned as its nuclear spin $I = 1/2 < 1$.

The hyperfine coupling constants of these quadrupolar nuclei for **8** and **9** are presented

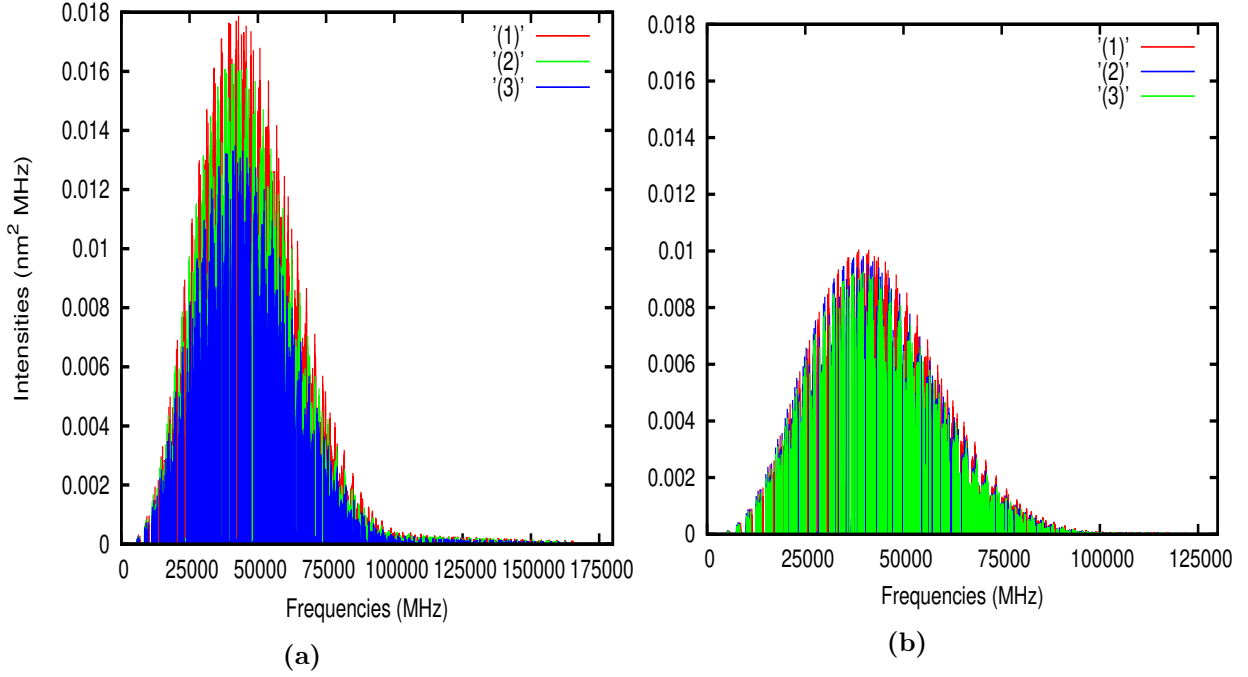


Figure 5.3 – Hyperfine spectra of (a) $2\text{C}^{14}\text{NT}$ (1), $2\text{C}^{15}\text{NT-3D}$ (2) and $^{33}\text{S-2C}^{15}\text{NT}$ (3); (b) $3\text{C}^{14}\text{NT}$ (1), $^{33}\text{S-3C}^{15}\text{NT}$ (2) and $3\text{C}^{15}\text{NT-2D}$ (3) (red, green and blue colors for ^{14}N , ^{33}S and ^2H quadrupolar nuclei, respectively) for $T = 10\text{ K}$.

(respectively) in Table 5.2 and Table 5.3. The calculated values [in $(\chi_{aa}, \chi_{bb}, \chi_{cc}, \chi_{ab}, \chi_+$ and $\chi_-)$ format] are $(-3.810, 2.328, 1.482, 0.483, 3.810, 0.845\text{ MHz})$ and $(-3.813, 2.157, 1.657, 0.553, 3.814, 0.500\text{ MHz})$ for the ^{14}N quadrupolar nucleus (respectively) for **8** and **9**. They are $(-26.906, 3.512, 23.393, -7.801, 26.905, -19.881\text{ MHz})$ and $(-2.262, -19.480, 21.747, 14.561, 2.267, -41.227\text{ MHz})$ for the ^{33}S nucleus (respectively) for **8** and **9**. The hyperfine coupling constants are also $(-0.043, 0.155, -0.112, 0.119, 0.036, 0.267\text{ MHz})$ and $(-0.080, 0.196, 0.117, -0.073, 0.313, 0.079\text{ MHz})$ for the ^2H nucleus (respectively) in **8** and **9**.

The experimental ^{14}N quadrupole coupling constants ($\chi_+ = 4.12 \pm 0.06\text{ MHz}$ and $\chi_- = 0$ for **9**^[49] and $\chi_+ = 4.04 \pm 0.16\text{ MHz}$ for **8**^[47]) were derived from observed hyperfine structures. However, no individual quadrupole coupling constants ($\chi_{aa}, \chi_{bb}, \chi_{cc}$ and χ_{ab}) are reported yet. For **8**, the determination of χ_- was unsuccessful^[47]. A comparison between theoretical and the experimental χ_+ values shows a good agreement, the calculated (Table 5.2 and Table 5.3) values both for **9** and **8** being a bit smaller than the experimental ones. For instance, the computed χ_+ values of 3.18 and 3.81 MHz for **8** and **9** (respectively) deviate from the experiment (4.04 and 4.12 MHz in the same order) of $\approx 0.4\text{ MHz}$. Similarly, computed χ_- values amount to 0.85 and 0.50 MHz for **8** and **9** respectively. The deviation from the experiment is $\approx 0.9\text{ MHz}$ for **9**.

Table 5.9 – Experimental and computed hyperfine splittings for **9**

$J'_{k-1, k+1} \leftarrow J''_{k-1, k+1}$	cal ¹ $F' \leftarrow F''$	exp ² $F' \leftarrow F''$	Int. ³	ν_{cal}	Δ_1 ⁴	ν_o ⁵	ν_{exp} ⁶	Δ_2 ⁷
$7_{52} \leftarrow 6_{51}$	8 \leftarrow 7	8 \leftarrow 7	5.8556	19097.3442	-0.0547	19097.3989	19097.6480	-0.2491
	7 \leftarrow 6		5.0445	19097.3575	-0.0414			
	9 \leftarrow 8		6.7814	19097.3946	-0.0043			
	6 \leftarrow 5	6 \leftarrow 5	4.3470	19097.4079	0.0090			
and								

(Continued)

Table 5.9 – (Continued)

$J'_{K-1K+1} \leftarrow J''_{K-1K+1}$	cal ¹ F' \leftarrow F''	exp ² F' \leftarrow F''	Int. ³	ν_{cal}	Δ_1 ⁴	ν_o ⁵	ν_{exp} ⁶	Δ_2 ⁷
$7_{53} \leftarrow 6_{52}$	8 \leftarrow 7		5.8556	19097.3414	-0.0547	19097.3961	19097.0000	0.3961
	7 \leftarrow 6	7 \leftarrow 6	5.0445	19097.3547	-0.0414			
	9 \leftarrow 8		6.7814	19097.3918	-0.0043			
	6 \leftarrow 5		4.3470	19097.4051	0.0090			
$7_{61} \leftarrow 6_{60}$	8 \leftarrow 7	8 \leftarrow 7	3.1377	19090.6255	-0.0692	19090.6947	19090.0400	0.6547
	7 \leftarrow 6		2.7030	19090.6463	-0.0484			
	9 \leftarrow 8		3.6337	19090.6984	0.0037			
	6 \leftarrow 5	6 \leftarrow 5	2.3293	19090.7192	0.0245			
and								
$7_{62} \leftarrow 6_{61}$	8 \leftarrow 7		3.1377	19090.6255	-0.0692	19090.6947	19090.0140	0.6807
	7 \leftarrow 6	7 \leftarrow 6	2.7030	19090.6463	-0.0484			
	9 \leftarrow 8		3.6337	19090.6984	0.0037			
	6 \leftarrow 5		2.3293	19090.7192	0.0245			
$8_{62} \leftarrow 7_{61}$	9 \leftarrow 8	9 \leftarrow 8	7.6964	21822.8677	-0.0415	21822.9092	21823.1210	-0.2118
	8 \leftarrow 7		6.7639	21822.8790	-0.0302			
	10 \leftarrow 9		8.7445	21822.9161	0.0069			
	7 \leftarrow 6	7 \leftarrow 6	5.9463	21822.9275	0.0183			
and								
$8_{63} \leftarrow 7_{62}$	9 \leftarrow 8		7.6964	21822.8676	-0.0415	21822.9091	21822.4660	0.4431
	8 \leftarrow 7	8 \leftarrow 7	6.7639	21822.8790	-0.0301			
	10 \leftarrow 9		8.7445	21822.9161	0.0070			
	7 \leftarrow 6		5.9463	21822.9274	0.0183			
$8_{71} \leftarrow 7_{70}$	9 \leftarrow 8	9 \leftarrow 8	4.0719	21816.8678	-0.0527	21816.9205	21817.2390	-0.3185
	8 \leftarrow 7		3.5785	21816.8843	-0.0362			
	10 \leftarrow 9		4.6263	21816.9340	0.0135			
	7 \leftarrow 6	7 \leftarrow 6	3.1459	21816.9505	0.0300			
and								
$8_{72} \leftarrow 7_{71}$	9 \leftarrow 8		4.0719	21816.8678	-0.0527	21816.9205	21816.3390	0.5815
	8 \leftarrow 7	8 \leftarrow 7	3.5785	21816.8843	-0.0362			
	10 \leftarrow 9		4.6263	21816.9340	0.0135			
	7 \leftarrow 6		3.1459	21816.9505	0.0300			
$9_{72} \leftarrow 8_{71}$	10 \leftarrow 9	10 \leftarrow 9	9.7277	24548.6296	-0.0223	24548.6519	24548.8700	-0.2181
	9 \leftarrow 8		8.6794	24548.6394	-0.0125			
	11 \leftarrow 10		10.8915	24548.6759	0.0240			
	8 \leftarrow 7	8 \leftarrow 7	7.7464	24548.6856	0.0337			
and								
$9_{73} \leftarrow 8_{72}$	10 \leftarrow 9		9.7277	24548.6296	-0.0223	24548.6519	24548.2330	0.4189
	9 \leftarrow 8	9 \leftarrow 8	8.6794	24548.6394	-0.0125			
	11 \leftarrow 10		10.8915	24548.6759	0.0240			
	8 \leftarrow 7		7.7464	24548.6856	0.0337			
$9_{81} \leftarrow 8_{80}$	10 \leftarrow 9	10 \leftarrow 9	5.0947	24543.0695	-0.0310	24543.1005	24543.399	-0.2985
	9 \leftarrow 8		4.5457	24543.0828	-0.0177			
	11 \leftarrow 10		5.7043	24543.1300	0.0295			
	8 \leftarrow 7	8 \leftarrow 7	4.0571	24543.1434	0.0429			
and								
$9_{82} \leftarrow 8_{81}$	10 \leftarrow 9		5.0947	24543.0695	-0.0310	24543.1005	24542.5640	0.5365
	9 \leftarrow 8	9 \leftarrow 8	4.5457	24543.0828	-0.0177			
	11 \leftarrow 10		5.7043	24543.1300	0.0295			
	8 \leftarrow 7		4.0571	24543.1434	0.0429			

¹cal & ²exp: calculate & experimental hyperfine components; ³Int: Intensities in $\times 10^{-7} \text{nm}^2 \text{MHz}$;

⁴ $\Delta_1 = \nu_{\text{cal}} - \nu_o$ in ; ⁵ ν_o : hypothetical unsplit line frequency (in MHz); ⁶ ν_{exp} : experimental frequency components (in MHz) from^[49]; ⁷ $\Delta_2 = \nu_o - \nu_{\text{exp}}$.

Referring to the orientation of the principal axis of the coordinate system of 2-cyanofurane ($\chi_- = 0.96$ MHz) and that of **8** which are similar and comparing their χ_+ ,^[47] suggested that their χ_- values should also be approximately the same. Nevertheless, our results show that the χ_- value for **8** is about two times larger than that of 2-cyanofurane.

Calculated nuclear coupling constants for **8** and **9** in comparison with those of some other homo or heterocyclic rings ($\chi_{\text{aa}} = -4.332$, $\chi_{\text{bb}} = 2.120$) for 4-cyanopyridine (N of the cyano-group)^[71], ($\chi_{\text{aa}} = -4.237$, $\chi_{\text{bb}} = 2.289$, $\chi_{\text{cc}} = 1.949$) for benzonitrile^[72] and ($\chi_{\text{aa}} = -4.908$, $\chi_{\text{bb}} = 1.434$, $\chi_{\text{cc}} = 3.474$) for pyridine^[71,73]) show that the quantities are in the same order of magnitude for both these aromatic compounds. Consequently, their structures and orientation within their inertia principle axes systems are similar.

The calculated inertial defect $\Delta I = I_{\text{aa}} + I_{\text{bb}} - I_{\text{cc}} \approx 0.001 \text{ amu} \cdot \text{\AA}^2$ for both **8** and **9** (it is zero for thiophene) confirms the planarity of their structures.

Table 5.10 – Line profile parameters for stronger lines computed from the calculated χ_{aa} , χ_{bb} , χ_{cc} and χ_{ab} hyperfine constants at 10.0 K for **8**.

$J'_{K-1K+1} \leftarrow J''_{K-1K+1}$	$F' \leftarrow F''$	ν_{cal}^1 (MHz)	ν_o^2 (MHz)	FWHM ³ (kHz)
$13_{211} \leftarrow 12_{210}$	12 \leftarrow 12	42933.1484	42933.4854	188.386
	13 \leftarrow 12	42933.3901		
	14 \leftarrow 13	42933.5660		
	12 \leftarrow 11	42933.5821		
	13 \leftarrow 13	42933.7904		
$15_{015} \leftarrow 14_{014}$	15 \leftarrow 15	42127.2362	42129.4885	47.096
	15 \leftarrow 14	42129.4683		
	14 \leftarrow 13	42129.4982		
	16 \leftarrow 15	42129.5064		
	14 \leftarrow 14	42131.8902		
$15_{115} \leftarrow 14_{114}$	15 \leftarrow 15	42120.7039	42122.9580	42.387
	15 \leftarrow 14	42122.9390		
	14 \leftarrow 13	42122.9675		
	16 \leftarrow 15	42122.9757		
	14 \leftarrow 14	42125.3626		
$12_{210} \leftarrow 11_{129}$	11 \leftarrow 11	40017.8781	40018.3895	211.934
	12 \leftarrow 11	40018.3118		
	13 \leftarrow 12	40018.4548		
	11 \leftarrow 10	40018.4711		
	12 \leftarrow 12	40018.8551		

ν_{cal}^1 : Computed line frequencies from calculated χ_{aa} , χ_{bb} , χ_{cc} and χ_{ab} hyperfine constants; ν_o^2 : Calculated line profile central frequency; FWHM³: Line profile FWHM

Table 5.8 and Table 5.9 compare the calculated and the experimental hyperfine coupling splittings for $2\text{C}^{14}\text{NT}$ and $3\text{C}^{14}\text{NT}$. An agreement is observed between the calculated and experimental data in both these two tables. The analysis of observed data in Table 5.8 for $2\text{C}^{14}\text{NT}$ ^[47] and Table 5.9 for $3\text{C}^{14}\text{NT}$ ^[49], especially in terms of observed rang for the values of J , shows that these transitions are very weak with intensities of the order of $10^{-7} \text{ nm}^2\text{MHz}$ (see the two tables).

Returning on the calculated hyperfine structures, a deep analysis of hyperfine coupling splittings for **8**, **9** and their isotopologues (Table 5.5, Table 5.6 and Table 5.7, respectively) reveals that the computed hyperfine components are characterized by $\Delta F = \pm 1$ whether for **8**, **9** and their isotopologues. As can be seen in Table 5.5 and Table 5.6, components corresponding to $\Delta F = 0$ are extremely weak in comparison with those characterized $\Delta F \neq 0$. It is worth noting that, for each spectral line in both **9** and **8** and their deuterated isotopologues, the strongest hyperfine splitting component is that corresponding to $F' (= J' + 1) \leftarrow F'' (= J')$ and the one characterized by $F' (= J'') \leftarrow F'' (= J')$ and finally that characterized by $F' (= J') \leftarrow F'' (= J' - 1)$. For example, the spectral terms for the brightest transition $J'_{K-1K+1} = 14_{113} \leftarrow J''_{K-1K+1} = 13_{112}$ of **9** are $F' = 15 \leftarrow F'' = 14$, $F' = 14 \leftarrow F'' = 13$ and $F' = 13 \leftarrow F'' = 12$ in the descending order. In contrast, as shown in Table 5.12 for $^{33}\text{S}-2\text{C}^{15}\text{NT}$ and $^{33}\text{S}-3\text{C}^{15}\text{NT}$, the strongest hyperfine splitting component is that corresponding to $F' = J' + 2 \leftarrow F'' = J' + 1$, followed by the one characterized by $F' = J' + 1 \leftarrow F'' = J'' + 1$, followed by the one characterized by $F' = J' \leftarrow F'' = J''$ and then that characterized by

Table 5.11 – Line profile parameters for stronger lines computed from the calculated χ_{aa} , χ_{bb} , χ_{cc} and χ_{ab} hyperfine constants at 10.0 K for **9** (frequency in MHz, FWHM in kHz).

$J'_{K-1K+1} \leftarrow J''_{K-1K+1}$	$F' \leftarrow F''$	ν_{cal}^1	ν_o^2	FWHM ³
$14_{113} \leftarrow 13_{112}$	14 \leftarrow 13	38618.2354	38618.2778	94.193
	15 \leftarrow 14	38618.3171		
	13 \leftarrow 12	38618.3191		
$15_{114} \leftarrow 14_{113}$	15 \leftarrow 14	41136.0488	41136.0925	87.128
	16 \leftarrow 15	41136.1332		
	14 \leftarrow 13	41136.1357		
$15_{015} \leftarrow 14_{014}$	15 \leftarrow 14	38288.5190	38288.5410	68.290
	14 \leftarrow 13	38288.5541		
	16 \leftarrow 15	38288.5597		
$16_{016} \leftarrow 15_{015}$	16 \leftarrow 15	40735.4680	40735.4867	47.096
	15 \leftarrow 14	40735.4976		
	17 \leftarrow 16	40735.5029		

ν_{cal}^1 : Computed line frequencies from calculated χ_{aa} , χ_{bb} , χ_{cc} and χ_{ab} hyperfine constants; ν_o^2 : Calculated line profile central frequency; FWHM³: Line profile FWHM

$F' = J' - 1 \leftarrow F'' = J'' - 1$. For each molecular species, the four strongest lines are fitted by a gaussian function so that its profile is :

$$\phi(\nu) = \frac{1}{\sqrt{2\pi}\sigma} e^{-(\nu+\nu_o)^2/2\sigma^2}$$

where ν_o is the line center frequency and σ is such that the full-width at half maximum (FWHM) is given by $\sqrt{8\ln 2}\sigma$. Table 5.10 and Table 5.11 compare the transition characteristics (line profile parameters) of four strongest lines for **9** and **8**, respectively. These results are also compared in turn to those of ³³S and D isotopologues in Table 5.12 also shown on Figure 5.3.

As expected, the line profiles results reveal that the more the line is intense the higher is its FWHM. Moreover, the comparison of transitions at different temperatures shows that the strongest transitions at a given temperature are not the strongest ones at another. But, for closer temperatures such as those prevailing in cold cores ($T \approx 8.6 - 10$ K), a strong transition at a given temperature remains among the strongest transitions in this range. The temperature plays then a great role in molecular detectability. The analysis of Figures 5.2a and 5.2b shows that line intensities at high temperatures (at 150 K for example) are extremely weak compared to line intensities at low temperature. The analysis of **8** and **9** line profile parameters (Table 5.10 and Table 5.11, respectively), reveals that rotational spectral bands are broader for **8** than **9**. However, two spectral bands corresponding to the transitions $15_{0,15} \leftarrow 14_{0,14}$ and $15_{1,15} \leftarrow 14_{1,14}$ centered at 42129.4885 and 42122.9580 MHz (respectively) are very narrow in comparison to others (including those for **9**). These ¹⁴N quadrupole hyperfine line intensities are also compared with those of ³³S and D Table 5.12 and Figures 5.2a for **8** and 5.2b for **9**. From the analysis in the three tables, it can be deduced that either for **8** or **9**, ¹⁴N quadrupole hyperfine lines are a bit stronger than those arising from ³³S and D quadrupole nuclei. Comparing, in turn, hyperfine lines arising from the ³³S and D nuclei, the results show that 2 C¹⁵NT-D lines are stronger than those of ³³S-2 C¹⁵NT (Figure 5.3a), the reverse being revealed for **9** isotopologues (Figure 5.3b).

Table 5.12 – Line profiles for the first strongest lines for deuterated $2\text{C}^{15}\text{NT} - \text{d}_3$ and $3\text{C}^{15}\text{NT} - \text{d}_2$; for $^{33}\text{S} - 2\text{C}^{15}\text{NT}$ and $^{33}\text{S} - 2\text{C}^{15}\text{NT}$ at 10.0 K.

Trans. ¹	$\frac{F'}{F''} \leftarrow$	ν_{cal}^2	ν_0^3	FWHM ⁴	Trans. ¹	$\frac{F'}{F''} \leftarrow$	ν_{cal}^2	ν_0^3	FWHM ⁴
		(MHz)	(MHz)	(kHz)			(MHz)	(MHz)	(kHz)
$2\text{C}^{15}\text{NT} - \text{d}_3$					$3\text{C}^{15}\text{NT} - \text{d}_2$				
$13_{211} \leftarrow 12_{210}$	$13 \leftarrow 13$	41338.4341	41338.4739	9.419	$15_{114} \leftarrow 14_{113}$	$15 \leftarrow 15$	39725.6274	39725.6615	11.303
	$12 \leftarrow 11$	41338.4693				$14 \leftarrow 13$	39725.6573		
	$14 \leftarrow 13$	41338.4702				$16 \leftarrow 15$	39725.6580		
	$13 \leftarrow 12$	41338.4780				$15 \leftarrow 14$	39725.6653		
	$12 \leftarrow 12$	41338.5170				$14 \leftarrow 14$	39725.6979		
$15_{015} \leftarrow 14_{014}$	$14 \leftarrow 14$	40535.8008	40535.8673	3.885	$14_{113} \leftarrow 13_{112}$	$14 \leftarrow 14$	37309.4025	37309.4437	10.597
	$16 \leftarrow 15$	40535.8666				$13 \leftarrow 12$	37309.4396		
	$14 \leftarrow 13$	40535.8668				$15 \leftarrow 14$	37309.4404		
	$15 \leftarrow 14$	40535.8681				$14 \leftarrow 13$	37309.4474		
	$15 \leftarrow 15$	40535.9297				$13 \leftarrow 13$	37309.4880		
$15_{115} \leftarrow 14_{114}$	$14 \leftarrow 14$	40530.8980	40530.9645	3.838	$16_{016} \leftarrow 15_{015}$	$15 \leftarrow 15$	39325.6626	39325.7161	4.003
	$16 \leftarrow 15$	40530.9639				$17 \leftarrow 16$	39325.7148		
	$14 \leftarrow 13$	40530.9641				$15 \leftarrow 14$	39325.7148		
	$15 \leftarrow 14$	40530.9653				$16 \leftarrow 15$	39325.7175		
	$15 \leftarrow 15$	40531.0271				$16 \leftarrow 16$	39325.7664		
$14_{014} \leftarrow 13_{013}$	$13 \leftarrow 13$	37923.6860	37923.7511	3.815	$15_{213} \leftarrow 14_{212}$	$15 \leftarrow 15$	41250.4623	41250.5405	3.061
	$15 \leftarrow 14$	37923.7504				$14 \leftarrow 13$	41250.5398		
	$13 \leftarrow 12$	37923.7506				$16 \leftarrow 15$	41250.5402		
	$14 \leftarrow 13$	37923.7520				$15 \leftarrow 14$	41250.5410		
	$14 \leftarrow 14$	37923.8120				$14 \leftarrow 14$	41250.6241		
$^{33}\text{S} - 2\text{C}^{15}\text{NT}$					$^{33}\text{S} - 3\text{C}^{15}\text{NT}$				
$13_{211} \leftarrow 12_{210}$	$14 \leftarrow 14$	41700.3344	41705.1480	2.355	$15_{114} \leftarrow 14_{113}$	$14 \leftarrow 14$	39748.9164	39749.7542	0.754
	$13 \leftarrow 12$	41704.7914				$15 \leftarrow 15$	39749.1145		
	$14 \leftarrow 13$	41704.7921				$16 \leftarrow 15$	39749.1541		
	$12 \leftarrow 11$	41705.1473				$15 \leftarrow 14$	39749.2069		
	$15 \leftarrow 14$	41705.1480				$17 \leftarrow 16$	39749.7542		
	$13 \leftarrow 13$	41705.3304				$14 \leftarrow 13$	39749.8350		
	$12 \leftarrow 12$	41709.6060				$16 \leftarrow 16$	39750.0669		
$15_{015} \leftarrow 14_{014}$	$15 \leftarrow 14$	40962.3584	40962.5032	1.413	$14_{113} \leftarrow 13_{112}$	$13 \leftarrow 13$	37294.6591	37296.0861	0.730
	$16 \leftarrow 15$	40962.4209				$14 \leftarrow 14$	37295.4107		
	$14 \leftarrow 13$	40962.4407				$15 \leftarrow 14$	37295.5031		
	$17 \leftarrow 16$	40962.5032				$14 \leftarrow 13$	37295.5777		
	$15 \leftarrow 15$	40963.4406				$16 \leftarrow 15$	37296.0861		
$15_{115} \leftarrow 14_{114}$	$15 \leftarrow 14$	40954.7553	40954.8977	1.648	$16_{016} \leftarrow 15_{015}$	$13 \leftarrow 12$	37296.1548	39397.3143	0.706
	$16 \leftarrow 15$	40954.8180				$15 \leftarrow 15$	37296.9989		
	$14 \leftarrow 13$	40954.8349				$17 \leftarrow 17$	39389.7397		
	$17 \leftarrow 16$	40954.8977				$16 \leftarrow 15$	39397.0363		
	$15 \leftarrow 15$	40955.8380				$17 \leftarrow 16$	39397.0560		
$14_{212} \leftarrow 13_{211}$	$15 \leftarrow 14$	44432.9149	44438.1193	3.297	$15_{015} \leftarrow 14_{014}$	$15 \leftarrow 14$	39397.2941	37032.6682	0.659
	$15 \leftarrow 14$	44437.7286				$18 \leftarrow 17$	39397.3143		
	$14 \leftarrow 13$	44437.7315				$16 \leftarrow 16$	39397.7460		
	$16 \leftarrow 15$	44438.1180				$15 \leftarrow 15$	39404.6148		
	$13 \leftarrow 12$	44438.1209				$16 \leftarrow 16$	37025.3519		
	$14 \leftarrow 14$	44438.2698				$15 \leftarrow 14$	37032.3466		
	$13 \leftarrow 13$	44442.9355				$16 \leftarrow 15$	37032.3643		

Trans.¹: $J'_{K-1K+1} \leftarrow J''_{K-1K+1}$; ν_{cal}^1 : Computed line frequencies from calculated χ_{aa} , χ_{bb} , χ_{cc} and χ_{ab} hyperfine constants; ν_0^2 : Calculated line profile central frequency; FWHM³: Line profile FWHM

These conclusions are also drawn for the comparison of the different hyperfine line intensities (Table 5.5, Table 5.6 and Table 5.7) and line profile parameters, i.e., the FWHMs (Table 5.10, Table 5.11 and Table 5.12) for the same temperature ($T = 10\text{ K}$). For instance, the ^{14}N strongest spectral band for **8** (the transition $13_{211} \leftarrow 12_{210}$ centered at 42933.4854 MHz) has a fwhm about $2\times$ greater than that of **9** ($14_{113} \leftarrow 13_{112}$ centered at 38618.2778 MHz). Its fwhm is also $\approx 250\times$ greater than that of the brightest ^{33}S quadrupole hyperfine line for **9**. The comparison between quadrupole hyperfine constants in Table 5.2 and Table 5.3 for the molecular species shows that ^{33}S quadrupole nucleus has the highest hyperfine coupling constants even though the spectral bands due its coupling splittings are weak. It can be

found that the presence of this nucleus splits the rotational line into many components (Table 5.12) in comparison to other quadrupolar nuclei (Table 5.9 and Table 5.10), the upper spectral term J' going up to $J' + 1$. At an astronomical point of view, these results are of paramount importance as hyperfine structure provides needed information for observer concerning the column density, the kinematic gas structure, etc.

5.4 Summary

A quantum chemical study of the quadrupole hyperfine structures were carried out for **8**, **9** and some of their isotopologues, having a spin $I \geq 1$ and an quadrupole electric moment different to zero ($^{33}\text{S}-3\text{C}^{15}\text{NT}$, $^{33}\text{S}-2\text{C}^{15}\text{NT}$ and $3\text{C}^{15}\text{NT}-2\text{D}$ and $2\text{C}^{15}\text{NT}-3\text{D}$). For the first time, a detailed theoretical and extensive analysis of quadrupole hyperfine structures is carried out at different temperatures quadrupole. The ^{14}N , ^{33}S and D quadrupole hyperfine constants as well as dipole moments for different species were calculated and the corresponding hyperfine structures analysed, taking into account the temperatures prevailing in ISM environments where they are expected to be detected. The strongest transition lines and the optimum regions of detectability were discussed. The results of the present work are expected to assist astrophysicists and astrochemists in the search of new species and their identification of molecular species in the ISM, the derivation of gas kinematic structure, etc.

5.5 References

- [1] C. P. Endres, S. Schlemmer, P. Schilke, J. Stutzki, and H. S. Müller. *J. Mol. Spectrosc.*, 327:95–104, 2016.
- [2] B. A. McGuire. *Astrophys. J. Suppl. Ser.*, 239(2):17, 2018.
- [3] D. McNaughton, M. K. Jahn, M. J. Travers, D. Wachsmuth, P. D. Godfrey, and J.-U. Grabow. *Mon. Not. R. Astron. Soc.*, 476(4):5268–5273, 2018.
- [4] S. Zeng, D. Quénard, I. Jiménez-Serra, J. Martín-Pintado, V. Rivilla, L. Testi, and R. Martín-Doménech. *MNRAS*, 484(1):L43–L48, 2019.
- [5] V. Rivilla, J. Martín-Pintado, I. Jiménez-Serra, S. Zeng, S. Martin, J. Armijos-Abendano, M. Requena-Torres, R. Aladro, and D. Riquelme. *MNRAS*, 483(1):L114–L119, 2019.
- [6] M. Agúndez, N. Marcelino, and J. Cernicharo. *Astrophys. J. Lett.*, 861(2):L22, 2018.
- [7] J. Cernicharo, M. Agúndez, L. V. Prieto, M. Guélin, J. Pardo, C. Kahane, C. Marka, C. Kramer, S. Navarro, G. Quintana-Lacaci, et al. *A&A*, 606:L5, 2017.
- [8] M. Agúndez, J. Cernicharo, and M. Guélin. *A&A*, 570:A45, 2014.
- [9] M. Agúndez, J. Cernicharo, P. De Vicente, N. Marcelino, E. Roueff, A. Fuente, M. Gerin, M. Guélin, C. Albo, A. Barcia, et al. *A&A*, 579:L10, 2015.
- [10] J. Anderson and L. M. Ziurys. *Astrophys. J. Lett.*, 795(1):L1, 2014.
- [11] A. Belloche, R. T. Garrod, H. S. Müller, and K. M. Menten. *Science*, 345(6204):1584–1587, 2014.
- [12] R. A. Loomis, A. M. Burkhardt, C. N. Shingledecker, S. B. Charnley, M. A. Cordiner, E. Herbst, S. Kalenskii, K. L. K. Lee, E. R. Willis, C. Xue, et al. *Nat. Astron.*, pages 1–9, 2021.
- [13] A. J. Remijan, J. Hollis, F. J. Lovas, D. F. Plusquellic, and P. Jewell. *ApJ*, 632(1):333, 2005.
- [14] L. Nguyen, A. Walters, L. Margulès, R. A. Motiyenko, J.-C. Guillemin, C. Kahane, and C. Ceccarelli. *A&A*, 553:A84, 2013.

- [15] H. S. Müller, B. J. Drouin, and J. C. Pearson. *A&A*, 506(3):1487–1499, 2009.
- [16] H. Calcutt, J. K. Jørgensen, H. Müller, L. E. Kristensen, A. Coutens, T. Bourke, R. Garrod, M. Persson, M. Van Der Wiel, E. Van Dishoeck, et al. *arXiv preprint arXiv:1804.09210*, 2018.
- [17] A. López, B. Tercero, Z. Kisiel, A. Daly, C. Bermúdez, H. Calcutt, N. Marcelino, S. Viti, B. Drouin, I. Medvedev, et al. *A&A*, 572:A44, 2014.
- [18] D. M. Mehringer, J. Pearson, J. Keene, and T. Phillips. *ApJ*, 608(1):306, 2004.
- [19] K. Demyk, H. Mäder, B. Tercero, J. Cernicharo, J. Demaison, L. Margulès, M. Wegner, S. Keipert, and M. Sheng. *A&A*, 466:255–259, 2007.
- [20] R. Martín-Doménech, I. Jiménez-Serra, G. M. Caro, H. Müller, A. Occhiogrosso, L. Testi, P. Woods, and S. Viti. *A&A*, 585:A112, 2016.
- [21] A. Daly, C. Bermúdez, A. López, B. Tercero, J. Pearson, N. Marcelino, J. Alonso, and J. Cernicharo. *ApJ*, 768(1):81, 2013.
- [22] L. Avery, N. Broten, J. MacLeod, T. Oka, and H. Kroto. *ApJ*, 205:L173–L175, 1976.
- [23] N. Broten, T. Oka, L. Avery, J. MacLeod, and H. Kroto. *ApJ*, 223:L105–L107, 1978.
- [24] N. Broten, J. MacLeod, L. Avery, W. Irvine, B. Hoglund, P. Friberg, and A. Hjalmarsen. *ApJ*, 276:L25–L29, 1984.
- [25] Y.-n. Chin, R. I. Kaiser, C. Lemme, and C. Henkel. Detection of interstellar cyanoallene and its implications for astrochemistry. In *AIP Conference Proceedings*, volume 855, pages 149–153. AIP, 2006.
- [26] B. A. McGuire, A. M. Burkhardt, C. N. Shingledecker, S. V. Kalenskii, E. Herbst, A. J. Remijan, and M. C. McCarthy. *Astrophys. J. Lett.*, 843(2):L28, 2017.
- [27] J. Cernicharo, A. M. Heras, A. Tielens, J. R. Pardo, F. Herpin, M. Guélin, and L. Waters. *Astrophys. J. Lett.*, 546(2):L123, 2001.
- [28] M. C. McCarthy, K. L. K. Lee, R. A. Loomis, A. M. Burkhardt, C. N. Shingledecker, S. B. Charnley, M. A. Cordiner, E. Herbst, S. Kalenskii, E. R. Willis, et al. *Nat. Astron.*, pages 1–5, 2020.
- [29] Z.-C. Wang and V. M. Bierbaum. *J. Phys. Chem. A.*, 121(19):3655–3661, 2017.
- [30] A. G. Tielens. *Annu. Rev. Astron. Astrophys.*, 46:289–337, 2008.
- [31] V. M. Bierbaum. *Proc. Int. Astron. Union.*, 9(S297):258–264, 2013.
- [32] M. Nuevo and S. A. Sandford. *ApJ*, 800(2):116, 2015.
- [33] M. A. Sephton. *Philos. Trans. Royal Soc. A*, 363(1837):2729–2742, 2005.
- [34] J. L. Eigenbrode, R. E. Summons, A. Steele, C. Freissinet, M. Millan, R. Navarro-González, B. Sutter, A. C. McAdam, H. B. Franz, D. P. Glavin, et al. *Science*, 360(6393):1096–1101, 2018.
- [35] M. Sephton, C. Pillinger, and I. Gilmour. *Planet. Space Sci.*, 49(1):101–106, 2001.
- [36] M. Bose, R. Root, and S. Pizzarello. *Meteorit. Planet. Sci.*, 52(3):546–559, 2017.
- [37] F. Robert and S. Epstein. *Geochim. Cosmochim. Acta*, 46(1):81–95, 1982.
- [38] J. Kerridge and S. Chang. *Meteoritics*, 18:323, 1983.
- [39] J. Yang and S. Epstein. *Nature*, 311(5986):544, 1984.
- [40] M. Lattalais, Y. Ellinger, A. Matrane, and J.-C. Guillemin. *Phys. Chem. Chem. Phys.*, 12(16):4165–4171, 2010.
- [41] B. A. McGuire, C. N. Shingledecker, E. R. Willis, K. L. K. Lee, M.-A. Martin-Drumel, G. A. Blake, C. L. Brogan, A. M. Burkhardt, P. Caselli, K.-J. Chuang, et al. *ApJ*, 883(2):201, 2019.
- [42] J. C. Laas and P. Caselli. *A&A*, 624:A108, 2019.
- [43] N. Marcelino, S. Brünken, J. Cernicharo, D. Quan, E. Roueff, E. Herbst, and P. Thaddeus. *A&A*, 516:A105, 2010.
- [44] F. F. van der Tak, H. S. Müller, M. E. Harding, and J. Gauss. *A&A*, 507(1):347–354,

- 2009.
- [45] F. J. Lovas, A. J. Remijan, J. Hollis, P. Jewell, and L. E. Snyder. *Astrophys. J. Lett.*, 637(1):L37, 2006.
 - [46] L. Pagani, E. Bergin, P. Goldsmith, G. Melnick, R. Snell, and C. Favre. 2019.
 - [47] J. Wiese, L. Engelbrecht, and H. Dreizler. *Z. Naturforsch.*, 32(2):152–155, 1977.
 - [48] T. Avirah, T. Malloy Jr, and R. L. Cook. *J. Mol. Struct.*, 29(1):47–52, 1975.
 - [49] J. Wiese and D. H. Sutter. *Z. Naturforsch.*, 32(8):890–896, 1977.
 - [50] R. Simbizi, G. Gahungu, and M. T. Nguyen. *SAA*.
 - [51] H. M. Pickett. *J. Mol. Spectrosc.*, 148(2):371–377, 1991.
 - [52] Z. Kisiel. Assignment and analysis of complex rotational spectra. In *Spectroscopy from Space*, pages 91–106. Springer, 2001.
 - [53] Z. Kisiel. Prospe, programs for rotational spectroscopy, 2015. <http://info.ifpan.edu.pl/kisiel/prospe.htm>.
 - [54] H. Pickett, R. Poynter, E. Cohen, M. Delitsky, J. Pearson, and H. Müller. *Journal of Quantitative Spectroscopy and Radiative Transfer*, 60(5):883–890, 1998.
 - [55] L. Coudert, L. Margulès, T. Huet, R. Motiyenko, H. Møllendal, and J.-C. Guillemin. *A&A*, 543:A46, 2012.
 - [56] B. S. Ray. *Zeitschrift für Physik*, 78(1-2):74–91, 1932.
 - [57] G. W. King. *J. Chem. Phys.*, 15(11):820–830, 1947.
 - [58] U. Kretschmer, W. Stahl, and H. Dreizler. *Z. Naturforsch.*, 48(5-6):733–736, 1993.
 - [59] J. Wiese, R. Schwarz, and D. Sutter. *Z. Naturforsch.*, 35(7):770–772, 1980.
 - [60] E. Roueff, J. Loison, and K. Hickson. *A&A*, 576:A99, 2015.
 - [61] P. Wannier. *Annual Review of Astronomy and Astrophysics*, 18(1):399–437, 1980.
 - [62] C. Kahane, J. Gomez-Gonzalez, J. Cernicharo, and M. Guélin. *A&A*, 190:167–177, 1988.
 - [63] T. Wilson. *Reports on Progress in Physics*, 62(2):143, 1999.
 - [64] D. Romano, F. Matteucci, Z.-Y. Zhang, R. J. Ivison, and P. Ventura. *MNRAS*, 490(2):2838–2854, 2019.
 - [65] L. Hallis. *Philos Trans A Math Phys Eng Sci*, 375(2094):20150390, 2017.
 - [66] E. Füre and B. Marty. *Nat. Geosci.*, 8(7):515–522, 2015.
 - [67] S. Wampfler, J. Jørgensen, M. Bizzarro, and S. Bisschop. *A&A*, 572:A24, 2014.
 - [68] J. Chantzios, S. Spezzano, C. Endres, L. Bizzocchi, V. Lattanzi, J. Laas, A. Vasyunin, and P. Caselli. *A&A*, 621:A111, 2019.
 - [69] E. Herbst and E. F. Van Dishoeck. *ARA&A*, 47:427–480, 2009.
 - [70] P. Pratap, J. Dickens, R. L. Snell, M. Miralles, E. Bergin, W. M. Irvine, and F. Schloerb. *ApJ*, 486(2):862, 1997.
 - [71] N. Vogt, K. R. Nair, J.-U. Grabow, and J. Demaison. *Mol. Phys.*, 116(23-24):3530–3537, 2018.
 - [72] K. Wohlfart, M. Schnell, J.-U. Grabow, and J. Küpper. *arXiv preprint arXiv:0709.2984*, 2007.
 - [73] N. Heineking, H. Dreizler, and R. Schwarz. *Z. Naturforsch.*, 41(10):1210–1213, 1986.

THERMODYNAMICS OF PROTONATION OF THIOPHENE, 2-CYANOTHIOPHENE AND 3-CYANOTHIOPHENE

6.1 Introduction

Aromatic molecules and their protonated together with their substituted (heterocyclic^[1]) derivatives form an important component of the interstellar medium (ISM)^[2]. At first glance, the ISM environments are harsh and unfavorable to the molecular formation. For instance, the ISM particle densities in our galaxy range from 10^{-4} cm^{-3} in diffuse regions to 10^5 cm^{-3} in dense clouds, with temperatures ranging from 10 K to 150 K^[3]. In general, the temperature of the ISM ranges from 3 K (for cold dark clouds) to 10^6 K (for hot ionized medium) and the density from 10^{-4} to $> 10^6 \text{ cm}^{-3}$ ^[4]. The near-zero pressures (10^{-14} atmospheres) and the intense ionizing radiation (including cosmic rays with high energies going up to 10^{21} eV)^[5] are further harmful conditions that are not likely to favor the chemical synthesis or chemical stability. However, a big number of polyatomic molecules and molecular ions have been detected in diffuse clouds, especially in hot cores regions characterized by hot temperatures ($T \sim 90 \text{ K}$), high number density ($n_{\text{H}} \sim 10^7 \text{ cm}^{-3}$) and by high abundances of fully hydrogenated molecules such as H_2O , NH_3 and H_2S , along with a rich variety of complex organic molecules^[6]. The question about how molecules could be formed in so harmful environments has along intrigued scientists^[7-9]. In early works, the ion-neutral reactions induced by cosmic rays have been suggested to be the leading reaction mechanism to form molecules in the ISM^[9-11]. Additionally, neutral-neutral reactions have been also suggested in hot cores, in circumstellar shells and in dense cloud regions where temperatures as low as 10 K prevail^[8]. Moreover, grain surface reactions have been also reported by Snow and al.^[12] to be important. Generally, three environments for molecular formation in the outer space were suggested in the literature: the *gas-phase*, the *bare dust surface* and the *ice bulk* or *its surface*^[5,13]. While the former is widely accepted to be a leading one for simple molecules^[5,14], the latter is known to be important in formation of complex molecules^[15]. Complex organic species have then been widely detected in hot cores embedded in high-mass star forming regions, but also in low-mass hot corinos where their formation towards warm sources is well reproduced by the so-called *warm-up scenario*^[16]. More specifically, unsaturated complex molecular species are likely to be observed in cold dense regions such as the Taurus Molecular Cloud 1 (TMC-1, $T \sim 10 \text{ K}$) where they had been found to be abundant^[17]. Unsaturated complex species are also found in the so-called *lukewarm corino* L1527 ($T \approx 30 \text{ K}$) which is known also to contain significant abundances of complex molecules, including anionic forms^[17].

It is well established that not only protonated aromatics XH^+ ($\text{X} = \text{aromatic compound}$) occur as intermediates in electrophilic aromatic substitution reactions, but also their spectra could allow their identification in the media where they are occurring^[18]. In general, protonation spectroscopic data are of great importance to unambiguously identify the protona-

tion site(s) in protonated aromatic systems (XH^+). In particular, hyperfine spectra, besides of identifying the protonation site(s), unravel also the structural assignment of various isomers^[19]. Likewise, it is of general knowledge that complex organic molecules in ISM gaseous regions play an crucial importance in understanding the chemical evolution of the Universe and in exploring the link between the early stages of star formation and the formation of solar system bodies^[20]. A non-negligible number of molecular species already detected in universe contain the cyano ($\text{C}\equiv\text{N}$) group^[21]. It has been reported that repetitive addition of unsaturated hydrocarbons to protonated nitriles can lead to cyanopolyynes ions which can, in turn, ultimately form cyanopolynes (the most abundant species in dark clouds)^[22]. The hydrogen cyanide (HCN), especially its protonated form (HCNH^+) has been the subject of extensive studies due to its important role in the chemical evolution process in interstellar clouds^[23]. Some studies focused on its vibrational bands^[24–30] and some others on its rotational spectrum^[31]. The detection of this compound in the universe was made through the observation of its rotational transitions $J = 1 \rightarrow J = 0$; $J = 2 \rightarrow J = 1$ and $J = 3 \rightarrow J = 2$ at 74, 148, and 222 GHz, respectively, towards Sgr B2^[32,33], but also by means of its electric quadrupole hyperfine structure^[34]. Similarly, the sulfur-containing compounds have been also extensively researched in the ISM, where about 26 such molecular species have been detected^[35]. These compounds are grouped into three sets: carbon-sulfur, oxygen-sulfur compounds and hydrides^[22]. However, no S-heterocyclic compound among them was yet detected. In the same way, even though Nitrogen and Oxygen containing molecular species were widely reported in the ISM and circumstellar environments, no N- or O-heterocyclic compound was also detected in those media^[36].

In this work, we focus our attention on S-heterocyclic molecular species. The investigation on insoluble organic matter (IOM) from Murchison meteorite revealed a non negligible proportion of sulfur-containing molecules, including thiophene^[37,38]. Through the investigation of the D and ^{15}N isotope excess observed in these meteorites, many works converged on its ISM origin^[38–40]. Moreover, thiophene and its methyl substituted derivatives (2- and 3-methylthiophene) and many other sulfur-bearing compounds are among the organic compounds recently observed in 3-billion-year-old mudstones at Gale crater on Mars^[41]. However, none among thiophene and its substituted derivatives was reported yet by astrochemists or astrophysicists in the ISM. In addition, it had been reported that sulfur is depleted in regions where it is expected to be abundant^[42]. The detection of new gas-phase sulfur-bearing molecules should play a key role in the observed sulfur depletion^[43].

The protonated molecular hydrogen, H_3^+ , has been found to be the most abundantly produced molecule of the ISM, next to H_2 , even though its steady state concentration is low due to its extremely high chemical reactivity^[44]. This ion plays a pivotal role in interstellar chemistry, by initiating the chains of reactions that lead to the production of many of the complex molecular species observed in the interstellar medium (including protonated species) by ion-neutral reactions^[44–48].

The protonation of halothiophenes has been experimentally investigated^[49–54]. Through some of these studies, protonation of halothiophenes were investigated by means of the $^1\text{H-NMR}$ ^[49–52]. It was found that the protonation occurs at the α -position in the thiophene ring regardless of whether both the two α -positions have already been substituted or not^[49]. The protonation of 2,3-dichlorothiophene was found to occur at 5-position. In case of one β - and two α -substituents, the same work revealed that the protonation occurs at α -position neighboring the β -substituent. Subsequently, an experimental work on 2,3-dichlorothiophene^[50] and a theoretical one on thiophene and chlorothiophene^[51] supported the above mentioned results. As regarding to Szajda and Lam^[54], their investigation on the thiophene protonation at S-, α - and β -positions yielded results in agreement with experi-

mental data from other works^[49–52]. They found that the protonation at α -position lowers the energy 48.95 kJ more than at the β -position.

Spectroscopic techniques, which are widely used to infer information about molecular structure and dynamics in planetary atmospheres and ISM are assisted by quantum-mechanical calculations of structures as well as spectroscopic and thermodynamic properties, such as transition frequencies and reaction enthalpies, to guide and support observations, line assignments, and data analysis in these new and chemically complicated situations^[55]. To the best of our knowledge, no theoretical or experimental on the protonation of CN-substituted derivatives of thiophene under this study was reported yet. The aim of this study is to investigate the protonation of thiophene and two of its nitrile substituted derivatives namely 2-cyanothiophene (2CNT) and 3-cyanothiophene (3CNT). The proton affinity (PA) of 2CNT and 3CNT as well as the enthalpies, entropies and Gibbs free energy changes (Δ_rH , Δ_rS and Δ_rG) of the reactions yielding these species and their protonated forms are computed using modern quantum chemical methods. The protonated cyanothiophenes ($C_4H_3S - CTNH^+$) are characterized by analysing their thermochemistry, their vibrational and rotational spectra. The comparison of $HCNH^+$ which had been already detected in the ISM^[32,33] and $R - CNH^+$ which were not explored yet is expected to give insight on their detection but also on their production in ISM environments.

6.2 Computational details

The species structures were visualized using GaussView 5.0^[56] and all calculations were done using Gaussian 09 program^[57]. The geometrical structures are calculated following the technique described in earlier work^[58]. Computations using Hartree-Fock (HF)^[59], Møller-Plesset perturbation theory MP2 and MP3^[60], and density functionals such as B3LYP^[61,62] and M06-2X^[63] and the one-electron basis sets including 6-31G(d), 6-31G(d,p), 6-311G(d), 6-311G(d,p), 6-311++G(d,p)^[64] were carried out on the parent thiophene for which experimental values are available, in order to find out the corrections for the geometrical parameters. It turned out that the M06-2X functional in conjunction with a modest basis set 6-31G(d,p) and jointly with corrections yielded more accurate structural parameters and rotational constants for the parent thiophene as compared to the remaining levels tested. This method was thereafter applied on the protonated species. However, as no experimental rotational constants for these species, the empirical adjustment was not performed.

Regarding the proton affinity, a set of seven levels of theory was tested specifically to benchmark their accuracy regarding the proton affinity (PA) for the thiophene. The tested methods are (i) the highly parameterized, empirical exchange correlation function (M06-2X)^[63] with two basis sets (6-31G(d,p) and aug-cc-pVTZ), (ii) a serie of Gaussian- G_n (G_n with $n=2,3,4$) using reduced Møller-Plesset order [G_2 (MP2), G_3 (MP2), G_4 (PM2)]^[65–67], (iii) a version of G3 using density functional geometries and zero-point energies (G3B3)^[68] and (iv) the complete basis set model chemistry using the B3LYP hybrid density functional geometries and frequencies (CBS-QB3)^[69]. The selected most accurate level of theory is thereafter used for all thermodynamics calculations and for all compounds. The harmonic frequencies for $RCNH^+$ were calculated at M06-2X/6-31G(d,p) level of theory from the structural geometries found by method described above. In order to get reliable frequencies, we used a correction approach described in a previous work^[58] and references therein. The fundamental vibration frequencies found were thereafter rescaled using MOLIVIB^[70,71]. For rotational spectra, the calculation of rotational transitions, as well as the analysis of quadrupole hyperfine splittings were done using the SPFIT/SPCAT package^[72].

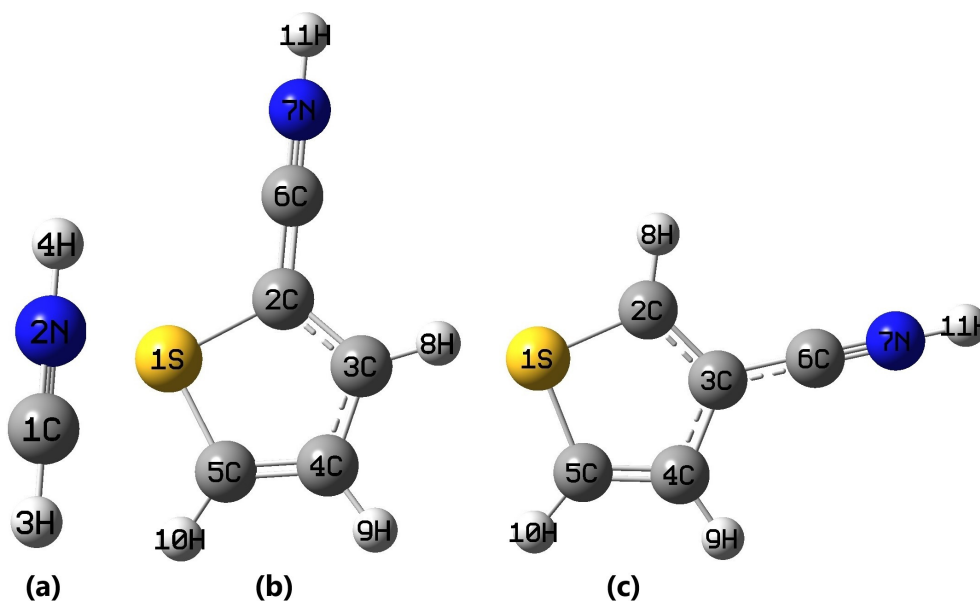


Figure 6.1 – M06-2X/6-31G(d,p) optimized geometries for (a) HCNH⁺, (b) 2CNTH⁺ and (c) 3CNTH⁺; yellow: S, gray=C, blue=N and light gray=H.

6.3 Results and discussion

6.3.1 Geometrical parameters

Table 6.1 – M06-2X/6-31G(d,p) structures (with empirical corrections) for 2CNTH⁺, 3CNTH⁺ and HCNH⁺ (bond lengths and angles in Å and °).

	2CNTH ⁺	3CNTH ⁺	HCNH ⁺
Bond lengths			
S1 - C2	1.7396	1.6870	
S1 - C5	1.7003	1.7267	
C2 - C3	1.3938	1.3897	
C3 - C4	1.4020	1.4380	
C4 - C5	1.3788	1.3574	
C2/C3 - C6	1.3852	1.3976	
C - N	1.1536	1.1516	1.1372 (1.1368) ^a
N-H	1.0080	1.0084	1.0153 (1.0091) ^a
C3/C2 - H8	1.0833	1.0818	
C4 - H9	1.0818	1.0817	
C5 - H10	1.0832	1.0813	
C-H			1.0825 (1.0779) ^a
Bond Angles			
S1 - C2 - C3	112.54	110.47	
S1 - C5 - C4	114.01	112.59	
C2 - S1 - C5	89.90	92.7610	
C2 - C3 - C4	111.35	113.81	
C3 - C4 - C5	112.21	110.37	
C2/C3 - C6 - N7	179.86	179.72	
C2-C3-H8/C6	123.54	122.65	
C4-C3-H8/C6	125.11	121.81	
C3-C4-H9	124.30	124.70	
S1 - C5 - H10	118.76	119.74	
S1 - C2 - C6/H8	122.18	121.64	

^a Experimental values from Amano and Keiichi Amano and Tanaka^[26], ^b The numbering scheme used is that of figure Figure 6.1.; ^c The values in parentheses are the differences of experimental from the calculated results.

The geometrical structures of the neutral forms for 2CNT and 3CNT had been discussed in our previous work^[73]. In the current report, we will only focus on the protonated

forms. The predicted geometrical structures for HCNH^+ , 2CNTH^+ and 3CNTH^+ are presented in Table 6.1 and their optimized geometries in Figure Figure 6.1. A comparison with available experimental structure for HCNH^+ shows a good agreement. This reinforces the credit to the computational method also recently used for 2CNT and 3CNT ^[73]. Reliable molecular structures for 2CNTH^+ and 3CNTH^+ for which no experimental data are available yet are therefore expected. It should be noted that HCNH^+ is a linear molecule belonging to the $C_{\infty V}$ point group whereas $\text{C}_4\text{H}_3\text{S-CN}^+$ is an asymmetric top molecule belonging to the C_1 point group.

6.3.2 Sites of protonation of thiophene and of its nitrile substituted derivatives.

The proton affinity (PA) of a chemical species B is the negative of the enthalpy change associated with the gas phase protonation reaction^[74]: $\text{B} + \text{H}^+ \rightleftharpoons \text{BH}^+$.

Table 6.2 – Proton Affinity (PA in kJ/mol) of thiophene at different sites, for different levels of theory and at $T = 298\text{ K}$ and $T = 10\text{ K}$.

Level of theory	Sites of protonation ^a					
	$T = 298\text{ K}$			$T = 10\text{ K}$		
	S	α -position	β -position	S	α -position	β -position
M06-2X/6-31G(d,p)	622.83	818.70	782.21	617.42	813.60	777.32
M06-2X/aug-cc-pVTZ	627.86	803.24	769.96	622.41	798.20	765.08
G2MP2	739.84	816.66	785.64	734.51	811.61	780.66
G3MP2	739.47	812.98	782.59	734.11	807.90	777.61
G4MP2	637.59	811.94	783.09	632.14	806.80	778.08
G3B3	634.09	813.96	783.90	628.79	808.77	778.84
CBS-QB3	690.93	808.24	777.56	624.82	802.96	772.49
NIST			815 ^b			

^a The site with higher PA is the position with higher susceptibility of proton attack.

^b NIST value (Hunter and Lias (1998)).

Table 6.3 – G2(MP2) and G3B3 Proton Affinity (PA in kJ/mol) of 2CNT , 3CNT and HCN at different sites for $T = 298\text{ K}$.

Site	2CNT		3CNT	
	G2(MP2)	G3B3	G2(MP2)	G3B3
1	676.65	674.93	673.84	672.67
2	732.32	727.75	758.97	756.24
3	723.51	721.54	697.68	694.00
4	726.48	724.53	728.31	726.20
5	752.89	750.15	753.40	750.28
N	812.24	809.03	813.02	812.83
	HCN			
N	713.73	708.22	(712.90) ^a	
C	416.30	412.14		

^a Experimental PA from Hunter and Lias^[75]. **1**= Sulfur atom; **2**= α -position; **3** = β -position; **4** = non-substituted position equivalent to β -position; **5** = non-substituted position equivalent to α -position; **N**: Nitrogen atom; **C**: The carbon atom of HCN .

The PAs for thiophene at different position as obtained for a set of seven levels of theory and for temperatures $T = 298\text{ K}$ and $T = 10\text{ K}$, i.e., temperatures in the range of temperatures prevailing in molecular clouds known to contain complex molecular species^[76,77] are presented in Table 6.2. Beside PAs computed at the different levels of theory, Table 6.2 contains also NIST PA for thiophene (PA = 815 kJ/mol)^[75]. An analysis of calculated

Table 6.4 – Comparison of G2(MP2) and G3B3 Proton Affinity (PA in kJ/mol) computed at different sites of 2CNT and 3CNT for T = 298 K and T = 150 K.

		Protonation sites											
		1		2		3		4		5		6	
T (K)		298	150	298	150	298	150	298	150	298	150	298	150
G2MP2													
C1		676.65	677.62	732.32	732.87	723.51	724.44	726.48	727.31	752.89	753.70	812.23	812.24
C2		673.84	671.74	758.97	756.58	697.68	695.16	728.30	726.06	752.89	751.06	813.01	810.83
G3B3													
C1		674.93	676.09	727.75	728.30	721.24	722.40	724.53	725.36	750.15	750.84	809.03	810.23
C2		672.67	670.70	756.24	753.75	694.00	675.23	726.20	723.91	750.30	747.88	812.84	811.27

C1=2 CNT; **C2**=3 CNT; **1**= Sulfur atom; **2**= α -position; **3**= β -position; **4**= position equivalent to β -position; **5**= position equivalent to α -position; **6**= Protonation at N atom.

Table 6.5 – Comparison of G2(MP2) and G3B3 Proton Affinity (PA in kJ/mol) computed at different sites of 2CNT and 3CNT for T = 10 K and T = 5 K.

		Protonation sites											
		1		2		3		4		5		6	
T (K)		10	5	10	5	10	5	10	5	10	5	10	5
G2MP2													
C1		671.89	671.79	727.27	727.17	718.79	718.69	721.66	721.56	748.07	747.97	807.49	807.39
C2		669.08	668.97	754.03	754.39	692.65	692.54	753.40	723.38	748.48	743.55	808.06	807.95
G3B3													
C1		670.36	670.28	722.72	722.63	716.71	716.61	719.69	719.60	745.18	745.08	804.54	804.44
C2		668.06	667.96	751.18	751.08	689.02	688.92	721.32	721.22	745.28	745.17	809.10	793.05

C1=2 CNT; **C2**=3 CNT; **1**= Sulfur atom; **2**= α -position; **3**= β -position; **4**= position equivalent to β -position; **5**= position equivalent to α -position; **6**= Protonation at N atom.

PAs reveals that there are levels of theory that yield results closer to the NIST value of PA for thiophene, especially in for α protonation at T = 298 K. This is the case for G3B3 (a deviation $\delta \sim 1$ kJ/mole), G2(MP2) ($\delta \approx 1,66$ kJ/mol), G3(MP3) ($\delta = 2.02$ kJ/mol) and G4(MP2) ($\delta = 3.03$ kJ/mol) and M06-2X/631G(d,p) ($\delta = 3.70$ kJ/mol). The remaining ones show higher deviation with respect to the NIST value: ≈ 12 and 7 kJ/mol for M06-2X/aug-cc-pVTZ and CBS-QB3 respectively. It is worthy noting that a simple level of theory with a modest basis set such as M06-2X/631G(d,p) yields the best result than the popular CBS-QB3^[78]. The G4(MP2), improved version with respect to G2(MP2) and G3(MP2), is expected to yield more accurate results than these two levels of theory of the preceding generations. However, the results summarized in the Table 6.2 show that it gives less accurate results for the PA of thiophene. We conclude then that G2(MP2) and G3B3 provide results close to the NIST value, with G3B3 giving slightly more accurate results than G2(MP2) (with a difference of ≈ 0.63 kJ/mol). Whereas this latter slightly overestimates the NIST datum, the former slightly underestimates it. The PAs for the compounds investigated in this study are expected to be in between G3B3 and G2(MP2) PAs. These two levels of theory will then be used for subsequent calculations. It is known that the higher the PA, the stronger the base and the weaker the conjugate acid^[79]. The higher PA value corresponds then to the site with higher susceptibility of proton attack. It follows that the position with higher value of PA is the favorable site of protonation. Hence, at both temperatures (T \approx 298 K and T = 10 K), the calculated PAs for thiophene are, in the decreasing order of, $PA(\alpha) > PA(\beta) > PA(S)$, implying that the α -position is the most favorable site of protonation.

G2(MP2) and G3B3 PAs are also calculated for 2CNT and 3CNT for different positions and at different temperatures, in the range of which COMs were widely found and where new ones are expected to be discovered, i.e., T \approx 5 K to T \approx 300 K^[76,77,80]. Analyzing results in these two tables, the general observation is that the lower the temperature is, the lower the PA. The calculated results at T = 298 K are reported in Table 6.3, including

Table 6.6 – MKS B3LYP/cc-pVQT calculated partial atomic charges (in electrons e) for 2CNT, 3CNT and HCN at $T = 298$ K

Atom	S1	C2	C3	C4	C5	C6	N
TN	0.062	-0.147	-0.111	-0.111	-0.147		
2 CNT	0.096	-0.085	-0.073	-0.123	-0.109	-0.049	-0.204
3 CNT	0.104	-0.142	0.171	-0.137	-0.129	-0.049	-0.204

those corresponding to HCN. The N-protonation calculated result for HCN (713.73 kJ/mol) agrees with the experimental value^[75] (by ≈ 0.63 kJ/mol) for G2(MP2). The results for two cyanothiophenes are also presented in Table 6.4 (for $T = 298$ K and $T = 150$ K) and Table 6.5 (for $T = 10$ K and $T = 5$ K). The results in these Tables show that the most favorable site of protonation is the nitrogen (N) atom for both 2CNT, 3CNT and HCN and at all temperatures.

Comparing then the protonation at substituted thiophene rings, the protonation results at α and β -positions whether for 2CNT or 3CNT show that it occurs in α -position for both 2CNT and 3CNT, i.e., the α position is the favorable site. For instance, considering the results at $T = 298.145$ K, the PAs are ≈ 753 and ≈ 724 kJ/mol for α and β protonation of 2CNT, respectively, and at G2(MP2) level of theory; they are also ≈ 750 and ≈ 722 kJ/mol in the same order for 2CNT and for G3B3 level of theory. Similarly, the PAs are ≈ 759 and ≈ 698 kJ/mol for α and β protonation of 3CNT, respectively, at G2(MP2) level of theory; they are also ≈ 756 and ≈ 694 kJ/mol in the same order for 23CNT and for G3B3 level of theory. This conclusion holds at all temperatures (see Table 6.3, Table 6.4 and Table 6.5). In general, the PAs for these compounds in the decreasing order are such that $PA(6) > PA(2) > PA(5) > PA(4) > PA(3) > P(1)$ for 3CNT and $PA(6) > PA(5) > PA(2) > PA(4) > PA(3) > P(1)$ for 2CNT, where (6) is the nitrogen atom of the cyano group. Moreover, for α -protonation, the non-substituted site is more favorable than the substituted one. Regarding the β -position, the position closer to the non-substituted α -site is the most favorable. See, for instance, the results computed at G3B3 level of theory and at $T = 10$ K in Table 6.5: $PA(4) \approx 720$ kJ/mol $>$ $PA(3) \approx 717$ kJ/mol for 2CNT and $PA(4) \approx 721$ kJ/mol $>$ $PA(3) \approx 689$ kJ/mol for 3CNT. Another general observation is that, for both the two levels of theory and at all temperatures, except in two positions (at 1, i.e., S atom and 3, i.e., carbon atom in β -position), the computed PA for 3CNT are greater than those for 2CNT.

Matczak^[81] have tested ten level of theory to benchmark their accuracy in computation of partial atomic charge from which he calculated the dipole moment μ for a set of organic compound. The results showed that the calculation at HF/def2-QZVPP and B3LYP/def2-QZVPP levels of theory using of Merz-Kollman-Singh (MKS) and Hu-Lu-Yang (HLY) models approximate the magnitude of the molecular dipole moments with the greatest accuracy. Table 6.6 and Figure 6.2 present the Partial atomic charges for the compounds investigated in the present work calculated at HF/def2-QZVPP using the MKS model. Raček et al.^[82] have reported that PACGs (hereafter, PACG stands for partial atomic charge) model the distribution of charge density in a molecule, and consequently, drive its interactions with its surroundings. These results can therefore supported the finding about protonation process. Confronting then, the results in Table 6.2 (for thiophene), Table 6.3 (for 2CNT and 3CNT with those in Table 6.6, it can be seen that PACG results agree with the PA ones. For example, the PACGs for N atom are the lowest values compared with those of the remaining atoms, i.e., -0.204 for both 2CNT and 3CNT. These values correlate with the favorable site of protonation both for 2CNT and 3CNT, i.e., the N atom. Note also that, the PACGs being the same for the two compounds, the PAs at

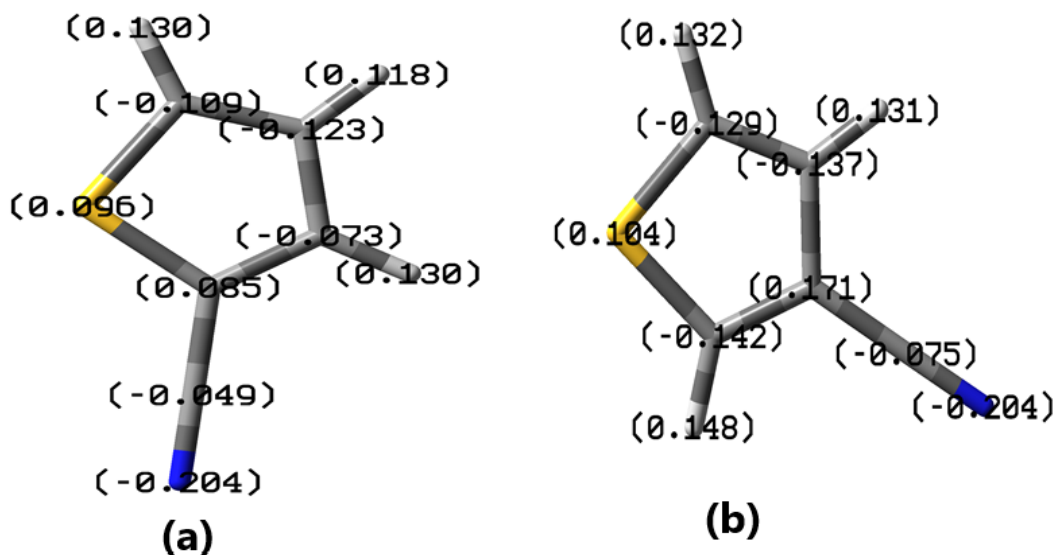


Figure 6.2 – Partial atomic charges calculated at HF/def2-def2-QZVPP using MKS model for (a) 2CNT and (b) 3CNT.

this position are also very close each other (≈ 812 kJ/mol for 2CNT and ≈ 813 kJ/mol for 3CNT). In the same way, regarding the thiophene ring protonation, the results presented in Table 6.6 agree also with those in Table 6.2 and Table 6.3, except a slight difference for 3CNT. In fact, the results PACGs confirm that the PA is higher in α -position than in β -position: $\text{PACG}(\alpha) < \text{PACG}(\beta) < \text{PACG}(\text{S})$. This conclusion agrees well with that derived above concerning the PA: $\text{PA}(\alpha) > \text{PA}(\beta) > \text{PA}(\text{S})$. According to Raček et al.^[82] statement, the lower is the PACGs, higher would be the PA at that position. Moreover, as shown by the PA values, the PACGs on thiophene ring of 2CNT and 3CNT, the protonation would have to favor the carbon atom in not yet substituted atom or that located away from the substituted position. However, based on the calculated PAGs in table Table 6.6, this requirement is not fulfilled both for 2CNT and 3CNT where $|\text{PACG}|_{\text{C}_3} > |\text{PACG}|_{\text{C}_2}$. This does not agree with the calculated PA, for example, at G2(MP2) where $\text{PA}(\text{C}_5) = 753$ kJ/mol $>$ $\text{PA}(\text{C}_4) = 726$ kJ/mol. Except this quoted difference, the results for the PACGs agree well with those for PAs whether for 2CNT, 3CNT and thiophene. It is worthy noting that the calculations of PACGs at HF/def2-QZVPP using the MKS or the natural population analysis (NPA) models give identical results for the thiophene (Table A.16). However, the calculation of PACGs at B3LYP/def2-QZVPP using the NPA model does not yield good results. For instance, in case of **9**, this calculation gives results which favor the protonation at ring positions rather at N atom (see Table A.16). Furthermore, the analysis of results in Table 6.4 reveals that, whereas the PA rises with the decreasing temperature for 2CNT, it decreases when temperature decreases for 3CNT. However, at low temperatures (see Table 6.5) this trend reverses for 2CNT and the PA decreases with the decreasing temperature both for 2CNT and 3CNT and at both the two levels of theory.

The protonation of dicyano-thiophens (2,3-dicyanothiophene, 2,4-dicyanothiophene and 2,5-dicyanothiophene) are computed at the same levels of theory at $T = 298$ K and $T = 10$ K (Table 6.7). The analysis of protonation for these compounds, at thiophene rings, confirms also the above mentioned result found for 2CNT and 3CNT: the protonation favors the N atom and the α -position incase of thiophene ring protonation. These result show again that it favors the non substituted site.

Table 6.7 – G2(MP2) Proton Affinity (PA in kJ/mol) at different sites of some dicyanothiophenes at T = 10 and 298 K.

	2		3		4		5	
	10	298	10	298	10	298	10	298
C1	681.51	686.45	643.23	648.04	675.01	679.68	696.81	701.49
C2	666.39	675.13	667.85	674.15	637.95	644.44	694.70	703.22
	6		7		8			
	10	298	10	298	10	298	10	298
C1	777.06	782.39	777.91	781.87	1224.52	1229.04		
C2	767.65	773.85	770.60	776.58	1261.86	1269.79		

C1: 23CNT; **C2:** 24CNT; **2=** α -position; **3=** β -position; **4=** position equivalent to β -position; **5=** position equivalent to α -position; **6=** Protonation only at N atom of the cyano-group in α -position; **7=** Protonation only at N atom of the cyano-group in β -position; **8=** Protationation at both the two Nitrogen atoms of the cyano-groups.

In the same way as Yokoyama et al.^[49] findings, our results show that the protonation at the rings of cyanothiophenes favors α -positions regardless whether these positions have been already substituted or not. In addition, the present results show that the PA for dicyanothiophenes is greater for diprotonation (protonation at the two cyano groups) than a monoprotection (at one of them). For instance, the PAs were found to be 1226 and 1262 kJ/mol (respectively) for diprotonated 2,3-dicyanothiophene and 2,4-dicyanothiophene at the two N sites (Table 6.7); they are ≈ 778 and 770 kJ/mol for N-monoprotection of the same compounds, respectively. This discrepancy between PAs for monoprotection and diprotonated species was expected as the proton affinities follow the additivity rule^[83].

In the following sections, our discussions will be based on the $-\text{NH}^+$ protomers: HCNH^+ (for N-protonated hydrogen cyanide), 2CNTH^+ (for N-protonated 2cyanothiophene) and 3CNTH^+ (for N-protonated 3cyanothiophene).

6.3.3 Enthapy, Gibbs free energy changes and entropy changes ($\Delta_r\text{H}$, $\Delta_r\text{G}$ and $\Delta_r\text{S}$) of the reactions producing HCN, 2CNT, 3CNT and their protonated forms

The equation (6.1) below gives the relationship between the enthalpy, entropy and Gibbs free energy changes changes for a given chemical reaction at a constant temperature and pressure:

$$\Delta\text{G} = \Delta\text{H} - \text{T}\Delta\text{S} \quad (6.1)$$

The Gibbs free energy changes change ΔG can be the used to predict the spontaneity or the non spontaneity of a the reaction. Brown et al.^[84] has summarized the different situations which are used to predict the the spontaneity or the non spontaneity of a the reaction. They are listed in the Table 6.8.

Table 6.8 – Relationship between the reaction spontaneity and temperature.

ΔH	ΔS	$-\text{T}\Delta\text{S}$	$\Delta\text{G} = \Delta\text{H} - \text{T}\Delta\text{S}$	Reaction
–	+	–	– (at all Temperatures)	Spontaneous at all Temperatures
+	–	+	+	Non spontaneous at all Temperatures
–	–	+	+	Non spontaneous at higher Temperatures
–	–	–	– (at lower Temperatures)	Spontaneous at lower Temperatures
+	+	–	+	Spontaneous at higher Temperatures
+	+	–	– (at lower Temperatures)	Non spontaneous at lower Temperatures

Table 6.9 – Gase phase G2(MP2) and G3B3 calculated enthalpy, entropy and Gibbs free energy changes ($\Delta_r H$, $\Delta_r S$ and $\Delta_r G$ in kJ mol^{-1}) of reaction producing hydrogen cyanide, cyanothiophenes and their protonated forms ($T = 298 \text{ K}$ and $T = 10 \text{ K}$ for $P = 10^{-5} \text{ atm}$).

Equation of the reaction		$\Delta_r H^{298}$	$\Delta_r G^{298}$	$\Delta_r S^{298}$	$\Delta_r H^{10}$	$\Delta_r G^{10}$	$\Delta_r S^{10}$	L.T.
$\text{H}_3^+ + \text{CN}^- \longrightarrow \text{HCN} + \text{H}_2$	(1)	-1047.01	-1040.68	-0.047	-1046.24	-1046.24	0.000	a
		-1048.61	-1045.03	-0.044	-1047.93	-1047.93	-0.000	b
$\text{C}_4\text{H}_3\text{S}^+ + \text{CN}^- \longrightarrow 2 \text{CNT} + \text{H}$	(2)	-611.22	-597.15	-0.047	-612.24	-611.83	-0.041	a
		-607.98	-595.01	-0.044	-609.84	-609.43	-0.042	b
$\text{C}_4\text{H}_3\text{S}^+ + \text{CN}^- \longrightarrow 3 \text{CNT} + \text{H}$	(3)	-615.65	-601.54	-0.047	-616.65	-616.25	-0.041	a
		-612.64	-599.65	-0.044	-614.51	-614.10	-0.041	b
$\text{CN-H} + \text{H}_3^+ \longrightarrow \text{HCNH}^+ + \text{H}_2$	(4)	-352.22	-344.67	-0.02	-350.69	-350.69	-0.000	a
		-353.63	-348.76	-0.032	-352.18	-352.20	-0.000	b
$\text{C}_4\text{H}_3\text{SCN} + \text{H}_3^+ \longrightarrow 2 \text{CNT-H}^+ + \text{H}_2$	(5)	-392.20	-386.81	-0.018	-392.24	-392.22	-0.002	a
		-387.24	-380.33	-0.02	-387.54	-387.52	-0.002	b
$\text{C}_4\text{H}_3\text{SCN} + \text{H}_3^+ \longrightarrow 3 \text{CNT-H}^+ + \text{H}_2$	(6)	-392.97	-387.13	-0.020	-392.81	-392.80	-0.002	a
		-391.04	-390.55	-0.002	-392.10	-392.07	-0.003	b

L.T.: Level of Theory; **a**=G2(MP2); **b**=G3B3.

Table 6.10 – Gase phase G2(MP2) and G3B3 calculated enthalpy, entropy and Gibbs free energy changes ($\Delta_r H$, $\Delta_r S$ and $\Delta_r G$ in kJ mol^{-1}) of the reactions yielding hydrogen cyanide, cyanothiophenes and their protonated forms ($T = 298 \text{ K}$ and $T = 10 \text{ K}$ for $P = 1 \text{ atm}$).

Reaction		$\Delta_r H^{298}$	$\Delta_r G^{298}$	$\Delta_r S^{298}$	$\Delta_r H^{10}$	$\Delta_r G^{10}$	$\Delta_r S^{10}$	L.T.
$\text{H}_3^+ + \text{CN}^- \longrightarrow \text{HCN} + \text{H}_2$	(7)	-1047.03	-1038.98	-0.027	-1046.24	-1046.10	0.015	a
		-1048.61	-1045.03	-0.012	-1047.93	-1047.93	-0.000	b
$\text{C}_4\text{H}_4\text{S}^+ + \text{CN} \longrightarrow 2 \text{CNT} + \text{H}$	(8)	-611.21	-597.15	-0.047	-577.91	-570.55	-0.736	a
		-607.98	-595	-0.044	-609.84	-609.43	-0.041	b
$\text{C}_4\text{H}_4\text{S}^+ + \text{CN}^- \longrightarrow 3 \text{CNT} + \text{H}$	(9)	-615.65	-601.54	-0.047	-582.33	-574.97	-0.736	a
		-612.64	-599.65	-0.044	-614.51	-614.09	-0.041	b
$\text{CN-H} + \text{H}_3^+ \longrightarrow \text{HCN-H}^+ + \text{H}_2$	(10)	-352.21	-342.91	-0.031	-350.67	-350.69	0.002	a
		-353.63	348.77	-0.016	-352.18	-352.18	0.000	b
$\text{C}_4\text{H}_3\text{SCN} + \text{H}_3^+ \longrightarrow 2 \text{CNT-H}^+ + \text{H}_2$	(11)	-392.19	-385.01	-0.024	-392.22	-392.22	0.000	a
		-387.27	-385.072	-0.008	-391.56	-391.54	-0.002	b
$\text{C}_4\text{H}_3\text{SCN} + \text{H}_3^+ \longrightarrow 3 \text{CNT-H}^+ + \text{H}_2$	(12)	-392.98	-385.42	-0.025	-392.79	-392.79	0.000	a
		-391.04	-390.81	-0.001	-392.10	-392.08	-0.002	b

L.T.: Level of Theory; **a**=G2(MP2); **b**=G3B3.

The equations of the reactions yielding R-CN and R-CNH⁺ and the corresponding enthalpy ($\Delta_r H$), entropy ($\Delta_r S$) and Gibbs free energy changes ($\Delta_r G$) changes calculated at G2MP2 and G3B3 levels of theory at $T = 298 \text{ K}$ and $T = 10 \text{ K}$ are summarized in Table 6.9 (for $P = 10^{-5} \text{ atm}$) and Table 6.10 (for $P = 1 \text{ atm}$). As shown in these tables, G2MP2 and G3B3 results are again close to each other. For both temperatures, the calculated enthalpy and Gibbs free energy changes are negative ($\Delta_r H < 0$ and $\Delta_r G < 0$), for reactions **(1)**-**(12)**, for all the two levels of theory and at all pressures. Following data in Table 6.8, these results imply then that none of these reactions have an energy barrier. They are, consequently, spontaneous. The remaining question is to know whether they are spontaneous at all temperatures or not. For this purpose, the entropy changes are deduced from the enthalpy and Gibbs free energy changes following the relation (6.1). Analyzing the values for the entropy changes, which are listed in the two tables (Table 6.10 and Table 6.11), it can be seen that:

1. For $T = 298 \text{ K}$, the values for entropy change are negative for all the reactions, for both

1. The choice of $P = 10^{-5} \text{ atm}$ was motivated by the fact that the pressure in the ISM is generally near-zero ($\sim 10^{-14} \text{ atm}$ ^[5]). The pressure $P = 10^{-5} \text{ atm}$ was the lower pressure limit for Gaussian 09.

the two levels of theory and for both the two pressures. Thus, $\Delta_r H < 0$, $\Delta_r G < 0$ and $\Delta_r S < 0$, implying that all the reactions are spontaneous at low temperatures.

2. Calculating $\Delta_r S$ at $T = 10\text{ K}$, the results show that at low pressure, i.e., at $P = 10^{-5}\text{ atm}$, $\Delta_r S < 0$ for reactions **(2)** and **(3)**, **(5)** and **(6)**, whereas it is about zero ($\Delta_r S \approx 0$) for **(1)** and **(4)**, i.e., reactions ending at the formation of HCN and its protonated form (HCNH^+). These results show again that the first set, i.e., reactions **(2)** and **(3)**, **(5)** and **(6)** can proceed also spontaneously at lower temperature, whereas the second set can imply that these reaction are able to proceed spontaneously at any temperature. At $P = 1\text{ atm}$, the conclusion is the same except that the reaction yielding the protonated forms of the cyanothiophenes computed at G2(MP2) are added to set of **(1)** and **(4)**, $\Delta_r S$ for these latter being a bit clearly positive.

To find out how these thermodynamics quantities depend on the temperatures, we calculated again them at high temperatures ($T = 1000\text{ K}$) and low temperatures ($T = 5\text{ K}$) and at low pressure ($P = 10^{-5}\text{ atm}$), complex organic molecules (COMs) being however expected to be found in starforming clouds ($5 < T < 300\text{ K}$ ^[76,80]) (see section 6.1).

Table 6.11 – Gase phase G3B3 calculated enthalpy, entropy and Gibbs free energy changes for the reactions ($\Delta_r H$ and $\Delta_r G$ in kJ mol^{-1}) producing hydrogen cyanide, cyanothiophenes and their protonated forms ($T = 1000\text{ K}$ and $T = 5\text{ K}$ for $P = 10^{-5}\text{ atm}$).

Reaction	$\Delta_r H^{1000}$	$\Delta_r G^{1000}$	$\Delta_r S^{1000}$	$\Delta_r H^5$	$\Delta_r G^5$	$\Delta_r S^5$
$\text{H}_3^+ + \text{CN}^- \rightarrow \text{HCN} + \text{H}_2$	(13) -1044.11	-1030.32	-0.046	-1018.84	-1170.50	0.509
$\text{C}_4\text{H}_4\text{S}^+ + \text{CN}^- \rightarrow 2\text{CNT} + \text{H}$	(14) -562.64	-433.66	-0.433	-574.21	-574.00	-0.001
$\text{C}_4\text{H}_4\text{S}^+ + \text{CN}^- \rightarrow 3\text{CNT} + \text{H}$	(15) -567.05	-438.47	-0.431	-578.93	-578.72	-0.001
$\text{CN-H} + \text{H}_3^+ \rightarrow \text{HCN-H}^+ + \text{H}_2$	(16) 381.56	-327.04	-0.094	-352.18	-290.50	-0.207
$\text{C}_4\text{H}_3\text{SCN} + \text{H}_3^+ \rightarrow 2\text{CNTH}^+ + \text{H}_2$	(17) -381.56	-374.56	-0.023	-391.58	-391.50	-0.0002
$\text{C}_4\text{H}_3\text{SCN} + \text{H}_3^+ \rightarrow 3\text{CNTH}^+ + \text{H}_2$	(18) -384.86	-385.77	0.003	-392.05	-391.97	-0.0002

The results are provided in Table 6.11. The analysis of these results reveals that, at $T = 1000\text{ K}$, all the reactions **(13)** - **(17)**, but **(18)**, have the same trends as at $T = 298\text{ K}$ (see Table 6.9 and Table 6.10): $\Delta_r H$, $\Delta_r S$ and $\Delta_r G$ are all negative. It implies that reactions are also spontaneous at this and lower temperatures, whereas $\Delta_r S > 0$ for the reaction **(18)** implies that it is spontaneous at all temperatures. Another peculiar observation is that $|\Delta_r S|$ higher at $T = 1000\text{ K}$ than at $T = 298\text{ K}$. At $T = 5\text{ K}$, $\Delta_r H$ and $\Delta_r G$ are also negative, but $\Delta_r S$ is positive for the reaction **(1)** and negative for others. These results confirm the conclusion drawn above from the two preceding tables. In addition, from results in this table, it is deduced that, 3CNTH^+ could be also formed at any temperature.

In general, it can be seen from this discussion that all the investigated reactions are spontaneous ($\Delta_r H < 0$ and $\Delta_r G < 0$ for all of them). However, it is a bit difficult to see how the spontaneity depends on the temperatures. The reason may be that, all the reactions, but **(14)** and **(15)**, are *enthalpy-driven* with $|\Delta_r H| \gg |\Delta_r S|$; the reactions **(14)** and **(15)** being both enthalpy and entropy, i.e., *enthalpy-entropy-driven* with $|\Delta_r H| \approx |\Delta_r S|$. For all the reactions, except **(14)** and **(15)**, we have then $\Delta_r H \approx \Delta_r G$. Moreover, the comparison of **(2)** and **(3)**, on one hand, and **(5)** and **(6)**, on the other hand, reveals that even though $\Delta_r H$ and $\Delta_r G$ values are higher for reactions yielding 3CNT and 3CNTH^+ than those producing 2CNT and 2CNTH^+ (respectively), the corresponding $\Delta_r S$ values are almost the same, meaning that **(2)** and **(3)** (or **(5)** and **(6)**) may have the same rate, especially at low temperatures.

According to millimeter and submillimeter spectroscopy of the dense ISM, deuterated molecular species are more abundant than the H version in cold dense regions^[85]. H_2D^+ molecular species, a singly deuterated form of H_3^+ , was found to play a crucial role in the

Table 6.12 – Gase phase G2(MP2) calculated enthalpy, entropy and Gibbs free energy changes ($\Delta_r H$, $\Delta_r S$ and $\Delta_r G$ in kJ mol^{-1}) of the reactions producing 2CNTD^+ and 3CNTD^+ ($T = 298\text{ K}$ and $T = 10\text{ K}$ for $P = 10^{-5}\text{ atm}$).

Reaction		$\Delta_r H^{298}$	$\Delta_r G^{298}$	$\Delta_r S^{298}$	$\Delta_r H^{10}$	$\Delta_r G^{10}$	$\Delta_r S^{10}$
$\text{C}_4\text{H}_3\text{SCN} + \text{H}_2\text{D}^+ \longrightarrow 2\text{CNT-D}^+ + \text{H}_2$	(19)	-389.19	-380.09	-0.031	-394.92	-394.70	-0.022
$\text{C}_4\text{H}_3\text{SCN} + \text{H}_2\text{D}^+ \longrightarrow 3\text{CNT-D}^+ + \text{H}_2$	(19')	-390.04	-380.44	-0.032	-395.55	-395.33	-0.022
$\text{C}_4\text{H}_3\text{SCN} + \text{H}_2\text{D}^+ \longrightarrow 2\text{CNT-H}^+ + \text{HD}$	(20)	-385.79	-377.35	-0.028	-390.90	-390.74	-0.015
$\text{C}_4\text{H}_3\text{SCN} + \text{H}_2\text{D}^+ \longrightarrow 3\text{CNT-H}^+ + \text{HD}$	(20')	-386.57	-377.66	-0.030	-391.46	-391.30	-0.016
$\text{C}_4\text{H}_3\text{SCN} + \text{D}_2\text{H}^+ \longrightarrow 2\text{CNT-D}^+ + \text{HD}$	(21)	-392.52	-385.37	-0.024	-393.17	-389.64	-0.021
$\text{C}_4\text{H}_3\text{SCN} + \text{D}_2\text{H}^+ \longrightarrow 3\text{CNT-D}^+ + \text{HD}$	(21')	-393.36	-385.72	-0.026	-393.80	-393.59	-0.021
$\text{C}_4\text{H}_3\text{SCN} + \text{D}_2\text{H}^+ \longrightarrow 2\text{CNT-H}^+ + \text{D}_2$	(22)	-382.47	-372.08	-0.035	-389.80	-389.64	-0.014
$\text{C}_4\text{H}_3\text{SCN} + \text{D}_2\text{H}^+ \longrightarrow 3\text{CNT-H}^+ + \text{D}_2$	(22')	-383.25	-372.38	-0.36	-390.34	-390.20	-0.014
$\text{C}_4\text{H}_3\text{SCN} + \text{D}_3^+ \longrightarrow 2\text{CNT-D}^+ + \text{D}_2$	(23)	-383.77	-373.07	-0.036	-391.67	-391.49	-0.019
$\text{C}_4\text{H}_3\text{SCN} + \text{D}_3^+ \longrightarrow 3\text{CNT-D}^+ + \text{D}_2$	(23')	-384.61	-373.42	-0.038	-392.31	-392.12	-0.019

interstellar ion chemistry, especially, by deuterating other molecules^[86–88]. In fact, this ion is a tracer of the H_3^+ which, having not a permanent dipole moment, could not be observed at millimeters/submillimeters^[85,89] due to the absence. H_2D^+ was widely detected in many ISM environments^[89–91]. This ion was found to be of similar abundance with one of its deuterated forms, i.e., D_2H^+ in low-mass prestellar cores and protostars where the $\text{D}_2\text{H}^+/\text{H}_2\text{D}^+$ ratio reaches unity and D_3^+ is more abundant than these two compounds^[85]. Many reactions ending at the formation of this molecular species were proposed by Millar^[88], but the adopted one at low temperature is:



The left-to-right reaction is an exoergic by an amount equivalent to $\Delta E/k = 220\text{ K}$ ^[92]. The reverse is endothermic with an energy barrier of about 220 K ^[93]. In general, H_2D^+ is produced via fractionation reactions involving HD, but it has argued that they favor the production of high deuterium content molecules^[85,87]. Beside H protonation, we also investigate on the D protonation, especially, on the formation of 2CNTD^+ and 3CNTD^+ in the environment where their H forms were studied. Table 6.12 presents the gase phase G2(MP2) calculated enthalpy, entropy and Gibbs free energy changes ($\Delta_r H$, $\Delta_r S$ and $\Delta_r G$ in kJ mol^{-1}) of the reactions producing 2CNTD^+ and 3CNTD^+ at $T = 298\text{ K}$ and $T = 10\text{ K}$ and a low pressure ($P = 10^{-5}\text{ atm}$).

Analyzing then the results in Table 6.12, i.e., the reactions **(19)**-**(23)** (reactions concerning 2CNTD^+ formation) and **(19')**-**(23')** (reactions concerning 3CNTD^+ formation), it is clear that $\Delta_r H$, $\Delta_r S$ and $\Delta_r G$ are all negative. This implies that, all these reaction are spontaneous at all temperatures. As in the cases of the reactions related to the H forms (preceding tables), these reactions are all enthalpy-driven as, obviously, $|\Delta_r H| > |\Delta_r S|$ with $\Delta_r H \approx \Delta_r G$.

These results, supported by those of the different works on the sulfur abundance in the ISM (e.g. Martín-Doménech et al.^[42]) and those of the work by McGuire et al.^[43], lead us to assert that cyanothiophenes (2CNT and 3CNT , their protonated forms, i.e. 2CNTH^+ , 3CNTH^+ , 2CNTD^+ and 3CNTD^+), but also their different isotopologues, do exist in the interstellar medium.

6.3.4 Vibrational spectrum of H-CNH⁺ vs vibrational spectrum of 2CNTH⁺ and 3CNTH⁺

The IR spectroscopy is an essential tool for the characterisation and identification of interstellar molecular species^[4,55]. One of the most puzzling questions concerning the identification of molecules in space by using the IR spectroscopy is the so-called unidentified infrared bands (UIRs), for which several sources have been proposed, including small carbonaceous molecules (SCMs), PAHs, or mixed aromatic and aliphatic molecules^[55]. However, for the species under consideration in this study, these spectroscopic data required in resolving this ambiguity are not available yet. A potential energy distribution (PED), in which the contribution of each vibrational mode and the molecular atoms involved for the 27 vibrational frequencies for each compound is investigated. This technique is expected to fully characterize the two compounds in the IR region. Table 6.13 and Table 6.14 present the results for the PED for for 2CNTH⁺ and 3CNTH⁺.

Table 6.13 – Potential energy distribution for 2CNTH⁺

Frequency (cm ⁻¹)	PED (%)	Mode	Atoms ¹				PED (%)	Mode	Atoms ¹			
			h	k	l	m			h	k	l	m
In - plane modes												
3539.33	97%	ν_{NH}	7	11	0	0						
3101.63	66%	ν_{CH}	4	9	0	0	27%	ν_{CH}	5	10	0	0
	5%	ν_{CH}	3	8	0	0						
3089.33	65%	ν_{CH}	5	10	0	0	19%	ν_{CH}	3	8	0	0
	16%	ν_{CH}	4	9	0	0						
3081.49	75%	ν_{CH}	3	8	0	0	18%	ν_{CH}	4	9	0	0
	7%	ν_{CH}	5	10	0	0						
2237.41	83%	$\nu_{\text{C}\equiv\text{N}}$	6	7	0	0	14%	ν_{CC}	2	6	0	0
1497.37	29%	$\nu_{\text{C}=\text{C}}$	2	3	0	0	23%	$\nu_{\text{C}=\text{C}}$	4	5	0	0
	11%	δ_{CCH}	4	3	8	0	7%	δ_{CCH}		3	8	0
	7%	ν_{CC}	2	6	0	0	8%	δ_{CCH}	3	4	9	0
1408.49	40%	ν_{CC}	3	4	0	0	15%	δ_{CCH}	5	4	9	0
	11%	δ_{CCH}	3	4	9	0	11%	$\nu_{\text{C}=\text{C}}$	4	5	0	0
	6%	δ_{CCH}	2	3	8	0						
1335.64	24%	$\nu_{\text{C}=\text{C}}$	4	5	0	0	23%	$\nu_{\text{C}=\text{C}}$	2	3	0	0
	14%	δ_{SCH}	1	5	10	0	14%	ν_{CC}	2	6	0	0
	14%	δ_{CCH}	4	5	10	0						
1236.89	20%	δ_{CCH}	2	3	8	0	18%	δ_{CCH}	4	3	8	0
	10%	ν_{CC}	2	6	0	0	10%	δ_{CCH}	5	4	9	0
	9%	δ_{CCH}	3	4	9	0	8%	δ_{CCH}	4	5	10	0
1173.73	29%	ν_{CC}	2	6	0	0	22%	ν_{SC}	1	2	0	0
	12%	$\nu_{\text{C}=\text{C}}$	2	3	0	0	7%	ν_{CC}	3	4	0	0
	6%	δ_{CCH}	2	3	8	0						
1086.10	27%	δ_{CCH}	4	5	10	0	25%	δ_{SCH}	1	5	10	0
	19%	$\nu_{\text{C}=\text{C}}$	4	5	0	0	14%	δ_{CCH}	5	4	9	0
	11%	δ_{CCH}	3	4	9	0						
1057.05	26%	ν_{CC}	3	4	0	0	21%	δ_{CCH}	4	3	8	0
	10%	δ_{CCH}	2	3	8	0	10%	δ_{CCH}	3	4	9	0
	9%	δ_{CCH}	5	4	9	0	6%	ν_{CC}	2	6	0	0
855.06	49%	ν_{SC}	1	5	0	0	16%	δ_{SCC}	1	5	4	0
	12%	δ_{CCC}	3	4	5	0	7%	δ_{SCH}	1	5	10	0
	6%	δ_{SCH}	3	4	9	0						
738.13	35%	ν_{SC}	1	5	0	0	22%	ν_{SC}	1	2	0	0
	13%	δ_{CCC}	3	4	5	0	13%	δ_{CCC}	2	3	4	0

(Continued)

Table 6.13 – (Continued)

Frequency (cm^{-1})	PED (%)	Mode	Atoms ¹				PED (%)	Mode	Atoms ¹			
			h	k	l	m			h	k	l	m
681.15	5%	δ_{CCH}	2	3	8	0	5%	δ_{CCH}	5	4	9	0
	26%	ν_{SC}	1	2	0	0	12%	δ_{CCN}	2	6	7	0
	10%	δ_{CSC}	2	1	5	0	9%	ν_{CC}	2	6	0	0
634.21	8%	ν_{SC}	1	5	0	0	8%	δ_{SCC}	1	5	4	0
	93%	δ_{CNH}	6	7	11	0	6%	δ_{CCN}	2	6	7	0
520.93	51%	δ_{CCN}	2	6	7	0	18%	ν_{SC}	1	2	2	0
	9%	δ_{CCC}	3	2	6	0	7%	δ_{CSC}	2	1	5	0
	6%	δ_{SCC}	1	2	6	0						
477.06	30%	ν_{CC}	2	6	0	0	20%	δ_{SCC}	1	2	3	0
	13%	δ_{CSC}	2	1	5	0	10%	ν_{SC}	1	2	0	0
	6%	δ_{CCC}	2	3	4	00						
143.33	44%	δ_{CCN}	2	6	7	0	28%	δ_{SCC}	1	2	6	0
	26%	δ_{CCC}	3	2	6	0						
Out - of - plane modes												
943.69	31%	γ_{HCCH}	8	3	4	9	27%	γ_{HCCH}	9	4	5	10
	10%	γ_{HCCS}	9	4	5	1	8%	γ_{CCCH}	2	3	4	9
	6%	γ_{CCCH}	6	2	3	8	6%	γ_{SCCH}	1	2	3	8
866.48	25%	γ_{HCCH}	9	4	5	10	15%	γ_{CCCH}	3	4	5	10
	14%	γ_{HCCC}	6	2	3	8	13%	γ_{HCCC}	8	3	4	5
	12%	γ_{SCCH}	1	2	3	8	9%	γ_{CSCH}	2	1	5	10
751.15	22%	γ_{CCCH}	3	4	5	10	22%	γ_{HCCS}	9	4	5	1
	20%	γ_{CCCH}	2	3	4	9	16%	γ_{CSCH}	2	1	5	10
	7%	γ_{CCCH}	6	2	3	8	6%	γ_{SCCH}	1	2	3	8
551.49	60%	γ_{CCN}	0	2	6	7	8%	γ_{SCCC}	1	2	3	4
	7%	γ_{CCCC}	2	3	4	5						
525.46	61%	γ_{CCN}	0	2	6	7	9%	γ_{CCCS}	3	4	5	1
	6%	γ_{CCCC}	2	3	4	5						
420.34	36%	γ_{CCN}	0	2	6	7	16%	γ_{CSCC}	5	1	2	3
	14%	γ_{CSCC}	2	1	5	4	11%	γ_{SCCC}	1	2	3	4
	9%	γ_{CCCS}	3	4	5	1						
287.26	69%	γ_{CNH}	0	6	7	11	17%	γ_{CCN}	0	2	6	7
134.42	32%	γ_{CCN}	0	2	6	7	24%	γ_{CSCCC}	6	2	3	4
	19%	γ_{CSCC}	5	1	2	6	17%	γ_{CCCH}	6	2	3	8
	5%	γ_{CNH}	0	6	7	11						

¹ See Figure 6.1 for atom numbering.

ν : stretching, δ : in-plane bending and γ : out-of-plane bending modes.

As it can be seen in these tables, the vibrational spectrum of each compound consists of 27 fundamental modes of vibration divided into the two symmetry representations of the C_s pointgroup: $\Gamma_{3N-6} = 19A'$ (in-plane modes) + $8A''$ (out-of-plane modes) as shown in Table 6.15.

Table 6.14 – Potential energy distribution for 3CNTH^+

Frequency (cm^{-1})	PED (%)	Mode	Atoms ¹				PED (%)	Mode	Atoms ¹			
			h	k	l	m			h	k	l	m
In - plane modes												
3545.56	97%	ν_{NH}	7	11	0	0						
3122.71	82%	ν_{CH}	5	10	0	0	16%	ν_{CH}	4	9	0	0
3111.54	99%	ν_{CH}	2	8	0	0						
3103.59	83%	ν_{CH}	4	9	0	0	17%	ν_{CH}	5	9	0	0

(Continued)

Table 6.14 – (Continued)

Frequency (cm^{-1})	PED (%)	Mode	Atoms ¹				PED (%)	Mode	Atoms ¹			
			h	k	l	m			h	k	l	m
2243.78	85%	$\nu_{\text{C}\equiv\text{N}}$	6	7	0	0	12%	ν_{CC}	3	6	0	0
1495.04	49%	$\nu_{\text{C}=\text{C}}$	4	5	0	0	11%	δ_{CCH}	3	4	9	0
	10%	$\nu_{\text{C}=\text{C}}$	2	3	0	0	6%	δ_{CCH}	5	4	9	0
1402.09	25%	$\nu_{\text{C}=\text{C}}$	2	3	0	0	16%	$\nu_{\text{C}=\text{C}}$	4	5	0	0
	15%	δ_{CCH}	3	2	8	0	14%	δ_{SCH}	1	2	8	0
	10%	ν_{CC}	3	6	0	0	5%	δ_{SCH}	1	5	10	0
1351.97	36%	ν_{CC}	3	4	0	0	25%	$\nu_{\text{C}=\text{C}}$	2	3	0	0
	9%	δ_{CCH}	5	4	9	0	8%	δ_{CCH}	4	5	10	0
1227.94	24%	δ_{CCH}	3	2	8	0	13%	δ_{SCH}	1	2	8	0
	12%	δ_{CCH}	4	5	10	0	11%	δ_{SCH}	5	4	9	0
	10%	δ_{SCH}	1	5	10	0	9%	δ_{SCH}	3	4	9	0
1167.85	34%	δ_{CCH}	1	2	8	0	27%	δ_{SCH}	3	2	8	0
	20%	ν_{CC}	3	6	0	0						
1091.36	20%	δ_{CCH}	5	4	9	0	19%	δ_{CCH}	4	5	10	0
	18%	δ_{CCH}	3	4	9	0	17%	δ_{SCH}	1	5	10	0
	10%	$\nu_{\text{C}=\text{C}}$	4	5	0	0						
920.50	15%	δ_{CCC}	3	4	5	0	15%	ν_{CC}	3	6	0	0
	14%	ν_{CC}	3	4	0	0	13%	$\nu_{\text{C}=\text{C}}$	2	3	0	0
	11%	δ_{SCH}	1	5	10	0	8%	δ_{SCC}	1	5	4	0
880.44	72%	ν_{SC}	1	2	0	0	15%	δ_{CCH}	1	2	8	0
	6%	δ_{CCC}	2	3	4	0						
800.41	63%	ν_{SC}	4	5		0	11%	δ_{SCC}	1	5	4	0
	6%	ν_{CC}	3	4	0	0						
637.28	64%	δ_{CNH}	6	7	11	0	8%	δ_{CSC}	2	1	5	0
	8%	ν_{SC}	1	5	0	0	7%	δ_{CCN}	3	6	7	0
627.50	53%	δ_{CNH}	6	7	11	0	13%	δ_{CSC}	2	1	5	0
	13%	ν_{SC}	1	5	0	0						
558.52	61%	δ_{CCN}	3	6	7	0	13%	δ_{CCC}	4	3	6	0
	11%	δ_{CCC}	2	3	6	0						
472.43	37%	ν_{CC}	3	6	0	0	14%	δ_{CCC}	2	3	4	0
	13%	ν_{SC}	1	2	0	0	9%	δ_{SCC}	2	1	5	0
147.54	47%	δ_{CCN}	3	6	7	0	25%	δ_{CCC}	2	3	6	0
	25%	δ_{CCC}	4	3	6	0						
Out - of - plane modes												
894.08	49%	γ_{HCCH}	9	4	5	10	11%	γ_{HCCS}	9	4	5	1
	10%	γ_{CCCH}	2	3	4	9	9%	γ_{CCCH}	3	4	5	10
	9%	γ_{CCCH}	6	3	4	9	7%	γ_{CSCH}	2	1	5	10
799.58	33%	γ_{HCCC}	8	2	3	6	26%	γ_{HCCC}	8	2	3	4
	21%	γ_{CSCH}	5	1	2	8						
713.74	27%	γ_{CCCH}	3	4	5	10	17%	γ_{CSCH}	2	1	5	10
	14%	γ_{HCCS}	9	4	5	1	11%	γ_{HCCC}	2	3	4	9
	10%	γ_{CCCH}	8	2	3	4	9%	γ_{CCCH}	6	3	4	9
604.43	53%	γ_{CCN}	3	6	7	0	10%	γ_{CCCC}	2	3	4	5
	8%	γ_{SCCC}	1	2	3	4	5%	γ_{CCCH}	8	2	3	4
497.78	74%	γ_{CCN}	0	3	6	7	6%	γ_{CCCS}	3	4	5	1
	5%	γ_{CCCC}	2	3	4	5						
441.05	21%	γ_{CCN}	0	3	6	7	20%	γ_{CSCC}	2	1	5	4
	19%	γ_{CSCC}	5	1	2	3	14%	γ_{SCCC}	1	2	3	4
	5%	γ_{CCCS}	3	4	5	1						
366.92	82%	γ_{CNH}	0	6	7	11	14%	γ_{CCN}	0	3	6	7
132.27	34%	γ_{CCN}	0	3	6	7	21%	γ_{SCCCC}	1	2	3	6
	18%	γ_{CCCC}	6	3	4	5	12%	γ_{CCCH}	6	3	4	9
	12%	γ_{HCCC}	8	2	3	6						

¹ See Figure 6.1 for atom numbering.

ν : stretching, δ : in-plane bending and γ : out-of-plane bending modes.

This table presents also M06-2X/6-31G(d,p) calculated frequencies (cm^{-1}), infrared intensities ($\text{km}\cdot\text{mol}^{-1}$) and Raman activities (in $\text{\AA}^4/\text{amu}$) and Raman intensities (in $\times 10^{-24}\text{F}^2\cdot\text{m}^{-1}\cdot\text{kg}^{-1}$) for 2CNTH^+ and 3CNTH^+ .

Beside the general interpretation of these two spectra, particular attention is made the behaviour caused by the introduction of the new bond due to the protonation. In fact, the 2CNTH^+ and 3CNTH^+ IR spectra compared to the ones for the corresponding non protonated forms leads to the appearance of the three additional modes resulted from the additional N–H. Thus, from Table 6.13), these three modes are:

- (i) the ν_{NH} stretching mode appearing at $\approx 3539\text{ cm}^{-1}$ with a PED of 97% for 2CNTH^+ and at $\approx 3546\text{ cm}^{-1}$ with again a PED of 97% for 3CNTH^+ . This mode gives rise to a highly strong transition with $\approx 1381\text{ km/mol}$ (2CNTH^+) and $\approx 1337\text{ km/mol}$ (3CNTH^+). As it can be seen from Table 6.15 and Figure 6.3(b) and (c), ν_{NH} stretching mode gives rise to stronger transition for 2CNTH^+ than that for 3CNTH^+ . Moreover, this transition is more than 2 times stronger than that arising from the $\nu_{\text{C}\equiv\text{N}}$ stretching vibrational mode with IR intensity of $\approx 667\text{ km/mol}$ for 2CNTH^+ and of $\approx 574\text{ km/mol}$ for 3CNTH^+ . This IR band from the $\nu_{\text{C}\equiv\text{N}}$ stretching vibrational mode was found to be the strongest one in non protonated forms (see Table 4.7 in section 4.3 in chapter 4). Regarding the Raman spectra of these two species, results presented in Table 6.15 and at Figure 6.3 show that this mode of vibration gives rise to a very weak IR transition ≈ 73 times weaker than the strongest Raman transition, i.e., that from the σ_{CH} stretching vibration mode.
- (ii) the in-plan bending mode δ_{CNH} gives rise to a transition at $\sim 634\text{ cm}^{-1}$ (PED $\approx 93\%$) for 2CNTH^+ and to a doublet at $\sim 637\text{ cm}^{-1}$ (PED $\approx 64\%$) and at $\sim 628\text{ cm}^{-1}$ (PED $\approx 53\%$) for 3CNTH^+ . These transitions are also relatively stronger for 2CNTH^+ than 3CNTH^+ . In fact, the calculated intensity for this transition is $\approx 133\text{ km/mol}$ in the former, whereas intensities found for the two transitions of 3CNTH^+ are ≈ 69 and $\approx 65\text{ km/mol}$, respectively. It is worthy noting that they are very weak compared to those rose from the ν_{NH} stretching vibrational modes. For instance, transition from δ_{CNH} is ≈ 10 times weaker than that from ν_{NH} for 2CNTH^+ and ≈ 20 times smaller for 3CNTH^+ . Note also that, this transition is about ≈ 2 times stronger for 2CNTH^+ than for 3CNT . Nonetheless, the Raman bands corresponding to these δ_{CNH} in-plan bending modes are stronger than those corresponding to the ν_{NH} (see Table 6.15, Table 6.13 (2CNTH^+) and Table 6.14 (3CNTH^+) and Figure 6.4). For instance, the transition at $\sim 637\text{ cm}^{-1}$ is 4 times stronger than that at 3546 cm^{-1} ; that at this latter is ≈ 2.5 smaller than that at $\sim 628\text{ cm}^{-1}$. For 2CNTH^+ the transition corresponding to the in-plan deformation δ_{CNH} is still weaker than that corresponding to the stretching mode ν_{NH} .
- (iii) the out-of-plan bending mode γ_{CNH} giving rise to the transition appearing at $\approx 287\text{ cm}^{-1}$ with 69% as PED for 2CNTH^+ and at $\approx 364\text{ cm}^{-1}$ with 82% as PED for 3CNTH^+ . The corresponding IR transitions, whether for 2CNTH^+ or 3CNTH^+ , are also strong, especially compared with those arising from the in-plane bending mode δ_{CNH} (see Table 6.15 and Figure 6.3). Thus, the transition at $\approx 287\text{ cm}^{-1}$ for 2CNTH^+ has about 180 km/mol as intensity, i.e., about 8 times smaller than that corresponding to ν_{NH} .

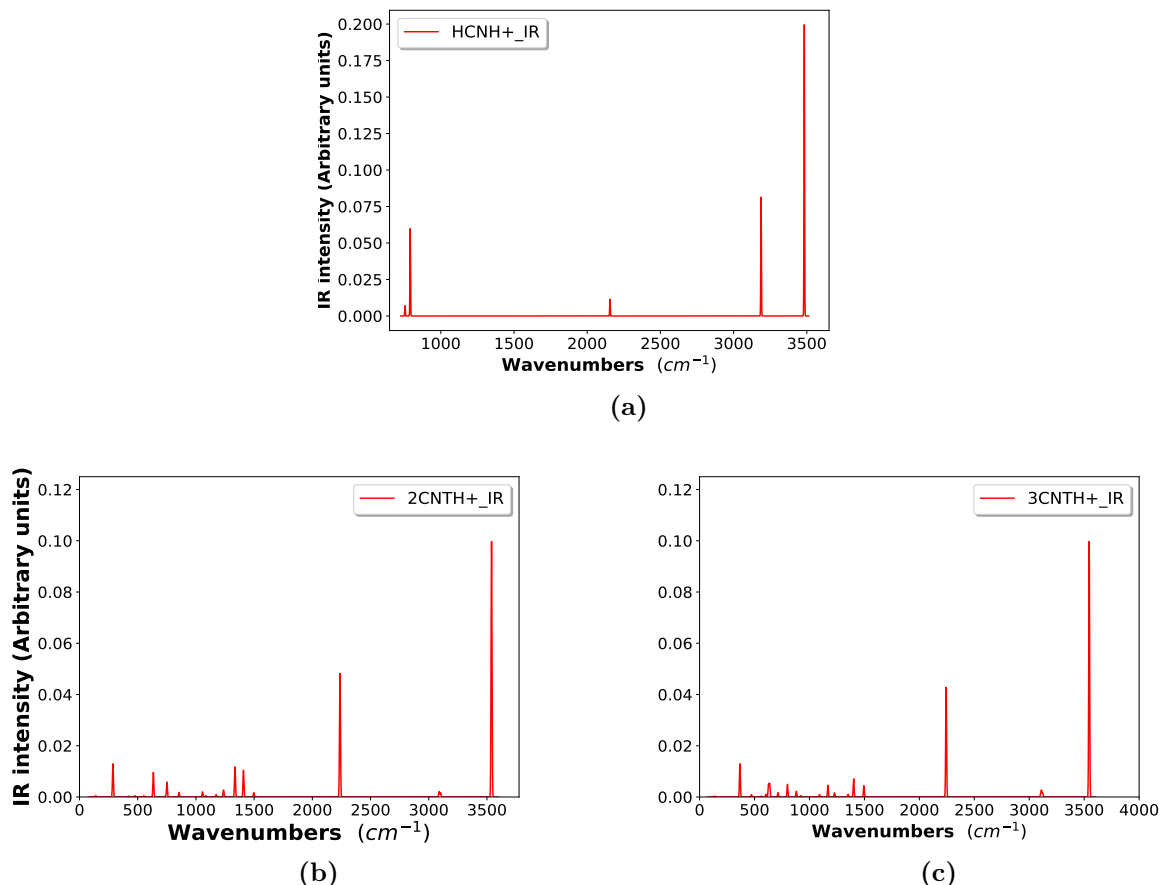


Figure 6.3 – M06-2X/6-31G(d,p) gas phase simulated IR spectra of (a) HCNH⁺, (b) 2CNTH⁺ and (c) 3CNTH⁺.

Likewise, the transition at $\approx 364 \text{ cm}^{-1}$ for 3 CNTH⁺ has $\approx 174 \text{ km/mol}$ as IR intensity (also about 8 times smaller that corresponding to ν_{NH}). Moreover, concerning the Raman intensities, the band appearing from this mode for 2 CNTH⁺ is 7 times that corresponding to the stretching mode, whereas that for 3 CNTH⁺ is ≈ 5 times that arising from ν_{NH} .

The NH and CH stretching modes for the studied species are characterized in region where they are postulated to appear, i.e., in the range $3000 - 3800 \text{ cm}^{-1}$ [1,94,95]. This part of the spectrum is characteristics of NH and CH stretching modes. Indeed, the calculated frequencies for the ν_{NH} and ν_{CH} stretching modes appear all and for both the 2 CNTH⁺ and 3 CNTH⁺ in the quoted region. In fact, as already stated above, the ν_{NH} stretching modes appear at $\approx 3539 \text{ cm}^{-1}$ for 2 CNTH⁺ and at $\approx 3546 \text{ cm}^{-1}$ for the 3 CNTH⁺, respectively. Likewise, regarding the ν_{CH} stretching modes, they are found at ≈ 3102 (PED= 98%), ≈ 3089 (PED= 100%) and 3081 cm^{-1} (PED= 99%) for 2 CNTH⁺; at ≈ 3123 (PED= 98%), ≈ 3112 (PED= 99%) and 3081 cm^{-1} (PED= 100%) for 3 CNTH⁺. As in the cases of non protonated forms, the $\nu_{\text{C}\equiv\text{N}}$ stretching mode gives rise to a strong transition whether in IR or Raman spectrum for both the two compounds. Another general observation is that, whereas protonated forms show stronger IR spectral lines than non protonated ones, these latter have stronger Raman spectral bands than the former.

Table 6.16 presents the PED for stretching and bending modes as well as their IR intensities for HCNH⁺. The comparison beteen S10 and S11 results show that the NH stretching modes in protonated cyanothiophenes intensities are more than two times greater

Table 6.15 – M06-2X/6-31G(d,p) calculated frequencies (cm^{-1}), infrared intensities (km. mol^{-1}) and Raman activities ($\text{\AA}^4/\text{amu}$) and Raman intensities ($\times 10^{-24} \text{F}^2 \cdot \text{m}^{-1} \cdot \text{kg}^{-1}$) for 2CNTH^+ and 3CNTH^+ .

2CNTH^+											3CNTH^+										
Sym	NSc.Freq.	Sc.Freq.	IR int.	Ram. Activ	Ram. Int.	Sym	NSc.Freq.	Sc.Freq.	IR int.	Ram. Activ	Rama. Int	Sym	NSc.Freq.	Sc.Freq.	IR int.	Ram. Activ	Rama. Int				
A'	3753	3539	1380.68	16.58	1.10	A'	3747	3546	1337.37	12.96	1.79	A'	3747	3546	1337.37	12.96	1.79				
A'	3289	3102	23.22	209.08	21.15	A'	3301	3123	20.99	150.13	73.06	A'	3301	3123	20.99	150.13	73.06				
A'	3276	3089	29.15	73.37	7.51	A'	3289	3112	34.28	55.95	8.29	A'	3289	3112	34.28	55.95	8.29				
A'	3268	3081	1.65	74.84	7.72	A'	3280	3104	13.57	63.80	1.27	A'	3280	3104	13.57	63.80	1.27				
A'	2388	2237	667.39	322.88	75.72	A'	2395	2244	573.87	343.51	35.43	A'	2395	2244	573.87	343.51	35.43				
A'	1560	1497	23.65	1.35	0.70	A'	1573	1495	59.30	36.55	10.82	A'	1573	1495	59.30	36.55	10.82				
A'	1467	1408	144.82	66.51	38.44	A'	1479	1402	95.13	24.85	4.86	A'	1479	1402	95.13	24.85	4.86				
A'	1395	1336	162.92	58.68	37.11	A'	1419	1352	14.53	4.04	0.13	A'	1419	1352	14.53	4.04	0.13				
A'	1278	1237	38.13	4.45	3.19	A'	1262	1228	21.69	7.30	10.42	A'	1262	1228	21.69	7.30	10.42				
A'	1231	1174	12.48	3.43	2.67	A'	1214	1168	61.18	9.65	4.18	A'	1214	1168	61.18	9.65	4.18				
A'	1121	1086	7.14	12.90	11.37	A'	1121	1091	12.52	1.75	5.26	A'	1121	1091	12.52	1.75	5.26				
A'	1094	1057	28.14	1.08	1.00	A'	958	920	7.03	5.79	0.20	A'	958	920	7.03	5.79	0.20				
A"	977	944	0.13	0.77	0.84	A"	934	894	0.36	0.15	31.68	A"	934	894	0.36	0.15	31.68				
A"	907	866	0.38	0.94	1.17	A'	928	880	30.25	5	6.05	A'	928	880	30.25	5	6.05				
A'	889	855	24.93	6.58	8.31	A'	846	800	0.58	22.77	0.18	A'	846	800	0.58	22.77	0.18				
A"	783	751	79.80	1.80	2.74	A"	833	800	65.76	0.14	6.56	A"	833	800	65.76	0.14	6.56				
A'	767	738	5.38	9.86	15.44	A"	745	714	23.43	3.20	1.53	A"	745	714	23.43	3.20	1.53				
A'	711	681	1.65	21.09	37.05	A'	662	637	69.17	2.16	7.60	A'	662	637	69.17	2.16	7.60				
A'	658	634	132.93	0.36	0.69	A'	652	627	65.12	5.27	5.30	A'	652	627	65.12	5.27	5.30				
A"	571	551	6.66	0.33	0.78	A"	625	604	14.52	0.06	2.50	A"	625	604	14.52	0.06	2.50				
A"	544	525	0.53	0.46	1.17	A'	581	559	4.42	2.08	14.47	A'	581	559	4.42	2.08	14.47				
A'	543	521	1.62	2.08	5.39	A"	515	498	0.50	3.91	19.05	A"	515	498	0.50	3.91	19.05				
A'	495	477	7.22	10.67	31.42	A'	494	472	12.55	11.86	80.05	A'	494	472	12.55	11.86	80.05				
A"	431	420	4.56	2.98	10.58	A"	453	441	0.35	0.39	6.44	A"	453	441	0.35	0.39	6.44				
A"	298	287	179.53	2.26	14.42	A"	381	367	173.99	1.90	5.60	A"	381	367	173.99	1.90	5.60				
A'	149	143	4.85	4.75	97.22	A'	153	148	3.06	3.76	14.88	A'	153	148	3.06	3.76	14.88				
A"	137	134	5.37	0.19	4.40	A"	136	132	4.71	0.08	0.86	A"	136	132	4.71	0.08	0.86				

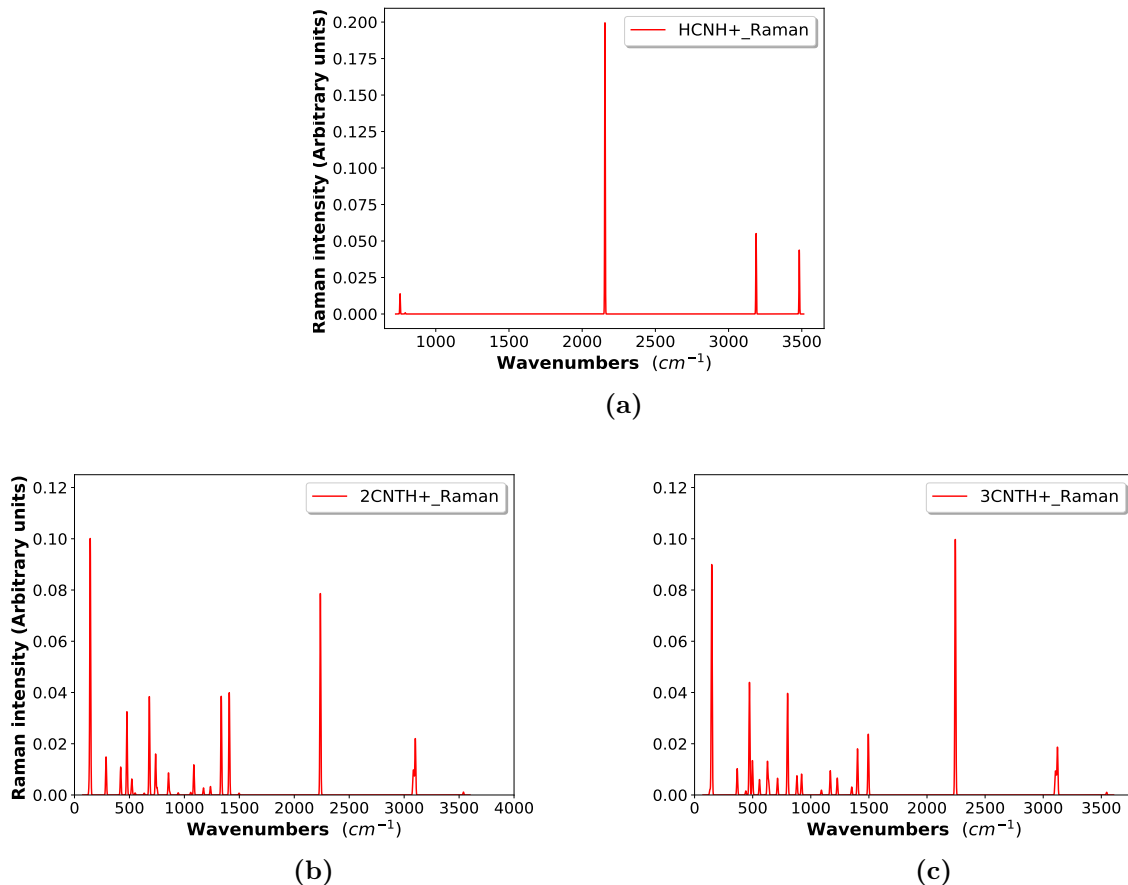


Figure 6.4 – M06-2X/6-31G(d,p) gas phase simulated Raman spectra of (a) HCNH⁺, (b) 2CNTH⁺ and (c) 3CNTH⁺.

Table 6.16 – Potential energy distribution for stretching and bending modes of HCNH⁺ and IR intensities.

Frequency (cm ⁻¹)	IR Int. (km/mol)	PED (%)	Mode	Atoms ¹				PED (%)	Mode	Atoms ¹			
				h	k	l	m			h	k	l	m
3482.94	611.57	98%	ν_{NH}	2	4	0	0						
3187.90	249.68	96%	ν_{CH}	1	3	0	0						
2155.69	35.05	98%	$\nu_{\text{C}\equiv\text{N}}$	1	2	0	0						
791.15	183.41	51%	γ_{NCH}	0	2	1	3	49%	γ_{CNH}	0	1	2	4
791.15	183.41	51%	δ_{NCH}	2	1	3	0	49%	δ_{CNH}	1	2	4	0
756.00	21.77	51%	δ_{CNH}	1	2	4	0	49%	δ_{NCH}	2	1	3	0
756.00	21.77	51%	γ_{CNH}	0	1	2	4	49%	γ_{NCH}	0	2	1	3

¹ See Figure 1 for atom numbering.

ν : stretching, δ : in-plane bending and γ : out-of-plane bending modes.

than in protonated cyanide. Conversely, CH stretching mode intensity in protonated is more than ten times greater than in protonated cyanothiophenes. In the work by Altman et al. [25], it has reported that CH stretch intensity is $\approx 30\%$ weaker than that of NH. Similarly, whether for 2CNTH⁺ and 3CNTH⁺, the NH intensity is found to be highly stronger than the CH. In fact, the NH stretch intensity is $1360.3 \text{ km}\cdot\text{mol}^{-1}$; 16.9, 40.5 and $14.5 \text{ km}\cdot\text{mol}^{-1}$ for the three CH stretching modes for 3CNTH⁺. For 2CNTH⁺, the calculated IR intensities are $1330.0 \text{ km}\cdot\text{mol}^{-1}$ for NH stretching mode; 23.1 28.4 and $2.8 \text{ km}\cdot\text{mol}^{-1}$ for the three CH stretching modes. The strongest of these last is $\approx 33\%$ weaker than the NH for 2CNTH⁺

and $\approx 46\%$ weaker for 3CNTH^+ , respectively. Our results provide new insights on the way towards the identification of the protonated cyanothiophenes in the ISM. They also are expected to assist experimental studies on these compounds. Thus, individual molecular IR data needed to thrash out the possible misassignment of the UIRs features for each of these molecules have been therefore provided.

6.3.5 Rotational spectrum of H-CN^+ vs rotational spectrum of 2CNTH^+ and 3CNTH^+

The calculated rotational parameters for the three protonated species are provided in Table 6.17. For comparison, experimental data for HCNH^+ are also provided. This work is the first investigation on rotational spectroscopic properties for 2CNTH^+ and 3CNTH^+ . However, these molecular properties are valuable as a great number of molecular species already detected in space were detected thanks to their rotational transitions (see the Cologne Database for Molecular Spectroscopy (CDMS) [96]).

Table 6.17 – M06-2X/6-31G(d,p) calculated (including empirical corrections) rotational constants, and dipole moments.

Rotational parameters	HCNH^+	2CNTH^+	3CNTH^+
A (MHz)	0.000	5249.831	6953.084
B (MHz)	37055.676 (37055.749) ^a	1756.883	1452.489
C (MHz)	37055.676 (37055.749) ^a	1316.356	1201.497
De (MHz)	0.042 (0.048) ^a	-	-
Δ_J (kHz)		0.102	0.045
Δ_K (kHz)		4.341	4.749
Δ_{KJ} (kHz)		0.117	0.736
δ_J (kHz)		0.035	0.010
δ_K (kHz)		0.535	0.612
μ_a (Debye)	0.392	-0.888	0.822
μ_b (Debye)	0.000	4.403	-5.972
μ_c (Debye)	0.000	0.000	0.000
μ_{tot} (Debye)	0.392	4.491	6.028
I_{aa} (amu \AA^2)	0.000	96.266	72.684
I_{bb} (amu \AA^2)	13.670	287.657	347.941
I_{cc} (amu \AA^2)	13.670	383.922	420.625
χ_{aa} (MHz)		1.120	1.057
χ_{bb} (MHz)		0.615	0.394
χ_{cc} (MHz)		-1.734	-1.451
χ_{ab} (MHz)		-0.060	-0.045
κ		-0.776	-0.913

^a Experimental values from Ziurys et al. [34].

A molecule has a rotational spectrum if it has a permanent dipole moment. From these results, it is clear that HCNH^+ has a very low dipole moment compared to those of 2CNTH^+ and 3CNTH^+ . It is known that the rotational intensity is proportional to the square of the dipole moment components [97,98]. For this reason, it would be observed that the higher the dipole moment of a molecular species, the stronger is its rotational transition. Nevertheless, the comparison of line intensities for HCNH^+ to those for 2CNTH^+ and 3CNTH^+ shows that the intensities in both these compounds are of the same order of magnitude. The line intensities in 3CNTH^+ and 2CNTH^+ are about twice those in HCNH^+ . It is not surprising that the HCNH^+ was among the earlier molecule species observed in the ISM by Ziurys *et al.* [32,33]. These authors observed, for the first time in ISM, its $J = 1 \leftarrow -0$, $J = 2 \leftarrow 1$ and $J = 3 \leftarrow 2$ rotational transitions towards Srg B2 at 74, 148 and 222 GHz. Despite its low

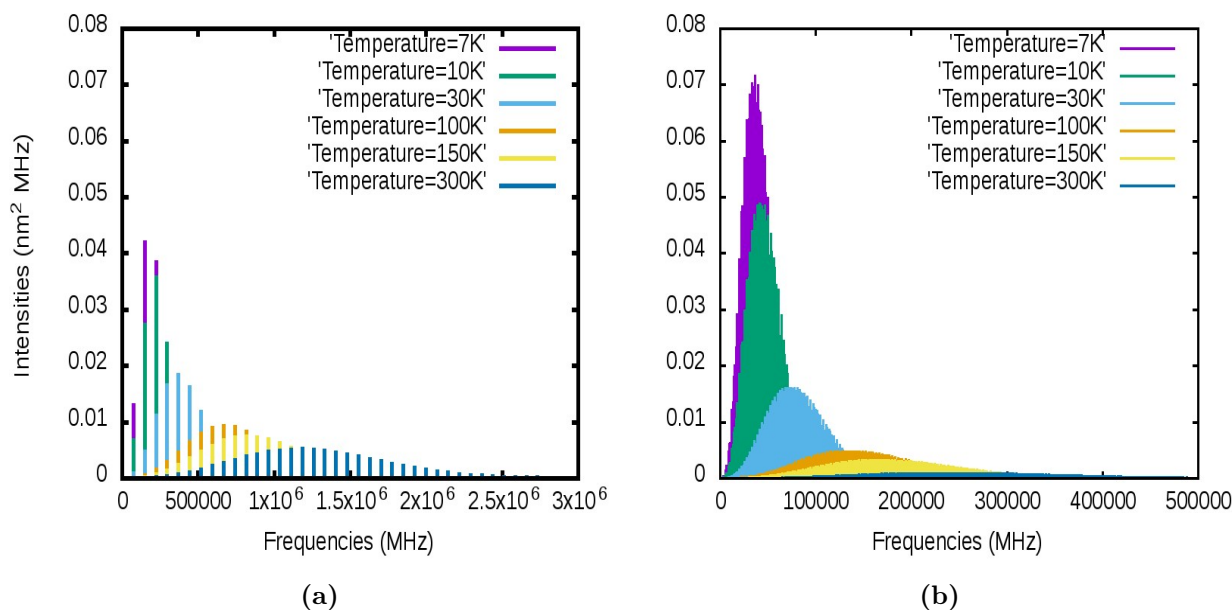


Figure 6.5 – Plots of rotational line transition intensities (including ^{14}N hyperfine quadrupole couplings) for (a) HCNH^+ and (b) 3CNTH^+ .

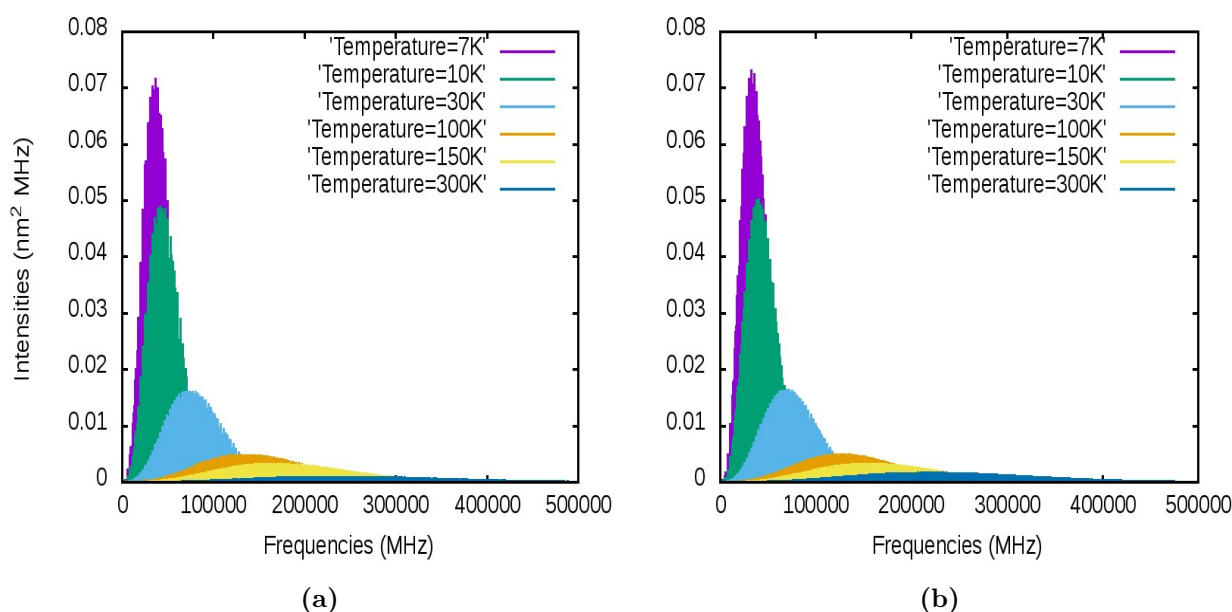


Figure 6.6 – Comparison of ^{14}N quadrupole hyperfine spectra of (a) 2CNTH^+ and (b) 3CNTH^+ for different temperatures ($T = 7, 10, 30, 100$ and 300 K).

dipole moment, H-CNH^+ has low moment of inertia and, consequently, very high rotational constants ($B=C$; A being zero) (Table 6.5) and hence, strong rotational transitions are expected. In contrast, the $\text{C}_4\text{H}_3\text{S-CNH}^+$ compounds (i.e., 2CNTH^+ and 3CNTH^+), despite their high dipole moments [$\mu(2\text{CNTH}^+) \approx 11 \times \mu(\text{H-CNH}^+)$ and $\mu(3\text{CNTH}^+) \approx 15 \times \mu(\text{H-CNH}^+)$], have high components of moment of inertia and, consequently, low rotational constants compared to those of HCNH^+ . Even though HCNH^+ have low dipole moment, its rotational parameters are extremely higher than those of $\text{C}_4\text{H}_3\text{SCNH}^+$ and, consequently, it possesses stronger transitions than those of protonated thiophenes. Based on earlier works, complex organic molecules (COMs), especially, unsaturated ones, were predominantly found in dense and cold regions such as TMC-1^[17]. The protonated cyanothiophenes under this

study, as well as their neutral forms, can therefore be expected to be found in these regions. Meanwhile, the HCNH^+ has been also detected in TMC-1 ($T \approx 10$ K) through the hyperfine structure of the $J = 1 \rightarrow 0$ transition by Ziurys et al.^[32], and through $J = 2 \rightarrow 1$ transition at 148221.422 MHz and $J = 3 \rightarrow 2$ transition at 222329.401 MHz by Schilke et al.^[99]. It has also been detected in L1544 ($T \approx 7$ K)^[100].

Table 6.18 – M06-2X/6-31G(d,p) calculated frequencies and intensities for hyperfine structures of HCNH^+ and for strongest rotational lines of 2CNTH^+ at 10 K.

HCNH^+				2CNTH^+		
Trans ^a	ν_{exp}	ν_{calc}	Int	Trans ^b	ν_{calc}	Int
$3_4 \leftarrow 2_3$	222329.2990	222329.2990	3.565E-02	$15_{0,15}16 \leftarrow 14_{0,14}15$	41301.013	4.880E-02
$2_3 \leftarrow 1_2$		148221.4671	2.726E-02	$15_{1,15}16 \leftarrow 14_{1,14}15$	41297.301	4.879E-02
$3_3 \leftarrow 2_2$		222329.2939	2.465E-02	$13_{2,11}14 \leftarrow 12_{2,10}13$	42136.555	4.866E-02
$4_5 \leftarrow 3_4$	296433.6520	296433.6613	2.398E-02	$14_{0,14}15 \leftarrow 13_{0,13}14$	38639.023	4.844E-02
$4_4 \leftarrow 3_3$		296433.6580	1.840E-02	$14_{3,11}15 \leftarrow 13_{3,10}14$	47015.540	4.844E-02
$3_2 \leftarrow 2_1$		222329.2725	1.664E-02	$14_{1,14}15 \leftarrow 13_{1,13}14$	38632.131	4.843E-02
$2_2 \leftarrow 1_1$		148221.4580	1.460E-02	$13_{3,10}14 \leftarrow 12_{3,9}13$	43730.185	4.834E-02
$4_3 \leftarrow 3_2$		296433.6489	1.402E-02	$12_{2,10}13 \leftarrow 11_{2,9}12$	39376.262	4.803E-02
$5_6 \leftarrow 4_5$		370533.3955	9.567E-03	$16_{0,16}17 \leftarrow 15_{0,15}16$	43963.855	4.794E-02
$5_5 \leftarrow 4_4$		370533.3932	7.771E-03	$16_{1,16}17 \leftarrow 15_{1,15}16$	43961.875	4.793E-02
$1_2 \leftarrow 0_1$	74111.3300	74111.3290	6.809E-03	$14_{2,12}15 \leftarrow 13_{2,11}14$	44766.624	4.773E-02
$2_1 \leftarrow 1_0$	148221.4500	148221.3512	6.491E-03	$13_{0,13}14 \leftarrow 12_{0,12}13$	35978.508	4.682E-02
$5_4 \leftarrow 4_3$	370533.3750	370533.3882	6.296E-03	$13_{1,13}14 \leftarrow 12_{1,12}13$	35965.863	4.679E-02
$2_1 \leftarrow 1_1$		148221.6716	4.868E-03	$15_{3,12}16 \leftarrow 14_{3,11}15$	50140.694	4.668E-02
$2_2 \leftarrow 1_2$		148221.3298	4.868E-03	$14_{1,13}15 \leftarrow 13_{1,12}14$	41437.796	4.668E-02
$1_1 \leftarrow 0_1$	74111.1400	74111.2008	4.085E-03	$13_{1,12}14 \leftarrow 12_{1,11}13$	38837.470	4.628E-02
$3_2 \leftarrow 2_2$		222329.4862	3.081E-03	$12_{3,9}13 \leftarrow 11_{3,8}12$	40306.271	4.620E-02
$3_3 \leftarrow 2_3$		222329.1565	3.081E-03	$14_{2,13}15 \leftarrow 13_{2,12}14$	41257.125	4.616E-02
$6_7 \leftarrow 5_6$	444627.3610	444627.3439	2.411E-03	$17_{0,17}18 \leftarrow 16_{0,16}17$	46627.186	4.598E-02
$6_6 \leftarrow 5_5$		444627.3422	2.031E-03	$17_{1,17}18 \leftarrow 16_{1,16}17$	46626.139	4.598E-02
$6_5 \leftarrow 5_4$		444627.3390	1.709E-03	$15_{1,14}16 \leftarrow 14_{1,13}15$	44057.406	4.594E-02
$1_0 \leftarrow 0_1$	74111.5400	74111.5213	1.362E-03	$15_{2,14}16 \leftarrow 14_{2,13}15$	43947.098	4.566E-02
$4_4 \leftarrow 3_4$		296433.5156	1.226E-03	$15_{0,15}15 \leftarrow 14_{0,14}14$	41301.013	4.564E-02
$4_3 \leftarrow 3_3$		296433.8412	1.226E-03	$15_{1,15}15 \leftarrow 14_{1,14}14$	41297.301	4.563E-02
$7_8 \leftarrow 6_7$	518714.3310	518714.3490	3.970E-04	$15_{2,13}16 \leftarrow 14_{2,12}15$	47315.313	4.559E-02
$7_7 \leftarrow 6_6$		518714.3478	3.431E-04	$11_{2,9}12 \leftarrow 10_{2,8}11$	36459.406	4.558E-02
$2_1 \leftarrow 1_2$		148221.5435	3.246E-04	$13_{2,12}14 \leftarrow 12_{2,11}13$	38551.037	4.541E-02
$5_4 \leftarrow 4_4$		370533.5713	3.238E-04	$14_{0,14}14 \leftarrow 13_{0,13}13$	38639.023	4.509E-02
$5_5 \leftarrow 4_5$		370533.2476	3.238E-04	$14_{3,11}14 \leftarrow 13_{3,10}13$	47015.540	4.508E-02
$7_6 \leftarrow 6_5$		518714.3455	2.964E-04	$14_{1,14}14 \leftarrow 13_{1,13}13$	38632.131	4.507E-02
$3_2 \leftarrow 2_3$		222329.3488	8.802E-05	$13_{2,11}13 \leftarrow 12_{2,10}12$	42136.555	4.504E-02
$6_5 \leftarrow 5_5$		444627.5170	5.804E-05	$16_{0,16}16 \leftarrow 15_{0,15}15$	43963.855	4.502E-02
$6_6 \leftarrow 5_6$		444627.1943	5.804E-05	$16_{1,16}16 \leftarrow 15_{1,15}15$	43961.875	4.502E-02
$8_9 \leftarrow 7_8$		592793.2536	4.358E-05	$12_{1,11}13 \leftarrow 11_{1,10}12$	36257.450	4.475E-02
$8_8 \leftarrow 7_7$		592793.2526	3.838E-05	$13_{3,10}13 \leftarrow 12_{3,9}12$	43730.185	4.474E-02
$8_7 \leftarrow 7_6$		592793.2510	3.379E-05	$14_{2,12}14 \leftarrow 13_{2,11}13$	44766.624	4.442E-02
$4_3 \leftarrow 3_4$		296433.6987	1.947E-05	$16_{1,15}17 \leftarrow 15_{1,14}16$	46691.873	4.420E-02
$7_6 \leftarrow 6_6$		518714.5203	7.148E-06	$12_{2,10}12 \leftarrow 11_{2,9}11$	39376.262	4.416E-02
$7_7 \leftarrow 6_7$		518714.1982	7.148E-06	$16_{2,15}17 \leftarrow 15_{2,14}16$	46626.213	4.404E-02
$5_4 \leftarrow 4_5$		370533.4256	3.271E-06	$12_{0,12}13 \leftarrow 11_{0,11}12$	33320.503	4.397E-02
$9_{10} \leftarrow 8_9$		666862.9003	3.230E-06	$12_{1,12}13 \leftarrow 11_{1,11}12$	33297.630	4.389E-02
$9_9 \leftarrow 8_8$		666862.8995	2.887E-06	$14_{3,12}15 \leftarrow 13_{3,11}14$	43489.921	4.373E-02
$9_8 \leftarrow 8_7$		666862.8983	2.579E-06	$15_{3,12}15 \leftarrow 14_{3,11}14$	50140.694	4.365E-02
$8_7 \leftarrow 7_7$		592793.4235	6.093E-07	$14_{1,13}14 \leftarrow 13_{1,12}13$	41437.796	4.344E-02
$8_8 \leftarrow 7_8$		592793.1018	6.093E-07	$16_{3,13}17 \leftarrow 15_{3,12}16$	53091.100	4.342E-02

(Continued)

Table 6.18 – (Continued)

HCNH ⁺			2CNTH ⁺			
Trans ^a	ν_{exp}	ν_{calc}	Int	Trans ^b	ν_{calc}	Int
6 ₅ ← 5 ₆		444627.3691	4.057E-07	12 _{2,11} 13 ← 11 _{2,10} 12	35822.299	4.335E-02

^a Trans.=Transition $J' \leftarrow J''$; ^b Trans.=Transition $J'_{K-1, K+1} \leftarrow J''_{K-1, K+1}$; int (intensity) in nm^2MHz .

^c Experimental values for HCNH⁺ in Quénard et al. [100].

Table 6.19 – M06-2X/6-31G(d,p) calculated frequencies and intensities for hyperfine strongest lines of 2CNTH⁺ and 3CNTH⁺ at 10 K.

2CNTH ⁺			3CNTH ⁺		
Trans. ^a	ν_{calc}	Int	Trans. ^a	ν_{calc}	Int
15 _{0,15} 16 ← 14 _{0,14} 15	41301.013	4.880E-02	15 _{1,14} 16 ← 14 _{1,13} 15	40440.825	5.018E-02
15 _{1,15} 16 ← 14 _{1,14} 15	41297.301	4.879E-02	14 _{1,13} 15 ← 13 _{1,12} 14	37963.137	5.003E-02
13 _{2,11} 14 ← 12 _{2,10} 13	42136.555	4.866E-02	15 _{0,15} 16 ← 14 _{0,14} 15	37647.125	4.968E-02
14 _{0,14} 15 ← 13 _{0,13} 14	38639.023	4.844E-02	16 _{0,16} 17 ← 15 _{0,15} 16	40052.973	4.962E-02
14 _{3,11} 15 ← 13 _{3,10} 14	47015.540	4.844E-02	16 _{1,16} 17 ← 15 _{1,15} 16	39952.859	4.929E-02
14 _{1,14} 15 ← 13 _{1,13} 14	38632.131	4.843E-02	15 _{1,15} 16 ← 14 _{1,14} 15	37513.859	4.920E-02
13 _{3,10} 14 ← 12 _{3,9} 13	43730.185	4.834E-02	15 _{2,13} 16 ← 14 _{2,12} 15	41843.709	4.912E-02
12 _{2,10} 13 ← 11 _{2,9} 12	39376.262	4.803E-02	16 _{1,15} 17 ← 15 _{1,14} 16	42880.665	4.909E-02
16 _{0,16} 17 ← 15 _{0,15} 16	43963.855	4.794E-02	14 _{0,14} 15 ← 13 _{0,13} 14	35244.992	4.859E-02
16 _{1,16} 17 ← 15 _{1,15} 16	43961.875	4.793E-02	14 _{2,12} 15 ← 13 _{2,11} 14	39059.133	4.858E-02
14 _{2,12} 15 ← 13 _{2,11} 14	44766.624	4.773E-02	13 _{1,12} 14 ← 12 _{1,11} 13	35442.884	4.853E-02
13 _{0,13} 14 ← 12 _{0,12} 13	35978.508	4.682E-02	17 _{0,17} 18 ← 16 _{0,16} 17	42462.406	4.848E-02
13 _{1,13} 14 ← 12 _{1,12} 13	35965.863	4.679E-02	16 _{2,14} 17 ← 15 _{2,13} 16	44593.865	4.827E-02
15 _{3,12} 16 ← 14 _{3,11} 15	50140.694	4.668E-02	17 _{1,17} 18 ← 16 _{1,16} 17	42388.117	4.825E-02
14 _{1,13} 15 ← 13 _{1,12} 14	41437.796	4.668E-02	14 _{1,14} 15 ← 13 _{1,13} 14	35070.215	4.794E-02
13 _{1,12} 14 ← 12 _{1,11} 13	38837.470	4.628E-02	17 _{1,16} 18 ← 16 _{1,15} 17	45290.169	4.694E-02
12 _{3,9} 13 ← 11 _{3,8} 12	40306.271	4.620E-02	15 _{1,14} 15 ← 14 _{1,13} 14	40440.825	4.693E-02
14 _{2,13} 15 ← 13 _{2,12} 14	41257.125	4.616E-02	16 _{0,16} 16 ← 15 _{0,15} 15	40052.973	4.660E-02
17 _{0,17} 18 ← 16 _{0,16} 17	46627.186	4.598E-02	13 _{2,11} 14 ← 12 _{2,10} 13	36244.576	4.660E-02
17 _{1,17} 18 ← 16 _{1,16} 17	46626.139	4.598E-02	14 _{1,13} 14 ← 13 _{1,12} 13	37963.137	4.656E-02
15 _{1,14} 16 ← 14 _{1,13} 15	44057.406	4.594E-02	15 _{0,15} 15 ← 14 _{0,14} 14	37647.125	4.646E-02
15 _{2,14} 16 ← 14 _{2,13} 15	43947.098	4.566E-02	18 _{0,18} 19 ← 17 _{0,17} 18	44874.977	4.638E-02
15 _{0,15} 15 ← 14 _{0,14} 14	41301.013	4.564E-02	13 _{0,13} 14 ← 12 _{0,12} 13	32846.029	4.634E-02
15 _{1,15} 15 ← 14 _{1,14} 14	41297.301	4.563E-02	16 _{1,16} 16 ← 15 _{1,15} 15	39952.859	4.629E-02
15 _{2,13} 16 ← 14 _{2,12} 15	47315.313	4.559E-02	18 _{1,18} 19 ← 17 _{1,17} 18	44820.416	4.623E-02

^a Trans.=Transition $J'_{K-1, K+1} \leftarrow J''_{K-1, K+1}$; int (intensity) in nm^2MHz

The M06-2X/6-31G(d,p) calculated and experimental hyperfine spectra for HCNH⁺ (for $J \leq 10$) as well as calculated strongest hyperfine transitions for 2CNTH⁺ at $T = 10$ K are presented in Table 6.18. A comparison of 3CNTH⁺ spectrum with that of 2CNTH⁺, at the same temperature, is shown in Table 6.19. Likewise, the hyperfine line intensities for various temperatures ($T = 7.00, 10, 30.00, 100.00, 150$ and 300 K) are plotted in Figures Figure 6.5 and Figure 6.6. A careful analysis of these spectra shows that lines are stronger for lower temperatures. The analysis of these spectra shows that, whereas transition lines are about of the same intensity for HCNH⁺ and 2CNTH⁺, they are about four times stronger for 3CNTH⁺ than for the two first compounds. A comparison of the transition line intensities at different temperatures reveals also that at low temperatures ($T = 7$ K and $T = 10$ K \equiv temperatures similar or approaching that prevailing in TMC-1 or in many cold molecular clouds^[101]), the brightest rotational lines for these molecular species fall almost in the same region, i.e., around ≈ 100 GHz.

These results are expected be of great importance for astro-scientists in the search of new species, espacially protonated species investigated in this work.

6.4 Conclusions

Theoretical and experimental spectroscopic data for protonated cyanothiophenes (R-CN^+ with $\text{R} = \text{C}_4\text{H}_3\text{S}$) which are needed for their interstellar search and/or detection are still lacking in the literature. A quantum chemical investigation on protonated thiophene and two of its nitrile substituted derivatives (2-cyanothiophene and 3-cyanothiophene) was performed for their characterization. The geometrical structures, IR, and rotational parameters were calculated at M06-2X/6-31G(d,p) level of theory, followed by an empirical correction for systematic errors (for geometrical structure). The thermodynamics properties investigated were computed using G2(MP2) and G3B3 levels of theory at different temperatures prevailing in the ISM regions where molecular species are expected to be found ($5 \leq T < 300 \text{ K}$). For the first time, the present work, (i) the IR and Raman spectra of the species under study are explored on the basis of PED; (ii) the rotational and hyperfine spectra for the title species and stronger lines frequencies and intensities discussed at $T = 10 \text{ K}$ (temperature prevailing in cold cores where they are expected to be found); (iii) the proton affinity for thiophene and $\text{R} - \text{CN}$ is analyzed: the protonation found to favor the α -position for thiophene ring whether this site is substituted or not, while occurring at N-atom for $\text{R} - \text{CN}$; (iv) $\Delta_r H$, $\Delta_r S$ and $\Delta_r G$ for the reaction yielding $\text{R} - \text{CN}^+$ and their neutral forms are studied at different temperatures ($T = 5, 10, 298$ and 1000 K) and pressures ($P = 1 \text{ atm}$ and $P = 10^{-5} \text{ atm}$) suggest spontaneous formation of the products in the ISM environments. These results are therefore expected to serve as a guide for laboratory works but also to assist astro-scientists in the search of new species in the ISM.

6.5 References

- [1] K. Chatterjee and O. Dopfer. *ApJ*, 865(2):114, 2018.
- [2] A. G. Tielens. *Annu. Rev. Astron. Astrophys.*, 46:289–337, 2008.
- [3] T. P. Snow and V. M. Bierbaum. 2008.
- [4] P. Ehrenfreund and S. B. Charnley. *ARA&A*, 38(1):427–483, 2000.
- [5] C. R. Arumainayagam, R. T. Garrod, M. C. Boyer, A. K. Hay, S. T. Bao, J. S. Campbell, J. Wang, C. M. Nowak, M. R. Arumainayagam, and P. J. Hodge. *Chem. Soc. Rev.*, 48(8):2293–2314, 2019.
- [6] F. L. Schöier, J. Jørgensen, E. Van Dishoeck, and G. . Blake. *A&A*, 390(3):1001–1021, 2002.
- [7] H. Gail and E. Sedlmayr. *Faraday Discuss.*, 109, 1998.
- [8] R. I. Kaiser. *Chem. Rev.*, 102(5):1309–1358, 2002.
- [9] T. Oka. *Faraday Discuss.*, 150:9–22, 2011.
- [10] W. D. Watson. *ApJ*, 183:L17, 1973.
- [11] E. Herbst and W. Klemperer. *ApJ*, 185:505–534, 1973.
- [12] T. P. Snow and B. J. McCall. *Annu. Rev. Astron. Astrophys.*, 44:367–414, 2006.
- [13] M. Agúndez. Interstellar chemical models. In *Laboratory Astrophysics*, pages 219–232. Springer, 2018.
- [14] K. I. öberg. *Chem. Rev.*, 116(17):9631–9663, 2016.
- [15] E. Herbst. *Int. Rev. Phys. Chem.*, 36(2):287–331, 2017.
- [16] J. Chantzou, S. Spezzano, C. Endres, L. Bizzocchi, V. Lattanzi, J. Laas, A. Vasyunin, and P. Caselli. *A&A*, 621:A111, 2019.
- [17] E. Herbst and E. F. Van Dishoeck. *ARA&A*, 47:427–480, 2009.
- [18] N. Solcà and O. Dopfer. *Angewandte Chemie International Edition*, 41(19):3628–3631, 2002.

- [19] N. Solcà and O. Dopfer. *Chem. Phys. Lett.*, 342(1-2):191–199, 2001.
- [20] H. Calcutt, J. K. Jørgensen, H. Müller, L. E. Kristensen, A. Coutens, T. Bourke, R. Garrod, M. Persson, M. Van Der Wiel, E. Van Dishoeck, et al. *arXiv preprint arXiv:1804.09210*, 2018.
- [21] D. McNaughton, M. K. Jahn, M. J. Travers, D. Wachsmuth, P. D. Godfrey, and J.-U. Grabow. *Mon. Not. R. Astron. Soc.*, 476(4):5268–5273, 2018.
- [22] W. D. Geppert and M. Larsson. *Mol. Phys.*, 106(16-18):2199–2226, 2008.
- [23] H. Tachikawa, T. Iyama, and T. Fukuzumi. *A&A*, 397(1):1–6, 2003.
- [24] R. S. Altman, M. W. Crofton, and T. Oka. *J. Chem. Phys.*, 80(8):3911–3912, 1984.
- [25] R. S. Altman, M. W. Crofton, and T. Oka. *J. Chem. Phys.*, 81(10):4255–4258, 1984.
- [26] T. Amano and K. Tanaka. *J. Mol. Spectrosc.*, 116(1):112–119, 1986.
- [27] P. Botschwina. *Chem. Phys. Lett.*, 124(4):382–390, 1986.
- [28] D.-J. Liu, S.-T. Lee, and T. Oka. *J. Mol. Spectrosc.*, 128(1):236–249, 1988.
- [29] W.-C. Ho, C. E. Blom, D.-J. Liu, and T. Oka. *J. Mol. Spectrosc.*, 123:251–253, 1987.
- [30] V. Brites and L. Jutier. *J. Mol. Spectrosc.*, 271(1):25–32, 2012.
- [31] M. Araki, H. Ozeki, and S. Saito. *Astrophys. J. Lett.*, 496(1):L53, 1998.
- [32] L. Ziurys and B. Turner. Detection of interstellar hcnh⁺. In *Bull. Am. Astron. Soc.*, volume 17, page 871, 1985.
- [33] L. M. Ziurys and B. Turner. *ApJ*, 302:L31–L36, 1986.
- [34] L. M. Ziurys, A. Apponi, and J. Yoder. *ApJ*, 397:L123–L126, 1992.
- [35] B. A. McGuire. *Astrophys. J. Suppl. Ser.*, 239(2):17, 2018.
- [36] D. Flower, G. P. Des Forêts, and C. Walmsley. *A&A*, 456(1):215–223, 2006.
- [37] S. Derenne and F. Robert. *Meteorit. Planet. Sci.*, 45(9):1461–1475, 2010.
- [38] M. Bose, R. Root, and S. Pizzarello. *Meteorit. Planet. Sci.*, 52(3):546–559, 2017.
- [39] L. Remusat, F. Palhol, F. Robert, S. Derenne, and C. France-Lanord. *Earth Planet. Sci. Lett.*, 243(1-2):15–25, 2006.
- [40] J. Yang and S. Epstein. *Nature*, 311(5986):544, 1984.
- [41] J. L. Eigenbrode, R. E. Summons, A. Steele, C. Freissinet, M. Millan, R. Navarro-González, B. Sutter, A. C. McAdam, H. B. Franz, D. P. Glavin, et al. *Science*, 360(6393):1096–1101, 2018.
- [42] R. Martín-Doménech, I. Jiménez-Serra, G. M. Caro, H. Müller, A. Occhiogrosso, L. Testi, P. Woods, and S. Viti. *A&A*, 585:A112, 2016.
- [43] B. A. McGuire, C. N. Shingledecker, E. R. Willis, K. L. K. Lee, M.-A. Martin-Drumel, G. A. Blake, C. L. Brogan, A. M. Burkhardt, P. Caselli, K.-J. Chuang, et al. *ApJ*, 883(2):201, 2019.
- [44] T. Oka. *Proc Natl Acad Sci USA*, 103(33):12235–12242, 2006.
- [45] A. Dalgarno. Terrestrial and extraterrestrial h₃⁺. In *Adv. At. Mol. Opt.*, volume 32, pages 57–68. Elsevier, 1994.
- [46] T. Geballe and T. Oka. *Nature*, 384(6607):334–335, 1996.
- [47] B. McCall, T. Geballe, K. Hinkle, and T. Oka. *ApJ*, 522(1):338, 1999.
- [48] B. J. McCall and T. Oka. *Science*, 287(5460):1941–1942, 2000.
- [49] Y. Yokoyama, Y. Yamashita, K. Takahashi, and T. Sone. *Chem. Lett.*, 10(6):813–814, 1981.
- [50] Y. Yokoyama, Y. Yamashita, K. Takahashi, and T. Sone. *Bull. Chem. Soc. Jpn.*, 56(8):2208–2211, 1983.
- [51] Y. Yamashita, H. Kobayashi, A. Yoshino, K. Takahashi, and T. Sone. *Bull. Chem. Soc. Jpn.*, 57(5):1312–1316, 1984.
- [52] Y. Yamashita, A. Yoshino, K. Takahashi, and T. Sone. *Magn. Reson. Chem.*, 24(8):699–704, 1986.

- [53] E. P. Hunter and S. G. Lias. *NIST Chemistry WebBook, NIST Standard Reference Database Number*, 69, 2005.
- [54] M. Szajda and J. N. Lam. *Comprehensive Heterocyclic Chemistry II*, pages 438–490, 1996.
- [55] V. Barone, M. Biczysko, and C. Puzzarini. *Acc. Chem. Res.*, 48(5):1413–1422, 2015.
- [56] R. Dennington, T. A. Keith, and J. M. Millam. *Inc., Wallingford*, 2008.
- [57] M. J. Frisch, G. Trucks, H. Schlegel, G. Scuseria, M. Robb, J. Cheeseman, G. Scalmani, V. Barone, B. Mennucci, G. Petersson, et al. *Inc.: Wallingford, CT*, 2009.
- [58] N. V. Riggs, L. Radom, M. Winnewisser, B. P. Winnewisser, M. Birk, et al. *Chem. Phys.*, 122(2):305–315, 1988.
- [59] C. C. J. Roothaan. *J Rev. Mod. Phys.*, 23(2):69, 1951.
- [60] J. A. Pople, J. S. Binkley, and R. Seeger. *Int. J. Quantum Chem.*, 10(S10):1–19, 1976.
- [61] A. Becke. *J. Chem. Phys.*, 98(5):648–5, 1993.
- [62] C. Lee, W. Yang, and R. G. Parr. *Phys. Rev. B*, 37(2):785, 1988.
- [63] Y. Zhao and D. G. Truhlar. *Theor. Chem. Acc.*, 120(1-3):215–241, 2008.
- [64] M. Towler. *European Summer School" Ab initio modelling in solid-state chemistry"*, Turin, 2000.
- [65] L. A. Curtiss, K. Raghavachari, and J. A. Pople. *J. Chem. Phys.*, 98(2):1293–1298, 1993.
- [66] L. A. Curtiss, P. C. Redfern, K. Raghavachari, V. Rassolov, and J. A. Pople. *J. Chem. Phys.*, 110(10):4703–4709, 1999.
- [67] L. A. Curtiss, P. C. Redfern, and K. Raghavachari. *J. Chem. Phys.*, 127(12):124105, 2007.
- [68] A. G. Baboul, L. A. Curtiss, P. C. Redfern, and K. Raghavachari. *J. Chem. Phys.*, 110(16):7650–7657, 1999.
- [69] J. A. Montgomery Jr, M. J. Frisch, J. W. Ochterski, and G. A. Petersson. *J. Chem. Phys.*, 110(6):2822–2827, 1999.
- [70] T. Sundius. *J. Mol. Struct.*, 218:321–326, 1990.
- [71] T. Sundius. *Vib. Spectrosc.*, 29(1-2):89–95, 2002.
- [72] H. M. Pickett. *J. Mol. Spectrosc.*, 148(2):371–377, 1991.
- [73] R. Simbizi, G. Gahungu, and M. T. Nguyen. *SAA*.
- [74] M. T. Nguyen, A. K. Chandra, et al. *J. Chem. Soc. Faraday Trans.*, 94(9):1277–1280, 1998.
- [75] E. P. Hunter and S. G. Lias. *J. Phys. Chem. Ref. Data*, 27(3):413–656, 1998.
- [76] A. Vasyunin and E. Herbst. *ApJ*, 769(1):34, 2013.
- [77] A. Bacmann, V. Taquet, A. Faure, C. Kahane, and C. Ceccarelli. *A&A*, 541:L12, 2012.
- [78] A. Yertisbayeva, Z. Salkenova, A. Sembayeva, and R. J. O'Reilly. *Chem. Data Collect.*, 9:98–103, 2017.
- [79] S. H. El-Demerdash and S. F. Gad. *Struct. Chem.*, 31(1):319–328, 2020.
- [80] F. Lique, F. Daniel, L. Pagani, and N. Feautrier. *Mon. Not. R. Astron. Soc.*, 446(2):1245–1251, 2015.
- [81] P. Matczak. *Computation*, 4(1):3, 2016.
- [82] T. Raček, O. Schindler, D. Toušek, V. Horský, K. Berka, J. Koča, and R. Svobodová. *Nucleic. Acids Res.*, 48(W1):W591–W596, 2020.
- [83] S. Sarkar, S. Shil, S. Paul, and A. Misra. *J. Mol. Struct. THEOCHEM*, 916(1-3):154–158, 2009.
- [84] T. L. Brown, H. E. LeMay Jr, and B. E. Bursten. *Chemical Thermodynamics of Zirconium. NEA OECD, Elsevier, ISBN-13*, pages 978–0, 2005.

- [85] C. Vastel, T. Phillips, and H. Yoshida. *Astrophys. J. Lett.*, 606(2):L127, 2004.
- [86] T. Millar, A. Bennett, and E. Herbst. *ApJ*, 340:906–920, 1989.
- [87] D. Gerlich, E. Herbst, and E. Roueff. *Planet. Space Sci.*, 50(12-13):1275–1285, 2002.
- [88] T. Millar. *Planet. Space Sci.*, 50(12-13):1189–1195, 2002.
- [89] R. Stark, F. F. van der Tak, and E. F. van Dishoeck. *Astrophys. J. Lett.*, 521(1):L67, 1999.
- [90] P. Caselli, F. Van der Tak, C. Ceccarelli, and A. Bacmann. *A&A*, 403(3):L37–L41, 2003.
- [91] R. Stark, G. Sandell, S. C. Beck, M. R. Hogerheijde, E. F. Van Dishoeck, P. Van Der Wal, F. F. van der Tak, F. Schäfer, G. J. Melnick, M. L. Ashby, et al. *ApJ*, 608(1):341, 2004.
- [92] T. Millar, H. Roberts, A. Markwick, and S. Charnley. *Philosophical Transactions of the Royal Society of London. Series A: Mathematical, Physical and Engineering Sciences*, 358(1774):2535–2547, 2000.
- [93] C. Ceccarelli and C. Dominik. *A&A*, 440(2):583–593, 2005.
- [94] K. Chatterjee and O. Dopfer. *J. Chem. Phys.*, 149(17):174315, 2018.
- [95] M. Schütz, Y. Matsumoto, A. Bouchet, M. Öztürk, and O. Dopfer. *Phys. Chem. Chem. Phys.*, 19(5):3970–3986, 2017.
- [96] C. P. Endres, S. Schlemmer, P. Schilke, J. Stutzki, and H. S. Müller. *J. Mol. Spectrosc.*, 327:95–104, 2016.
- [97] H. Pickett, R. Poynter, E. Cohen, M. Delitsky, J. Pearson, and H. Müller. *Journal of Quantitative Spectroscopy and Radiative Transfer*, 60(5):883–890, 1998.
- [98] H. Pickett, R. Poynter, and E. Cohen. 1992.
- [99] P. Schilke, C. Walmsley, T. Millar, and C. Henkel. *A&A*, 247:487–496, 1991.
- [100] D. Quénard, C. Vastel, C. Ceccarelli, P. Hily-Blant, B. Lefloch, and R. Bachiller. *Mon. Not. R. Astron. Soc.*, 470(3):3194–3205, 2017.
- [101] P. Solomon, D. Sanders, and A. Rivolo. *ApJ*, 292:L19–L24, 1985.

GENERAL CONCLUSIONS

Quantum chemical calculations on the structures and basic spectroscopic properties, from which spectroscopic properties of relevant astrophysical interest are computed, were carried out for both cyanothiophene compounds 2CNT and 3CNT and some of their isotopologues and protonated forms at M06-2X/6-31G(d,p) level of theory. Thermodynamic properties were carried out using G2(MP2) and G3B3. Following then the empirical corrections for systematic deficiencies of methods and basis sets to adjust geometrical parameters, the molecular geometry for the parent thiophene was determined and an excellent agreement with experimental data achieved. An agreement between the available experimental and calculated values for the fundamental vibrational frequencies of the parent compound (thiophene) was also fulfilled. The same strategy was subsequently used for both cyano derivatives 2CNT and 3CNT, some of their isotopologues and protonated forms. Geometrical parameters and thereby the rotational, centrifugal and quadrupole coupling constants, dipole moments (total and axis components), moments of inertia, etc for different molecular species investigated in this work have thus been obtained. In the present work i) reliable molecular geometries are provided, ii) a complete description of both IR and Raman spectra made, including IR frequency assignment on the basis of PED analysis, iii) both IR and Raman spectra for deuterated derivatives are predicted, iv) electronic UV-VIS spectra for both 2CNT and 3CNT as well as thiophene are predicted 2CNT being expected to absorb the interstellar in the UV region at 218 nm, the main electronic transitions are elucidated and corresponding Molecular Orbitals plotted, v) IR and Raman spectral bands for all the fundamental vibrational modes, including C-D modes, are identified and assigned vi) Rotational spectra and quadrupole hyperfine structures were carried out for 2CNT, 3CNT and some of their isotopologues, having a spin $I \geq 1$ and a quadrupole electric moment different to zero ($^{33}\text{S}-3\text{C}^{15}\text{NT}$, $^{33}\text{S}-2\text{C}^{15}\text{NT}$ and $3\text{C}^{15}\text{NT}-2\text{D}$ and $2\text{C}^{15}\text{NT}-3\text{D}$) as well as for protonated cyanothiophenes (2CNTH^+ and 3CNTH^+); line intensities and line profiles for strong lines are discussed for different temperatures, temperatures prevailing, especially, in regions where these compounds are expected to be detected, vii) the thermodynamics properties were investigated using G2(MP2) and G3B3 levels of theory at different temperatures prevailing in the ISM regions where molecular species are expected to be found ($5.00 \leq T < 300.00 \text{ K}$): the proton affinity for thiophene and R – CN is analyzed and the protonation found to favor the α -position for thiophene ring whether this site is substituted or not and occurs at N-atom for R – CN; viii) $\Delta_r\text{H}$, $\Delta_r\text{S}$ and $\Delta_r\text{G}$ for the reaction yielding R – CNH^+ , R – CND^+ and their neutral forms are studied at different temperatures ($T = 5.00, 10.00, 298.15$ and 1000.00 K) and pressures ($P = 1 \text{ atm}$ and $P = 10^{-5} \text{ atm}$) suggest spontaneous formation of the products in the ISM environments. These results, supported by those of the different works on the sulfur abundance in the ISM (e.g. ?¹) and those of the work by McGuire et al.^[2], lead us to assert that cyanothiophenes (2CNT and 3CNT, their protonated forms, i.e. 2CNTH^+ , 3CNTH^+ , 2CNTD^+ and 3CNTD^+), but also their different isotopologues, do exist in the interstellar medium. The different spectroscopic results in this thesis are therefore intended to contribute to their detection in different ISM environments. We hope then that these predicted results are helpful to assist astrophysicists

and astrochemists in the experimental search of these aromatic species in the interstellar space, hoping also that they could influence or induce other research works, particularly, experimental ones aiming at the search of these species in space.

APPENDIX

A.1 Geometric structure corrections

Table A.1 – Geometrical parameters of **1** (bond lengths in Å, bond angles in °) and rotational constants (in GHz) calculated at different levels of theory

Parameter	HF		MP2		MP3		B3LYP		M062X		Exp ¹
	6-31G*	6-311G**	6-31G*	6-31G**	6-31G*	6-311G*	6-31G*	6-31G**	6-31G**	6-311++G**	
S-C	1.726	1.724	1.718	1.717	1.728	1.724	1.736	1.736	1.723	1.721	1.714
C=C	1.345	1.345	1.376	1.376	1.365	1.368	1.367	1.367	1.363	1.362	1.370
C-C	1.437	1.436	1.420	1.419	1.433	1.435	1.430	1.430	1.429	1.427	1.432
C2-H	1.071	1.071	1.082	1.078	1.081	1.080	1.082	1.081	1.080	1.079	1.078
C3-H	1.074	1.074	1.085	1.080	1.084	1.083	1.085	1.084	1.083	1.081	1.081
∠C-S-C	91.3	91.3	92.0	91.9	91.4	91.5	91.5	91.5	91.7	91.6	91.2
∠S-C-C	111.8	111.8	111.6	111.6	111.9	112.0	111.5	111.5	111.7	111.7	111.5
∠C=C-C	112.5	112.5	112.4	112.4	112.4	112.2	112.7	112.7	112.5	112.5	112.5
∠S-C-H	120.4	120.3	120.2	120.2	120.1	120.0	120.1	120.0	120.1	120.0	119.9
∠C-C-H	123.9	123.6	124.4	124.5	124.1	124.2	123.9	123.9	124.1	124.2	124.3
∠C2=C3-H	123.3	123.6	123.1	123.1	123.5	123.5	123.4	123.3	123.4	123.4	123.3
A	8050.66	8051.62	8060.34	8079.05	8020.78	8027.45	7968.59	7971.78	8040.84	8061.70	8041.77
B	5455.41	5458.39	5385.63	5388.31	5369.02	5368.45	5353.85	5356.57	5410.07	5417.07	5418.12
C	3251.84	3254.92	3228.47	3232.44	3216.06	3217.02	3202.31	3203.80	3234.09	3239.97	3235.77

¹ from Kretschmer et al. (1993).

Table A.2 – Differences between experimental and calculated geometrical (bond lengths in Å, bond angles in °) and rotational parameters (A, B and C in GHz) at different levels of theory for **1**.

Parameter	HF		MP2		MP3		B3LYP		M062X	
	6-31G*	6-311G**	6-31G*	6-31G**	6-31G*	6-311G*	6-31G*	6-31G**	6-31G**	6-311++G**
Δ SC	0.013	0.010	0.004	0.003	0.014	0.010	0.022	0.022	0.09	0.007
Δ C=C	-0.025	-0.025	0.006	0.006	-0.005	-0.002	-0.003	-0.003	-0.007	-0.008
Δ C-C	0.005	0.004	-0.012	-0.013	0.001	0.003	-0.002	-0.002	-0.003	-0.005
Δ C2-H	-0.007	-0.007	0.004	0.000	0.003	0.002	0.004	0.003	0.002	0.001
C3-H	-0.007	-0.007	0.004	0.001	0.003	0.002	0.004	0.003	0.002	0.000
σ^*	0.015	0.014	0.006	0.006	0.008	0.005	0.011	0.011	0.006	0.006
Δ A	8.89	9.85	18.57	37.28	-20.99	-14.32	-73.18	-69.99	-0.93	19.93
Δ B	37.29	40.27	-32.49	-29.81	-49.10	49.67	-64.27	-61.55	-8.05	-1.05
Δ C	16.07	19.15	-7.30	-3.33	-19.71	18.75	-33.46	-31.97	-1.68	4.20

σ^* \equiv standard deviation. $\Delta \equiv$ Calc-Exp.

Table A.3 – Geometrical parameters of **8** (bond lengths in Å, bond angles in °) and rotational constants (in GHz) calculated at different levels of theory

Parameter	HF		MP2		MP3		B3LYP		M062X		Exp ¹
	6-31G*	6-311G**	6-31G*	6-31G**	6-31G*	6-311G*	6-31G*	6-31G**	6-31G*	6-31G**	
S1-C2	1.733	1.730	1.728	1.727	1.736	1.731	1.751	1.751	1.732	1.732	1.732
S1-C5	1.718	1.717	1.715	1.714	1.723	1.719	1.728	1.728	1.716	1.716	1.716
C2=C3	1.352	1.351	1.386	1.386	1.372	1.375	1.379	1.379	1.372	1.372	1.371
C4=C5	1.348	1.348	1.379	1.378	1.367	1.370	1.371	1.371	1.366	1.366	1.366
C2-O6	1.430	1.427	1.420	1.420	1.429	1.429	1.416	1.416	1.424	1.424	1.424
C-C	1.429	1.428	1.413	1.412	1.426	1.428	1.420	1.420	1.421	1.421	1.421
C6-N	1.137	1.131	1.185	1.185	1.161	1.154	1.165	1.165	1.158	1.158	1.158
C5-H	1.071	1.071	1.083	1.078	1.083	1.081	1.082	1.081	1.081	1.081	1.081
C3-H	1.073	1.073	1.085	1.080	1.083	1.083	1.084	1.083	1.083	1.083	1.082
∠C-S-C	90.7	90.7	91.5	91.4	90.8	90.9	91.0	91.0	91.0	91.0	91.0
∠S-C2-C3	112.0	112.0	111.7	111.7	112.1	112.2	111.2	111.2	111.8	111.8	111.8
∠S-C5-C4	112.6	112.6	112.1	112.2	112.6	112.7	112.3	112.3	112.5	112.5	112.5
∠S-C2-C6	121.6	121.6	121.5	121.5	121.5	121.4	121.3	121.3	121.2	121.2	121.2
∠S-C-H	119.9	119.8	119.7	119.7	119.6	119.6	119.7	119.6	119.6	119.6	119.6
∠C2=C3-C4	112.4	112.4	112.1	112.1	112.1	112.0	112.7	112.7	112.2	112.2	112.2
∠C5=C4-C3	112.3	112.3	112.6	112.6	112.4	112.2	112.7	112.7	112.4	112.4	112.4
∠C3=C2-C6	126.4	126.4	126.9	126.6	126.4	126.4	127.5	127.5	127.0	127.0	127.0
∠C2=C3-H	123.2	123.2	122.6	122.6	123.1	123.0	122.7	122.6	122.8	122.8	122.8
∠C5=C4-H	123.9	123.9	123.2	123.2	123.6	123.7	123.5	123.4	123.5	123.5	123.5
A	5436.533	5445.394	5364.023	5367.612	5348.573	5354.485	5326.186	5327.839	5384.067	5385.430	5402.387
B	1820.933	1828.393	1797.880	1798.792	1803.500	1808.457	1799.334	1799.671	1811.562	1811.830	1816.253
C	1360.052	1368.794	1346.550	1347.290	1348.721	1351.869	1344.967	1345.260	1355.485	1355.722	1358.614

¹ from Wiese et al. (1977).

Table A.4 – Geometrical parameters of **9** (bond lengths in Å, bond angles in °) and rotational constants (in GHz) calculated at different levels of theory

Parameter	HF		MP2		MP3		B3LYP		M062X		Exp ¹
	6-31G*	6-311G**	6-31G*	6-31G**	6-31G*	6-311G*	6-31G*	6-31G**	6-31G*	6-31G**	
S1-C2	1.713	1.711	1.709	1.708	1.718	1.714	1.723	1.723	1.711	1.711	1.711
S1-C5	1.726	1.725	1.717	1.716	1.728	1.725	1.737	1.737	1.724	1.724	1.724
C2=C3	1.351	1.350	1.384	1.384	1.372	1.374	1.378	1.378	1.371	1.371	1.371
C4=C5	1.343	1.342	1.374	1.373	1.362	1.365	1.363	1.363	1.360	1.360	1.360
C3-C6	1.438	1.435	1.428	1.428	1.437	1.437	1.427	1.427	1.433	1.433	1.433
C-C	1.439	1.437	1.425	1.425	1.437	1.438	1.437	1.437	1.433	1.433	1.433
C6-N	1.136	1.130	1.184	1.184	1.161	1.154	1.164	1.164	1.157	1.157	1.157
C2-H	1.070	1.070	1.083	1.078	1.081	1.081	1.081	1.081	1.081	1.081	1.080
C4-H	1.072	1.072	1.084	1.080	1.083	1.082	1.083	1.083	1.082	1.082	1.082
∠C-S-C	91.6	91.6	92.3	92.3	91.7	91.8	91.8	91.8	92.0	92.0	92.0
∠S-C2-C3	111.5	111.6	111.2	111.2	111.5	111.6	111.4	111.4	111.4	111.4	111.3
∠S-C5-C4	112.1	112.1	112.0	112.0	112.3	112.3	111.8	111.8	112.0	112.0	112.0
∠S-C2-H	121.3	121.2	121.2	121.2	121.1	121.0	121.1	121.0	121.2	121.2	121.2
∠S-C5-H	120.3	120.3	120.2	120.2	120.0	120.0	120.0	120.0	120.0	120.0	120.0
∠C5=C4-H	124.6	124.5	124.2	124.2	124.6	124.6	124.4	124.3	124.6	124.6	124.6
∠C2=C3-C4	112.9	112.9	112.8	112.7	112.9	112.7	112.7	112.7	112.8	112.8	112.9
∠C5=C4-C3	111.9	111.9	111.8	111.8	111.6	111.6	112.3	112.3	111.8	111.8	111.8
∠C4=C3-C6	123.7	123.7	124.1	124.1	124.0	124.0	124.0	123.9	124.0	124.0	124.0
∠C2-C3-C6	123.4	123.4	123.1	123.1	123.1	123.3	123.4	123.4	123.2	123.2	123.2
A	7138.797	7152.949	7105.880	7118.812	7073.731	7082.739	7046.301	7048.037	7100.872	7101.458	7115.180
B	1501.143	1505.934	1476.929	1476.849	1480.990	1482.615	1479.479	1479.859	1488.988	1489.435	1491.299
C	1240.327	1244.025	1222.779	1223.107	1224.599	1225.982	1222.745	1223.0569	1230.883	1231.206	1232.535

¹ from and D. H. Sutter (1977).

Table A.5 – Variation of rotational constants of **1**, **8** and **9** with respect to the bond lengths variation.

Parameter	Compound 1				Compound 8				Compound 9			
	P.V. ³	ΔA	ΔB	ΔC	ΔA	ΔB	ΔC	ΔC	ΔA	ΔB	ΔC	ΔC
S-C	P ¹	-7/-14/-21	-8/-15/-23	-4/-8/-11	-8/-16/-23	-1/-2/-3	-1/-2/-3	-1/-2/-3	-7/-13/-20	-1/-2/-2	-1/-2/-2	-1/-1/-2
	N ²	7/14/21	8/15/23	4/8/11	8/16/22	1/2/3	1/2/3	1/2/3	7/13/20	1/2/2	1/2/2	1/1/2
C=C	P ¹	-4/-7/-10	-6/-12/-19	-3/-5/-8	-6/-13/-17	-1/-1/-2	-1/-1/-2	-1/-1/-2	-4/-9/-17	-1/-2/-3	-1/-2/-3	-1/-2/-2
	N ²	3/6/19	7/14/21	3/6/9	7/13/15	1/1/2	1/1/2	1/1/2	4/9/16	1/2/3	1/2/3	1/2/2
C-C	P ¹	-9/-9/-15	1/1/-4/-5	-1/-3/-4	1/-3/-4	-1/-1/-1	0/-1/-1	0/-1/-1	-6/-12/-15	0/-1/-1	0/-1/-1	0/-1/-1
	N ²	9/18/27	-1/-2/-3	1/2/3	-1/-2/2	1/2/1	0/1/1	0/1/1	6/12/14	0/1/1	0/1/1	0/-1/-1
C2-C6	P ¹	-	-	-	0/0/0	-2/-3/-5	-1/-2/-3	-1/-2/-3	0/0/0	-1/-3/-4	-1/-2/-3	-1/-2/-3
	N ²	-	-	-	0/0/0	2/2/3	1/1/2	1/1/2	0/0/0	1/2/4	1/2/4	1/2/3
C≡N	P ¹	-	-	-	0/0/0	-1/-2/-3	-1/-1/-2	-1/-1/-2	0/0/0	-1/-2/-2	-1/-2/-2	-1/-1/-2
	N ²	-	-	-	1/1/2	1/2/2	0/1/1	0/1/1	0/0/0	1/2/2	1/2/2	1/1/2
C2-H6	P ¹	-2/-5/-7	0/0/0	0/-1/-1	0/0/0	0/0/0	0/0/0	0/0/0	-2/-3/-4	0/0/0	0/0/0	0/0/0
	N ²	3/5/7	0/0/0	0/1/1	0/0/0	0/0/0	0/0/0	0/0/0	1/2/4	0/0/0	0/0/0	0/0/0
C3-H7	P ¹	-1/-2/-2	-1/-2/-3	0/-1/-1	-1/-2/-3	0/0/0	0/0/0	0/0/0	-1/-2/-3	0/0/0	0/0/0	0/0/0
	N ²	1/2/2	1/2/3	0/1/1	1/2/3	0/0/0	0/0/0	0/0/0	1/2/3	0/0/0	0/0/0	0/0/0
S-C=C	P ¹	7/16/25	-9/-15/-22	-2/-3/-4	-4/-7/-10	1/1/2	0/0/0	0/0/0	2/4/6	-1/-1/-2	0/0/-1	0/0/-1
	N ²	-12/-21/-30	5/11/18	0/1/1	2/5/8	0/-1/-1	0/0/0	0/0/0	-1/-3/-5	0/1/2	0/1/1	0/1/1
C=C-C	P ¹	-6/-10/-13	0/3/6	-1/0/0	2/6/9	1/-1/-2	0/0/-1	0/0/-1	0/0/0	0/0/1	0/0/1	0/0/1
	N ²	1/5/10	-5/-7/-11	-2/-2/-2	-4/-8/-12	1/2/3	0/1/1	0/1/1	1/1/2	0/-1/-1	0/0/1	0/0/1
S-C-H	P ¹	-4/-5/-6	-2/-2/-2	-1/-1/-2	-1/-1/-1	0/0/0	0/0/0	0/0/0	0/0/-1	0/0/0	0/0/0	0/0/0
	N ²	-1/0/-1	-2/-3/-2	-1/-1/-1	-1/-1/-1	0/0/0	0/0/0	0/0/0	1/2/3	0/0/0	0/0/0	0/0/0
C=C-C6	P ¹	-	-	-	-2/-3/-4	0/0/0	0/0/0	0/0/0	5/9/15	-1/-1/-2	0/-1/-1	0/-1/-1
	N ²	-	-	-	-1/0/1	0/1/1	0/0/0	0/0/0	-4/-9/-14	0/1/2	0/0/1	0/0/1

¹ Positive variation P=0.002/0.004/0.006 for bond length variation; P=0.2/0.4/0.6 for bond angle variation

² Negative variation N=-0.002/-0.004/-0.006 for bond length variation; P=-0.2/-0.4/-0.6 for bond angle variation

³ P.V.=Parameter variation.

Table A.6 – Corrections for **1** geometrical parameters (bond lengths in Å, bond angles in degree) and their predicted values from analysis of compounds **2**, **3**, **4**, **5**, **6** and **7**

	C=C					C-C				
	HF	MP2	MP3	B3LYP	M06-2X	HF	MP2	MP3	B3LYP	M06-2X
	6-31G*	6-31G**	6-311G*	6-31G**	6-31G**	6-31G*	6-31G**	6-311G*	6-31G**	6-31G**
2^a	-0.022	0.004	0.000	0.000	-0.005	0.01	-0.004	0.011	0.004	0.003
3^b	-0.024	0.001	-0.003	-0.004	-0.009	0.01	0.001	0.012	0.008	0.006
4^c	-0.029	0.005	-0.004	-0.006	0.012	0.006	-0.014	0.003	-0.002	0.002
5^d	-0.024	0.008	-0.004	-0.001	-0.006	0.020	0.001	0.015	0.013	0.011
6^e	-0.023	0.008	0.0	-0.002	-0.006	0.032	0.015	0.029	0.026	0.023
7^f	-0.037	-0.006	-0.015	-0.015	-0.020	0.017	-0.001	0.015	0.009	0.008
Mean	-0.027	0.003	-0.004	-0.005	-0.006	0.016	0.000	0.014	0.010	0.009
Corrected val. ^g	1.372	1.373	1.372	1.372	1.369	1.421	1.419	1.419	1.420	1.420
Average of ^h Corrected val.	1.372					1.420				
	C-H1					C-H2				
	HF	MP2	MP3	B3LYP	M06-2X	HF	MP2	MP3	B3LYP	M06-2X
	6-31G*	6-31G**	6-311G*	6-31G**	6-31G**	6-31G*	6-31G**	6-311G*	6-31G**	6-31G**
2^a	-0.007	0.000	0.002	70.004	0.003	-0.009	-0.001	0.002	0.004	0.002
3^b	-0.006	0.000	0.004	0.004	0.003	-0.006	0.000	0.004	0.004	0.003
4^c	-0.025	-0.018	-0.015	-0.015	-0.016	-0.025	-0.019	-0.015	-0.015	-0.015
5^d	-0.019	-0.012	-0.015	-0.009	-0.010	-0.015	-0.008	-0.011	-0.005	-0.006
6^e	-0.001	0.007	0.008	0.010	0.009	-0.002	0.006	0.007	0.009	0.009
7^f	-	-	-	-	-	-	-	-	-	-
Mean	-0.012	-0.005	-0.003	-0.001	-0.002	-0.011	-0.004	-0.003	-0.001	-0.001
Corrected val. ^g	1.083	1.083	1.083	1.082	1.082	1.085	1.084	1.086	1.085	1.084
Average of ^h Corrected val.	1.083					1.085				
	S-C					C-S-C				

continued

Table A.6 – (continued)

	HF 6-31G*	MP2 6-31G**	MP3 6-311G*	B3LYP 6-31G**	M06-2X 6-31G**	HF 6-31G*	MP2 6-31G**	MP3 6-311G*	B3LYP 6-31G**	M06-2X 6-31G**
4^c	0.007	0.005	0.004	0.017	0.006	-0.9	-0.1	-0.6	-0.7	-0.2
5^d	0.014	0.003	0.015	0.023	0.010	-1.2	-0.5	-1.1	-1.0	-0.8
6^e	0.015	0.006	0.014	0.028	0.015	-0.5	-0.1	-0.5	-0.5	-0.3
7^f	0.011	0.003	0.011	0.021	0.009	-0.8	-0.2	-0.6	-0.6	-0.5
Mean	0.012	0.004	0.011	0.022	0.010	-0.9	-0.2	-0.7	-0.7	-0.5
Corrected val. ^g	1.714	1.713	1.713	1.714	1.713	92.2	92.1	92.2	92.2	92.2
Average of ^h Corrected val.	1.713					92.2				
	$\angle C=C-C$					$\angle C-C-H$				
2^a	-0.5	-0.1	-0.4	0.0	-0.2	-0.4	-0.4	-0.3	-0.6	-0.4
3^b	-0.3	-0.1	-0.2	0.0	-0.1	-0.2	0.1	-0.2	-0.3	-0.2
4^c	-0.2	-0.4	-0.5	0.0	-0.4	-	-	-	-	-
5^d	-1.1	-1.2	-1.2	-1.0	-1.1	-	-	-	-	-
6^e	-1.2	-1.3	-1.g5	-0.7	-1.3	0.1	0.4	0.2	-0.5	-0.2
7^f	-	-	-	-	-	-	-	-	-	-
Mean	-0.7	-0.6	-0.8	-0.3	-0.6	-0.2	0.0	-0.1	-0.5	-0.3
Corrected val. ^g	113.2	113.0	113.0	113.0	113.1	124.0	124.5	124.3	124.4	124.4
Average of ^h Corrected val.	113.1					124.3				
	$\angle S-C-H$					$\angle C=C-H$				
2^a	-	-	-	-	-	0.7	0.1	0.5	0.1	0.4
3^b	-	-	-	-	-	0.5	0.1	0.3	0.2	0.2
4^c	-0.7	-0.7	-0.9	-1.0	-0.9	-0.2	-0.8	-0.4	-0.5	-0.4
5^d	0.6	0.4	0.3	0.2	0.2	-	-	-	-	-

continued

Table A.6 – (continued)

	HF 6-31G*	MP2 6-31G**	MP3 6-311G*	B3LYP 6-31G**	M06-2X 6-31G**	HF 6-31G*	MP2 6-31G**	MP3 6-311G*	B3LYP 6-31G**	M06-2X 6-31G**
6^e	-0.2	-0.4	-0.6	-0.6	-0.6	0.1	0.4	0.2	-0.5	-0.2
7^f	-	-	-	-	-	-	-	-	-	-
Mean	-0.1	-0.2	-0.4	-0.5	-0.4	0.3	-0.1	0.2	-0.2	0.0
Corrected val. ^g	120.5	120.4	120.4	120.5	120.5	123.0	123.2	123.2	123.5	123.4
Average of ^h Corrected val.	123.3					120.5				

^a Experimental values are from Bak et al. (1962); table values =calculated values (at each level of theory) - Experimental values.

^b Experimental values are found from Nielsen et al. (1969); table values =calculated values (at each level of theory) - Experimental values.

^c Experimental values are found from Tanabe et al. (1995); table values =calculated values (at each level of theory) - Experimental values.

^d Experimental values are found from Ogata et al. (1972) ; table values =calculated values (at each level of theory) - Experimental values.

^e Experimental values are found from Kovtun et al. (2015); table values =calculated values (at each level of theory) - Experimental values.

^f Experimental values are found from Jin et al. (2019); table values =calculated values (at each level of theory) - Experimental values.

^g Relevant calculated values are given in Table A.1.

^h Average of all functionals

Table A.7 – Experimental and Calculated frequencies (cm^{-1}), infrared intensities (km mol^{-1}) and Raman activities ($\text{\AA}^4/\text{amu}$) and Raman intensities ($\times 10^{-24} \text{F}^2 \cdot \text{m}^{-1} \cdot \text{kg}^{-1}$) of deuterated form of **1**

N.Sc. Freq.	Exp. ¹	Exp. ²	Cal.	IR Int	Ram Int
3324	3126	3126	3118	1.81	228.62
3321	3112	3125	3116	0.13	5.46
3284	3078	3098	3080	2.10	123.51
3270	3065	3098	3068	4.18	94.47
1583	1510	1507	1517	0.34	0.14
1478	1410	1409	1408	10.05	24.62
1417	1364	1360	1365	4.17	17.92
1280	1256	1256	1260	9.32	0.01
1107	1085	1085	1081	3.76	10.11
1103	1082	1083	1078	5.68	10.95
1072	1036	1036	1028	1.70	8.39
935	900	898	905	0.00	1.23
900	873	872	878	0.57	0.85
896	866	867	873	1.14	0.04
868	840	839	840	28.26	12.70
772	754	751	749	0.01	4.69
730	712	712	712	117.60	1.29
698	684	683	679	0.00	4.28
621	609	608	602	0.26	6.51
585	564	565	568	0.00	0.00
466	452	452	447	0.79	1.48

¹ Bozłowski1 et al. (995).

² Rico et a. (1965).

Table A.8 – Corrections for **8** geometrical parameters (bond lengths in Å, bond angles in degree) and their predicted values from analysis of similar compounds¹

	C=C					C-C				
	HF 6-31G*	MP2 6-31G**	MP3 6-311G*	B3LYP 6-31G**	M06-2X 6-31G**	HF 6-31G*	MP2 6-31G**	MP3 6-311G*	B3LYP 6-31G**	M06-2X 6-31G**
Mean^a	-0.027	0.003	-0.004	-0.005	-0.006	0.016	0.000	0.014	0.010	0.009
Corrected val. ^{b,1}	1.378	1.381	1.378	1.383	1.377	1.423	1.425	1.424	1.427	1.424
Corrected val. ^{b,2}	1.369	1.370	1.369	1.368	1.366					
Average of ^g Corrected val.	1.379 (C2=C3) & 1.368 (C4=C5)					1.425				
	C2-H					C4-H				
Mean	-0.012	-0.005	-0.003	-0.001	-0.002	-0.011	-0.004	-0.003	-0.001	-0.001
Corrected val. ^b	1.082	1.083	1.084	1.082	1.082	1.084	1.085	1.085	1.084	1.084
Average of Corrected val. ^g	1.083					1.084				
	S-C2 & S-C5					$\angle C-S-C$				
Correction^a value	0.012	0.004	0.011	0.022	0.010	-0.9	-0.2	-0.7	-0.7	-0.5
Corrected val. ^b	1.701	1.704	1.703	1.701	1.701	92.5	91.6	92.5	92.5	92.5
Corrected val. ^c	1.714	1.712	1.714	1.714	1.714					
Aver. Corrected val. ^g	1.702 (S1-C2) & 1.714 (S-C5)					92.3				
	$\angle C5 = C4 - H$					$\angle S1 - C2 - H$ & $\angle S1 - C5 - H$				
Mean	0.3	-0.1	0.2	-0.2	0.0	-0.1	-0.2	-0.4	-0.5	-0.4

continued

Table A.8 – (continued)

	HF 6-31G*	MP2 6-31G**	MP3 6-311G*	B3LYP 6-31G**	M06-2X 6-31G**	HF 6-31G*	MP2 6-31G**	MP3 6-311G*	B3LYP 6-31G**	M06-2X 6-31G**
10 ^b	-	-	-	-	-	-	-	-	-	-
11 ^c	-0.4	-0.7	-0.4	-1.0	-1.4	0.1	0.6	0.5	0.8	1.3
Corrections	-0.4	-0.7	-0.4	-1.0	-1.4	0.1	0.6	0.5	0.8	1.3
Corrected val. ^a	123.8	123.8	123.7	124.4	124.6	123.6	123.5	123.5	123.1	122.7
Average of Corrected val. ^h	124.1					123.3				

^a Corrections used for corresponding geometrical parameters in thiophene (Table A.6).

^b Relevant calculated values are given in Table A.3; 1 & 2 indicate the first and second parameter, respectively.

^c Average of all functionals.

¹ Compounds used in Table A.6 for the ring and C-H bond and compounds **10**, **11** and **12** for the remaining geometrical parameters.

^d Experimental values are found in Pappenfus et al. (2018); table values =calculated values (at each level of theory) - Experimental values.

^e Experimental values are found in Blake et al. (1999); table values =calculated values (at each level of theory) - Experimental values.

^f Experimental values are found in Ziegler & Nemykin (2012); table values =calculated values (at each level of theory) - Experimental values.

^g Relevant calculated values are given in Table A.3.

^h Average of all functionals

Table A.9 – Corrections for **9** geometrical parameters (bond lengths in Å, bond angles in degree) and their predicted values from analysis of similar compounds¹

	C2=C3 & C4=C5					C3-C4				
	HF 6-31G*	MP2 6-31G**	MP3 6-311G*	B3LYP 6-31G**	M06-2X 6-31G**	HF 6-31G*	MP2 6-31G**	MP3 6-311G*	B3LYP 6-31G**	M06-2X 6-31G**
Mean ^a	-0.027	0.003	-0.004	-0.005	-0.006	0.016	0.000	0.014	0.010	0.009
Corrected val. ^{b,1}	1.378	1.381	1.378	1.383	1.377	1.423	1.425	1.424	1.427	1.424
Corrected val. ^{b,2}	1.369	1.370	1.369	1.368	1.366					
Average of ^g Corrected val.	1.379 (C2=C3) & 1.368 (C4=C5)					1.425				
	C2-H					C4-H				
Mean	-0.012	-0.005	-0.003	-0.001	-0.002	-0.011	-0.004	-0.003	-0.001	-0.001
Corrected val. ^b	1.082	1.083	1.084	1.082	1.082	1.084	1.085	1.085	1.084	1.084
Average of Corrected val. ^g	1.083					1.084				
	S-C2 & S-C5					∠C – S – C				
Correction ^a value	0.012	0.004	0.011	0.022	0.010	-0.9	-0.2	-0.7	-0.7	-0.5
Corrected val. ^b	1.701	1.704	1.703	1.701	1.701	92.5	91.6	92.5	92.5	92.5
Corrected val. ^c	1.714	1.712	1.714	1.714	1.714					
Aver. Corrected val. ^g	1.702 (S1-C2) & 1.714 (S-C5)					92.3				
	∠C5 = C4 – H					∠S1 – C2 – H & ∠S1 – C5 – H				

continued

Table A.10 – (continued)

	HF	MP2	MP3	B3LYP	M06-2X	HF	MP2	MP3	B3LYP	M06-2X
	6-31G*	6-31G**	6-311G*	6-31G**	6-31G**	6-31G*	6-31G**	6-311G*	6-31G**	6-31G**
9 ^a	-	-	-	-	-	-	-	-	-	-
10 ^b	-	-	-	-	-	-	-	-	-	-
11 ^c	-0.4	-0.7	-0.4	-1.0	-1.4	0.1	0.6	0.5	0.8	1.3
Corrections	-0.4	-0.7	-0.4	-1.0	-1.4	0.1	0.6	0.5	0.8	1.3
Corrected val. ^a	123.8	123.8	123.7	124.4	124.6	123.6	123.5	123.5	123.1	122.7
Average of Corrected val. ^h	124.1					123.3				

^a Corrections used for corresponding geometrical parameters in thiophene (Table A.4).

^b Relevant calculated values are given in Table A.2; 1 & 2 indicate the first and second parameter, respectively.

^c Average of all functionals.

¹ Compounds used in Table A.4 for the ring and C-H bond and compounds **10**, **11** and **12** for the remaining geometrical parameters.

^d Experimental values are found in Pappenfus et al.(2018) ; table values =calculated values (at each level of theory) - Experimental values.

^e Experimental values are found in Blake, et al. (1999); table values =calculated values (at each level of theory) - Experimental values.

^f Experimental values are found in Ziegler & Nemykin (2012); table values =calculated values (at each level of theory) - Experimental values.

^g Relevant calculated values are given in Table A.4.

^h Average of all functionals

Table A.11 – Difference between the original quantum chemical and the final results for geometrical and rotational parameters of **1**, **8** and **9** (distances in Å°, angles in ° and rotational constants in MHz).

Compound	Thiophene	2CNT	3CNT
Bond lengths			
$\Delta S1C2$	-0.0044	-0.0073	0.0025
$\Delta S1C5$	-0.0044	-0.0064	0.0026
$\Delta C2C3$	0.0072	0.0005	-0.0026
$\Delta C3C4$	-0.005	-0.008	-0.0020
$\Delta C4C5$	0.0072	0.0055	0.0015
$\Delta C2/C3C6$	-	0.003	-
$\Delta C6N7$	-	-0.002	- 0.0020
$\Delta C2/C3H6/H8$	-0.002	0.0005	0.0004
$\Delta C3/C2H7/H8$		-	0.0016
$\Delta C4H8/H9$	-0.002	0.003	0.0016
$\Delta C5H9/H10$	0.0009	0.0005	0.0004
Bond Angles			
$\Delta S1C2C3$	-0.31	-0.62	0.17
$\Delta S1C5C4$	-0.31	0.52	0.09
$\Delta C2S1C5$	0.41	0.20	-0.37
$\Delta C2C3C4$	0.06	0.15	-0.10
$\Delta C3C4C5$	0.06	0.15	0.00
$\Delta S1C2H6/H8$	0.13	-	-0.01
$\Delta C3C2C6$	-	-0.10	-
$\Delta C4C3C6$	-	-	-0.40
$\Delta S1C5H9/H10$	0.13	0.20	1.19
ΔA	0.616	-18.013	14.078
ΔB	7.334	4.421	1.604
ΔC	2.722	3.552	1.519

$\Delta \equiv \text{Cal}_{QE} - \text{Cal}_Q$, where Cal_{QE} is the calculated value at M06-2X/6-31G(d,p)+empirical corrections (in Table 2) and Cal_Q , the calculated value at M06-2X/6-31G(d,p) (in Tables S1 for **1**, S2 for **8** and S3 for **9**).

Table A.12 – Experimental *vs* calculated frequencies (cm^{-1}), infrared intensities (km. mol^{-1}) and Raman activities ($\text{\AA}^4/\text{amu}$) and Raman intensities ($\times 10^{-24} \text{F}^2 \cdot \text{m}^{-1} \cdot \text{kg}^{-1}$) for **1**

	Exp [*]	NonScaled	Scaled	Scaling Factors	IR Int.	Ram. Activ	Ram. Int
<u>A₁ species</u>							
ν_1	3126	3324	3118	0.9381	1.81	228.62	8.95
ν_3	3078	3284	3080	0.9380	2.10	123.51	5.01
ν_6	1410	1476	1408	0.9533	10.05	24.62	5.59
ν_7	1364	1417	1365	0.9631	4.17	17.92	4.29
ν_{10}	1082	1103	1078	0.9772	5.68	10.95	3.84
ν_{11}	1036	1072	1028	0.9589	1.70	8.39	3.16
ν_{15}	840	868	840	0.9675	28.26	12.70	6.46
ν_{19}	609	621	602	0.9693	0.26	6.51	5.35
<u>B₁ species</u>							
ν_{14}	866	896	873	0.9740	1.14	0.04	0.02
ν_{17}	712	730	712	0.9749	117.60	1.29	0.84
ν_{21}	452	466	447	0.9599	0.79	1.48	1.87
<u>A₂ species</u>							
ν_{12}	900	935	905	0.9677	0.00	1.23	0.56
ν_{18}	684	698	679	0.9731	0.00	4.28	2.96
ν_{20}	564	585	568	0.9716	0.00	0.00	0.00
<u>B₂ species</u>							
ν_2	3112	3321	3116	0.9381	0.13	5.46	0.21
ν_4	3065	3270	3068	0.9380	4.18	94.47	3.88
ν_5	1510	1583	1517	0.9582	0.34	0.14	0.03
ν_8	1256	1280	1260	0.9845	9.32	0.01	0.00
ν_9	1085	1107	1081	0.9766	3.76	10.11	3.53
ν_{13}	873	900	878	0.9754	0.57	0.85	0.41
ν_{16}	754	772	749	0.9702	0.01	4.69	2.82

* Klots et al. (1994).

Table A.13 – Potential energy distribution of fundamental vibrational modes of the compound **1**

Frequency (cm^{-1})	PED (%)	Mode	Atoms ¹				PED (%)	Mode	Atoms ¹			
			h	k	l	m			h	k	l	m
In - plane modes												
3118	47%	νCH	2	6	0	0	47%	νCH	5	9	0	0
3116	48%	νCH	5	9	0	0	48%	νCH	2	6	0	0
3080	47%	νCH	4	8	0	0	47%	νCH	3	7	0	0
3068	48%	νCH	3	7	0	0	48%	νCH	4	8	0	0
1517	30%	$\nu\text{C}=\text{C}$	4	5	0	0	30%	$\nu\text{C}=\text{C}$	2	3	0	0
	9%	δCCH	4	3	7	0	9%	δCCH	3	4	8	0
1408	35%	νCC	3	4	0	0	11%	$\nu\text{C}=\text{C}$	4	5	0	0
	11%	$\nu\text{C}=\text{C}$	2	3	6	0	10%	δCCH	2	3	7	0
	10%	δCCH	5	4	8	0	6%	δCCH	4	3	7	0
1365	23%	$\nu\text{C}=\text{C}$	2	3	0	0	23%	$\nu\text{C}=\text{C}$	4	5	0	0
	11%	νSCH	1	2	6	0	11%	δSCH	1	5	9	0
	10%	δCCH	3	2	6	0	10%	δCCH	4	5	9	0

(Continued)

Table A.13 – (Continued)

Frequency (cm^{-1})	PED (%)	Mode	Atoms ¹				PED (%)	Mode	Atoms ¹			
			h	k	l	m			h	k	l	m
1260	13%	δCCH	5	4	8	0	13%	δCCH	2	3	7	0
	12%	δCCH	4	5	9	0	11%	δCCH	3	2	6	0
	10%	δSCH	1	5	9	0	10%	δSCH	1	2	6	0
1081	16%	δSCH	1	5	9	0	16%	δSCH	1	2	6	0
	12%	δSCH	1	2	6	0	12%	δSCH	1	5	9	0
	8%	$\nu\text{C}=\text{C}$	2	3	0	0	8%	$\nu\text{C}=\text{C}$	4	5	0	0
1078	11%	δSCH	1	5	9	0	11%	δSCH	1	2	6	0
	11%	δCCH	4	5	9	0	11%	δCCH	3	2	6	0
	11%	δCCH	5	4	8	0	11%	δCCH	2	3	7	0
1028	53%	νCC	3	4	0	0	7%	δCCH	4	3	7	0
	7%	δCCH	3	4	8	0						
873	20%	νSC	1	2	0	0	20%	νSC	1	5	0	0
	11%	δSCC	1	2	3	0	11%	δSCC	1	5	4	0
	9%	δCCC	2	3	4	0	10%	δCCC	3	4	5	0
840	30%	νSC	1	5	0	0	30%	νSC	1	2	0	0
749	28%	νSC	1	2	0	0	28%	νSC	1	5	0	0
	13%	δCCC	3	4	5	0	13%	δCCC	2	3	4	0
	5%	δCCH	5	4	8	0	5%	δCCH	2	3	7	0
602	32%	δCSC	2	1	5	0	15%	νSC	1	5	0	0
	15%	νSC	1	2	0	0	13%	δSCC	1	5	4	0
	13%	δSCC	1	2	3	0						
Out-of-plane modes												
905	28%	γHCCH	6	2	3	7	18%	γHCCH	7	3	4	8
	18%	γHCCH	8	4	5	9	18%	γSCCH	1	2	3	7
	8%	γSCCH	1	5	4	8	6%	γCCCH	5	4	3	7
878	25%	γHCCH	8	4	5	9	25%	γHCCH	6	2	3	7
	7%	γCCCH	2	3	4	8	7%	γCCCH	5	4	3	7
	7%	γCCCH	4	3	2	6	7%	γCCCH	3	4	5	9
712	15%	γCCCH	4	3	2	6	15%	γCCCH	3	4	5	9
	14%	γSCCH	1	2	3	7	14%	γSCCH	1	5	4	8
	11%	γCCCH	5	4	3	7	11%	γCCCH	2	3	4	8
679	22%	γCCCH	3	4	5	9	22%	γCCCH	4	3	2	6
	13%	γCSCH	2	1	5	9	13%	γCSCH	5	1	2	6
	8%	γHCCH	7	3	4	8	7%	γHCCH	8	4	5	9
568	27%	γCCCC	2	3	4	5	17%	γSCCC	1	2	3	4
	17%	γCCCS	3	4	5	1	9%	γCCCH	5	4	3	7
	9%	γCCCH	2	3	4	8						
447	25%	γCSC	4	5	1	2	25%	γSCCC	5	1	2	3
	16%	γCCCS	3	4	5	1	16%	γSCCC	1	2	3	4

^a Only contributions greater than 5% were taken into account; ^b See scheme 1 for atom numbering; ^c ν : stretching, δ : in-plane bending modes, γ : out-of-plane bending modes.

Table A.14 – Experimental and M06-2X/6-31G(d,p) (with empirical corrections) calculated rotational parameters.

	Exp ¹	Exp ²	Calc
A (MHz)	8041.770	8041.594	8041.456
B (MHz)	5418.120	5418.262	5417.404
C (MHz)	3235.770	3235.781	3236.812
Δ_J (kHz)	0.697	0.697	0.9596
Δ_K (kHz)	1.789	1.789	2.2477
Δ_{KJ} (kHz)	0.530	0.530	-0.2898
δ_J (kHz)	0.307		0.2976
δ_K (kHz)	0.867	0.307	0.087
μ_a (Debye)	-		0.5707
μ_b (Debye)	-		0.000
μ_c (Debye)	-		0.0000
μ_{tot} (Debye)	-		0.5707
I_{aa} (amu \AA^2)	62.863		62.847
I_{bb} (amu \AA^2)	93.304		93.288
I_{cc} (amu \AA^2)	156.232		156.135
κ			-0.092

¹ Bak et al. (1961); ² Kretschmer et al. (1993).

Table A.15 – Comparison of experimental and calculated (from M06-2X/6-31G(d,p) results) rotational transitions and their corresponding frequencies (in MHz) for ^{34}S -3CNT and ^{15}N -3CNT

^{15}N -3CNT				^{34}S -3CNT			
Rot. trans. $J''_{K-K_+} \leftarrow J'_{K-K_+}$	Exp. ¹ freq.	Calc. freq.	$\Delta\nu^2$	Rot. trans. $J''_{K-K_+} \leftarrow J'_{K-K_+}$	Exp. ¹ freq.	Calc. freq.	$\Delta\nu^2$
$4_{14} \leftarrow 3_{11}$	10090.103	10090.767	0.664	$5_{15} \leftarrow 4_{11}$	12712.925	12713.047	0.122
$4_{04} \leftarrow 3_{00}$	10517.886	10518.153	0.267	$5_{05} \leftarrow 4_{00}$	13213.230	13213.255	0.025
$4_{23} \leftarrow 3_{22}$	10589.007	10589.123	0.116	$5_{14} \leftarrow 4_{11}$	13966.574	13966.600	0.026
$4_{22} \leftarrow 3_{22}$	10666.204	10666.283	0.079	$6_{16} \leftarrow 5_{11}$	15235.434	15235.443	0.009
$4_{13} \leftarrow 3_{11}$	11068.864	11068.887	0.023	$6_{15} \leftarrow 5_{11}$	16734.449	16734.459	0.010
$7_{07} \leftarrow 6_{00}$	18129.744	18129.322	-	$7_{07} \leftarrow 6_{00}$	18289.946	18289.905	-
			0.422				0.041
$7_{26} \leftarrow 6_{22}$	18480.989	18481.065	0.076	$8_{18} \leftarrow 7_{11}$	20250.964	20250.873	-
							0.091
$7_{25} \leftarrow 6_{22}$	18892.302	18892.190	-	$8_{08} \leftarrow 7_{00}$	20771.237	20771.083	-
			0.112				0.154
$8_{18} \leftarrow 7_{11}$	20073.459	20073.285	-	$8_{27} \leftarrow 7_{22}$	21300.806	21300.795	-
			0.174				0.011
$8_{08} \leftarrow 7_{00}$	20594.190	20593.138	-	$8_{17} \leftarrow 7_{11}$	22220.048	22219.978	-
			1.052				0.070
$8_{27} \leftarrow 7_{22}$	21095.486	21095.416	-	$9_{19} \leftarrow 8_{11}$	22743.234	22743.254	0.020
			0.070				
$8_{26} \leftarrow 7_{22}$	21690.485	21690.367	-	$9_{09} \leftarrow 8_{00}$	23219.705	23219.841	0.136
			0.118				
$8_{17} \leftarrow 7_{11}$	21994.579	21994.550	-	$9_{28} \leftarrow 8_{22}$	23928.745	23928.744	-
			0.029				0.001
$9_{09} \leftarrow 8_{00}$	23023.776	23024.716	0.940	$9_{27} \leftarrow 8_{22}$	24783.074	24783.069	-
							0.005
$9_{28} \leftarrow 8_{22}$	23699.689	23699.606	-	$9_{18} \leftarrow 8_{11}$	24929.388	24929.451	0.063
			0.083				
$9_{27} \leftarrow 8_{22}$	24509.776	24509.841	0.065				
$9_{18} \leftarrow 8_{11}$	24680.423	24680.629	0.206				

¹ $\Delta\nu = \nu_{\text{Calc}} - \nu_{\text{Exp}}$

² From J. Wiese, R. Schwarz and D. H. Sutter (1980).

Table A.16 – MKS and NPA HF/def2-QZVPP calculated partial atomic charges for thiophene and NPA B3LYP/def2-QZVPP calculated partial atomic charges for **9**.

compound	Model	S1	α	β
Thiophene	MKS HF/def2-QZVPP	0.062	-0.147	-0.111
	NPA HF/def2-QZVPP	0.062	-0.147	-0.111

Compound	Model	S1	C2	C3	C4	C5	C6	N
3CNT	NPA B3LYP/def2-QZVPP	0.073	-0.069	0.239	-0.105	-0.033	-0.136	-172